From Polymer Precursors to Metal Oxides:

Preparation and Characterization of Zinc Oxide and ZnO-Based Mixed Metal Oxide Nanoparticles

Dissertation zur Erlangung des Grades
„Doktor der Naturwissenschaften“
am Fachbereich Chemie, Pharmazie und Geowissenschaftern
der Johannes-Gutenberg-Universität in Mainz

vorgelegt von

Guangqiang Lu
geboren in Anhui / P. R. China

Mainz, 2006

Tag der mündlichen Prüfung: Dezember 11, 2006.

Die vorliegende Arbeit wurde im Zeitraum von Oktober 2003 bis Oktober 2006 am Max-Planck-Institut für Polymerforschung in Mainz unter der Anleitung von Herrn Prof. Dr. G. Wegner angefertigt.

For my families

List of Abbreviations and Symbols

Chemicals

AA	acrylic acid
BPO	benzoylperoxide
ES5P	zinc-loaded polymer sample using Span 60 as emulsifier
ES8P2	zinc-loaded polymer sample using Span 80 as emulsifier
MMO	mixed metal oxide
PAA	polyacrylic acid
PAA5K	polyacrylic acid with molecular weight of 5000
$PANH_45K$	ammonium polyacrylate with molecular weight of 5000
SDS	sodium dodecyl sulphate
Span 60	sorbitane monostearate
Span 80	sobitan monooleate
ZnCoPA	zinc-cobalt polyacrylate
ZnMgPA	zinc-magnesium polyacrylate
ZnPA	zinc polyacrylate
ZnPA5K	zinc polyacrylate with molecular weight of 5000
ZnCoO	zinc-cobalt oxide
ZnMgO	zinc-magnesium oxide

Methods and related acronyms

AAS	Atomic absorption spectroscopy
AFM	Atomic force microscopy
CW-EPR	Continuous wavelength-electron paramagnetic resonance spectroscopy
CELREF	Free software used for refinement of XRD data
DLS	Dynamic light scattering
DSC	Differential scanning calorimetry
DTGA	First-order differential TGA
EA	Elementary analysis
EDX	Energy dispersive X-ray spectroscopy
EPR	Electron paramagnetic resonance spectroscopy
FTIR	Fourier transfer infrared spectroscopy

HRTEM	High-resolution TEM
LS	Light scattering
MAS-NMR	NMR spectroscopy measured under rotation of the sample at magic angle of 54.7°
PL	Photoluminescence
^{31}PNMR	^{31}P nuclear magnetic resonance spectroscopy
SEM	Scanning electron microscopy
SQUID	Superconducting quantum interference device
TEM	Transmission electron microscopy
TGA	Thermogravimetric analysis
TG-MS	TGA coupled with mass spectra
XRD	X-ray diffraction
UV/Vis	Ultraviolet / visible absorption spectroscopy
BSE	Primary backscattered electrons
DMS	Dilute magnetic semiconductor
DVLO	Theory of colloidal stability developed by Derjaguin, Verwey, Landau and Overbeek
FFT	Fast Fourier transform
FWHM	Full width at half maximum
HCP	Hexagonal close packing
JCPDS	Joint Committee on Powder Diffraction Standards
NBE	Near-band-edge emission
SE	Secondary electrons
SDC	Shallow donor center
TADC	Theory of average dielectric constant

Symbols

β	Heating rate (in Ch.2) Full width at half maximum (in Ch.4)
η	Viscosity
η_{red}	Reduced Viscosity
λ	Wavelength (nm)
λem	Emission wavelength
λexc	Excitation wavelength

μm	Micrometer (10^{-6}m)
nm	Nanometer (10^{-9}m)
Π	Osmotic pressure
Δp	Laplace pressure
$\Delta\nu_{a-s}$	Frequency difference of carboxylate antisymmetric and symmetric stretching
θ	Angle (^{o})
ζ	Zeta-potential
κ	Debye length (in Ch.2)
	Susceptibility (in Ch.4)
a	Lattice parameter
c	Concentration (in Ch.2)
	Lattice parameter (in Ch.4)
f	Filling factor
g	g-factor of EPR (in Ch.2, 4)
	Shape factor (in Ch.5)
t	Time
tM	3d-transition metal ions
x	Composition of mixed metal oxide
$E\mathrm{a}$	Activation energy
L_{hkl}	Crystallite size or coherence length
M	Magnetization
M_n	Number averaged molecular weight
N_{A}	Avogadro’s number
O_i	Interstitial Oxygen
R_h	Hydrodynamischer Radius
T	Temperature
T_C	Curie temperature
T_P	Peak Temperature of DTGA
V_O	Oxygen vacancies
V_{Zn}	Zinc vacancy
Zn_i	Zinc interstitial

Abstract

We report on a strategy to prepare metal oxides including binary oxide and mixed metal oxide (MMO) in form of nanometer-sized particles using polymer as precursor. The process consists of wet chemistry, precipitation and pyrolysis three steps, which starts from aqueous solution to form a metal polyacrylate precursor under mild preparation conditions. The metal polyacrylate precursor is purified by precipitation into a nonsolvent. The polymer precursor could be redissolved and loaded with different kinds of metal ions. The purified cation-loaded complex in dry form is calcined at relatively low temperature to give nanosized crystals of binary oxide or MMO powders. The composition of the precursor polymer defines the stoichiometry of the mixed metal oxide. Moreover, the polymer-metal salt solution can also be processed by spin coating, drop casting or similar procedure to obtain polymer precursor films for production of nanocrystalline metal oxide films.

We chose zinc oxide as the model system to prove the concept of this strategy due to the simple (hexagonal) crystal structure of zinc oxide and its increasing interests in industrial application and fundamental research. The zinc polyacrylate (ZnPA) precursor is amorphous as confirmed by X-ray diffraction (XRD) and transmission electron microscopy (TEM). Dynamic light scattering (DLS) results reveal that zinc cations mainly form intra-polymer complexes with polyacrylate. Viscosity and UV results show that the precursor was effectively purified during precipitation into the nonsolvent acetone, which proves that the zinc source of ZnO formation is the polymer precursor and not the free zinc ion or other zinc-containing species.

The transformation from polymer precursor via degradation, nucleation followed by crystallization into ZnO crystal during pyrolysis was investigated by means of XRD, thermogravimetric analysis (TGA) and FTIR spectroscopy. The XRD results show that the precursor remains amorphous when heated even over 370 ^{o}C, while the polymer precursor from Pechini method and some zinc salts like zinc nitrate hexahydrate, zinc acetate dihydrate convert to zinc oxide at about 300 ^{o}C. The TGA results exhibit three weight loss stages in the pyrolysis process i.e. 150-260 ^{o}C , 260-350 ^{o}C and 350-460 ^{o}C. By combination with mass spectra (MS), it is revealed that the main weight loss is due to escape of H_2O and CO_2. The as-synthesized ZnO consists of mainly individual particles with a diameter around 40 nm with a narrow size distribution as shown by scanning electron microscopy (SEM). Due to Oswald ripening, the particles grow to 100 nm at 650 ^{o}C. The effects of various parameters like polymer molecular weight and zinc content in the precursor on the crystal morphology were studied too. The as-synthesized ZnO surface absorbs some organic groups like OH- and C-O indicated from FT-IR spectra. The photoluminescence (PL) and electron paramagnetic (EPR) properties of the material are investigated, too. It is generally assumed that the PL emission originates from oxygen defect centres located on the particle surface or in the bulk.

Employing this method, ZnO nanocrystalline films are fabricated via pyrolysis of a zinc polyacrylate precursor film on solid substrate like silicon and quartz glass. The results of XRD, UV spectra as well as the TEM images prove that both the ZnO nanopowder and film undergo same decomposition steps with the crystallation from ZnPA precursor to ZnO taking place at around 450 ^{o}C. Comparing the photoluminescence of films fabricated in different gases (O_2, N_2, air and argon), it is assigned that the blue emission of the ZnO film is due to oxygen-favorable defects center of zinc vacancy and green emission from oxygen-unfavorable center of oxygen vacancy.

Two kinds of nanometer-sized mixed metal oxide particles ($Zn_{1-x}Mg_xO$ and $Zn_{1-x}Co_xO$) with very precise stoichiometry are prepared employing this versatile polymer-based method. The precursor is formed by loading different metal ions in polyacrylates sequentially and purified via repeated precipitation/redissolution cycles. The calcination of polymer precursor at relatively low temperature (550 ^{o}C) gives metastable solid solution of oxide systems in a particular range of composition. The MMO crystal particles are typically 20-50 nm in diameter. Doping of Mg in ZnO lattice causes shrinkage of lattice parameter c, while it remains unchanged with Co incorporation. Effects of band gap engineering on the optical band gap are seen in the Mg:ZnO system. The photoluminescence in the visible is also affected and its maximum shifts from 2.12 eV (pure ZnO) to 2.32 eV at $x = 0.21$.
The photoluminescence in the visible is enhanced by incorporation of magnesium on zinc lattice sites, while the visible emission is suppressed in the Co:ZnO system. This points toward the usefulness of our approach to create photo emissive materials with tuneable sensitivity. Magnetic property of cobalt doped-ZnO is checked too and ferromagnetic ordering is not found in our sample.

An alternative way to prepare zinc oxide nanoparticles is presented upon calcination of zinc-loaded polymer powders, which is synthesized via inverse miniemulsion polymerization of the acrylic acid and zinc nitrate mixture. The obtained polymer latex in the inverse miniemulsion has a size of 50-100 nm predefined by the droplet size of the inverse miniemulsion. Proper choice of the surfactant is key to the morphology and quality of the polymer latex. In this work, we use span 80 as emulsifier, with which monodisperse latex particles could be achieved as characterized by means of DLS and SEM.

The calcination of the precursor in the dry form gives nanosized ZnO nanopowders in diameter of 20-40 nm. The photoluminescence property of the as-prepared zinc oxide is checked, which exhibits strong orange-to-yellow emission with 15 nm red shift in comparison with the ZnO obtained by the polymer-salt complex method. And the IR spectra of the samples differ with each other as well. The FT-IR spectrum shows that the as-prepared ZnO surface has unidentate complex between zinc ions and carboxylate and also reveals a slight aggregated state of the sample morphology. The difference in the optical property between the ZnO samples prepared from different preparation methods actually reflects the difference of composition and architecture of the precursor polymers.

The obtained ZnO and ZnO-based mixed metal oxide nanoparticles undergo surface modification to separate the weakly-aggregated particles and enhance their compatibility as well as stability with polymer. The nanoparticles are treated in ethanolic solution of tetrabutylammonium phosphate with applying ultrasonication. The surface reaction achieves anchoring the phosphate groups on the particle with preservation the spherical structure and size of the particles as characterized by means of elementary analysis, FT-IR, ^{31}PNMR, and electron microscopy. Light scattering results indicate the decrease of amount of aggregated ZnO particles after the surface reaction. And stability of the ZnO nanoparticles in aqueous dispersion is enhanced as indicated by the zeta-potential increasing from -9.3 mV (unmodified ZnO) to -28.8 mV (modified ZnO) due to the significant change of the charge density on the particle surface.

Table of Contents

3. Formation of ZnO Nanocrystalline Film 77

4. Preparation of ZnO-Based Mixed Metal Oxide Nanoparticles 97

1 Introduction

1.1 Review on the synthesis of nanosized crystals

1.1.1 Nanocrystal as research topic

‘There is plenty of room at the bottom.’- R. Feynman, 1959. Nanosized materials have become one of the most vibrant fields and have attracted tremendous interest in fundamental research as well as industrial application since the end of the last century. The US National Nanotechnology Initiative announced at the beginning of 2000 and brought the US government’s investment in nanoscience to a total of 500 million USD in the 2001 financial year (an increase of 83% compared to 2000). Statistics have shown that research and development investments in nanotechnology world widely have increased by more than six-fold to about 3 billion USD from 1997 to 2003.[1-2]

Table 1.1. *Effects of nanomaterials and applications due to the reduced dimension.*[1]

Effects	Applications
Higher surface to volume ratio, enhanced reactivity, improved transport kinetics	Catalysis, solar cells, batteries, gas sensors, hydrogen storage
Higher resistivity with decreasing grain size	Conductivity of materials
Increased hardness with decreasing grain size	Hard coatings, thin protection layers
Variation of bandgap with grain size	Optoelectronics, quantum dot
Lower percolation threshold	Electronics, passive components, sensors
Lower melting and sintering temperature	Low sintering materials

The great interest in nanomaterials is due to their unique behaviour and technical application based on the small size and structure. The nanoscience and technology deal with particles with diameter of 1 to 100 nm, or about 10 to 10^6 atoms or molecules per particle. Because of the small particle size, the materials have very large surface area to volume ratio, bringing out new physical and chemical properties which are different with their lager scale counterparts. The mechanisms of the property change of the material include size effect for instance quantum effects, change of dimensionality of the system, change of atomic structure (e.g. average atomic density, nearest-neighbour coordination, etc.).[1-4] Nanomaterials are versatile and have been widely used in the fields of information and communication technologies, biotechnology and medicine, optoelectronics (Table 1.1). For example, nanosized ZnSe and ZnS particles, due to quantum confinement, are promising materials emitting in the blue to the ultra violet range.[6-7] Another good example is that the sensing ability of individual SnO_2 nanowires and nanoribbons as gas sensors was improved significantly after functionalization with Pd catalyst nanoparticles by in situ deposition.[8]

A nanocrystal is defined as a fragment of a solid comprising somewhere between a few atoms and a few ten thousand of atoms. Considerable advances have been achieved in the chemistry of nanocrystals by the development of diverse synthesis methods to gain nanocrystals with different chemical composition and shape. Because of the small size, the ratio of bulk to surface free energy is dominant and the nanocrystals are unstable. Accordingly, surface modification methods like surface etching, functionalization and coating have also been developed. Along with the advances in nanocrystal synthesis, modern characterization tools capable of studying individual clusters have been developed and these—together with more conventional structural, electronic and optical probes—have allowed to obtain detailed information and insights into the properties of nanocrystal materials.

1.1.2 Nanocrystal synthesis methods

Several main synthesis methods for nanocrystal are reviewed in the following. According to Riman,[28] the chemical methods of synthesis can be classified as compiled in Table 1.2.

Table 1.2. *Synthesis methods for nanocrystals.[28]*

Type	Method
Chemistry in liquid phase	Sol-gel type reactions Chemical precipitation
Chemistry in heterogeneous phase	Hydrothermal synthesis Pyrolysis
Chemistry in a droplets	Emulsion/microemulsion Spray pyrolysis
Chemistry in vapor phase	Chemical vapor deposition

The sol-gel method is a widely used method because of its simplicity.[9] The process involves inorganic precursors (a metal salt or organometallic molecule) that undergo various reactions resulting in the formation of a threedimensional covalent network.[10] Nanocrystals are then formed upon thermal decomposition under proper gas atmosphere. A general scheme is presented (scheme 1.1) for the hydrolysis and condensation of metal alkoxides to form larger metal oxide crystals: where M represents the metal and R the alkyl group.

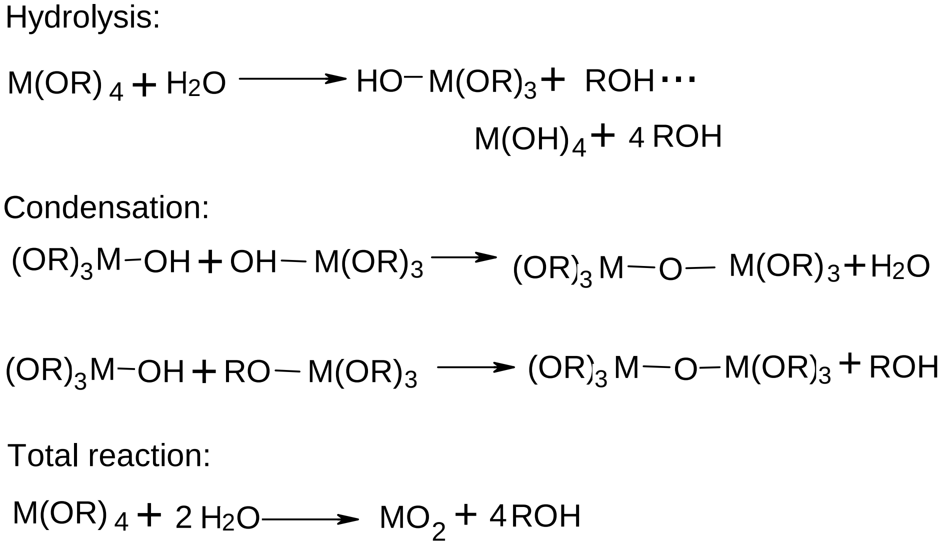

Hydrolysis:

$$M(OR)_4 + H_2O \longrightarrow HO{-}M(OR)_3 + ROH \cdots$$
$$M(OH)_4 + 4\,ROH$$

Condensation:

$$(OR)_3M{-}OH + OH{-}M(OR)_3 \longrightarrow (OR)_3M{-}O{-}M(OR)_3 + H_2O$$

$$(OR)_3M{-}OH + RO{-}M(OR)_3 \longrightarrow (OR)_3M{-}O{-}M(OR)_3 + ROH$$

Total reaction:

$$M(OR)_4 + 2\,H_2O \longrightarrow MO_2 + 4\,ROH$$

Scheme 1.1

The size of the gel particles depends on the solution composition, pH, and temperature. By controlling these factors, one can tune the size of the particles. This method has been used to synthesize metal oxide nanostructures, such as TiO_2,[11] $WO_{2.72}$,[12] ZrO_2,[13] CeO_2,[14] SnO_2,[15] SiO_2,[16] CuO,[17] Al_2O_3,[18] etc. Some mixed metal oxides such as $Ti_{1-x}Sn_xO_2$,[19] $BaTiO_3$,[20] $BaZrO_3$,[21] $CaSnO_3$,[22] etc. have also been produced. The method has been employed as well for preparation of some non-oxide nanocrystals.[23-24]

Chemistry in a liquid phase, the so-called 'wet chemistry' method is an approach in which the nanostructure and its physical properties are controlled by nucleation, growth and ageing processes in solution. The particle size is influenced by the conditions such as reactant concentration, pH, and temperature etc. Coprecipitation of cations and anions in the solution is a straightforward and simple method which forms inorganic particles directly or an intermediate precursor which is then subject to a heating treatment to produce nanocrystals. Normally, it is very difficult to experimentally determine whether the as-prepared precursor is a single-phase solid solution or a multiphase, nearly-homogeneous mixture for instance in the cases of coprecipitated hydroxides or carbonates of mixed metals. Using the coprecipitation method metal oxides like Fe_2O_3,[25] Fe_3O_4,[26] ZnO,[27] non-oxide nanocrystals like AlN,[28] Si_3N_4,[29] CdS[30] and even very complex nanostructures such as CdS/HgS/CdS,[30] CdS/(HgS)2/CdS[31] and other core/shell structures can be prepared.

It is worthwhile mentioning a technique in the wet chemical synthesis which makes use of an appropriate capping reagent to control kinetically the growth rates of nanocrystals and prevent agglomeration of the particles. Monodisperse silver nanocrystal of different morphology were synthesized in large quantities by reducing silver nitrate with ethylene glycol in the presence of poly(vinyl pyrrolidone) (PVP).[32] The authors found that the ratio of PVP to silver nitrate played an important role in determining the shape and size of the product. And the as-synthesized silver cubes could be used as sacrificial templates to generate single-crystalline gold nanoboxes. Pt nanoparticles were produced in the presence of capping polymer. The influence of the polymer on the morphology of the product is demonstrated.[33] $CoPt_3$, FePt, $CoPd_2$ et al. semiconductor nanocrystals grown up in the presence of carboxylic acids and amines have been investigated, too.[34] The size of the nanocrystals can be precisely tuned in a predictable and reproducible way. Semiconductors like CdSe,[35] CdS,[36] ZnO,[37] Fe_2O_3[38] are also produced using a similar mechanism.

Hydrothermal synthesis, which strictly should be called ‘solvothermal’ when the reaction solvent is not water, is another common method to synthesize crystals. Rabenau reviewed the development of this method since the nineteenth century.[39] According to the definition given by him, the hydrothermal synthesis is an approach by using water as solvent in a sealed reaction container when the temperature is raised above 100 °C. This method exploits the solubility of almost all inorganic substances in water at elevated temperatures and pressures and subsequent crystallization of the dissolved material from the fluid. Solvent at hydrothermal conditions (elevated temperatures and high pressure) provides a mass transport path promoting phase transformation kinetics. The properties of the reactants, including their solubility and reactivity, change at high temperatures as well. The changes mentioned above provide more parameters to produce different kinds of high-quality nanocrystals with different shapes, which are not possible to be formed at low temperatures. The synthesis parameters such as water or organic solvent, pressure, temperature, reaction time, and the respective precursor-product system can be adjusted in the experiment to maintain a high nucleation rate and good size distribution. Different types of nanoparticles such as TiO_2,[40] $BaTiO_3$,[41] ZrO_2,[42] $SrTiO_3$;[43] nanotubes such as SnS_2,[44] Hematite (a-Fe_2O_3)[45] and Bi_2S_3 nanowires,[46] hydroxyapatite $Ca_{10}(PO_4)_6(OH)_2$ nanorods [47] and inorganic/organic hybrid materials $[NH_3(CH_2)_2NH_2(CH_2)_2NH_3]_2[Mo_9O_{30}]$[48] have been successfully synthesized in this way.

It is worth noting that recently Niederberger and coworkers[49] presented a widely applicable solvothermal route to nanocrystalline iron, indium, gallium, and zinc oxide based on the reaction between the corresponding metal acetylacetonate as metal oxide precursor and benzylamine as both solvent and reactant. A combined solvolysis-condensation mechanism was proposed. Fig. 1.1 shows TEM images of the different nanocrystallites and their respective electron diffraction pattern. The authors expect that the method can be easily scaled-up to satisfy industrial requirements.

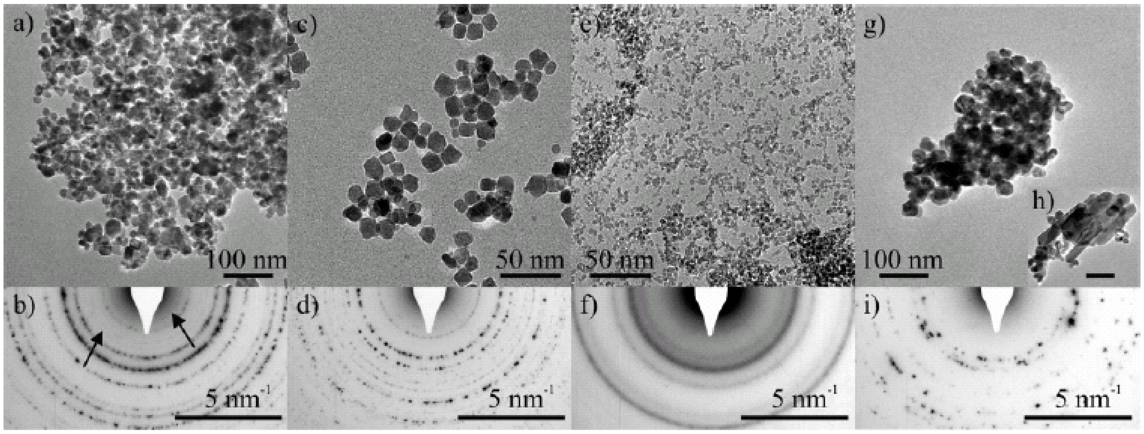

Fig. 1.1. *TEM overview images of (a) iron oxide, (c) indium oxide, (e) gallium oxide, (f) zinc oxide and their respective SAED patterns(b, d, f, i). (Reprinted with permission from Ref. [49]. Copyright 2005 American Chemical Society.)*

Other methods like direct pyrolysis of a precursor, chemical or physical vapour deposition, templating, and synthesis in microemulsion are also successful in some nanocrystal synthesis. For example, Wang et al.[50] have prepared a series of semiconducting oxides of zinc, tin, indium, cadmium, and gallium in form of ribbon-like nanostructures (so-called nanobelts) by simply evaporating the desired commercial metal oxide powders at high temperatures. The as-synthesized oxide nanobelts are pure, structurally uniform, and single crystalline free of crystal defects with typical width of 30 to 300 nm in a rectangular cross section and width-to-thickness ratios of 5 to 10, at a length of up to a few millimeters. Mann and his colleagues[51] synthesized $BaCrO_4$ nanoparticles in an inverse (water-in-oil) microemulsion. They believe that the microemulsion-based process could be of general importance for controlling the secondary growth of the pre-organized nanoparticle-based superstructures. The recent advances in the preparation methods of nanostructured crystals can be found in some publications.[28, 52]

1.2 Introduction of the status of research about zinc oxide

1.2.1 Synthesis methods for ZnO and shape control

Various metal oxides in form of crystals exhibiting different size and shapes have been prepared using the common synthesis methods. Amongst the metal oxides, zinc oxide is one of the most important and promising materials based on several intrinsic virtues: Firstly, ZnO has high thermal and chemical stability, which plays an important role in material chemistry and nanotechnology. Secondly, it is one of the few oxides that show quantum confinement effects, allowing a fine-tuning of the band gap in an experimentally accessible size range.

Zinc oxide crystallizes in hexagonal structure, namely zincite. Its crystal structure has Zn atoms tetrahedrally coordinated to four O atoms, where the Zn d-electrons hybridize with the O p-electrons. The structure is composed of two interpenetrating hexagonal-close-packed (hcp) sublattices, each of which consists of one type of atom displaced with respect to each other along the threefold *c*-axis. (Scheme 1.2)

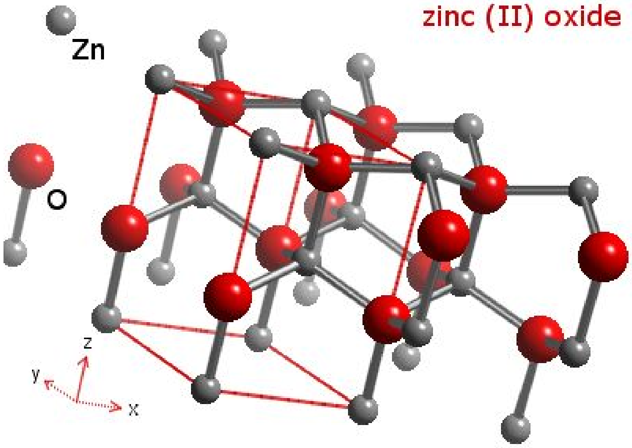

Scheme 1.2

Schematic representation of a wurtzite ZnO structure

(Reprinted with permission from WebElements [http://www.webelements.com/])

ZnO is a wide-bandgap semiconductor (3.37 eV) with a large exciton binding energy (60 meV) at room temperature.[53] It has been used in a wide range of technical areas such as optical devices,[54] transparent conducting electrodes,[55] field-effect transistors,[56] gas sensors,[57] varistors,[58] catalysts, [59] etc. For instance, one-dimensional structured ZnO is a potential alternative for carbon-nanotubes in field-emission devices based on its outstanding thermal and chemical stability. Furthermore, it is one of the few oxides that show quantum confinement effects, allowing variation of the position of the electronic bands in an experimentally accessible size range.[60] Various techniques have been employed for the preparation of ZnO nanocrystal with different size and shape, such as sol-gel method,[61] spray pyrolysis,[62] pulsed laser deposition,[63] template method,[64] vapour synthesis,[65] wet chemical route,[66] emulsion/microemulsion,[58c,67] hydrothermal,[68] polymer precursor (so-called Pechini method),[69] thermal decomposition,[70] microwave methods,[71] etc.

Nanostructured zinc oxide particles with abundant morphologies have been produced, including individual ZnO nanoparticles,[66b,70a,72] nanowires[53,73] and dendritic nanowires,[74] nanobelts,[50, 75] nanorods,[37b,56,73,76] nanotubes,[77] and nanocantilevers.[78] Certainly, the morphology of the ZnO nanocrystal is related to the synthesis methods and experimental conditions. Cross et al.[53] report preparation of ZnO nanowire by depositing a 150 nm thick layer using room temperature radio frequency magnetron sputtering followed by hydrothermal growth at 90 °C. The nanowires grow preferentially along the *c*-axis of ZnO up to 2 micron long in average. Han et al.[65b] prepared ZnO with unusual nanocone array structure via vapour synthesis at low temperature. The as-synthesized ZnO crystals are *c*-axis oriented too and the growth mechanism is proved to be a self-catalyzed vapor-liquid-solid (VLS) process. Hsu and coworkers[76] achieved directed growth of ZnO nanorods on a silver film in a predetermined pattern using an organic template. Another group prepared ZnO one-dimensional nanostructures via hydrothermal process using polyethylene glycol (PEG) to assist crystal formation.[73] They found that ZnO nanowires and nanorods can be selectively synthesized using a short-chain polymer PEG400, while a relatively long-chain polymers (such as PEG10000) did not work. Two-dimensional ZnO nanocrystals have also been prepared. Wang et al.[79] employed a solution-based synthesis of ZnO rings and disks at low temperature and on a large scale, using NaAOT as template. The as-synthesized materials are structurally uniform. The two morphologies are interchangeable, i.e. disks could be converted into rings by simply controlling growth temperature and molar ratio of reactants. The technique is believed to be applicable for synthesis of a wide range of nanomaterials. Using such well-structured materials as building blocks, one could design a diverse range of nanodevices, from nanoscale lasers to sensors and photonic crystals.

Some unusual morphological forms such as flower-[68c,80] prism-like[81] shapes have been produced as well. Qian et al. shows the formation of ZnO flower-, tower- and tube-like structures by a solution route. The change of the morphology is simply controlled by variation of pH, reaction temperature and concentration of the reactants.[80]

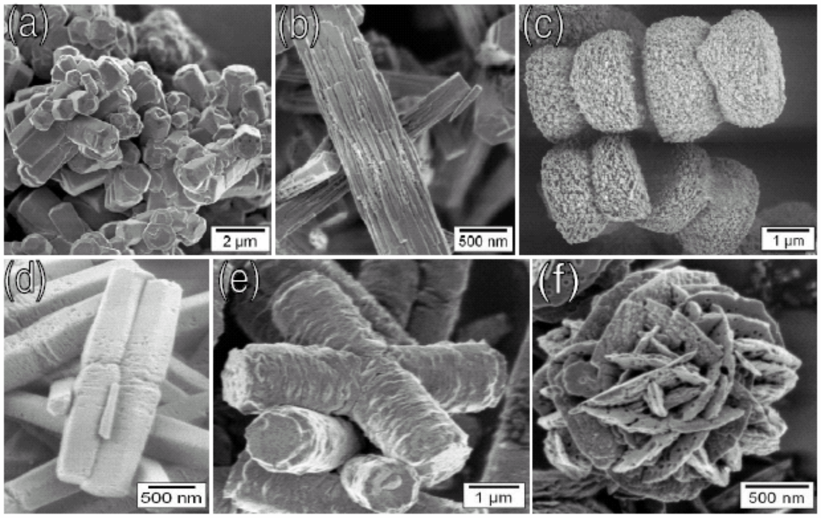

Fig. 1.2. *SEM images showing the formation of composite crystals in ZnO precipitated from aqueous medium in the presence of different latex additives: (a) clusters formed by aggregation, (b) parallel growth, (c) twins, (d) partially interpenetrate twins, (e) and (f) interpenetration of crystals. (Reprinted from Ref. [86] with courtesy of R. Munoz-Espi.)*

The control of the ZnO nanocrystal morphology by ions, small molecules or polymers as the structure-directing agents, which are called morphological modifier in some publications as well, has also been investigated in recent years. Liu et al.[82] reported a low-temperature, solution-based approach for the preparation of oriented ZnO nanostructures, achieving the systematic modification of their crystal morphology. They found that citrate anions that selectively adsorb on ZnO basal planes can suppress crystal growth along the *c*-axis and with increasing citrate concentration the ZnO nanomaterial shows an *in situ* column-to-plate morphological transition. Similar results were reported by Imai et al.,[83] They obtained a seaweed-like ZnO nanostructure by using phosphate as modifier. The significant effects of certain polymers including block,[84] graft copolymers,[85] functionalized polystyrene latex from miniemulsion polymerization[86] and even biogenic polymers like starch[87] on ZnO crystal habit have been shown recently. The ZnO crystal can be controlled by the presence of polymer additives and various morphological forms have been produced such as nanoneedles, nanorods, stack of pancakes, onion- and flower-like structures etc. Some representative ZnO nanostructures are shown in Fig. 1.2.

1.2.2 Production of ZnO-based mixed metal oxides materials

1.2.2.1 Application of ZnO-based mixed metal oxides materials

Mixed metal oxides (MMO) formed by more than one kind of different metal cations expand the utility of binary oxides and attract a lot of interest in fundamental research as well as technical application. ZnO-based metal oxides alloys or so-called doped-ZnO materials in the case when only several percent of impurity ions which exist dissolved in the ZnO lattice exhibit modified electrical and optical properties, which make the materials promising for applications such as sensors,[88] field-emitters,[89] p-n diodes,[90] bandgap engineered devices[91] and diluted magnetic semiconductors (DMS) for spintronics.[92]

The doping of foreign cations can modify photoluminescence (PL) of zinc oxide. For instance, there have been disputes for decades on the origin of the green emission, centered at about 550 nm in the undoped ZnO. Some researchers believe that it is related to intrinsic defect levels formed by point crystal defects like a doubly ionized zinc vacancy (V_{Zn})[93] or an ionized interstitial (Zn_i),[94] oxygen vacancies (V_O),[95] and/or interstitial oxygen (O_i),[95] have also been involved. While others consider that it comes from unintentional impurity of copper cations.[96] Further work[97] unified the controversy through the experimental results and suggests that the green emission band with a characteristic fine structure is most likely related to the copper impurities, whereas the structureless green emission band at nearly the same position and width may be related to a native point defect such as V_O or V_{Zn}.

Li and Al doping in ZnO also produce extrinsic defects as acceptor and donor levels, respectively. Fujihara et al.[98] prepared (Al, Li)-doped ZnO thin films of desired the Al and Li concentrations via metal-organic decomposition method. They found when the Al concentration was fixed to 1 at. % and Li was varied between 0 and 3 at. %, the films exhibited a yellow emission centred at approximately 525 nm and its intensity decreased with Li content increase. It can be therefore proposed that the shallow levels can indeed produce yellow emission. The PL properties of the codoped ZnO films annealed under air, O_2, N_2, and H_2/N_2 atmospheres respectively have also been examined but none of them exhibited bluish PL. It is concluded that doping by aliovalent cations in ZnO can quench the green emissions in comparison with the finding that undoped ZnO annealed under a reducing atmosphere can emit intense green PL centered at 498 nm.

ZnO nanoneedle arrays are suggested to be one of the most promising candidates for field emitters. And it has been demonstrated that field emission characteristics of ZnO 1D nanostructures could be enhanced by an increase in electrical conductivity by means of doping. Xu *et al*[89a] reported that the enhancement of field emission characteristics of ZnO nanofibre arrays can be achieved by Ga doping, and Jo *et al*[89b] also demonstrated that hydrogen annealing can affect the enhancement of ZnO nanowire field emission properties.

ZnO in wurtzite structure is naturally an n-type semiconductor because of small deviations from stoichiometry due to the presence of intrinsic defects such as oxygen vacancies and Zn interstitials.[99] Undoped ZnO shows intrinsic n-type conductivity with very high electron densities of about 10^{21} cm^{-3}.[100] Compared to p-type, n-type doping in ZnO is much easier to obtain. Group-III elements Al, Ga, and In as substitutional elements for Zn and group-VII elements Cl and I as substitutional elements for O can be used as n-type dopants. The obstacles to achieve *p*-type ZnO are due to some reasons. Dopants may be compensated by low-energy native defects, such as Zn_i or V_O, or background impurities (H).Low solubility of the dopant in the host material is also another possibility. A few papers[101] on *p*-type ZnO epitaxial thin films have been published.

There is a strong interest in the development of wide band gap semiconductor gas sensors for applications for instance in detection of fuel leak detection in automobiles, spacecraft and aircraft, fire detectors, exhaust diagnosis and emissions from industrial processes etc. ZnO is one of the most promising materials for gas sensor applications. Wang et al.[88] found that the conductivity increased rapidly over three orders of magnitude when Cd-doped ZnO nanowires were exposed to moist air of 95% relative humidity, which shows a promising application as humidity sensor.

As a most important II–VI semiconductor, ZnO has been applied in the field of dilute magnetic semiconductor (DMS) as a host material, in which 3*d* transition-metal ions (some magnetic ions, or ions which bear a net magnetic moment) including Co, V, Fe, Mn, substitute Zn cations in the zinc oxide lattice position.[92,99,102] As a consequence, the incorporated 3d metal ions bear two competing effects: strong localized 3d-host hybridization and strong Coulomb interactions between 3d-3d electrons. The hybridization between the transition-metal 3d and the host (ZnO) valence band leads to a number of peculiar and interesting magneto-optical and magnetoelectrical effects. A single-phase ferromagnetic material could be potentially applied in devices based on the spin of electrons, such as polarized light emitters, chips that integrate memory and microprocessor functions, magnetic devices exhibiting gain and ultra-low power transistors.[99,102]

A new nomenclature has thereafter emerged as 'spintronics' (Spin transfer electronics). According to Ueda,[103] spintronics is the technology that transforms reading and writing information by spin rather than by electron charge. The key requirement for achieving practical application of spintronic devices is that the material is ferromagnetic (or Curie temperature (T_C) above room temperature). ZnO-based DMS materials have been considered as the most promising spintronic candidate by theoretical prediction and experimental results.

Up to now, T_C values higher than 300 ^{o}C are reported including Co-doped,[92b,103] V-doped,[104] Fe-doped and Co, Fe-codoped ZnO films.[105] However, there is still a great deal of controversy and discrepancy about the origin of the ferromagnetism in transition-metal-doped ZnO films. For instance, Ueda et al.[103] claimed the Curie point higher than 280 K for the Co:ZnO film grown by the pulsed-laser deposition method, but the reproducibility was less than 10% for their method. A more recent report gave their Curie points higher than 350 K and demonstrated intrinsic ferromagnetic behaviour for Co-doped ZnO films, whereas Jang et al.[106] claim that the room-temperature ferromagnetism was an extrinsic phenomenon caused by the presence of Co clusters. Norton and coworkers[107] reported the presence of Co nanoclusters in Co^+-implanted ZnO which exhibits ferromagnetism at room temperature, but the possibility of the component of the magnetic property due to Co substitution of the Zn in ZnO lattice could not be precluded.

Addition of impurities into a wide-bandgap semiconductor often induces variation of the band gap energy, the so-called bandgap engineering, which leads to the dramatic change in their electrical and optical properties.[91] For example, the fundamental bandgap energy of undoped ZnO material increases from 3.3 to 4.0 eV by alloying with MgO, depending on the Mg content, which might be practically used for fabrications of ZnO/ZnMgO heterostructure light emitters as well as ultraviolet photodetectors.[91b] The ZnO bandgap could be also narrowed to 2.8 eV by incorporating Cd into ZnO lattice, which is desirable for wavelength tunability. Band gaps corresponding to the visible spectrum are attained.[108] Due to the incorporation of foreign atoms, lattice parameters of ZnO wurtzite structure often change as well, because of the unmatched atomic radii of different metals . Fig. 1.3[91a] shows the *a* lattice parameter as a function of room temperature bandgap values in some wide-gap semiconductors.

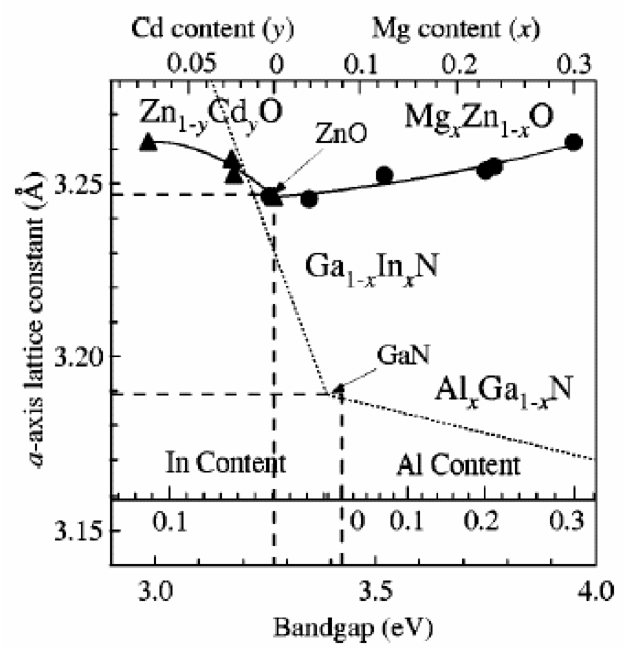

Fig. 1.3. Optical and structural properties of Cd and Mg mixed ZnO alloys with regard to the a-axis length and room-temperature bandgap energy. (In,Ga)N and (Al, Ga)N alloys are also shown. (Reprinted with permission from Ref. [91a]. Copyright 2001 American Institute of Physics.)

1.2.2.2 Synthesis methods

In order to prepare ZnO-based MMO of high quality, several synthesis methods have been employed, including sol-gel,[109] polar laser deposition (PLD),[91b,c] metal organic vapor-phase epitaxy (MOVPE),[108] and molecular beam epitaxy (MBE).[91a] Nanostructured doped-ZnO materials such as nanowires,[110] nanoparticles[58a] have also been produced. It is worth noting that Wang et al.[110a] recently prepared large-scale Ni-doped ZnO nanowire arrays for the first time using a metal vapor vacuum arc (MEVVA) ion source doping technique. The doped nanowires have high crystallinity and few defects upon proper heating treatment. The electrical conductivity of as-synthesized Ni doped-ZnO nanowires was greatly enhanced and it was over 30 times after doping. The photoluminescence (PL) spectrum was red shifted, suggesting possible doping induced band edge bending.

Indeed, the synthesis methods for metal oxide alloys are not as abundant as for binary oxides due to the difficulties to control the stoichiometry and composition homogeneity. The size and shape of the particles or microstructure of MMO thin films are important parameters for the possible application as materials. Mechanical mixing of precursors followed by a firing process to achieve the desired MMO is the traditional method. The process starts by ball-milling a mixture of different kinds of pure metal oxides or thermally labile metal salts (e.g. carbonates, acetates, nitrates) and the resulting blend is then subjected to temperature controlled heating protocols.[111] However, due to the problems of controlling the grain growth and segregation phenomena occurring during calcination and contamination introduced in the course of the blending, it is difficult to create high quality materials. This method is obsolete for modern material synthesis.

Spray pyrolysis is another method frequently used to synthesize MMO of homogeneous composition at the atomic length scale for instance the case of $Y_3Al_5O_{12}$.[112] A further method rests on sol-gel chemistry starting from hydrolysis of metal ion containing precursors to produce an intermediate oxy-hydroxyl-gel which is then subjected to controlled heating (calcination) to give ceramic powders of desired composition. Sin and Odier[113] reported the synthesis of a series of MMO of the type $La_{0.85}So_{0.15}MnO_3$, $La_2Cu\ NiO_6$ and $BaZrO_3$ in which the EDTA complexes of the metal ions were stabilized in a polyacrylamide gel prepared in situ. The pyrolysis of the dry mixture of the gel with the EDTA metal complex at temperatures above 700°C gave the desired MMO. This is a variation of the Pechini method,[114] which has been widely used in the past.

Hydrothermal synthesis is an approach in which nucleation and growth of the desired MMO particles takes place in water or another liquid medium at relatively low temperature and under mild conditions. $PbZr_{0.7}Ti_{0.3}O_3$[115] and $BaTiO_3$[116] have been obtained using such method.

In this work, a polymer-based method is used to prepare binary oxides and ZnO-based mixed metal oxides nanoparticles.

1.3 Synthesis of metal oxides via polymer precursor as a promising method

The so-called polymer precursor method is not a typical ‘method’ that conforms to the classification of methods as listed above. The process may be involved in either sol-gel process, or hydrothermal, or wet chemical route or even emulsion process. The definition employed here is to refer to a strategy for preparation of ceramics or inorganic powders derived from a pre-synthesized polymeric (organic or inorganic) precursor. Typically, the precursor is homogeneous and amorphous and is used as an intermediate to the final product.

Early work using a polymer as precursor attempted to produce inorganic ceramics, for instance, β-SiC,[117] B_4C[118]. The pioneering synthesis of SiC was performed by Yajima and coworkers.[117]

They prepared polysilanes as a precursor from chlorosilane, which was then converted to the ultimate product upon controlled pyrolysis after thermally-induced crosslinking of the polymer. The concept of polymer as precursor was further applied in the synthesis of (mixed) metal oxides because of the innate advantages over other methods, for example, homogenous morphology and high purity of the resulting oxides, lower processing temperature, low cost and environmental friendliness etc. The synthesis of metal oxides via hydrolysis of metal alkoxides, a typical sol-gel process, is within the context of polymer precursor 'method'. As shown in scheme 1.1, an inorganic polymer forms as gel-like precipitation and is then subject to a heating treatment to give desired metal oxides.

Further development in the polymer precursor method was achieved by Pechini,[114] who used water soluble metal salts instead of non-ionic alkoxides to prepare metal oxides. Typically, the synthesis begins with complexation of metal salts with hydroxycarboxylic acids (citric acid) to form a uniform aqueous solution. Subsequently, the solution is evaporated until a viscous mass is obtained, which forms a homogeneous precursor via esterification with a polyhydroxyl alcohol (ethylene glycol) upon a short heat treatment at temperatures lower than 300 ^{o}C. The obtained amorphous precursor is then pyrolyzed to form (mixed) metal oxides. The method is successful in preparation of more than hundred (mixed) metal oxides. Tai et al. [119] worked out the optimal reaction conditions for the Pechini method by varying the organic mass ratio between the citric acid and ethylene glycol. They found that the most porous precursor was achieved at equal molar ratio of the two components. And a premixing of the organics prior to adding of metal salts leads the whole process more controllable. Perovskite $PbTiO_3$ powders were prepared by the typical Pechini process at relatively low temperatures, viz. 400-600 °C.[120] A yellowish transparent polymeric gel was formed without any precipitation via heating of a mixed solution of citric acid (CA), ethylene glycol (EG), and Pb and Ti ions with a molar ratio of (Pb/Ti/CA/EG) 1/1/10/40 at 130 °C, which after pyrolysis at 300 °C was converted to a powder precursor for $PbTiO_3$. Chemical analyses showed no PbO loss during calcination of the powder precursors at 400-700 °C, which led to the conclusion that a solid-state reaction between isolated PbO and TiO2 particles was not responsible for $PbTiO_3$ formation, but $PbTiO_3$ formed directly by thermal decomposition of the powder precursor above 400 °C.

A variation was introduced by Ober and coworkers,[121] who prepared a preceramic polymer precursor by conventional radical polymerization of a metal acrylate of desired compositions. The as-synthesized Cr-doped forsterite (Cr-Mg_2SiO_4) nanoparticles from calcination of precursor were less than 100 nm in diameter. The material showed interesting photoluminescence features in the near- IR range and was suggested for possible utility as a tuneable laser source.

Metal oxides of special morphology could be accomplished by combination with other techniques. It was reported very recently that a three-dimensionally ordered macroporous (3DOM) materials of perovskite-type $La_{1-x}Sr_xFeO_3$ (x: 0-0.4) MMO is produced using a colloidal crystal template.[122] The preparation process is actually based on the typical Pechini method. Mixed metal nitrates were dissolved in ethylene glycol-methanol mixed solvent and allowed to penetrate into the colloidal template of polystyrene spheres. During the calcination process, the mixed metal nitrates react with ethylene glycol and are converted to mixed metal glyoxylates in the voids of the colloid before the polymer spheres burst. After removing the template, the mixed metal glyoxylates were converted to the mixed metal oxides.

1.4 Motivation and strategy of this work

Notwithstanding the merits of the Pechini method, it has some disadvantages due to the nature of the sol-gel process, for example, inhomogeneities in the product phase, imprecise stoichiometry between the different metal components in the MMO and impurities introduced by the metal salts etc.

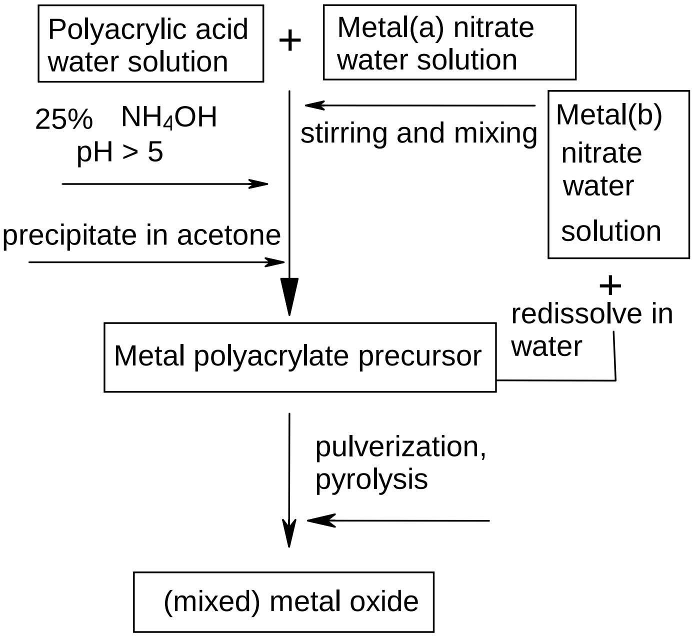

Scheme 1.3

Synthesis of (mixed) metal oxide powders by pyrolysis of (mixed) metal poly(acrylates)

In this work, a process which differs in important details from previous methods is used to prepare binary oxide and mixed metal oxide nanoparticles with controlled composition. The method starts with the preparation of a defined polymer-metal salt complex which is water soluble and can be purified by precipitation/redissolution cycles. Such complexes can be prepared to contain one or more different metal ions. The metal ion density which refers to the ratio between the ionogenic sites fixed to the polymer backbone and the number of metal ions per chain can also be changed by dilution with non-metallic counterions. These cation-loaded polymer precursors can be used as starting material for synthesis of (mixed) metal oxide by various methods such as hydrothermal synthesis, thermal decomposition, spray pyrolysis, etc. In this work, the purified complex in dry form is calcined at relatively low temperature to give nanosized crystals of binary metal oxide or MMO powders. The polymer-metal salt solution can also be processed by spin coating, drop casting or similar procedure to obtain polymer precursor films for further production of metal oxide films. The composition of the precursor polymer defines the stoichiometry of the MMO in cases in which a phase segregation of MMOs of different structure doesn't occur during calcination (Scheme 1.3).

In chapter 2, the synthetic method is applied for preparation of pure zinc oxide nanoparticles. The polymer precursor is obtained based on established method of polymer chemistry and zinc oxide is formed by controlled calcinations of the precursor. The obtained ZnO powder was characterized by various tools like XRD, SEM, TEM and its optical properties were studied by photoluminescence, electron paramagnetic resonance (EPR), FTIR and Raman spectroscopy as well. The sintering and growth of the nanoparticles by thermal annealing is investigated and the influence on the PL of the material is also studied.

In chapter 3, nanocrystalline ZnO film is prepared via pyrolysis of a precursor film, owing to the solubility of the polymer precursor in water. The obtained ZnO films are checked for deep understanding on the nanoparticles formation and growth by means of SEM and TEM. The optical properties of the films fabricated in different atmospheres are studied.

In chapter 4, metastable type mixed metal oxides (MMO) including $Zn_{1-x}Mg_xO$ and $Zn_{1-x}Co_xO$ are successfully prepared by controlled pyrolysis of the corresponding polymer precursor at relatively low temperature. The MMO nanoparticles are characterized by electron microscopy such as SEM, TEM and X-ray powder diffraction. The effects of band gap engineering is seen in the Mg:ZnO system. The photoluminescence in the visible is enhanced by incorporation of Mg ions on Zn ions in the hexagonal lattice sites, while the visible emission is suppressed in the

Co:ZnO system. The magnetic property of the Co-doped ZnO is investigated and no ferromagnetism is found in the samples.

In chapter 5, an alternative way to prepare polymer precursor and corresponding metal oxide is presented, which starts from a water-in-oil miniemulsion and the polymer precursor is formed by radical polymerization. As a supplementary method, it is believed to be applicable in many metal oxide synthesis. Zinc oxide nanoparticles are synthesized using the method and the product is compared with that obtained from polymer-salt complex method.

In chapter 6, surface modification of the as-synthesized ZnO nanoparticles was investigated via a phosphate modifier. The morphology of the modified particles is checked by SEM. And the dispersibility of the ZnO nanoparticles is improved after surface modification as proved by means of dynamic light scattering and zeta-potential measurements.

In the last chapter (chapter 7), a summary and conclusion of this Ph.D. work is presented.

1.5 Reference

[1] P. Moriarty, *Rep. Prog. Phys.* **2001**, *64*, 297.

[2] M. C. Roco in *The Nano-Micro Interface* (Eds: H.-J. Fecht, M. Werner), WILEY-VCH, Weinheim, **2004**, Ch.1.

[3] X. Duan, Y. Huang, R. Agarwal, C. M. Lieber, *Nature* **2003**, *421*, 241.

[4] Y. Lin, H. Skaff, T. Emrick, A. D. Dinsmore, T. P. Russell, *Science* **2003**, *299*, 226.

[5] K. J. Klabunde, *Nanoscale Materials in Chemistry* John Wiley & Sons, Inc., **2001**.

[6] L. S. Li, N. Pradhan, Y. Wang, X. Peng, *Nano. Lett.* **2004**, *4*, 2261.

[7] N. Pradhan, D. Goorskey, J. Thessing, X. Peng, *J. Am.Chem. Soc.* **2005**, *127*, 17586.

[8] A. Kolmakov, D. O. Klenov, Y. Lilach, S. Stemmer, M. Moskovits, *Nano. Lett.* **2005**, 5, 667.

[9] a) C. J. Brinker, G. W. Scherer, *Sol-Gel Science*, Academic Press: New York, **1990**; b) B. O'Regan, J. Moser, M. Anderson, M., Grätzel, *Nature* **1991**, *335*, 737.

[10] a) C. J. Brinker, G. W. Scherer, *Sol-Gel Science: The Physics and Chemistry of Sol-Gel Processing*, Academic Press: San Diego, **1990**; b) R. A. Caruso, M. Antonietti, *Chem. Mater.* **2001,** *13,* 3272; c) J. N. Hay, H. M. Raval, *Chem. Mater.* **2001,** *13,* 3396.

[11] a) S. Lee, C. Jeon, Y. Park, *Chem. Mater.* **2004,** *16,* 4292; b) Y. Zhou, M. Antonietti, *J. Am. Chem. Soc.* **2003**, *125*, 14960; c) K. Kanie, T. Sugimoto, *Chem. Commun.* **2004,** *14,* 1584; d) S. Eiden-Assmann, J. Widoniak, G. Maret, *Chem. Mater.* **2004,** *16,* 6; e) V. F. Stone, R. J. Davis, *Chem. Mater.* **1998,** *10,* 1468.

[12] M. J. Hudson, J. W. Peckett, P. J. F. Harris, *J. Mater. Chem.* **2003**, *13*, 445.

[13] S. Dire, R. Campostrini, R. Ceccato, *Chem. Mater.* **1998,** *10,* 268.

[14] B. Ksapabutr, E. Gulari, S. Wongkasemjit, *Mater. Chem. Phys.* **2004**, *83*, 34.

[15] a) J. Huang, N. Matsunaga, K. Shimanoe, N. Yamazoe, T. Kunitake, *Chem. Mater.* **2005,** *17,* 3513; b) T. F. Baumann, S. O. Kucheyev, A. E. Gash, J. H. Satcher, *Adv. Mater.* **2005**, *17*, 1546.

[16] N. I. Kovtyukhova, T. E. Mallouk, T. S. Mayer, *Adv. Mater.* **2003**, *15*, 780.

[17] A. Y. Oral, E. Mensur, M. H. Aslan, E. B. Basaran, *Mater. Chem. Phys.* **2004**, *83*, 140.

[18] L. Ji, J. Lin, H. C. Zeng, *Chem. Mater.* **2000,** *12,* 3466.

[19] a) M. M. Oliveira, D. C. Schnitzler, A. J. G. Zarbin, *Chem. Mater.* **2003,** *15,* 1903; b) H. Uchiyama, H. Imai, *Chem. Commun.* **2005**, *48*, 6014.

[20] M. Niederberger, G. Garnweitner, N. Pinna, M. Antonietti, *J. Am.Chem. Soc.* **2004**, *126*, 9120; b) J.-H. Choa, M. Kuwabara, *J. Eur. Ceram. Soc.* **2004**, *24*, 2959.

[21] M. Veith, S. Mathur, N. Lecerf, V. Huch, T. Decker, H. P. Beck, W. Eiser, R. Haberkorn, *J. Sol-Gel Sci. Technol.* **2000**, *17*, 145.

[22] A. M. Azad, M. Hashim, S. Baptist, A. Badri, A. U. Haq, *J. Mater. Sci.* **2000**, *35*, 5475.

[23] J. Xu, R. M. Almeida, *J. Sol-Gel Sci. Technol.* **2000**, *19*, 243.

[24] K. W. Volger, E. Kroke, C. Gervais, T. Saito, F. Babonneau, R. Riedel, Y. Iwamoto, T. Hirayama, *Chem. Mater.* **2003,** *15,* 755.

[25] M. N. Rumyantseva, V. V. Kovalenko, A. M. Gaskov, T. Pagnier, D. Machon, J. Arbiol, J. R. Morante, *Sens. Actuators, B Chem.* **2005**, *109*, 64.

[26] S. H. Sun, H. Zeng, *J. Am. Chem. Soc.* **2002**, *124*, 8204.

[27] a) N. Uekawa, R. Yamashita, Y. J. Wu, K. Kakegawa, *Phys. Chem. Chem. Phys.* **2004,** *6*, 442; b) Z. S. Hu, G. Oskam, R. Lee Penn, N. Pesika, P. C. Searson, *J. Phys. Chem. B* **2003,** *107,* 3124.

[28] R. E. Riman in *Surface and Colloid Chemistry in advanced Ceramics Precessing* (Eds: R. J. Pugh, L. Bergström), Marcel Dekker, Inc. New York, **1994**, Ch. 2.

[29] a) G. M. Crosbie, R. L. Predmesky, J. M. Nicholson, E. D. Stiles, Ceram, Bull. **1989**, *68*, 1010; b) T. Iwai, T. Kawahito, T. Yamada, U.S. Patent 2 020 264 A; c) T. Iwai, T. Kawahito, T. Yamada, U.S. Patent 4 405 589.

[30] A. Mews, A. Eychmueller, M. Giersig, D. Schooss, H. Weller, *J. Phys. Chem.* **1994**, *98*, 934.

[31] M. Braun, C. Burda, M. Mohamed, M. El-Sayed, *Phys. Rev. B* **2001**, *64*, 035317/1.

[32] a) Y. Sun, Y. Yin, B. T. Mayers, T. Herricks, Y. Xia, *Chem. Mater.* **2002**, *14*, 4736; b) Y. Sun, Y. Xia, *Science*, **2002**, *298*, 2176.

[33] a) T. S. Ahmadi, Z. L. Wang, T. C. Green, A. Henglein, M. A. El-Sayed, *Science*, 1996, *272*, 1924; b) K. Niesz, M. Grass, G. A. Somorjai, *Nano. Lett.* **2005**, 5, 2238.

[34] E. V. Shevchenko, D. V. Talapin, H. Schnablegger, A. Kornowski O. Festin, P. Svedlindh, M. Haase, H. Weller, *J. Am. Chem. Soc.* **2003**, 125, 9090.

[35] a) C. B. Murray, C. R. Kagan, M. G. Bawendi, *Science* **1995**, *270*, 1335; b) C. B. Murray, D. B. Norris, M. G. Bawendi, *J. Am. Chem. Soc.* **1993**, *115*, 8706.

[36] X. H. Zhong, S. H. Liu, Z. H. Zhang, L. Li, Z. Wei, W. Knoll, *J. Mater. Chem.* **2004**, *14*, 2790.

[37] a) M. Oner, J. Norwig, W. H. Meyer, G. Wegner, *Chem. Mater.* **1998,** *10,* 460; b) L. Vayssieres, K. Keis, S. E. Lindquist, A. Hagfeldt, *J. Phys. Chem. B* **2001**, *105*, 3350.

[38] T. K. Jain, M. A. Morales, S. K. Sahoo, D. L. Leslie-Pelecky, V. Labhasetwar, *Molecular Pharmaceutics* **2005**, *2*, 194.

[39] A. Rabenau, *Angew. Chem. Int. Ed. Engl.* **1985**, *24*, 1026.

[40] J. Yang, S. Mei, J. M. F. Ferreira, *Mater. Sci. Eng. C* **2001**, *15*, 183.

[41] a) P. Pinceloup, C. Courtois, J. Vicens, A. Leriche and B. Thierry, *J. Eur. Ceram. Soc.* **1999**, *19*, 973; b) S. W. Lu, B. I. Lee, Z. L. Wang, J. K. Guo, *J. Cryst. Growth* **2000**, *219*, 269.

[42] a) M. Z. C. Hu, M. T. Harris, C. H. Byers, *J. Colloid Interface Sci.* **1998**, *198*, 87; b) Y. Hakuta, T. Ohashi, H. Hayashi, K. Arai, *J. Mater. Res.* **2004**, *19*, 2230.

[43] C. C. Chen, X. Jiao, D. Chen, Y. Zhao, *Mater. Res. Bull.* **2001**, *36*, 2119.

[44] X. F. Qian, X. M. Zhang, C. Wang, W. Z. Wang, Y. Xie, Y. T. Qian, *J. Phys. Chem. Solids* **1999**, *60*, 415.

[45] C.-J. Jia, L.-D. Sun, Z.-G. Yan, L.-P. You, F. Luo, X.-D. Han, Y.-C. Pang, Z. Zhang, C.-H. Yan, *Angew. Chem. Int. Ed.* 2005, 44, 4328.

[46] Y. Yu, C. H. Jin, R. H. Wang, Q. Chen, L. M. Peng, *J. Phys. Chem. B* **2005**, *109*,18772.

[47] R. Gonzalez-McQuire, J. Y. Chane-Ching, E. Vignaud, A. Lebugle, S. Mann, *J. Mater. Chem.* **2004**, *14*, 2277.

[48] L. Xu, C. Qin, X. L. Wang, Y. G. Wei, E. Wang, *Inorg. Chem.* **2003**, *42*, 7342.

[49] N. Pinna, G. Garnweitner, M. Antonietti, M. Niederberger, *J. Am. Chem. Soc.* **2005**, 127, 5608.

[50] Z. W. Pan, Z. R. Dai, Z. L Wang, *Science* **2001**, *291*, 1947.

[51] C. J. Johnson, M. Li, S. Mann, *Adv. Funct. Mater.* **2004**, *14*, 1233.

[52] a) D. Segal in *Materials Science and Technology*, Vol. 17A (Eds: E. W. Cahn, P. Haasen, E. J. Kramer), WILEY-VCH, Weinheim, **1996**, Ch. 3; b) P. Moriarty, *Rep. Prog. Phys.* 2001, *64*, 297; c) C. Burda, X. B. Chen, R. Narayanan, M. A. El-Sayed, *Chem. Rev.* **2005,** *105*, 1025; d) M. Law, J. Goldberger, P. D. Yang, *Annu. Rev. Mater. Res.* **2004**, *34*, 83; e) C. B. Murray, C. R. Kagan, M. G. Bawendi, *Annu. Rev. Mater. Sci.* **2000**, *30*, 545.

[53] R. B. M. Cross, M. M. De Souza, E. M. S. Narayanan, *Nanotechnology* **2005**, *16*, 2188.

[54] a) H. Shibata, M. Watanabe, M. Sakai, K. Oka, P. Fons, K. Iwata, A. Yamada, K. Matsubara, K. Sakurai, H. Tampo, K. Nakahara, S. Niki, *phys. stat. sol.* **2004**, *4*, 872 ; b) S. Monticone, R. Tufeu, A.V. Kanaev, *J. Phys. Chem. B* **1998**, *102,* 2854 ; c) C. L. Yang, J. N. Wang, W. K. Ge, L. Guo, S. H. Yang, D. Z. Shen, *J. Appl. Phys.* **2001**, *90*, 4481; d) K. Vanheusden, C. H. Seager, W. L. Warren, D. R. Tallant, J. A. Voigt, *Appl. Phys. Lett.* **1996**, *68*, 403.

[55] M. Hilgendorff, L. Spanhel, C. Rothenhäusler, G.J. Müller, *J. Electrochem. Soc.* **1998**, *145*, 3633.
[56] B. Q. Sun, H. Sirringhaus, *Nano Lett.*, **2005**, *5*, 2408.
[57] J. Müller, S. W. Fresnius, *J. Anal. Chem.* **1994**, *349*, 380.
[58] a) P. Duran, F. Capel, J. Tartaj, C. Moure, *Adv. Mater.* **2002**, *14*, 137. b) H. K. Varma, S. Ananthakumar, K. G. K. Warrier, A. D. Damodaran, *Ceram. Inter.* **1996**, *l22*, 53; c) M. Singbal, V. Cbbabra, P. Kang, D.O. Shah, *Mater. Res. Bull.* **1997**, *32*, 239.
[59] L. Q. Jing, Z. L. Xu, X. J. Sun, J. Shang, W. M. Cai, *App. Surf. Sci.* **2001**, *180*, 308.
[60] D. W. Bahnemann, C. Kormann, M. R. Hoffmann, *J. Phys. Chem.* **1987**, *91,* 3789.
[61] a) X. Y. Kang, T. D. Wang, Y. Han, M. D. Tao, M. J. Tu, *Mater. Res. Bull.* **1997**, *32*,1165; b) L. Spanhel, M.A. Anderson, *J. Am. Chem. Soc.* **1991**, *113*, 2826. c) E.A. Meulenkamp, *J. Phys. Chem. B* **1998**, *102*, 5566; d) C. L. Carnes, K. J. Klabunde *Langmuir* **2000,** *16,* 3764.
[62] B.J. Lokhande, P. S. Patil, M. D. Uplane, *Mater. Lett.* **2002**, *57*, 573.
[63] L. Vayssieres, K. Keis, S.-E. Lindquist, A. Hagfeldt, *J. Phys. Chem. B* **2001**, *105,* 3350.
[64] S. H. Yu, M. Yoshimora, *Adv. Mater.* **2002**, *14*, 296.
[65] a) S. M. Smith, H. B. Schlegel, *Chem. Mater.* **2003,** *15,* 162; b) X. H. Han, G. Z. Wang, J. S. Jie, W. C. H. Choy, Y. Luo, T. I. Yuk, J. G. Hou, *J. Phys. Chem. B* **2005**, *109,* 2733; c) G. Malandrino, M. Blandino, L. M. S. Perdicaro, I. L. Fragala, P. Rossi, P. Dapporto, *Inorg. Chem.* **2005**, *44*, 9684.
[66] a) S.Music, D. Dragcevic, M. Maljkovic, S. Popovic, *Mater. Chem. Phys.* **2002**, *77*, 521; b) P. Cozzoli, A. Kornowski, H. Weller, *J. Phys. Chem. B* **2005**, *109,* 2638; c) A. P. A. Oliveira, J.-F. Hochepied, F. Grillon, M.-H. Berger, *Chem. Mater.* **2003,** *15,* 3202; d) B. Liu, H. C. Zeng, *Langmuir*, **2004**, *20*, 4196.
[67] C.-H. Lu, C.-H. Yeh, *Mater. Lett.* **1997**, *33*, 129.
[68] a) H. Y. Xu, H. Wang, Y. C. Zhang, W. L. He, M. K. Zhu, B. Wang, H. Yan, *Ceram. Inter.* **2004**, *30*, 93 ; b) H. C. Du, F. L. Y, S. L. H., J. L. Li, Y. F. Zhu, *Chem. Lett.* **2004**, *33*, 770 ; c) H. Zhang, D. Yang, X. Y. Ma, Y. J. Ji, J. Xu, D. L. Que, *Nanotechnology* **2004**, *15*, 622.
[69] Y. J. Kwon, K. H. Kima, C. S. Limb, K. B. Shim, *J. Ceram. Proc. Res.* **2002**, *3,* 146.
[70] a) Z. J. Wang, H. M. Zhang, L. G. Zhang, J. S. Yuan, S. G. Yan, C. Y. Wang, N*anotechnology* **2003**, *14*, 11; b) P. D. Cozzoli, M. L. Curri, A. Agostiano, G. Leo, M. Lomascolo, *J. Phys. Chem. B* **2003,** *107,* 4756.
[71] S. Komarnenia, M. Brunoa, E. M., *Mater. Res. Bull.* **2000**, *35*,1843.
[72] G. Rodrıguez-Gattorno, P. Santiago-Jacinto, L. Rendon-Va´zquez, J. Nemeth, I. Dekany, D. Diaz, *J. Phys. Chem. B* 2003, *107,* 12597.
[73] Z. Q. Li, Y. J. Xiong, Y. Xie, *Inorg. Chem.* **2003**, *42*, 8105.
[74] H. Q. Yan, R. R. He, J. Johnson, M. Law, R. J. Saykally, P. D. Yang, *J. Am.Chem. Soc.* **2003**, 125, 4728.
[75] J. S. Jie, G. Z. Wang, X. H. Han, Q. X.Yu, Y. Liao, G. P. Li, J. G. Hou, *Chem. Phys. Lett.* **2004**, *387*, 466.
[76] J. W. P. Hsu, Z. R. R. Tian, N. C. Simmons, C. M. Matzke, J. A. Voigt, J. Liu, *Nano Lett.*, **2005**, *5*, 83.
[77] X.-P. Shen, A.-H. Yuan, Y.-M. Hu, Y. Jiang, Z. Xu, Z. Hu, N*anotechnology* **2005**, *16*, 2039.
[78] Z. L.Wang, X. Y. Kong, J. M. Zuo, *Phys. Rev. Lett.* **2003**, *91*, 185502.
[79] F. Li, Y. Ding, P. X. Gao, X. Q. Xin, Z. L. Wang, *Angew. Chem. Int. Ed.* 2004, 43, 5238.
[80] Z. Wang, X.-F. Qian, J. Yin, Z.-K. Zhu, *Langmuir* **2004,** *20,* 3441.
[81] Y. Hu, J. F. Chen, X. Xue, T. W. Li, Y. Xie, *Inorg. Chem.* **2005**, *44*, 7280.

[82] Z. R. R. Tian, J. A.Voigt, J. Liu, B. Mckenzie, M. J. Mcdermott, M. A. Rodriguez, H. Konishi, H. F. Xu, *Nat. Mater.* **2003**, *2*, 821.
[83] H. Imai,_ S. Iwai, S. Yamabi, Chem. Lett. **2004**, *33*, 768.
[84] a) A. Taubert, G. Glasser, D. Palms, *Langmuir* **2002,** *18,* 4488; b) M. Oner, J. Norwig, W. H. Meyer, G. Wegner, *Chem. Mater.* **1998,** *10,* 460.
[85] G. Wegner, P. Baum, M. Müller, J. Norwig, K. Landfester, *Macromol. Symp.* **2001**, *175*, 349.
[86] R. Munoz-Espi, *PhD thesis*, University of Mainz, **2006**.
[87] A. Taubert, G. Wegner, *J. Mater. Chem.* **2002**, *12*, 805.
[88] Q. Wan, Q. H. Li, Y. J. Chen, T. H. Wang, X. L. He, X. G. Gao, J. P. Li, *Appl. Phys. Lett.* **2004**, *84*, 3085.
[89] a) C. X. Xu, X. W. Sun, B. J. Chen, *Appl. Phys. Lett.* **2004**, *84*, 1540; b) S. H. Jo, J. Y. Lao, Z. F. Ren, R. A. Farrer, T. Baldacchini, J. T. Fourkas, *Appl. Phys. Lett.* **2003**, *83*, 4821.
[90] A. Tsukazaki *et al.*, *Nat. Mater.* **2005**, *4*, 42.
[91] a)T. Makino, Y. Segawa, M. Kawasaki, A. Ohtomo, R. Shiroki, K. Tamura, T. Yasuda, H. Koinuma, *Appl. Phys. Lett.* **2001**, *78*, 1237; b) A. Ohtomo, M. Kawasaki, T. Koida, K. Masubuchi, H. Koinuma, Y. Sakurai, Y. Yoshida, T. Yasuda, Y. Segawa, *Appl. Phys. Lett.* **1998**, *72*, 2466; c) A. K. Sharma, J. Narayan, J. F. Muth, C. W. Teng, C. Jin, A. Kvit, R. M. Kolbas, O. W. Holland, *Appl. Phys. Lett.* **1999**, *75*, 3327; d) Y. Ogawa, S. Fujihara, *phys. stat. sol.* **2005**, *202*, 1825.
[92] a) T. Fukumura, Z. W. Jin, A. Ohtomo, H. Koinuma, M. Kawasaki, *Appl. Phys. Lett.* **1999**, *75*, 3366; b) J. M. D. Coey, M. Venkatesan, C. B. Fitzgerald, *Nature Mater.* **2005**, *4*, 173; c) H.-T. Lin, T.-S. Chin, J.-C. Shih, S.-H. Lin, T.-M. Hong, R.-T. Huang, F.-R. Chen, J.-J. Kai, *Appl. Phys. Lett.* **2004**, *84*, 621; d) J. M. Baik, J.-L. Lee, *Adv. Mater.* **2005**, *17*, 2745; e) S. W. Yoon, S.-B. Cho, S. C. We, S. Yoon, B. J. Suh, H. K. Song, Y. J. Shin, *J. Appl. Phys.* **2003**, *93*, 7879.
[93] E. G. Bylander, *J. Appl. Phys.* **1978**, *49*, 1188.
[94] E. Mollwo, *Z. Phys.* **1954**, *138*, 478.
[95] a) K. Vanheusden, C. H. Seager, W. L. Warren, D. R. Tallant, J. A. Voigt, *Appl. Phys. Lett.* **1996**, *68*, 403; b) P. Viswanathamurthi, N. Bhattarai, H. Y. Kim, D. R. Lee, *Nanotechnology* **2005**, *16*, 2188.
[96] a) I. Broser, R. K. Germer, H. J. Schulz, and K. Wisznewski, *Solid State Electron.* **1978**, *21*, 1597; b) R. Kuhnert, R. Helbig, *J. Lum.* **1981**, *26*, 203; c) D. J. Robbins, D. C. Herbert, P. J. Dean, *J. Phys. C* **1981**, *14*, 2859.
[97] N. Y. Garces, L. Wang, L. Bai, N. C. Giles, L. E. Halliburton, G. Cantwell, *Appl. Phys. Lett.* **2002**, *81*, 622.
[98] S. Fujihara, Y. Ogawa, A. Kasai, *Chem. Mater.* **2004,** *16,* 2965.
[99] Ü. Özgür, Y. I. Alivov, C. Liu, A. Teke, M. A. Reshchikov, S. Doğan, V. Avrutin, S.-J. Cho, H. Morkoç, *J. Appl. Phys.* **2005**, *98*, 041301.
[100] T. Minami, H. Sato, H. Nanto, S. Takata, *Jpn. J. Appl. Phys., Part 2* **1985**, *24*, L781.
[101] a) D. C. Look, D. C. Reynolds, C. W. Litton, R. L. Jones, D. B. Eason, G. Cantwell, A*ppl. Phys. Lett.* **2002**, *81*, 1830; b) Y. W. Heo, Y. W. Kwon, Y. Li, S. J. Pearton, D. P. Norton, A*ppl. Phys. Lett.* **2004**, *84*, 3474.
[102] S. J. Pearton, W. H. Heo, M. Ivill, D. P. Norton, T. Steiner, *Semicond. Sci. Technol.* **2004**, *19*, R59.
[103] K. Ueda, H. Tabata, T. Kawai, A*ppl. Phys. Lett.* **2001**, *79*, 988.
[104] H. Saeki, H. Tabata, T. Kawai, *Solid-State Commun.* **2001**, *120*, 439.
[105] Y. M. Cho, W.-K. Choo, H. Kim, D. Kim, Y.-E. Ihm, *Appl. Phys. Lett.* **2002**, *80*, 3358.
[106] J. H. Park, M. G. Kim, H. M. Jang, S. Ryu, Y. M. Kim, *Appl. Phys. Lett.* **2004**, *84*, 1338.

[107] D. P. Norton, M. E. Overberg, S. J. Pearton, K. Pruessner, J. D. Budai, L. A. Boatner, M. F. Chisholm, J. S. Lee, Z. G. Khim, Y. D. Park, R. G. Wilson, *Appl. Phys. Lett.* **2003**, *81*, 5488.

[108] T. Gruber, C. Kirchner, R. Kling, F. Reuss, A. Waag, F. Bertram, D. Forster, J. Christen, M. Schreck, *Appl. Phys. Lett.* **2003**, *81*, 3290.

[109] V. Fathollahi, M. M. Amini, *Mater. Lett.* **2001**, *50*, 235.

[110] a) J. H. He, C. S. Lao, L. J. Chen, D. Davidovic, Z. L. Wang, *J. Am.Chem. Soc.* **2005**, *127*, 16376; b) B. D. Yuhas, D. O. Zitoun, P. J. Pauzauskie, R. R. He, P. D. Yang, *Angew. Chem. Int. Ed.* **2006**, *45*, 420.

[111] T. Ishii, R. Furuichi, T. Nagasawa, K. Yokoyama, *J. Themal Anal.* **1980**, *19,* 467.

[112] J. Marchal, T. John, R. Baranwal, T. Hinklin, R. M. Laine, *Chem. Mater.* **2004,** *16,* 822.

[113] A. Sin, P. Odier, *Adv. Mater.* **2000**, *12,* 649.

[114] M. P. Pechini, U.S. Patent 3 330 697, **1967**.

[115] M. Oledzka, M. M. Lencka, P. Pinceloup, K. Mikulka-Bolen, L. E. McCandlish, R. E. Riman, *Chem. Mater.* **2003**, *15*, 1090.

[116] a) M. Oledzka, N. E. Brese, R. E. Riman, *Chem. Mater.* **1999,** *11,* 1931; b) B. Grohe, G. Miehe, G. Wegner, *J. Mater. Res.* **2001**, *16*, 1901.

[117] S. Yajima, Y. Hasegawa, J. Hayashi, M. Imura , *J. Mater. Sci.* **1978**, *13*, 2569.

[118] D. Seyferth, W. S. Rees, J. S. Haggerty, A. Lightfoot, Chem. Mater. **1989**, *1*, 45.

[119] L.-W. Tai, P. A. Lessing, *J. Mater.Res.* **1992**, *7*, 502.

[120] M. Kakihana, T. Okubo, M. Arima, O. Uchiyama, M. Yashima, M. Yoshimura, *Chem. Mater.* **1997,** *9,* 451.

[121] L. L. Beecroft, C. K. Ober, *Adv. Mater.* **1995**, 7, 1009.

[122] M. Sadakane, T. Asanuma, J. Kubo, W. Ueda, *Chem. Mater.* **2005,** *17,* 3546.

2 ZnO Nanoparticles: Synthesis and Characterization

2.1. Introduction

The application of polymer as precursor to produce high quality inorganic particles has been studied for decades.[1-3] Pechini[4] firstly exploited the popular polymer-to-ceramic method for metal oxides production, in which a chelate is formed between cations and citric acid and thereafter the polymeric precursor comes into being by crosslinking reactions with ethylene glycol at a temperature around 300 °C. The method has been modified in the later years. Lessing[5-6] and coworkers attempted to replace citric acid with polyacrylic acid for more homogeneous mixing and wished to obtain more uniform particles and homogeneous morphology of the products. However, As well known, this Pechini process actually is based on a sol-gel mechanism. Therefore, the intrinsic disadvantages of the sol-gel process is inevitable, for instance, imprecise control of the stoichiometry, contamination introduced during the mixing of metal salts. All these drawbacks impair the quality of the final product. Especially, the structure of the expected network-like polymer precursor and the effects of the different species (complexing groups, counterions and coions) on the final product are hitherto not clear yet although some preliminary characterization using C^{13}NMR and IR[7] confirms the binding of metal cations and the complexing groups. The mechanism of crystal nucleation and growth of the metal oxides has not been elucidated yet.

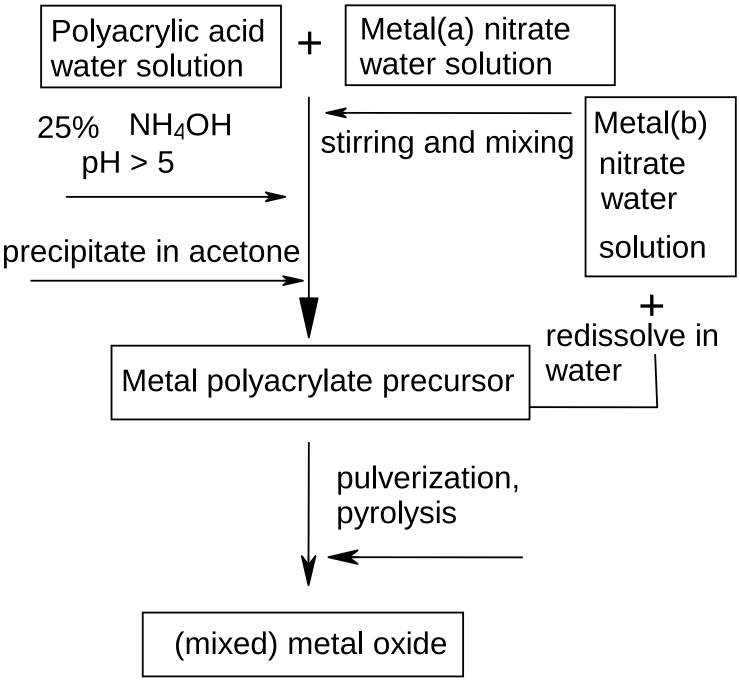

Scheme 2.1

Synthesis of metal oxide by pyrolysis of metal polyacrylate

Based on the polyelectrolyte system and established methods in polymer chemistry, the method used here (see scheme 2.1) has some virtues for metal oxides synthesis. As an environmental and economical friendly system, the mild and simple preparation conditions ensure its wide industrial application, while the process from polyelectrolyte system to solid-state chemistry ensure its interest and importance in fundamental research; it is suitable for various metal ions like Mg, Zn, Co, Fe et al. The precursor can absorb different kinds of metal ions. Thus, by sequentially adding different metal salts with predetermined ratio of concentration which prevents the polymer from preferential retention of a certain cation, preparation of mixed-oxide compounds with very precise stoichiometry could be achieved, like $Zn_{1-x}Mg_xO$ and $Zn_{1-x}Co_xO$. This part of work is described in detail in Chapter 4; finally, due to the good solubility of the polymer precursor in water, the polymer-metal salt solution can also be processed readily by spin coating, drop casting or similar procedure to obtain polymer precursor films.

Table 2.1 Properties and parameters of wurtzite ZnO[9]

Property	Parameter
Lattice parameter at 300 K	
a	0.32495 nm
c	0.52069 nm
a/c	1.602 (ideal hexagonal structure shows 1.633)
Density	5.606 g/cm^3
Melting point	1975 °C
Thermal conductivity	0.6, 1-1.2
Linear expansion coefficient	*a*: 6.5×10^{-6} /°C *c*: 3.0×10^{-6} /°C
Static dielectric constant	8.656
Refractive index	2.008, 2.029
Band gap	3.4 eV
Intrinsic carrier concentration	$<10^6$ cm^{-3} (max n-type doping$>10^{20}$ cm^{-3} electrons; max p-type doping$<10^{17}$ cm^{-3} holes
Exicton binding energy	60 meV
Electron effective mass	0.24
Electron Hall mobility at 300 K for low n-type conductivity	200 cm^2/V s
Hole effective mass	0.59
Hole Hall mobility at 300 K for low p-type conductivity	5-50 cm^2/V s

Zinc oxide is one of the most important and representative metal oxides, which is promising for wide range of technical applications such as pigments, cosmetics, varistors, chemical sensors and optoelectronics.[8] ZnO has only one crystal phase, i.e. hexagonal structure and the basic physical parameters are already known (see Table 2.1). Thus, we choose ZnO as a model synthesis via this polymer-based method.

2.2 Preparation of zinc polyacrylate precursor

2.2.1 Characterization of the ZnPA precursor

The polymer precursor for production of zinc oxide is prepared by simply mixing of polyacrylic acid (PAA) and zinc salts (typically zinc nitrate) in aqueous solution with the initial molar ratio (K = [COOH]/[Zn]) 10 for high retention of metal cations to the polymer. Next, the pH of the solution is adjusted by ammonia to over 5. It is well known that in aqueous solution zinc cation complexes with carboxylate group by one or several coordination types in neutral or alkali medium.[10] The main reactions which occur in the system may be described as follows:

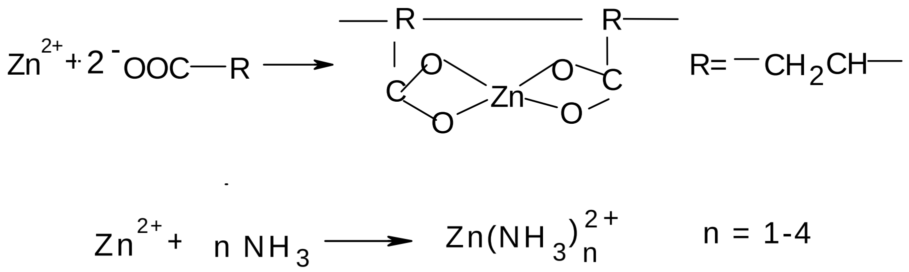

Scheme 2.1

It is estimated that several kinds of species such as zinc polyacrylate (ZnPA) complex, Zn^{2+}, $Zn(NH_3)_n^{2+}$, NO_3^{2-}, NH_4^+ and OH^-, etc coexist in the reaction mixture. In order to separate the ZnPA precursor from other species, the reaction mixture was precipitated into the nonsolvent acetone. The ZnPA was collected by centrifugation and washed and finally dried in vacuo at relatively low temperature (less than 50 °C). The solid polymer complex appears as a colorless powder.

UV spectrum is a powerful tool to study the solution system. As shown in Figure 2.1a, pure PAA shows slight absorption beyond 273 nm, possibly due to oligomer or unreacted monomer, while zinc nitrate solution has only one evident pick at 300 nm due to nitrate ions. The simple mixing of the two solutions doesn't result in any new absorption peak in the UV/Vis range. With adding ammonia, when pH is over 6, the peak at 273 nm splits into two peaks at 268 and 275 nm. Comparing the UV spectra (Fig. 2.1b) of the reaction mixture and the redissolved precursor, it is found that all the absorption at 268, 275 and 300 nm disappeared after precipitation which indicates that the polymer precursor is effectively purified in the process.

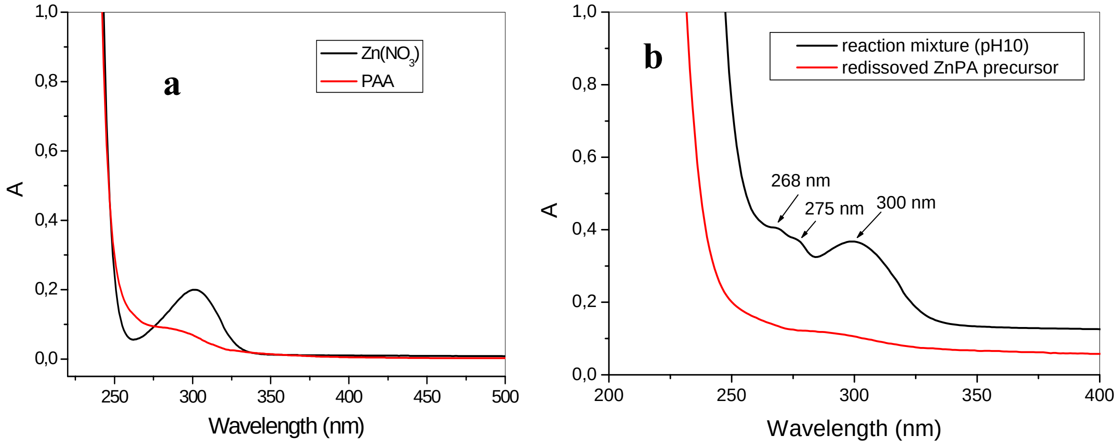

Fig. 2.1. *UV spectra showing differences in absorption between (a) Zn(NO$_3$) and PAA; (b) reaction mixture and redissolved ZnPA precursor.*

For deeper insight to the wet chemical process, we need to understand the zinc ion behavior in aqueous solution under different conditions. Fig. 2.2 is the phase diagram of zinc species in aqueous solution at different pH and concentration.[11] In the diagrams the dashed lines denote the thermodynamic equilibrium between the Zn(II) soluble species and the solid phases. The solid lines represent the total concentration of the soluble species as a function of pH, i.e., the solubility of the solid phases. The diagrams indicate that at concentration of Zn^{2+} around 0.01 M, the soluble species become unstable over pH 7. The red area is the working area in this experiment. With the conditions (initial zinc concentration, pH) employed here, a direct ZnO or zinc hydroxide deposition is expected. However, in our experiment no such precipitate or deposit was found before pouring the solution into nonsolvent. And the UV profile as seen in Fig. 2.1b does not show any trace of ZnO band gap in the redissolved precursor solution within the range of 300 to 400 nm where crystalline ZnO has a strong absorption.

The reasonable explanation is that the zinc ions are mostly absorbed by the polymer chain and the ammonia has functioned as ligand, which may prohibit the formation of ZnO precipitates.[12] Yamabi and coworkers[11] systematically examined the deposit of zinc oxide or zinc hydroxide by adjusting the conditions such as R (the ratio of ammonium to zinc ions) and pH in aqueous solution. It was found that ZnO crystals (wurtzite structure) were precipitated at pH values from 9 to 13. The mode of the deposition was influenced by value of R, i.e. the ammonia concentration with regard to zinc species. At low R conditions (~20), precipitation rapidly occurred via homogeneous nucleation in the bulk without heterogeneous nucleation. No solid phases were produced with relatively high R values (30–50) at pH 8.5–11.5 and above 12.5. When a great amount of the complexing agent (R>50) was used, the soluble species were apparently stabilized. Thus, an increase in R could suppress the homogeneous nucleation of crystals from the bulk solution.

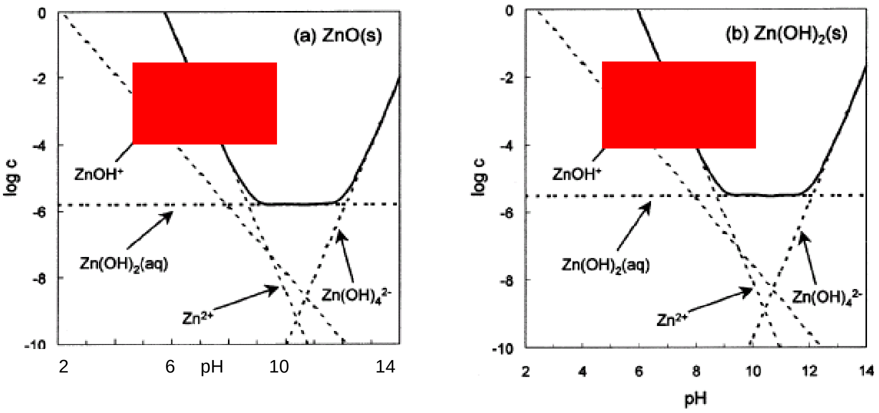

Fig. 2.2. *Phase stability diagrams for the a) $ZnO(s)–H_2O$ and b) $Zn(OH)_2(s)–H_2O$ systems at 25 °C as a function of pH.*[11] *The red area is the working conditions employed in this experiments.*

It is assumed therefore that in our experiment due to the formation of a polymer-metal complex and ammonia, zinc ions do not generate solid deposits even in the basic environment. The stability of the ZnPA complex in aqueous solution was checked by UV spectra. Fig. 2.3 shows the change in UV spectra of the redissolved ZnPA solution with regard to time. It is found that ZnPA UV spectra remain unchanged after 5 days, but at the 11th day, the wavelength lower than 300 nm began to show absorption; at 15th day, two slight absorptions at 281 and 312 nm appear, indicating the formation of new species (possibly nuclei of ZnO) in the solution. Actually, plume-like deposit could be observed in the redissolved ZnPA solution after 15 days. Therefore, the precursor of ZnPA complex may undergo a very slow deposition reaction in the aqueous solution.

In summary, a deep understanding of the reaction which takes place in the wet chemistry process is possible based on the results listed above. Simultaneously, the zinc ions may complex with carboxylate group of the polymer chain and ammonia in the solution. The formation of ZnPA complex causes the free zinc ions concentration to decrease significantly, while the rest Zn^{2+} is mostly captured by ammonia which can retard the ZnO or $Zn(OH)_2$ formation[12] and is subsequently removed in the precipitation process. Due to the significant decrease of Zn^{2+} concentration, the system ‘jumps’ out the ZnO precipitation area in the phase diagram.

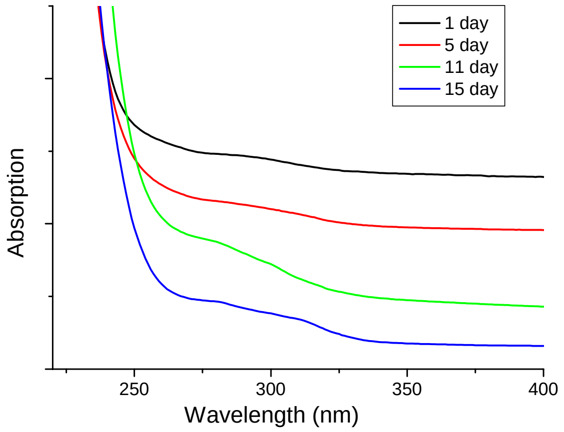

Fig. 2.3. *UV spectra showing the stability of ZnPA redissolved solution with time.*

The viscosity of the as-synthesized ZnPA precursor was investigated, too. As is well known, one of the primary differences that distinguish polyelectrolytes from neutral polymers is the viscosity behaviour. Typical polyelectrolytes in a salt-free aqueous solution exhibit a specific behavior, i.e. decrease in the reduced viscosity with an increase in polyelectrolyte concentration. This behavior is explained as that with decrease of the polyelectrolyte concentration, the ionization degree (dissociation degree α) increases and the released ions form an ionic atmosphere higher than the diameter of polymeric coil. The repulsion among the ions increases the rigidity of the chain, expanding the polymeric coil with a consequent increase of the viscosity.[10c] However, adding an inert low molecular weight electrolyte like NaCl, the strong electrostatic interactions are increasingly screened and the polyelectrolyte behaves more like a neutral polymer.

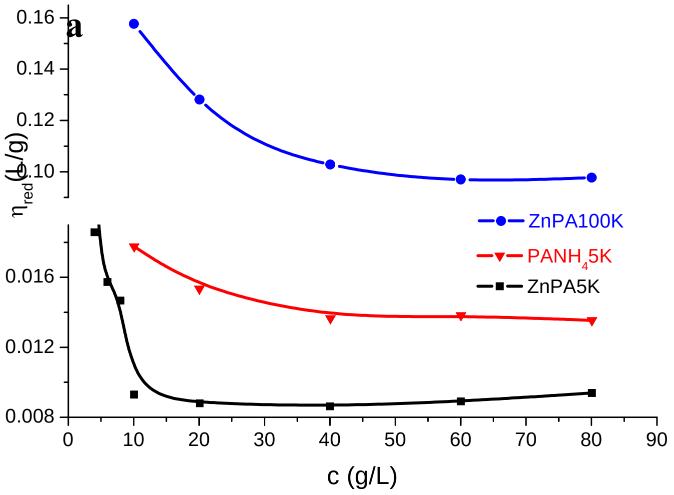

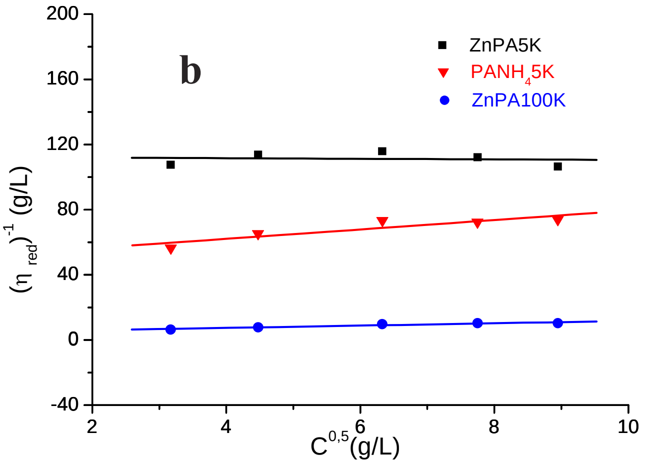

Fig. 2.4. *ZnPA and PANH$_4$ a) reduced viscosity versus concentration; b) intrinsic viscosity determined by Fuoss equation.*

Commercial PAA used in this experiment with a labeled molecular weight of 5,000 and 100,000 was therefore named as PAA5K and PAA100K respectively and ZnPA5K and ZnPA100K were the corresponding zinc-loaded polymer precursors. Fig. 2.4a shows viscosity of the redissolved ZnPA precursors measured by Ubbelohde viscometry at room temperature. Ammonium polyacrylate prepared via the same procedure as ZnPA was used as reference and named PANH$_4$5K. We can assume that the structure of ZnPA5K is very similar as that of PANH$_4$ with the only difference that zinc ions substitute some portion of ammonium groups. Both the polymer precursors of ZnPA as well as PANH$_4$ show typical polyelectrolyte behavior which indicates that the ZnPA solution is a 'salt-free' system, because presence of salts in the solution will change the shape of the viscosity curve. And it further proves the purification ability of the precipitation process. In the past, the separation of metal polyacrylate complex from the coions and other spies has been attempted by methods like dialysis or similar membrane separation.[13] However, due to the inefficiency of the methods, a large scale synthesis of salt-free polymer metal complex was difficult.

From the curves it is found that the viscosity of ZnPA is lower than that of PANH$_4$. The reasonable explanation is that the complexation between zinc and carboxylate group makes the macromolecular coil tighter, which decreases the volume of the polymer chain. The results also indicate the interaction of carboxylate groups and zinc ions is preferentially intrapolymer. Otherwise, the viscosity of ZnPA would be enlarged considerably. It is incorrect to simply compare the reduced viscosity of ZnPA and PAA, because the ZnPA is obtained from solution at pH 10, while the pH increase stretches the PAA chain and increase the viscosity, so that $PANH_4$ employed as reference in this experiment is necessary and reasonable.

Generally, in the case of pure polyelectrolyte solutions the η_{red}–c curves cannot be extrapolated to zero polyelectrolyte concentration for intrinsic viscosity [η] determination. This problem can be solved in two ways: (1) by means of empirical equation; (2) through screening the polyelectrolyte behaviour by addition of low-molecular weight salts. Fuoss[14] equation provides a usable method to determine the intrinsic viscosity of polyelectrolyte solutions.

$$\eta_{sp} / C = A / (1 + B \cdot C^{0.5}) \qquad (2.1)$$

Fig. 2.4b gives the results of applying this method in samples ZnPA5K, $PANH_4$ and ZnPA100K. As seen, straight lines are obtained for all samples in the concentration range and the intrinsic viscosity is calculated 0.00890, 0.0198 and 0.220 L/g respectively, although practically these values have no physical meaning.

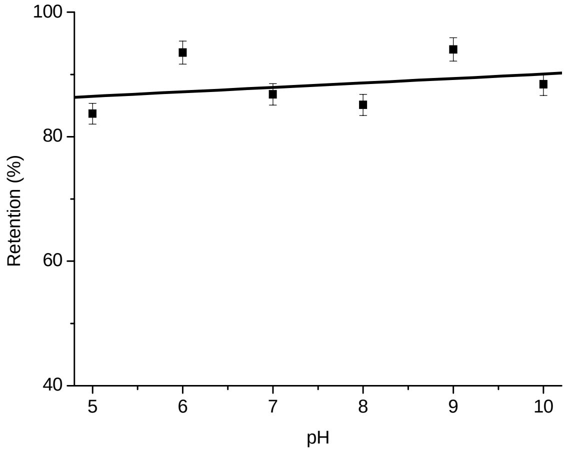

Fig. 2.5. *The effect of pH on the retention of the zinc ion onto the polyacrylate chain.*

The composition of the ZnPA precursor could be analyzed by means of atomic absorption spectroscopy (AAS) and elementary analysis (EA). Fig. 2.5 is the retention of zinc ions in the precursor at different pH solutions defined as the ratio of the amount of zinc bound to the polymer to the initial amount of zinc. The result indicates that in a wide pH range about 87% of initial zinc was bound to the polymer. The pH has no obvious influence on the retention of zinc, but it affects the ratio of ammonium and zinc in the precursor as shown in Fig. 2.6. This is due to the neutralization degree of the carboxylic acid which increases with pH. The molar ratio of zinc with regard to the carboxylate group in the polymer precursor is defined as loading. The loading of zinc with respect to the initial ratio between the carboxyl and zinc salts concentration in the feed is described in Figure 2.7. It is found when the ratio is below 3, the polymer complex directly precipitates out from the reaction solution. The reason possibly comes from two aspects: One is that the interpolymer structure gradually becomes dominant when the zinc ion concentration increases and it cannot dissolve in water any more. In other word, zinc ions induce crosslinking of the PAA chains; the other is that more carboxylate group are quenched by oppositely charged zinc cations, forming coulombic bonds or site-specific bonds, which are insoluble in water.

Because the carboxyl group concentration is by far larger than that of zinc cations (normally 10 folds in molar ratio), it is expected that intrapolymer other than interpolymer complex is predominant, as drawn in scheme 2.2. The results of dynamic light scattering (DLS) support this suggestion.

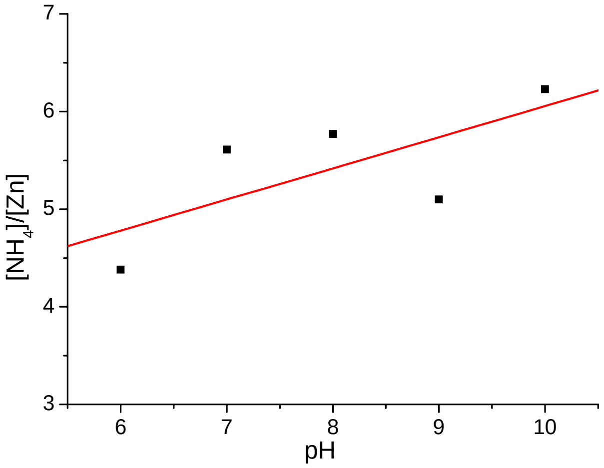

Fig. 2.6. *pH effect on the ratio of ammonium and zinc ions in the ZnPA precursor.*

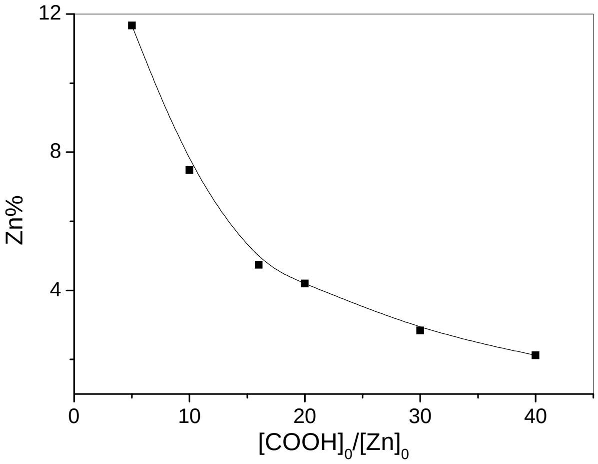

Fig. 2.7. *Loading of zinc in the precursor versus the initial ratio of carboxyl to zinc.*

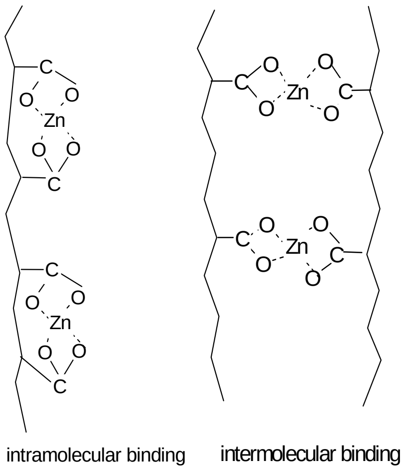

Scheme 2.2

In short, according to the principle of DLS,[15] in a typical polyelectrolyte system consisting of polyions, counterions, co-ions, and solvent, the overall scattering intensity contains contributions from different particles (scatterers) or dynamic modes in the system. These contributions can be separated provided their time autocorrelation functions decay on different time scales. By mathematic treatment, the spectrum of relaxation time obtained from correlation functions is frequently a multimodal distribution where separate peaks can be ascribed to different modes. The position of the peak on the time axis corresponds to the relaxation time of the particular mode and the peak area corresponds to the portion of scattering intensity due to this mode.

Fig. 2.8a is the correlation function of reaction mixture of PAA with and without zinc ions adjusted with ammonium hydroxide to pH 6 and pH 10. At this pH range, the hydrogen bonding between the polymer chains is suppressed significantly. All the curves have typically two modes. With inverse Laplace transformation as seen in Fig. 2.8b, it clearly shows two peaks corresponding to single polymer chain and supramolecular structure, respectively. No new peaks appeared and no obvious difference between the solution with and without zinc cations was found in the figure. It means that cations are mainly loaded on single chain which doesn’t change the scale of hydrodynamic size of a single polymer chain and therefore intramacromolecular is the dominant complex structure in our system.

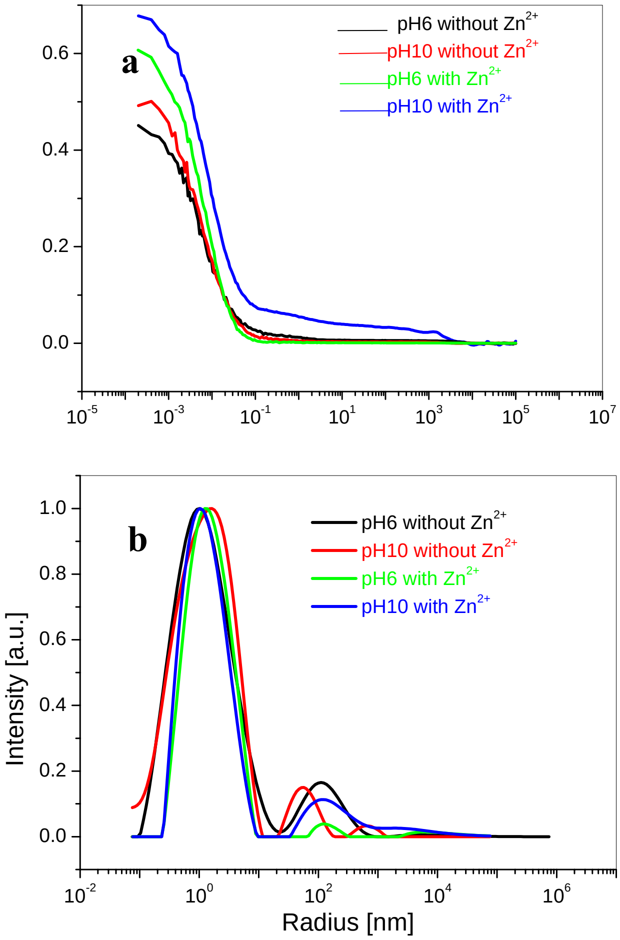

Fig. 2.8. *a) DLS correlation function and b) size distribution of ZnPA solution at different pH. The scattering angle is 90^o.*

The powder of zinc polyacrylate was examined by powder X-ray diffraction (XDR) which shows a pattern confirming the amorphous structure of the polymer precursor (Fig. 2.9).

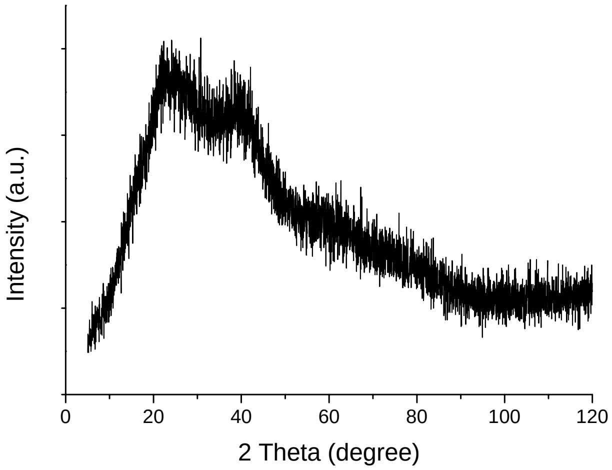

Fig. 2.9. *XRD pattern of ZnPA precursor confirming the amorphous structure.*

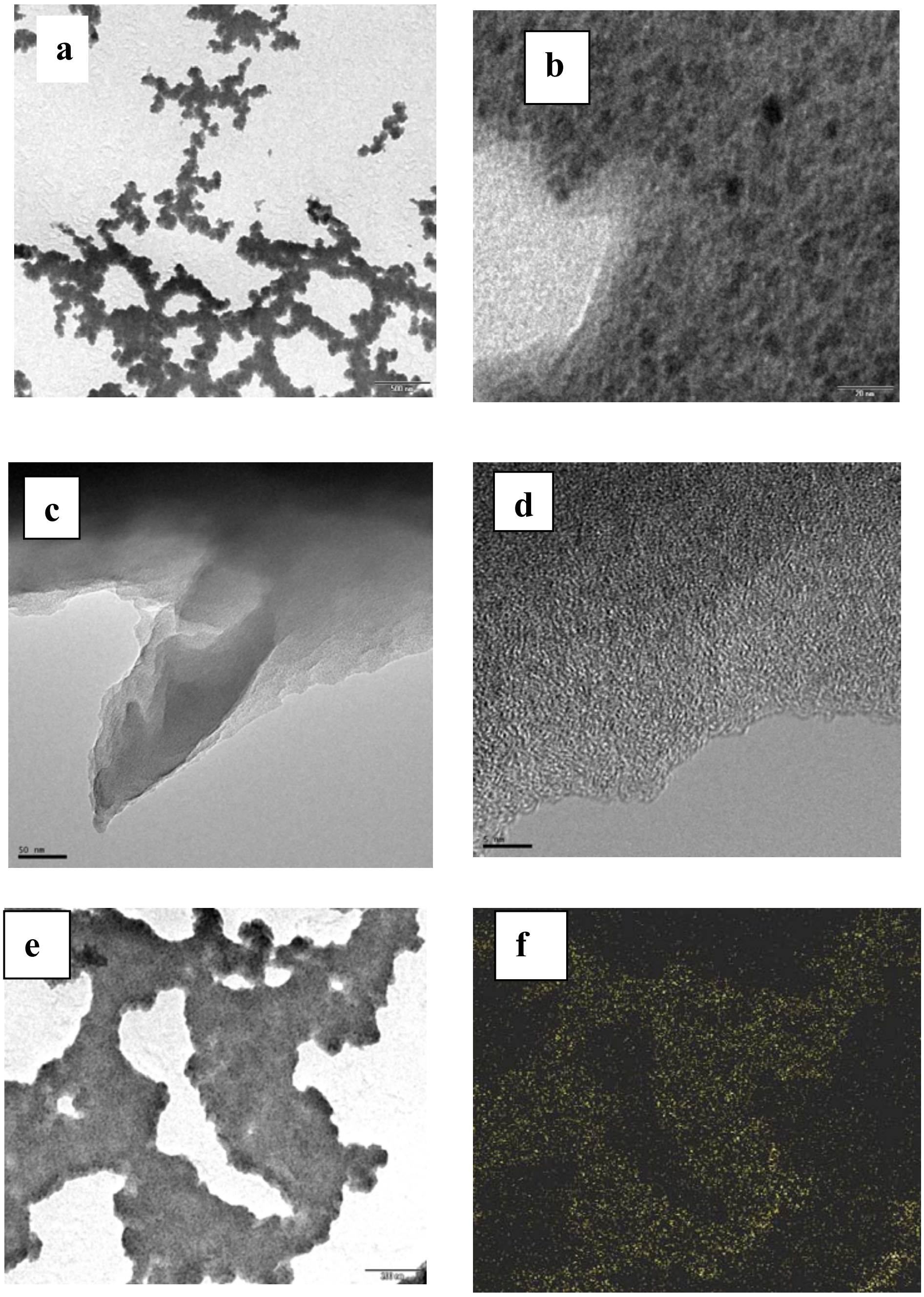

Fig. 2.10. *(a) TEM image showing the morphology of ZnPA. Scale bar: 500 nm; (b) HR-TEM of the sample. Scale bar: 20 nm; (c) TEM showing layered structure. Scale bar: 50 nm; (d) HR-TEM showing amorphous structure. Scale bar: 5 nm; (e,f) TEM and Zn mapping of the ZnPA sample. Scale bar: 200 nm.*

TEM images exhibit the morphology of the zinc polyacrylate prepared by spraying a dilute precursor solution on an amorphous carbon film covered grid. The images show generally unfeatured structures and small particles sized at about 7-8 nm are seen in the polymer matrix, which is probably due to the aggregation of the polymer chains (Fig. 2.10a, b). High-resolution TEM images prove the amorphous structure of the polymer precursor (Fig. 2.10d). The zinc mapping of the image indicates that the zinc elements are homogeneously distributed in the whole polymer matrix (Fig. 2.10e,f). It is worthwhile to note the not very clear layered structures shown in Fig. 2.10c with the interlayer gap clearly seen, possibly interpreting the broad peak in the correspondent x-ray diffraction pattern at low angle.

2.2.2 Interaction of zinc ions and carboxylate groups

It is interesting to understand the short and long-range structure of the zinc polyacrylate precursor, for example, the interaction of zinc ion with carboxylate group of the polymer. The research interest started from the interaction of the polyelectrolyte with the counterion in solution. A titration method has been used to determine the complex formation of polyacrylic acid with various divalent metal ions and gave the stability sequence as $Cu^{2+} > VO^{2+} > Co^{2+} > Ni^{2+}, Zn^{2+}$.[16] With more advanced techniques like light scattering, deeper insights into the fine structure and chemistry of the complex were obtained. Kolawole et al.[17] found the molecular weight of polymethacrylic acid doubled in the presence of Zn^{2+} or Cu^{2+} via an intermolecular binding. A conformational change of the polyelectrolyte induced by metal ions was also detected. Huber[18] studied the conformation of diluted polyacrylate solution in water with Sr counterions using anomalous small-angle X-ray scattering. The counterions were found to be located in sphere-like clusters, which are compatible with collapsed subdomains within the polyacrylate macroions. A model of pearl-necklace–like structure was generated therefrom. Based on the experimental results, several theories have been derived for interpretation of the interaction between the metal ions and the polyelectrolyte. Manning's limiting law[19] assumes that the interaction is long-range and counterions are nonspecifically electrostatically attracted by the polyelectrolyte. Counterions condense onto the polymer or become free dependent on the charge density of the polyelectrolyte. Harvey et al.[20] generated a lattice theory in which site-specific short range interactions are also considered. They derived that the short-range interaction increases with the valence of the metal ion increasing but its magnitude is relatively unimportant in comparison with the long-range interactions. However, because of the complexity of the polyelectrolyte system and many parameters like ionic strength, morphology of counterions and polyions, temperature that may influence the interaction, the theory still needs to be advanced to meet the experimental results.

Spectroscopic methods such as IR, Raman and X-ray absorption spectroscopy (EXAFS) have also been applied in the study of complexes or coordination structures of the carboxylate (especially acetate) group with metal ions.

Generally, there are four representative modes of bonding that could be exhibited by the carboxylate (COO-) group toward a divalent metal ion: ionic, unidentate, bidentate (chelate), and bridging (see scheme 2.3). The bidentate form refers to the structure that a metal ion interacts equally with the two oxygen atoms of the COO- group, whereas in the unidentate form it interacts with only one of those oxygen atoms. In the bridging form, a metal ion interacts with one of those oxygen atoms, and another metal ion interacts with the other oxygen atom. When one of these metal ions is replaced by a hydrogen atom of a water molecule, the system is called to exist in a pseudobridging form.

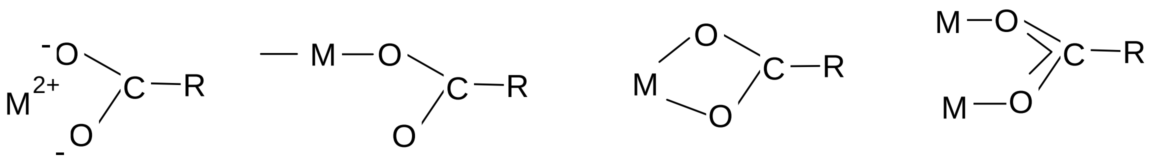

ionic unidentate bidentate bridging

Scheme 2.3

The correlation between the carboxylate group stretching frequencies and the types of COO- coordination has been reported, although controversial spectroscopic data were reported by different researchers. Deacon and Phillips[21] examined the structures and vibration frequencies observed from a number of acetate salts in the solid state and summarized an empirical rule for the correlation between $\nu_{a\text{-}s}$ (frequency difference between the carboxylate antisymmetric and symmetric stretches) and the types of coordination of the COO- group to divalent metal cations, which is expressed as $\nu_{a\text{-}s}$ (unidentate) > $\nu_{a\text{-}s}$ (ionic) ≈ $\nu_{a\text{-}s}$ (bridging) > $\nu_{a\text{-}s}$ (bidentate). They found that the existence of the COO- antisymmetric stretching band at 1553 cm^{-1} and the COO^- symmetric stretching band at 1424 cm^{-1} is a feature characteristic of Ca^{2+}-bound proteins. Nara[22] confirmed the correlation between the vibration and the coordination type and clarified the theoretical basis by means of *ab initio* molecular orbit calculation of several carboxylate compounds, which is the first case in which quantitative derivation of the vibration frequencies was achieved. The case of zinc cations with carboxylate has been studied too. Sakohara[23] gave the correlation between the frequency difference of the carboxylate antisymmetric with symmetric stretches and the types of coordination of the COO^- group to zinc as unidentate ($\Delta\nu$:152 cm^{-1}), bidentate ($\Delta\nu$:94 cm^{-1}) and bridging ($\Delta\nu$:159 cm^{-1}) .

Zinc complexes with polymer have been investigated by measurement of extended x-ray absorption fine-structure (EXAFS). The near-neighbour environment of the bound cation in several ionomer systems, which is defined as copolymers containing less than 10 mol % ionic comonomer has been determined. Grady[24] studied a series of zinc-neutralized ethylene-methacrylic acid ionomers by EXAFS. Neutralization methodology, neutralization level and methacrylic acid content were varied to test whether any of these factors affected the local environment of the zinc cations. Despite the substantial differences in sample preparation procedures, the local environments around the zinc atoms were identical in all materials, resembling the arrangement of atoms in the crystal structure of monoclinic anhydrous zinc acetate (tetracoordinated). Ishioka[25] concluded in the study of the same ionomer that in infrared spectra the 1620 cm^{-1} could be assigned to the zinc acid salt, while the 1565 and 1536 cm^{-1} was due to hexa-coordinated complex structure and 1585 cm^{-1} to tetra-coordinated structure.

Rheology results from Vanhoorne[26] proved the existence of a ‘special interaction’ between zinc ions and carboxylate groups in the zinc-loaded ionomer of ethylene-methacrylic acid, which shows distinctly different behavior in comparison with sodium neutralized ionomers. The zero-shear viscosity is significantly higher for Zn ionomers. The free acid groups substantially lower the viscosity of Na ionomers but have no discernable effect in Zn ionomers. Thus, the conclusion is derived that Na ions can hop between the COO^- groups but Zn ions can’t because they are trapped in a complex.

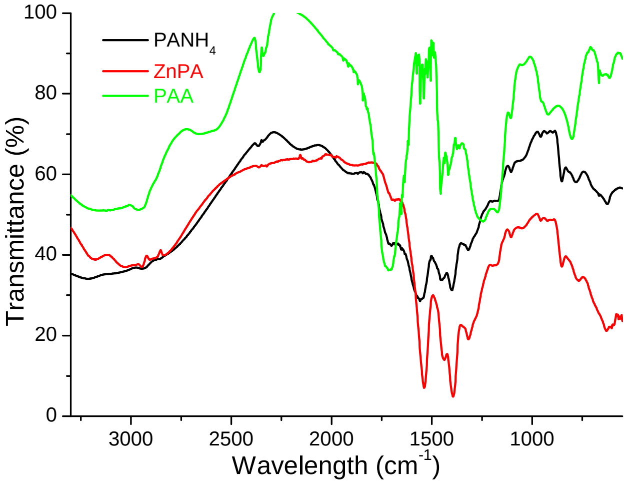

Fig. 2.11. *FT Infrared spectra of $PANH_4$, ZnPA and PAA.*

Pan et al.[27] found that the Zn-O bond length increases with the zinc coordination number increasing from 4 to 6. And they suggest to determine the nearest neighbour coordination number of zinc carboxylate complex via measurement of the bond length in tetra-, penta- and hexacoordinated compounds.

Fig. 2.11 presents the FTIR spectra of PAA, ZnPA and $PANH_4$. It is seen that PAA has a strong peak at 1700 cm^{-1} due to the COOH group. For the samples of ZnPA and $PANH_4$, the intensity of COOH decreases significantly, indicating the neutralization reaction with ammonia. In the region of 1200-1600 cm^{-1}, ZnPA shows absorption bands at 1538 and 1436 cm^{-1} corresponding to antisymmetric and symmetric stretching of the carboxylate group respectively. The difference is consistent with the bidentate form. However, a simple assignment of the absorption at 1436 cm^{-1} to the symmetric stretching of COO^- group seems audacious because of the interference of the polymer backbone (CH_2 bending), which shows weak absorption around 1440 cm^{-1} as well. Moreover, the ammonium polyacrylate shows very similar profile as zinc polyacrylate, which makes the assignment more complicated.

Fig. 2.12 is the Raman spectra of PAA and ZnPA. In the range of 2000-500 cm^{-1}, different bands of PAA and ZnPA are observed. The band at 1576 cm^{-1} is due to the antisymmetric stretching of the carboxylate group. Both of the absorptions at 1459 and 1405 cm^{-1} should be assigned to the symmetric stretching of carboxylate because in Raman spectrum the CH_2 group shows only a very week band.[28] This indicates possibly two different binding structures between zinc ion and carboxylate group. The bend at 688 cm^{-1}, the out-of-plane vibration at 626 cm^{-1} and the rocking band at 520 cm^{-1} of the carboxylate group are also seen.

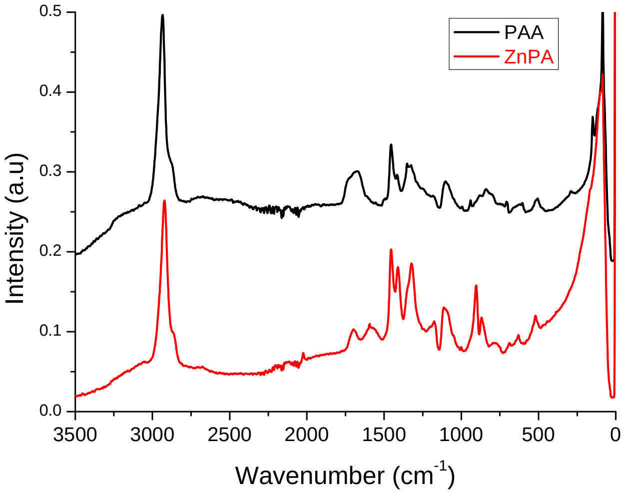

Fig. 2.12. *FT Raman spectra of PAA and ZnPA.*

Although no absolute structural conclusions can be drawn based solely on IR and Raman data of the ZnPA precursor, several points regarding the nature of the chemical structure could be concluded through the above discussion and comparison of the obtained results with the reported ones. Firstly, the interaction of the divalent metal ion is different from that of monovalent metal. Because of the high valence and stronger coulombic interaction, it is very difficult for zinc atoms to hop among the carboxylate groups in the polymer. Secondly, several different zinc carboxylate bonding structures may coexist in the polymer complex due to the relatively weak interaction of zinc ion with the polymer. The coordination structure such as unidentate and bidentate which exists widely in the zinc carboxylate salts likely exists also in this case.

2.3 Formation of ZnO Particles from the ZnPA precursor and Characterization

The obtained colorless powder is amorphous, which converts to zinc oxide powder by pyrolysis in a high-temperature oven with a heating rate of 5 ^{o}C/min. The pyrolysis process was followed and investigated by various tools like thermoanalysis, X-ray diffraction, spectroscopy, etc.

2.3.1 Thermoanalysis

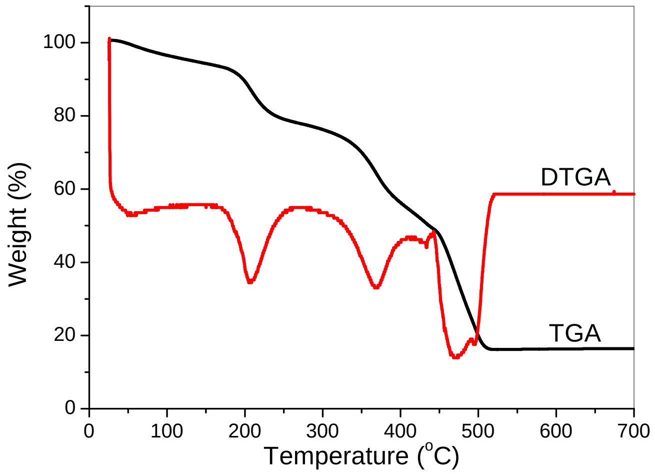

Fig. 2.13. *Typical TGA and DTGA curve of zinc polyacrylate with a heating rate of 5 ^{o}C/min.*

Among thermal analysis techniques thermogravimetry (TGA) is the one in which the change of sample mass in a variety of gas atmosphere is determined as a function of time or temperature. Quantitative measurements of the mass-change are possible. The first order derivative of the mass change with respect to the time, the so-called DTGA, is a useful way to differentiate the reaction steps. Typically a series of peaks are obtained in which the area under the peak is proportional to the total mass-change of the sample. Fig. 2.13 shows the representative curves of TGA and corresponding DTGA of a ZnPA sample.

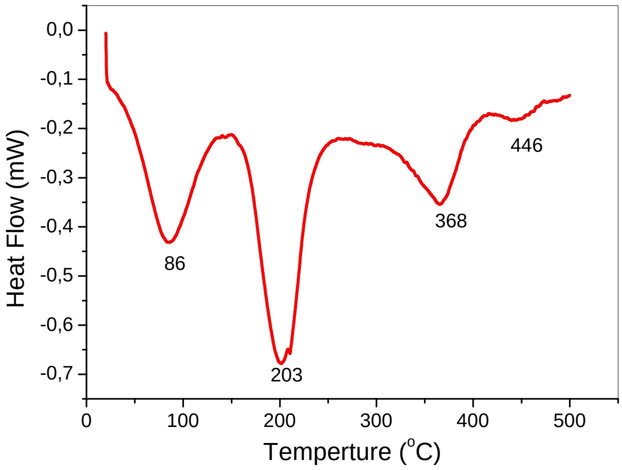

Fig. 2.14. *DSC curve of the ZnPA sample with a heating rate of 5 °C/min.*

The theoretical yield of ZnO calculated from the zinc content in ZnPA is around 10%, depending on the precise content of zinc in the precursor. The curves give a constant weight at 16.2% after 500 °C. From DTGA it is shown that the pyrolysis process undergoes three main weight loss steps, i.e. 50-260 °C , 260-400 °C and 400-500 °C. The result is consistent with that of DSC as seen in Fig. 2.14, where the curve shows exothermal peaks centered at 86, 203, 368 and 446 °C, corresponding to the decomposition steps. The first peak may be due to the small amount of water release in the wet sample. The other three conform well to the DTGA results.

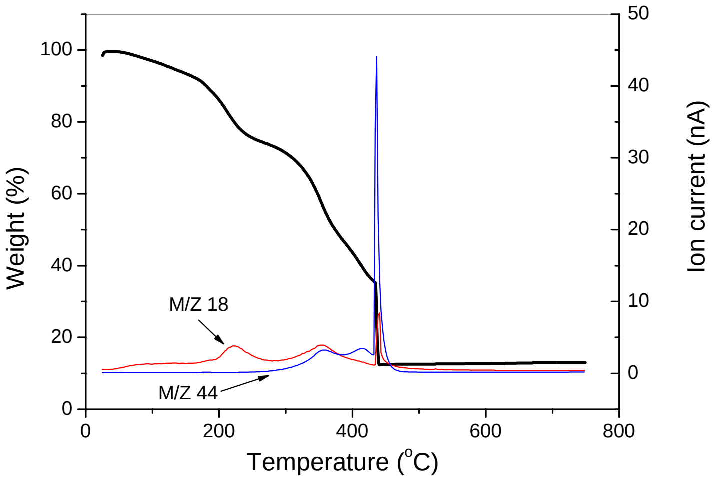

Fig.2.15. *TG-MS plot of ZnPA precursor. The M/Z values of 18 and 44 indicate water and CO_2 molecules as products of thermal decomposition.*

The chemical process involved in each steps could be further characterized by Mass Spectra which is connected to the TGA equipment as seen in Fig.2.15. The peaks of M/Z 18, 44 indicate that the main weight loss is due to the escape of water and CO_2.

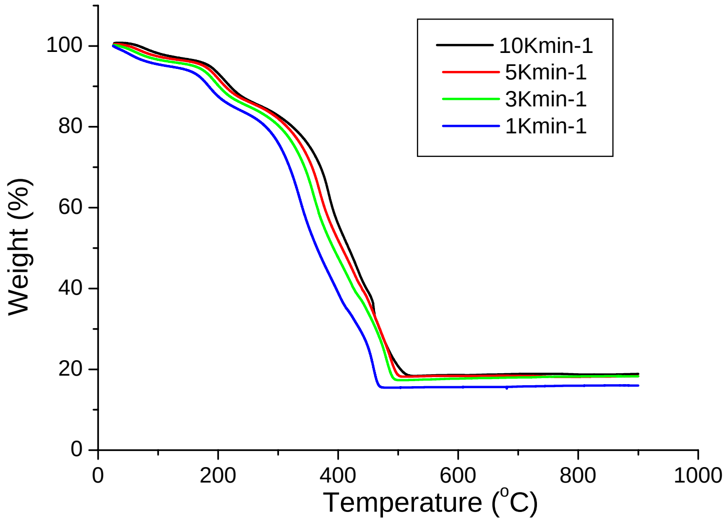

Fig.2.16. *TGA plots of ZnPA with different heating rates.*

Pyrolysis of ZnPA at different heating rates was checked by means of TGA. Fig. 2.16 shows the TGA curves of ZnPA at different heating rates from the slowest of 1 °C•min^{-1} to the fastest of 10 °C•min^{-1} using air as carrier gas and Fig. 2.17 is the corresponding first order differential TGA , so-called DTGA,results. All the curves show similar profiles indicating the same pyrolysis steps.

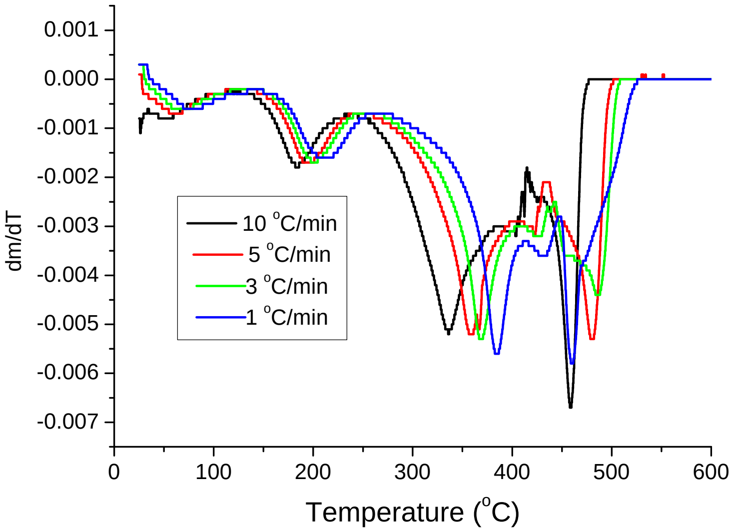

Fig.2.17. *DTGA plots of ZnPA with different heating rates.*

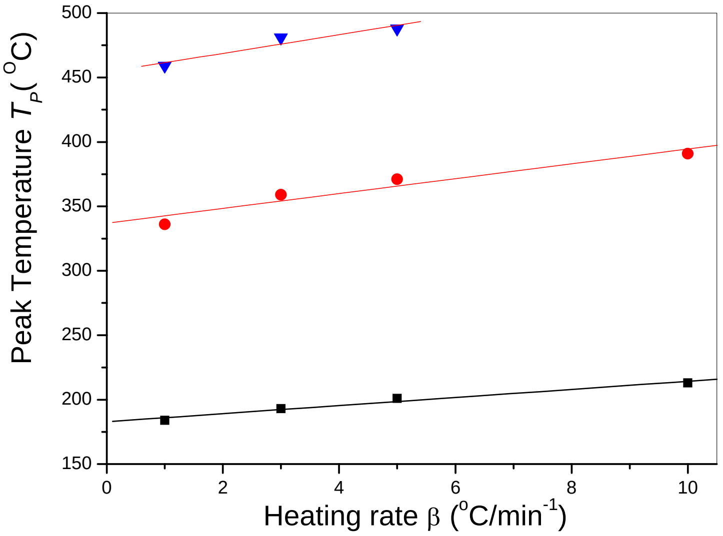

Fig. 2.18. *The relation of the peak temperature from DTGA with different heating rates.*

The experiment with the lowest heating rate gives the lowest yield of ZnO, which is due to the longer calcination time and therefore less unvolatilized residue left. And with faster heating rate, the peak positions appear at higher temperatures. The peak temperature (T_P) derived from DTGA is plotted with respect to heating rates (β) as seen in Fig. 2.18. A linear relation of peak temperature with regard to the heating rate is observed.

2.3.2 X-ray diffraction

The XRD patterns show the evolution of zinc oxide from the precursor upon calcination (Fig. 2.19). The typical protocol for the heating treatment of the precursor powder is set up as following:

$$\text{Room temperature} \xrightarrow{\text{heating } 5\ ^{o}\text{C /min}} 500\ ^{o}\text{C} \xrightarrow{\text{isothermal 1 h}} 500\ ^{o}\text{C}$$

The precursor remains amorphous when the temperature arrived at 125, 250 °C even as high as 370 °C. This is the unique property of this precursor polymer, which is quite different from previous reports. Shim et al.[29] followed the typical Pechini method and reported that in their experiment the amorphous-crystal transition from polymer precursor to zinc oxide took place at 300 °C and was complete at 400 °C. It is notable that 300 °C is a critical temperature at which a good many of zinc salts convert to ZnO by direct thermal decomposition such as zinc nitrate hexahydrate,[30] zinc acetate dihydrate[31] and zinc oxalate.[32] Therefore, the stability at high temperature is unique to this polymer precursor and distinguishes it from those obtained by previous methods.

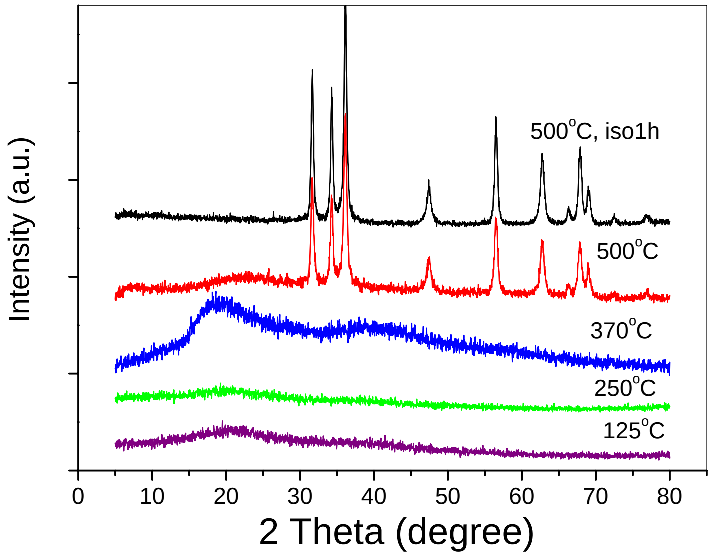

Fig. 2.19. *XRD pattern showing the ZnPA precursor pyrolyzed at different temperatures and formation of the ZnO.*

The crystallization of zinc oxide in our experiment happens actually in the third weight loss stage. When the temperature was increased to 500 °C, the formation of zinc oxide is observed. The diffraction pattern is consistent with JCPDS card 36-1451. The difference between the samples with and without isothermal annealing is also distinguishable. After the 1 h isothermal annealing at 500 °C, the amorphous halo between 2θ 20-30° disappeared, indicating the increase of crystallinity.

2.3.3 FTIR and Raman Spectra

2.3.3.1 FTIR spectra

The evolution of zinc oxide from zinc polyacrylate precursor powder was investigated by means of FTIR spectroscopy. The experiment is set by calcination of a series of ZnPA powders under the same conditions. The intermediate products calcined at predetermined temperatures from 230 to 500 °C were taken out of the hot oven and then measured by FTIR by standard KBr pellet method (Fig. 2.20). For the sample calcined at 230 °C, absorption band at 1717 cm^{-1} is evident in addition to the characteristic absorption of the carboxylate group at 1569, 1456 and 1402 cm^{-1}. The band shown at 1717 cm^{-1} is due to the carboxylic group (COOH), indicating the conversion of COO^- group to COOH. Because of the invariance of absorption of COO^- in the range of 1400-1600 cm^{-1}, it is inferred that the conversion between

COO^- and COOH takes place at ammonium bound carboxylate groups, as described in Scheme 2.4. This could be proved by controlled experiments. Fig. 2.21 gives the FTIR spectra of ammonium polyacrylate and calcined sample at 250 °C. It shows that after calcination at 250 °C, the band at 1717 cm^{-1} due to carboxylic group is much stronger than the band of the carboxylate group, indicating that the most of the carboxylate groups have been converted to carboxylic groups at this temperature.

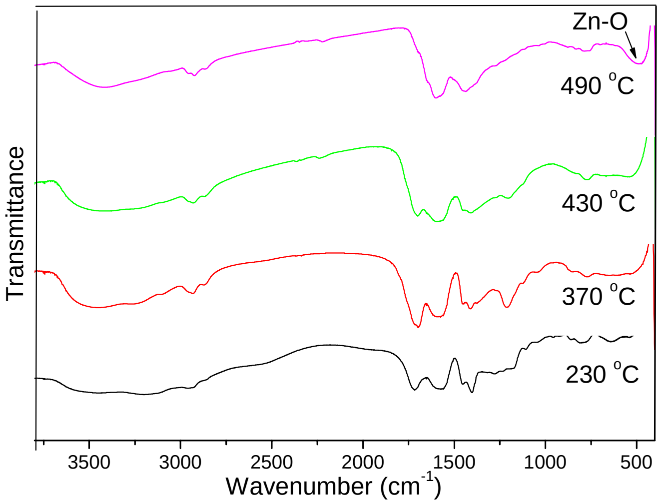

Fig. 2.20. *FTIR spectra showing the pyrolysis process of ZnPA precursor. The heating rate is 5 K/min.*

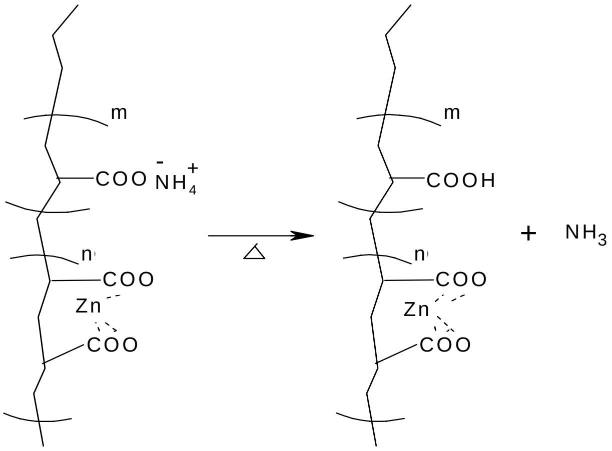

Scheme 2.4

With higher temperature, the absorption of COOH continuously shrinks and at 490 °C the typical Zn-O stretching band appears indicating the formation of zinc oxide.

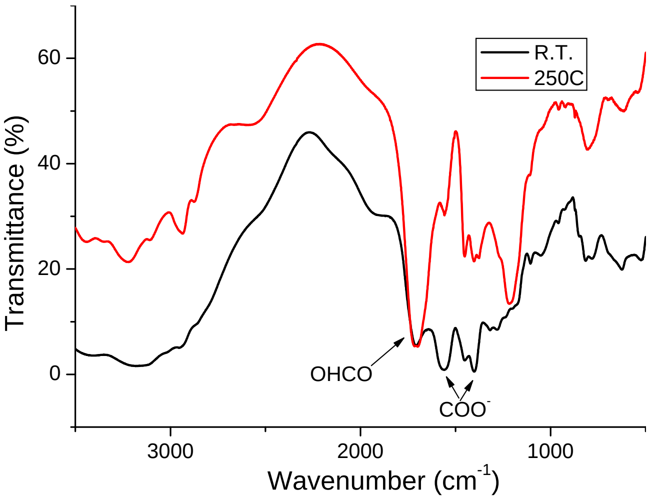

Fig. 2.21. *FTIR spectra of ammonium polyacrylate and sample calcined at 250 °C.*

FTIR spectrum of a typical as-synthesized ZnO sample is shown in Fig. 2.22, reflecting the surface feature of the nanoparticle. 'Typical' ZnO in this chapter means that the precursor of the ZnO was prepared using PAA with Mn of 5,000 and the ratio of zinc to carboxylate group set as 1:10. The ZnO was formed by calcination of the precursor at 500 °C with additional annealing for 1 h at this temperature. The absorption at 3432 cm^{-1} is due to OH- stretching at the particle surface. The weak bands at 2920 and 2850 cm^{-1} could be assigned to the antisymmetric and symmetric C-H stretching respectively,[33] ascribable to the trace amount of the organic residue from the polymer. The intense bands at 1552 and 1439 cm^{-1} are ascribable to antisymmetric and symmetric carboxylate stretching, indicating the complexation of carboxylate groups with surface Zn ions of the ZnO crystal. Their frequency difference (Δv = 108 cm^{-1}) reveals that the mode of binding of the carboxylate group to the ZnO surface might be interpreted as bidentate. The strong band centred at 479 cm^{-1} due to the characteristic Zn-O bonds stretching in zinc oxide is observable.[33a]

It is worthwhile to mention the theory of average dielectric constant (TADC) which explains the correlation between the ZnO morphology and the IR spectra. In general, three factors might affect the IR spectrum of a powder sample in addition to the crystal structure and composition: (i) the dielectric constant of the matrix in which the material is diluted, (ii) the shape of the microcrystals expressed by form factor or shape factor (g) with the assumption that an individual particle has the shape of a rotation ellipsoid around axis c. and (iii) the particle aggregation determined by the filling factor (f). As KBr was used for sample preparation, effects of the matrix could be ignored. In the zinc oxide microcrystalline samples, which has a wurtzite structure with two transverse optical modes at $\upsilon_{T\parallel}$ = 377 cm^{-1} and $\upsilon_{T\perp}$ =

406 cm^{-1}, the particle shape affects the position and intensity of the two optical modes, as illustrated in Fig. 2.23 for selected morphologies. It can be seen that the two absorptions of ZnO move in opposite directions in going from the slab ($g_I = 1$) to the cylinder ($g_I = 0$) morphology, being 0.33 for ideal spheres.

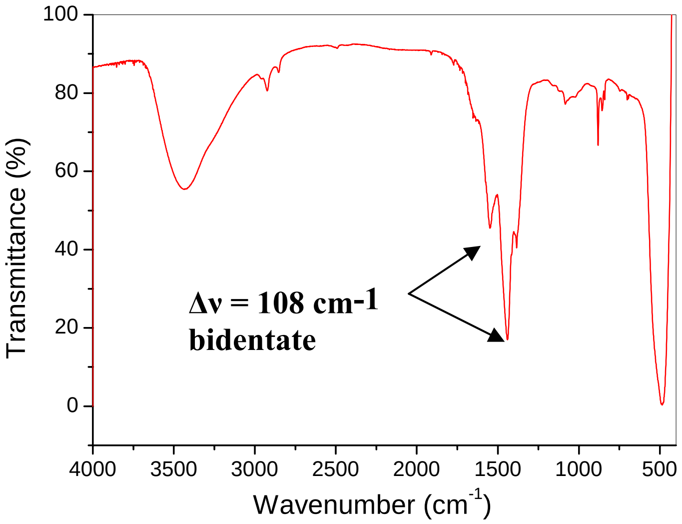

Fig. 2.22. *A typical FTIR spectrum of as-synthesized ZnO powder.(The precursor of the ZnO was prepared using PAA with Mn of 5,000 and the ratio of zinc to carboxylate group set as 1:10. The ZnO was formed by calcination of the precursor at 500 °C with additional annealing for 1 h at this temperature.)*

The filling factor f enables to take the interactions between particles in the sample into consideration and as a result to distinguish the case of a system with non-interacting individual particles when f is close to 0 and aggregates when f to 1. In the reported literature, the calculations results of the IR-absorption spectra forms of spherical particles for several values of f are given. This enables the graphical presentation of $\upsilon_{\max} = F(f)$ (Fig. 2.24) to work as a standard curve.

It should be mentioned that the obtained dependence of $\upsilon_{\max}$ with respect to various values of g and f, only emphasizes the complexity and difficulties existent in working with real systems. These systems are most often characterized by a set of different states. The absorption zones from different origins often superpose in a narrow frequency range, leading to their unique identification based only on IR analysis difficult.

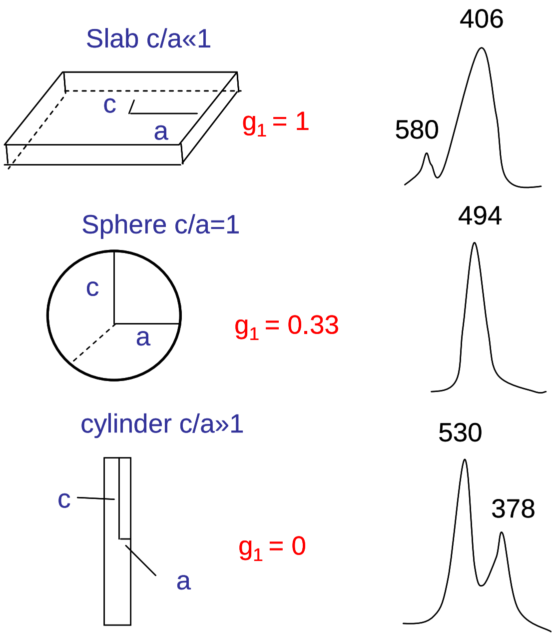

***Fig. 2.23.** Calculated IR spectra of ZnO microcrystals corresponding to different axial ratios (c/a). In every case the crystallographic c axis is considered to be coincident with the revolution axis of the ellipsoid.*[34]

From the electron microscopic observation, the as-synthesized ZnO shows mostly spherical particles, which will be discussed in detail later. Therefore, the shape factor that influences the IR spectra is not considered here. The value of *f* is determined to be about 0.3 as marked in Fig.2.24, indicating a mainly non-aggregated state.

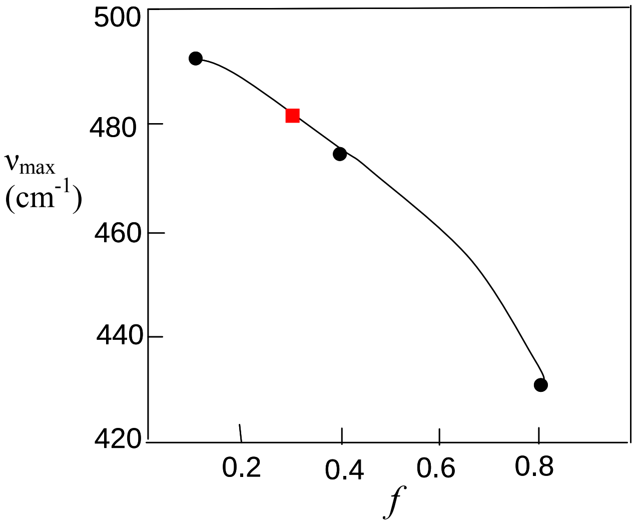

***Fig. 2.24.** The dependence of the position of the IR-absorption peak for spherical particles as function of the filling factor f.*[35] *The red point denotes the position of as-synthesized ZnO (same sample as Fig. 2.22).*

2.3.3.2 Raman spectra

***Table 2.2**. Reported bulk ZnO phonon mode frequency (cm^{-1}) from Raman measurement.*

	Ashkenov *et al.*[36b]	Damen *et al.*[37]	Callendar *et al.*[38]	Bairamov *et al.*[39]
$\omega[E_1(TO)]$	410	407	407	409.5
$\omega[E_1(LO)]$	591	583	583	588
$\omega[A_1(TO)]$	379	380	381	378
$\omega[A_1(LO)]$	…	574	…	576
$\omega[E_2^{(1)}]$	102	101	…	98
$\omega[E_2^{(2)}]$	437	437	441	437.5

Wurtzite-type ZnO belongs to the space group C_{6v}^4 with two formula units in the primitive cell. The optical phonons at the Γ point of the Brillouin zone belong to the following irreducible representation:

$$\Gamma_{opt} = 1\,A_1 + 2\,B_1 + 1\,E_1 + 2\,E_2.$$

Both A_1 and E_1 modes are polar and split into transverse (TO) and longitudinal optical (LO) phonons, all being Raman and infrared active. The two nonpolar E_2 ($E_2^{(1)}, E_2^{(2)}$) modes are Raman active only. The B_1 modes are infrared and Raman inactive (silent modes). Table 2.2 shows the IR and Raman results of phonon mode frequencies of ZnO bulk samples selected from some previous reports.

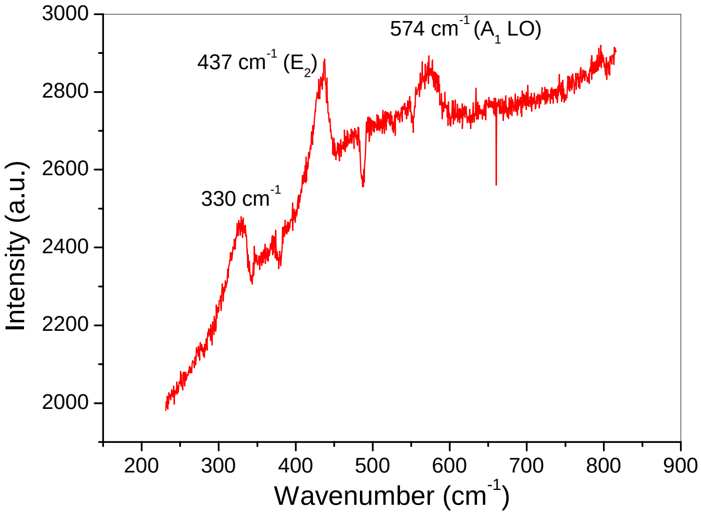

***Fig. 2.25.** FT Raman spectrum of the as-synthesized ZnO powder (The same sample as that of Fig. 2.22).*

Fig. 2.25 shows the polarized Raman spectrum of as-prepared ZnO nanoparticles. The ZnO $E_2^{(2)}$ phonon mode occurs at 437 cm^{-1}, and the line at 330 cm^{-1} was assigned to multiple-phonon processes.[36] The ZnO A_1(LO) (574 cm^{-1}) mode shows strong absorption as well. The strong background is due to the fluorescence of the sample.

2.3.4 Morphology of zinc oxide

The morphology of zinc oxide prepared at different conditions has been checked by means of microscopes such as SEM, TEM and AFM. Most SEM images show that the as-prepared ZnO consists of mainly individual particles sized around 40 nm in diameter with a narrow size distribution. Various parameters and experimental conditions that could affect the morphology of ZnO are investigated.

(1) Temperature

Fig. 2.26 shows the zinc oxide nanoparticles obtained at temperatures of 500, 600, 650 °C respectively. The samples were annealed for 1 hour at their respective temperature. ZnO shows the morphology of well-grown particles. The primary particles do not aggregate but a few twinned crystals also appear. The mean particle size and its distribution were obtained from the images by the statistic method and a Gaussian fit. The results show that both the particle size and size distribution increase with temperature. The particle size obtained from SEM and calculated from X-ray diffraction patterns using Scherer formula is tabulated with respect to sample annealing temperature (Table 2.3). It is noted that the size determined by Scherer formula is by far smaller than the size observed from SEM. The obvious difference between the two size values is due to the nature of Scherer method, which actually examines the coherent grain boundary, namely crystallite, in the field of view of microscope.

Table 2.3. *ZnO particle size determined by different methods versus annealing temperature.*

Annealing temperature	500 °C	550 °C	650 °C
XRD size (nm)	19	20	24
SEM size (nm)	39	50	101

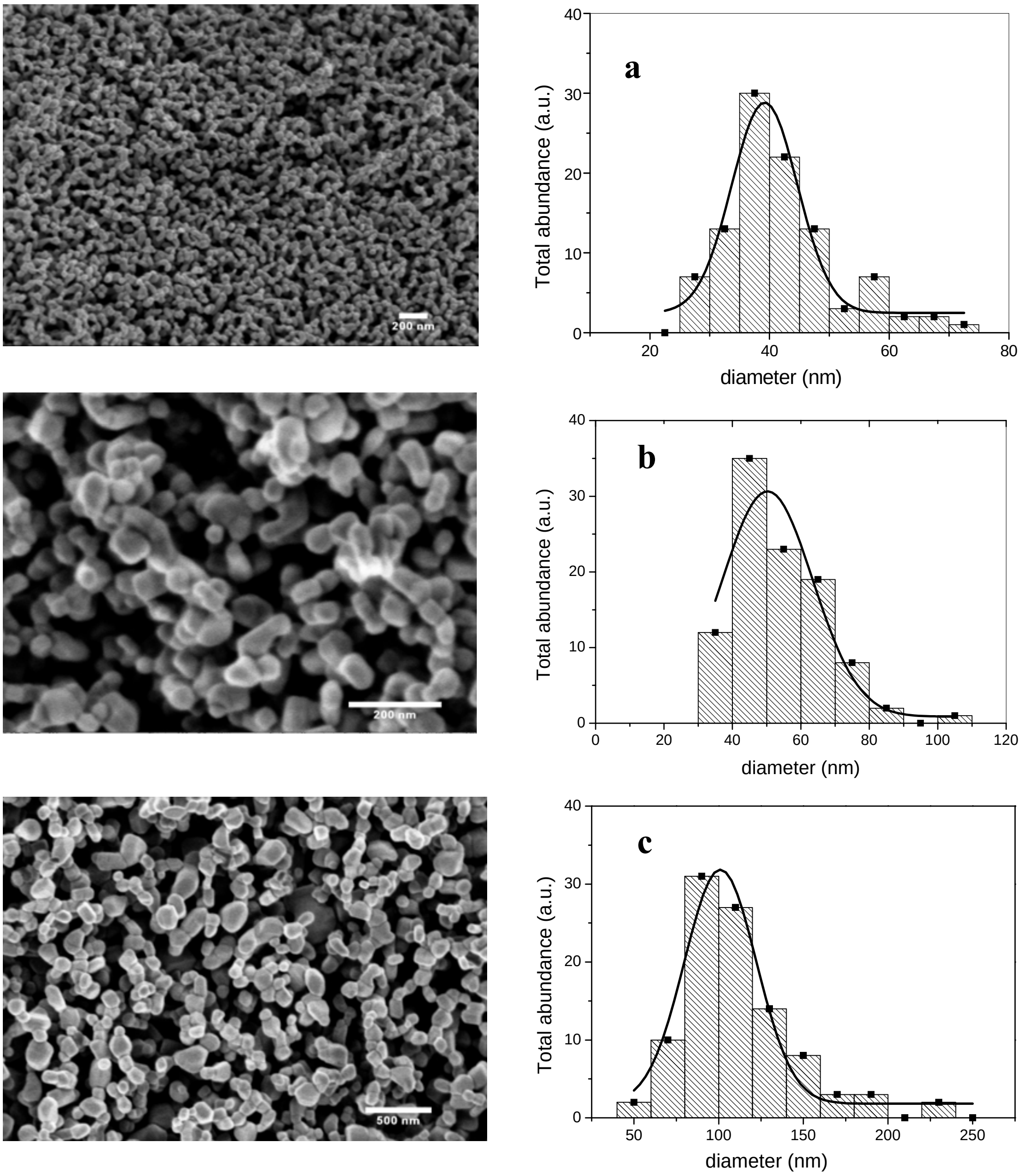

Fig. 2.26. *SEM images of ZnO nanoparticles and correspondent size distribution histograms of samples at different heating temperatures at (a) 500 (b) 550 (c) 650 °C.*

(2) Structure evolution process

The process of in-situ pyrolysis of the ZnPA precursor is also monitored by SEM. We have tried to investigate the intermediate samples and find out information on the nucleation and growth process of the ZnO particles. The pyrolysis was conducted with a heating rate of 5 ^{o}C•min^{-1} from room temperature to 500 ^{o}C using air as carrying gas. The samples were taken from the hot oven at 125, 230, 370, 430, 455 and 490 ^{o}C and their color became darker with temperature increase. At 125 ^{o}C, the morphology of the powder is similar with that of ZnPA at room temperature. The images show big agglomeration of particles with diameter about 200 nm (Fig.2.27a, b). When heated to 230 ^{o}C, craters on the surface began to appear indicating the release of water or gas (Fig.2.27c). The craters became denser with temperature (Fig.2.27d, e) and at 490 ^{o}C small particles appeared with size of about 20 nm, indicating the formation of ZnO nanoparticles (Fig.2.27f).

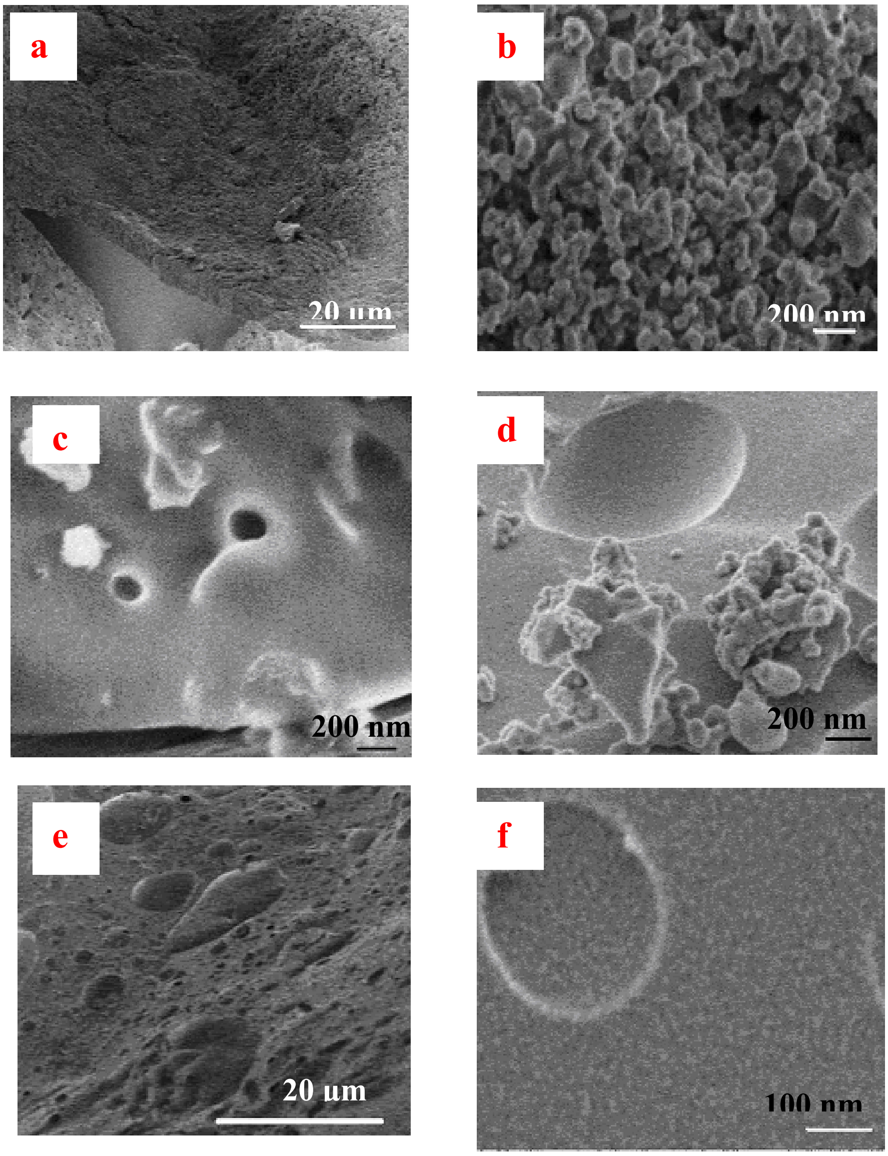

Fig.2.27. SEM images exhibiting the pyrolysis process of ZnPA from room temperature to 500 ^{o}C with a heating rate of 5 ^{o}C/min. The intermediate samples at (a,b) 125 ^{o}C (c)230 ^{o}C ; (d)430 ^{o}C; (e) 450 ^{o}C and (f) 490 ^{o}C are shown.

(3) Heating rate

The heating rate can also influence the ZnO morphology. It is seen that with faster heating rate more inhomogeneous particles with twinned or agglomerated structures are obtained. The abnormal ZnO morphology shown in Fig.2.28 is remarkable, which exhibits a layered structure. The sample is heated with a rate of 10 ^{o}C/min. It has a sandwich-like structure with upper and underneath layers consisting of rods and is in-between composed of nanoparticles. A possible explanation is that the structure was developed due to the uneven heat transportation from the surface to the center of the powder. At the surface area, the zinc oxide tends to aggregate because of excessive heat gaining. Thus, in the experiment operation, the ZnPA precursor samples need to be spread as very thin layer on the crucible for pyrolysis.

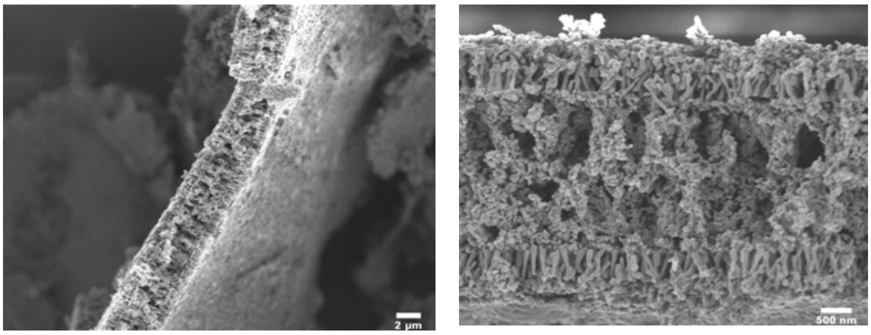

Fig. 2.28. *SEM images showing abnormal sandwich-like structure of ZnO crystal caused by a quick heating rate of 10* ^{o}*C/min.*

(4) Loading of polymer precursor

Fig.2.29 shows the effects of loading of zinc in the ZnPA precursor on the morphology of the final products (ZnO). It shows that with higher zinc concentration in the polymer precursor, the obtained ZnO tends to aggregate or compactly connect with neighboring particles (Fig. 2.29a, c, e). While with lower zinc content in the precursor, actually lower nucleation density, and individual nanoparticles are the main product (Fig. 2.29b, d, f). This indicates that an existing equilibrium between the minimum aggregation and reasonable yield of ZnO may be achieved by adjusting the loading of metal ion in the polymer.

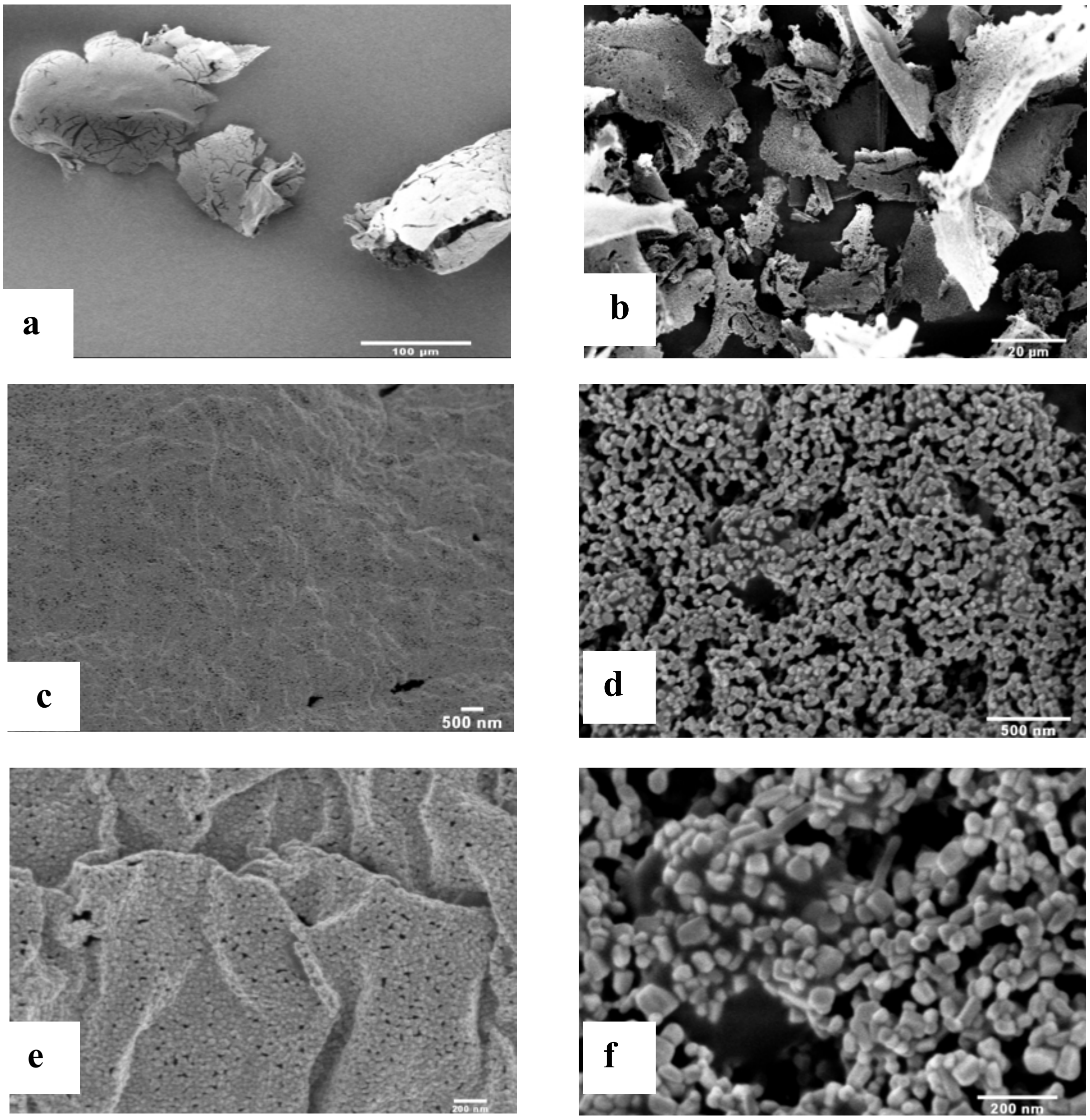

Fig. 2.29. *SEM images of ZnO nanoparticles obtained from polymer precursor (Mn: 1×10^5) with different zinc loading. (a, c, e) ZnO from precursor with $[COOH]_0/[Zn]_0=10$; (b, d, f) ZnO from the precursor with $[COOH]_0/[Zn]_0=40$. The scale bar is 100µm in a, 20 µm in b, 500 nm in c and d, 200 nm in e and f. The ZnPA was pyrolyzed with a heating rate of 3 °C/min.*

(5) Molecular weight (Mn) of polyacrylic acid

PAA with three different molecular weights (5000, 1×10^5 and 4.5×10^5) were employed as starting material for ZnPA preparation. The SEM images of corresponding ZnO nanoparticles show different morphologies, indicating significant effects of molecular weight on the final product. With smallest molecular weight, the ZnO forms leaf-like thin layers (Fig.2.30a) (agglomerates of ZnO nanoparticles) with the length about 20 µm. With higher magnification, individual particles with clear boundary are seen ((Fig.2.30b). These particles could possibly be separated into single particles by means of surface modification. But with higher molecular polymer precursor, the ZnO forms bigger layer at the scale of 100 μm (Fig.2.40c) and eventually develop into a hollow sphere (Fig.2.30e). The nanoparticle size is within 20-40 nm but highly aggregated (Fig.2.30d, f). This suggests that a low molecular weight of precursor is favorable for the synthesis of non-aggregate ZnO material.

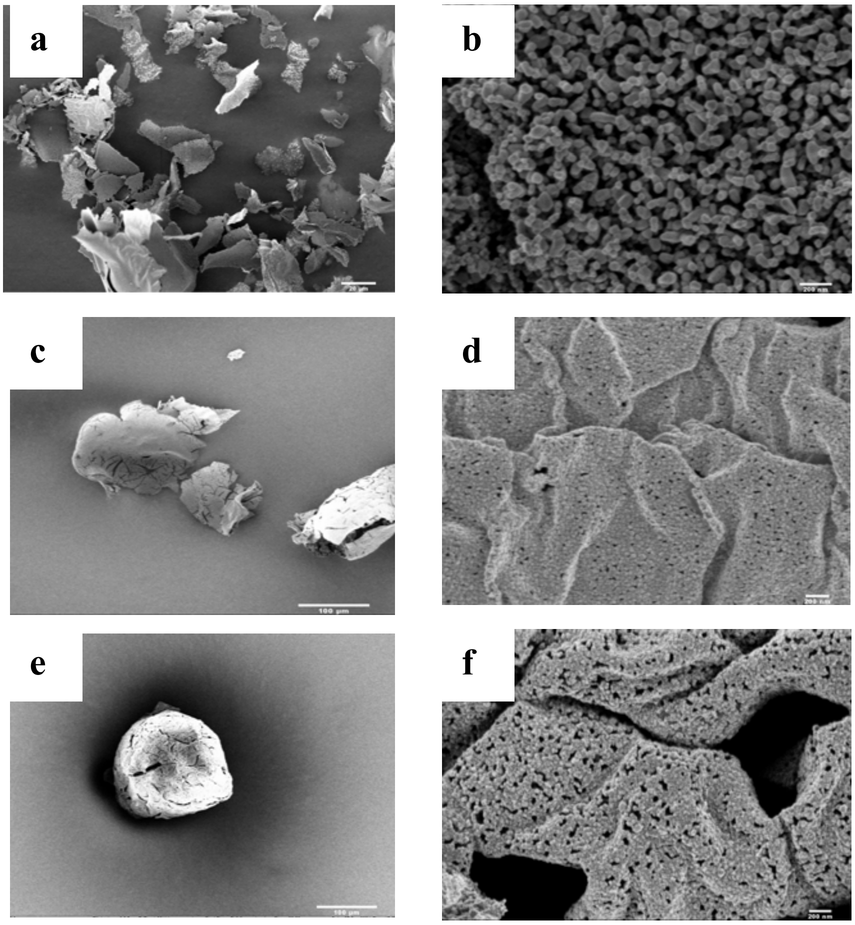

Fig. 2.30. *SEM images of ZnO nanoparticles obtained at 550 °C from polymer precursor with different molecular weight (a,b) 5,000 (c,d) 100,000 (e,f) 450,000. For all the three samples keeping* $[COOH]_0/[Zn]_0=10$ *for the precursor. The scale bar is 20μm in a, 100 μm in c and e, 200 nm in b, d and f.*

For more information about the morphology of the as-prepared ZnO, ZnO samples were cast on a Si wafer for electron microscopy observation. The sample was elaborately prepared by forming a suspension of ZnO powder in toluene via refluxing over night. Then, a drop of the suspension was cast onto a clean silicon wafer and dried at 50 °C in vacuo. The sample was examined by SEM (Fig.2.31a, b) and atom force microscopy (AFM) (Fig.2.31c, d), respectively. Both the images show some individual particles with the particle size consistent with that measured in solid state. Large cluster of ZnO particles (indicated by arrows) due to the heavy aggregation are also seen. A further treatment is necessary to highly disperse the ZnO by breaking up the aggregates by means of chemical treatment.

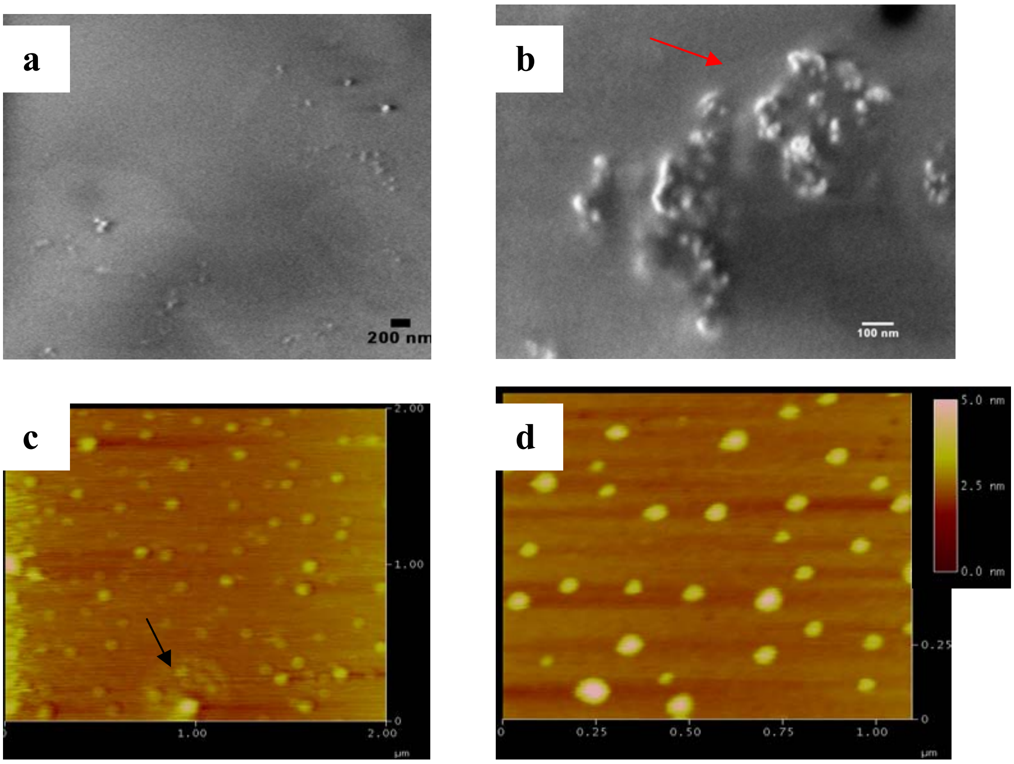

Fig. 2.31. *ZnO nanoparticles prepared on a silicon wafer and observed by (a, b) SEM; (c, d) AFM. The ZnO was obtained at 550 ^oC and annealed for 1 h at the temperature.*

2.4 Photoluminescence and EPR spectra of zinc oxide

2.4.1 General introduction

As an important low-voltage phosphor material which is promising for application in the next generation of flat panel displays, the optical properties of ZnO have attracted great research interest. ZnO typically exhibits a UV near-band-edge (NBE) emission and a broad visible band (in the continuum from red to violet) emission due to crystal defects. The UV emission has already been ascribed to direct recombination of free excitons. But the assignment of visible emission has been always controversial. It has proved that the emission is due to intrinsic defects of the material and not an extrinsic impurities such as Cu or Li doping.[40]

Various techniques have been used to investigate the origin of the visible emission, including electron paramagnetic resonance (EPR), photoluminescence (PL), positron annihilation spectroscopy (PAS) as well as theoretical calculations. In spite of many controversial results, some explanations have been proposed to explain the nature of the visible emission. A widely adopted mechanism is the transition between a singly charged oxygen vacancy and a photoexcited hole.[41] It has been accepted as explanation of peaks from 495 nm (tetrapod ZnO nanorods)[42] to 583 nm (tubular ZnO whiskers)[43] in different forms of ZnO samples such as single crystals, thin films and powders.

However, PAS results contradict the PL results on the nature of defects. A direct relationship between positron lifetime and visible (yellow) emission is not found.[44] And Liu et al found that Mn doping quenches the visible emission but doesn't influence the defect concentration as detected by PAS. They concluded that PAS did not probe directly the PL defect centers and suggested Zn_i and O_i are responsible for green and yellow emission respectively.

Egelhaaf and coworkers[45] suggested a donor-acceptor-type transition to interpret the observed green luminescence of polycrystalline ZnO seen in diffuse reflection, steady state and time-resolved photoluminescence as well as photoconductivity.

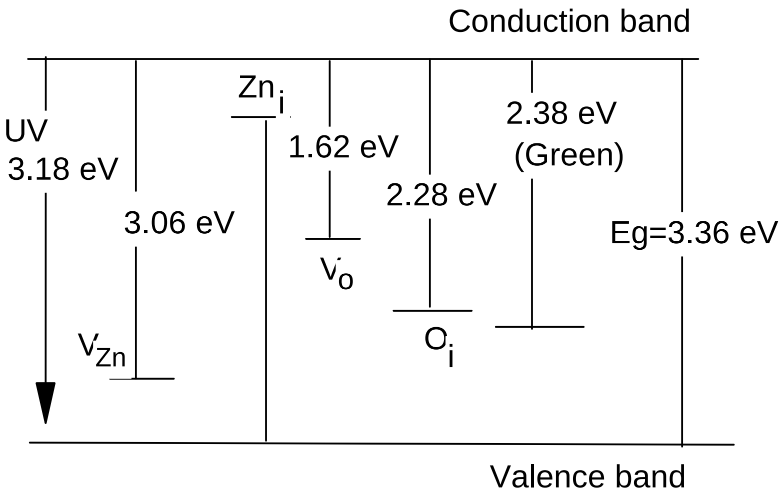

Fig. 2.32. Scheme of the calculated defect levels in ZnO films.[46]

Fu et al.[46] studied PL properties of the ZnO film deposited on a Si substrate by dc reactive sputtering. The defect levels were calculated and drafted in Fig. 2.32. The energy interval from the bottom of the conduction band to the O_{Zn} level (2.38 eV) is exactly consistent with the energy of the green emission in their experiment, whereas the O_i level (2.28 eV) is also close to the value, but the probability of forming O*i* is small due to the large diameter of oxygen atom. The V_{Zn} could not be related to the green emission, because the energy interval, 3.06 eV, is far beyond the visible emission energy. Therefore, the suggestion of green emission due to the antisite defect O_{Zn} level seems most probable in their case.

For nanostructured ZnO materials, surface features are especially important for PL emission. Due to the large surface area to volume ratio, the defects centers are most likely located on the particle surface. Surface coating of the ZnO tetrapod structures results in the suppression of the green emission, which may support the hypothesis.[47] Similar results are also obtained in poly-(vinylpyrrolidone) (PVP) capped ZnO nanoparticles.[48] Several theories have been proposed to interpret the effect of nanoparticle surface on the luminescence properties. For instance, Henglein[49] suggested the mechanism of surface anion vacancies, while Behneman[50] attributed it to the tunneling of surface-bound electrons to preexisting trapped holes.

In addition to the common green emission, violet and blue emission has been also observed from ZnO thin films, nanoparticles and whiskers including the emissions centred at 405 nm,[51] ~420 nm,[52] 466 nm[53] and ~485 nm.[54] The violet emission at 405 nm as reported by Wu and coworkers[55] is assigned to a zinc vacancy. The peak at 420 nm was assigned to O_i and 485 nm to the transition between Vo and O_i by comparison of the structure similarity of ZnS and ZnO. The blue emission at 466 nm was detected by Chen et al.[53] in the chemically synthesized ZnO nanowires. The emission is tentatively attributed to the oxygen or zinc defects generated in the process of ZnO growth. Moreover, red emission (640 nm)[56] in ZnO film prepared by spray pyrolysis and yellow emission (583 nm)[57] from single crystal tabular ZnO whiskers are also reported.

As powerful tool, EPR spectroscopy has been used frequently in combination with PL, to investigate the defect nature of ZnO materials. The defect evolution of ZnO crystals was investigated in the process of mechanic thermal treatments based on EPR method. And all the detected EPR signals were assigned to the corresponding defects centres.

Vanheusden et al.[41] attempted to correlate the commonly observed EPR signal at $g = 1.96$ with the green PL emission for interpretation of the origin of the visible emission. They believe the EPR signal is from the singly charged oxygen vacancy (V_o^+). However, theoretical calculation indicates that oxygen vacancy is a deep donor,[58] while the EPR signal at $g = 1.96$ has been unambiguously assigned to shallow donor centres independent on shallow donor identity. And it is found that V_o^+ produces EPR signals at $g_\perp = 1.9945$ and $g_\parallel = 1.9960$ as well.[59] Some experimental results have demonstrated no relationship between green emission and $g = 1.96$ EPR signal.[60]

2.4.2 Photoluminescence of ZnO nanoparticles

Fig. 2.33 is the typical excitation and emission spectra of our ZnO powder sample. The sample was prepared with same procedure as that of Fig. 2.22. The excitation spectrum exhibits the exciton peak at 371 nm, which is consistent with the bulk ZnO material band gap 3.3 eV. A weak NBE emission is observable at 376 nm and two intense and partially overlapping blue emission centered at 416 nm and 439 nm in addition to the strong yellow emission at 590 nm are also detected. The intensity ratio between the blue and orange emission varies under different excitation wavelength. The weak NBE emission is due to the high defect density of the crystal. In the light of the introduction, the origin of the blue and yellow emission recorded here is tentatively attributed to V_{Zn} and O_i respectively, considering the formation of the crystal powder in an oxygen-rich atmosphere.

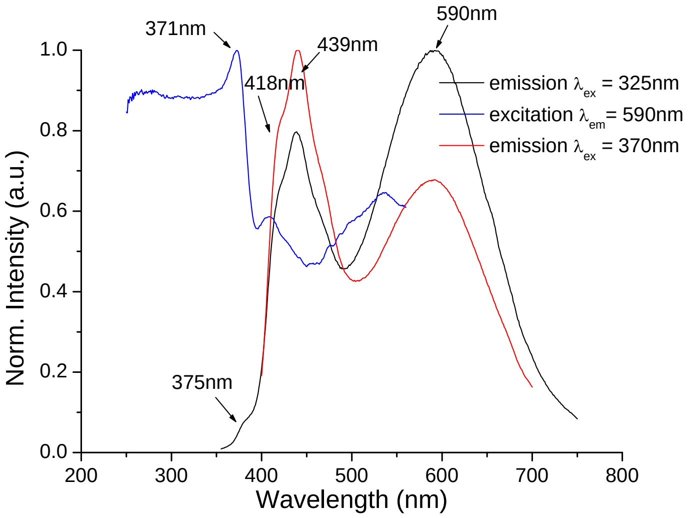

Fig. 2.33. *PL spectra of as-synthesized zinc oxide powder. (The same sample is same as that of Fig. 2.22). The excitation wavelength is 325 and 370 nm respectively.*

Temperature-dependent PL measurement was also carried out for the powder of ZnO nanoparticles from room temperature to 100 K via cooling the system by liquid nitrogen (Fig. 2.34). The sample is same as that of Fig. 2.22. The ZnO powder shows relatively weak visible emission at room temperature. Decreasing the temperature causes the increase in the intensity of the emission centres at 375 nm, 421 nm and 552 nm, which is the result of freeze-out of phonons and suppression of nonradiative recombination processes.[36a, 61] The emission centred at 552 nm becomes dominant at low temperature and the peak shifts gradually to 572 nm at 100 K. The temperature dependence of the PL intensity, $I(T)$, might be expressed by a simple thermal activation model according to the equation[36a]

$$I(T) = \frac{I_0}{1 + A\exp(\frac{-E_a}{k_B T})} \qquad (2.2)$$

where I_0 is the emission intensity at 0 K, A is a constant, and Ea is the activation energy of the thermal quenching process.

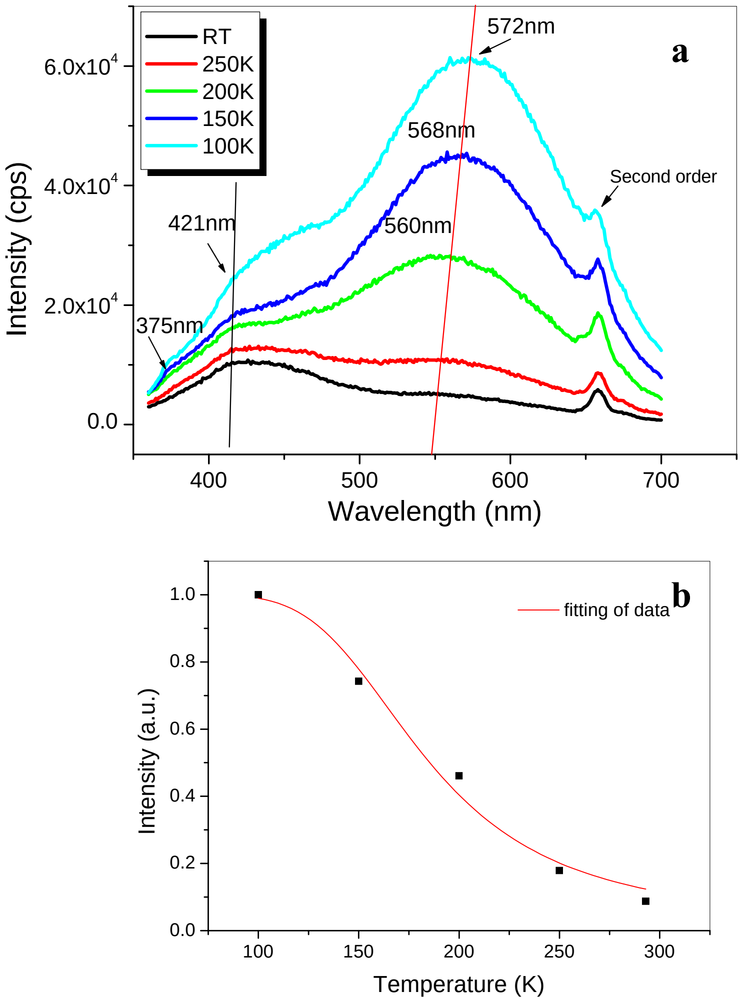

Fig. 2.34. (a) *Temperature dependent PL spectra of a ZnO powder sample excited at 325 nm. (The sample was prepared with same procedure as that of Fig. 2.22) (b) Normalized PL intensity versus temperature. The solid line is the data fitting according to formula (2.2).*

Fitting of the data with equation (2.2) gives the value of estimated activation energies E_a = 85 meV (Fig. 2.34b). Greene et al. reported that well-aligned ZnO nanowires have the activation energy of 71 meV by fitting their photoluminescent data, whileas ZnO crystals synthesized in the presence of surface-functionalized latex have Ea for visible emission ranging from 35 to 84 meV.[61] All these reported values are comparable to our result.

The excitation spectra were recorded at the maximum of the corresponding emission spectra. (Fig. 2.35a) The absorption tail reflects the bandgap of ZnO and the intensity of exciton peak increases with decreasing the temperature. The intensity of maximum of excitation spectra is simply plotted with temperature (Fig. 2.35b), showing almost linear relation of the PL intensity and temperature.

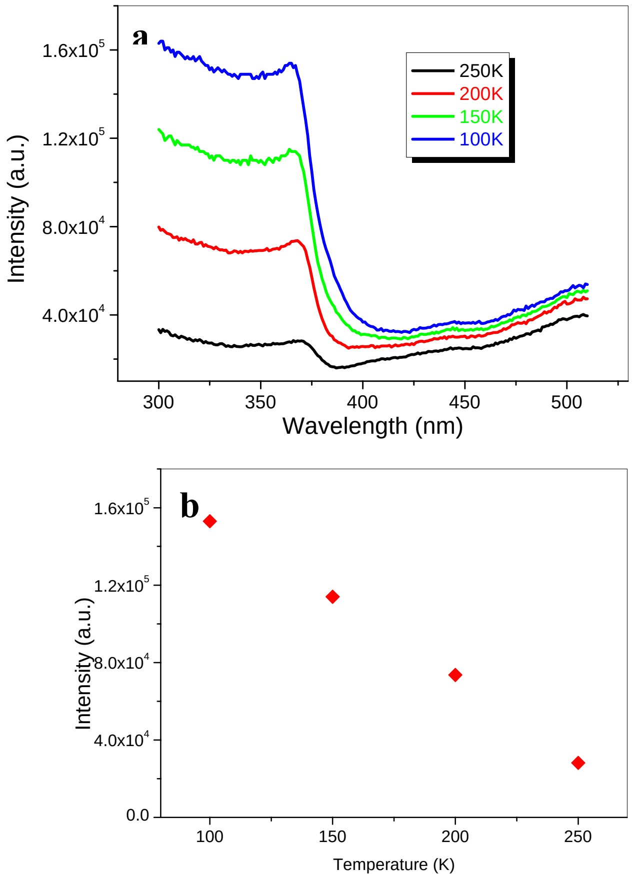

Fig. 2.35. *(a) Temperature-dependent excitation spectra of ZnO. (b) intensity of PL spectra versus temperature.*

Time-resolved PL spectra may give information about the life time of the visible emission of the as-prepared ZnO sample. The spectra is recorded at an excitation wavelength of 355 nm using a pulsed laser radiation of Nd:YAG laser. The obtained spectra (Fig. 2.36a) show a very broad yellow-to-orange emission band that spans about 1 eV. The emission is centred at 2.02 eV, about 0.1 eV red shift compared with the steady-state spectra. The intensity decay is observed with time, the first-order exponential fitting of which gives the lifetime of 24 µs (Fig. 2.36b). PL emission generated from excitonic recombination decays very rapidly, normally below nanosecond (in the scale of hundreds of picoseconds),[62] while defect- related visible emission have much longer lifetimes (in the microsecond scale). Van Dejken et al.[63a] prepared quantum dot of ZnO nanocrystals, which shows visible emission at 2.3 eV (540 nm). The lifetime of their ZnO is around 1 µs. This value is close to the green emission in ZnO film reported by Studenikin.[63b] The visible emission lifetime of our sample is longer than the reported values, possibly reflecting the effects of different preparation conditions.

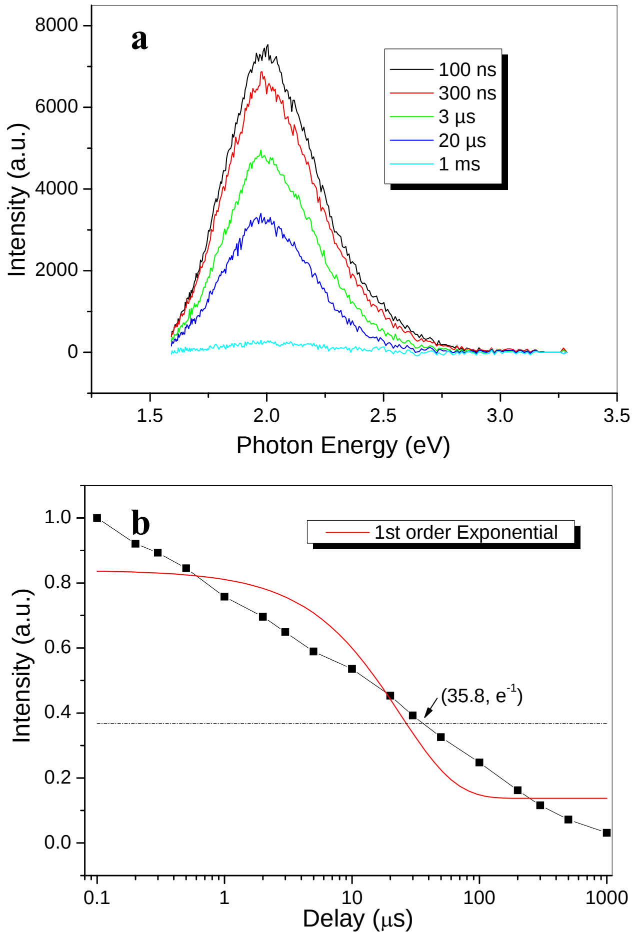

Fig 2.36. (a) *Time-resolved PL emission spectra of a ZnO sample which was prepared using same procedure as that of Fig. 2.22. (b) The decay of the emission of the same sample.*

2.4.3 EPR investigation of ZnO nanoparticles

Fig. 2.37 exhibits EPR spectrum of a ZnO sample recorded at room temperature. All the EPR results in this work is obtained using the same ZnO sample which is prepared by pyrolysis of ZnPA with Mn of 5,000 at 500 °C followed by annealing for 1 h at the temperature, the same procedure as that of Fig. 2.22. Two signals with $g = 1.96$ and $g = 2.00$ are observed and labelled as I and II. Sigal I has been clearly attributed to shallow donor centres irrespective to their identity. The g-value of Signal II is very close to that of a free electron ($g = 2.0023$). Therefore, it is expected that this signal comes from dangling bonds from the organic residue. A series of ZnPA samples pyrolyzed from 230 °C to 490 °C are examined by EPR spectroscopy (Fig. 2.38a). An intense signal at $g = 2.0044$ dominates the spectrum whose intensity increases with the increase of sample annealing temperature. Fig. 2.38b shows the exponential increase of the maximal EPR intensity with regards to the annealing temperature.

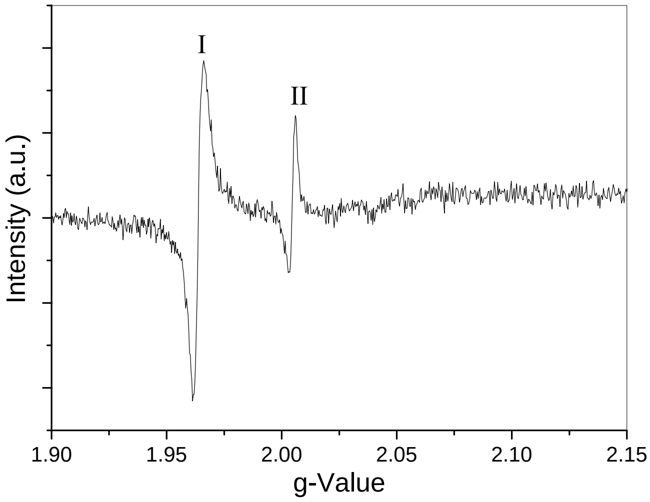

Fig. 2.37. *EPR spectrum of a ZnO sample. The sample was obtained by pyrolysis of ZnPA (Mn: 5,000) at 500 °C followed with annealing for 1 h at the temperature, the same procedure as that of Fig. 2.22.*

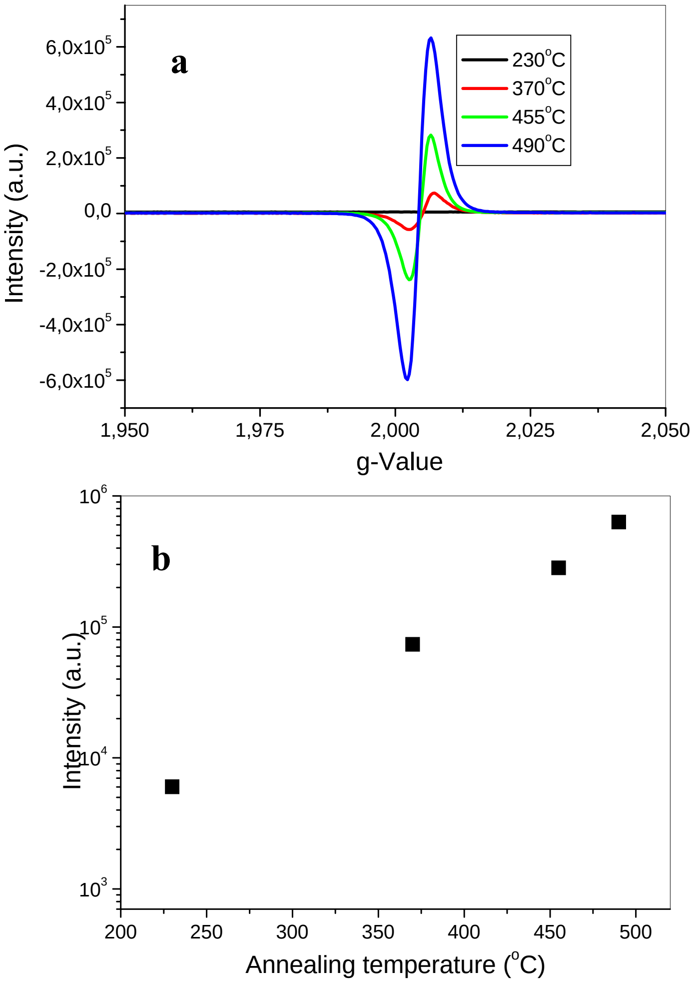

Fig. 2.38. *(a) EPR spectra of ZnPA samples (Mn: 5,000) annealed at different temperatures. (b) the intensity of EPR signal versus the annealing temperature.*

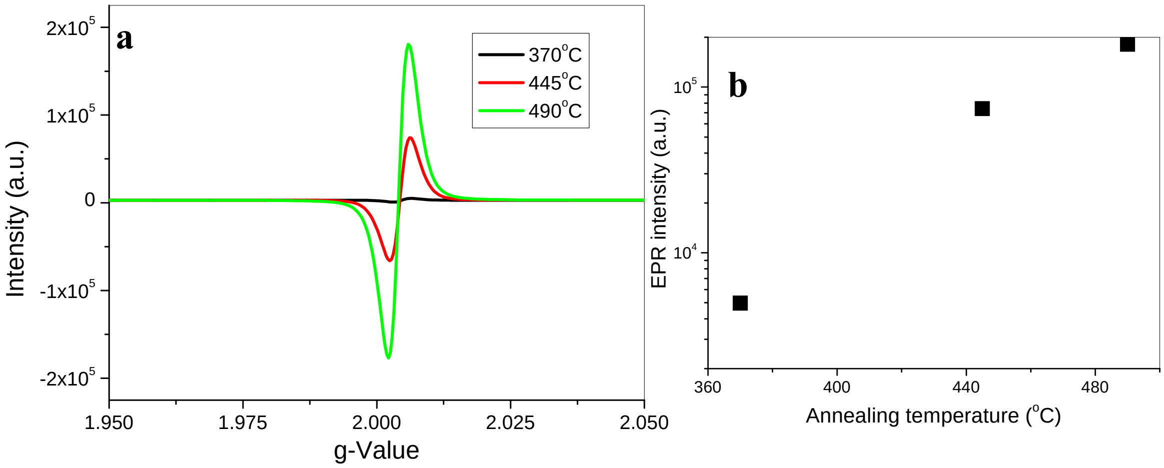

Fig. 2.39. *(a) EPR spectra of PAA samples (Mn: 5,000) annealed at different temperatures. (b) The intensity of EPR signals versus the annealing temperature.*

The result is consistent with the assumption that the Signal II in ZnO EPR spectrum is due to the organic remnant formed during heating treatment. In order to prove the hypothesis, pyrolysis of a series of polyacrylic acid (PAA) powder samples under same condition (heating program, air as carrying gas) was conducted. The EPR results of the samples annealed at different temperatures are shown in Fig. 2.39a. The spectra are similar with that obtained from pyrolyzed ZnPA samples with strong signal at $g = 2.0043$, which again confirms the origin of the signal II related to the organic component of the polymer precursor. The intensity of this EPR signal has a relation with the annealing temperature similar as that of pyrolyzed ZnPA samples (Fig. 2.39b).

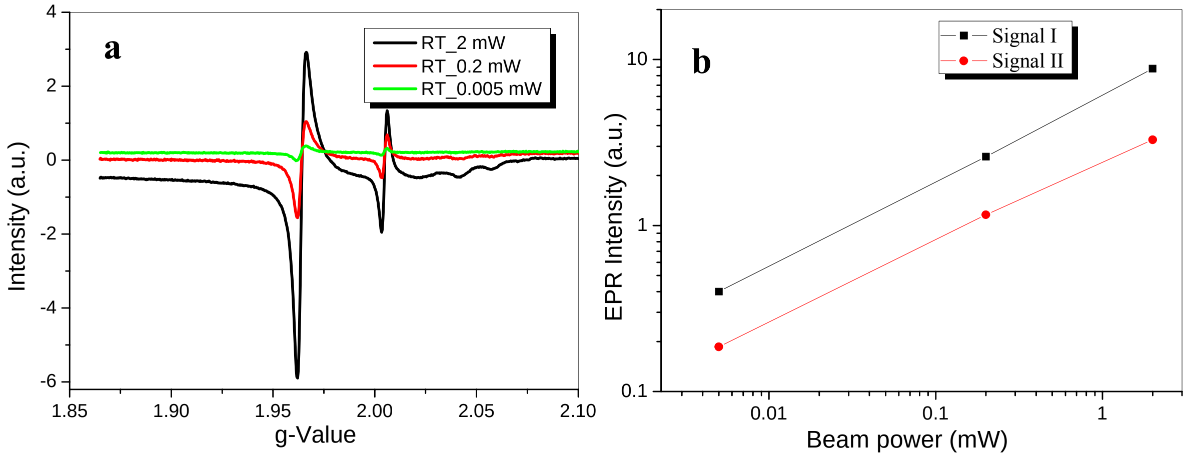

Fig. 2.40. *(a) EPR spectra of the ZnO powder generated using different beam power at room temperature; (b) The intensity of the two signals versus beam power.*

The intensity of the EPR signal of the ZnO nanoparticles is obviously affected by some parameters like beam power as presented in Fig. 2.40. Both signals increase their intensity exponentially with increasing the beam power. Temperature is another important parameter that may affect the EPR intensity. Temperature dependent measurement of ZnO powder was carried out using liquid helium for cooling the system. The sample was measured from 6 K to room temperature. The intensity decreases significantly with the temperature increasing (Fig. 2.41a). Notably, at very low temperature e.g. 6 K, Signal II is much stronger than the intensity of the two signals. With temperature increasing, Signal II intensity decreases faster than Signal I and becomes weaker than Signal I after 100K as shown in Fig. 2.41b. The ratio of the intensity between the two signals is plotted with regard to the temperature, showing a trend of monotonic increase with temperature.

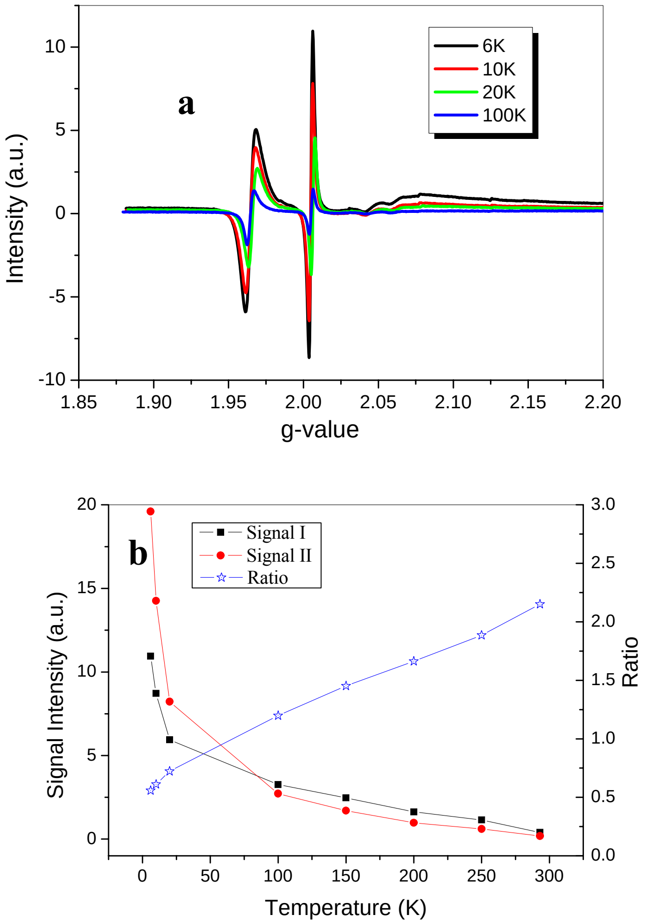

Fig. 2.41. *(a) The EPR spectra of the ZnO powder at different temperatures. (b) The trend of the EPR signals versus temperature. The square and circle stand for the intensity of the two signals. The star indicates the ratio of the intensity of signal I to that of signal II.*

2.5 Sintering and growth of ZnO nanoparticles upon isothermal annealing

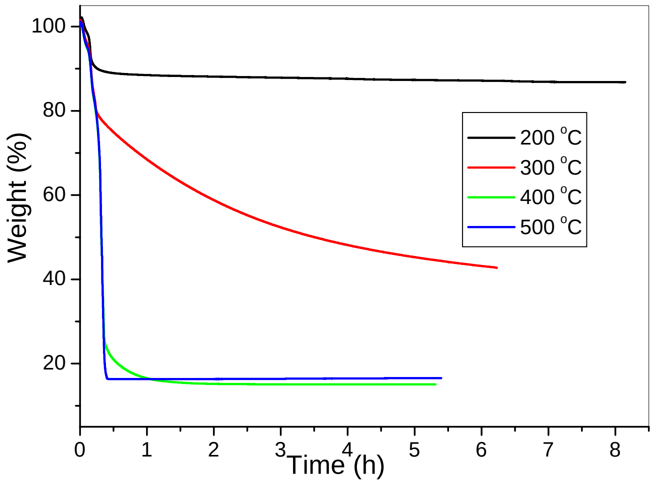

Fig. 2.42. *TGA curves of isothermal annealing of ZnPA precursor set at different temperature.*

It is well known that in the course of the annealing of ceramics, the particle size and size distribution of the samples increase with temperature increasing, owing to the Oswald mechanism. With the aid of thermoanalysis, an optimal heating condition could be achieved, at which the organic part of the polymer precursor could be completely removed and small particle size and limit degree of aggregation is preserved. Isothermal treatment using TGA gives information about the crystal growth and sintering under continuous annealing.

A series ZnPA powder samples was annealed at 200, 300, 400, 500 °C for a certain time respectively, after quick heating (20 °C/min) to the preset temperature from room temperature. As seen from Fig. 2.42, the results show that only maximal 10% weight is eliminated even after 8 hours continuous isothermal treatment at 200 °C, while at higher temperature such as 300 °C, it shows an exponential decrease in weight and 60% mass is removed after 5 h. And annealing at 400 h for 1 hour the sample reached a constant residue weight of about 18%.

However, the results obtained from TGA have some deviation with the *in situ* experimental results. The experimental data were obtained by simply calculating the weight loss of each powder sample, which was taken out from the hot oven at predetermined time. The samples were heated from 25 °C with 5 °C/min to the isothermal temperature (400 or 500 °C) and then kept for annealing for a certain time. Fig. 2.43 shows the results. It is found that after the temperature reaches 400 °C, only 40% weight is removed and the isothermal treatment results in an exponential loss of mass, which is obviously different from the TGA result. And heated to 500 °C, 30% residue still remained and one hour isothermal annealing made the sample reach the constant weight at 8.3%. This shows the necessity of isothermal annealing in the ZnO synthesis for complete removal of the organic component of the polymer precursor.

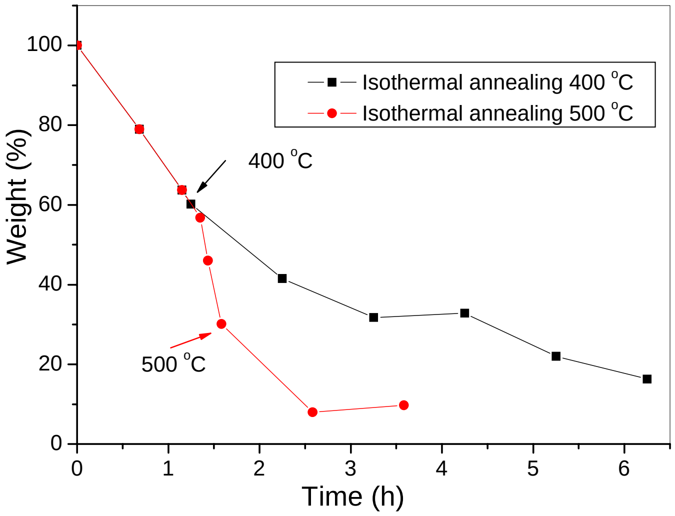

Fig. 2.43. *Experimental results of weight loss versus isothermal annealing time at different temperature.*

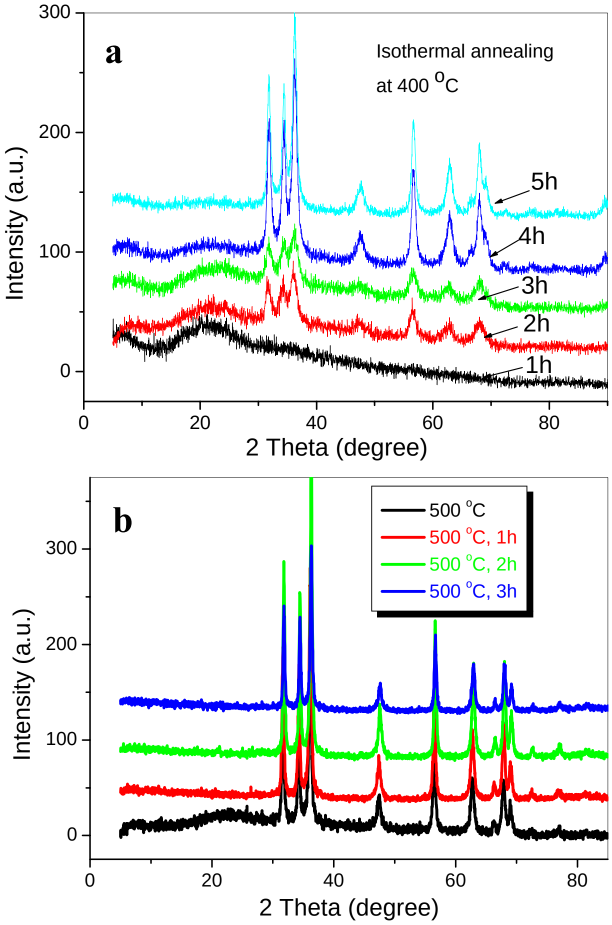

Fig. 2.44. *XRD patterns of the ZnO samples isothermal annealed at a) 400 °C; b) 500 °C, respectively for certain period.*

The isothermal annealed ZnPA / ZnO samples were examined by X-ray diffraction. It shows that after 1 h annealing at 400 °C, the powder remains amorphous (Fig. 2.44a). Characteristic peaks of crystalline ZnO crystal appear after 2 hours annealing, but broad and evidently amorphous structure shown at around 20 degree in the XRD pattern is still seen, which only disappears after 5 h annealing at 400 °C. The intensity of the peaks increases and they become narrower with annealing time, indicating a better crystallinity. The ZnO samples annealed at 500 °C for different times are also checked by XRD (Fig. 2.44b) and their crystallite size derived from Scherer formula is plotted in Fig. 2.45. As already interpreted before, these sizes do not reflect the size of particles seen under the microscope.

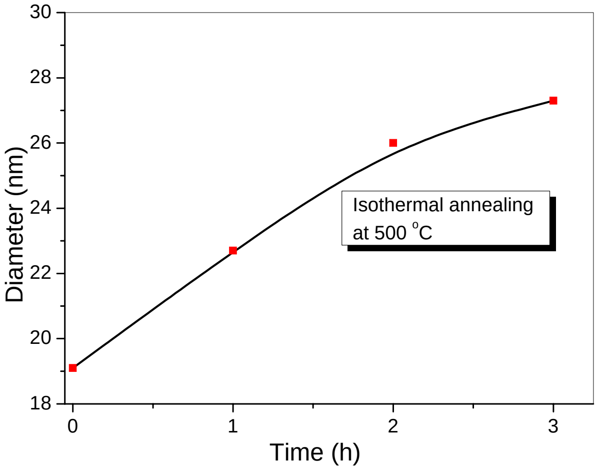

Fig. 2.45. *ZnO nanoparticles size increasing with annealing time at 500 °C. The size is calculated by Scherer equation based on (100) peak of XRD patterns.*

SEM is used to investigate the evolution process of the ZnO nanoparticles upon isothermal sintering. Fig. 2.46 gives the ZnO SEM images, which exhibits the growth of particles upon continuous isothermal annealing at 400 °C. After 1 h, no particles are distinguishable which is consistent with the XRD result that no zinc oxide forms at this stage (Fig. 2.46a). And 40% weight is still left as calculated from the weight loss. After one more hour annealing, clear particulate structure appears sized around 10 nm (Fig. 2.46b). The nanoparticles grow larger with time and tend to aggregate (Fig. 2.46c, d). This points to that long-time thermal annealing may bring detrimental effects to the ZnO morphology. The situation is even worse in the case of higher annealing temperature. The sintering of ZnO crystals is observed in the samples that have been annealed at 500 °C (Fig. 2.47). Many abnormal by structured particles and heavy aggregates appear at longer annealing time.

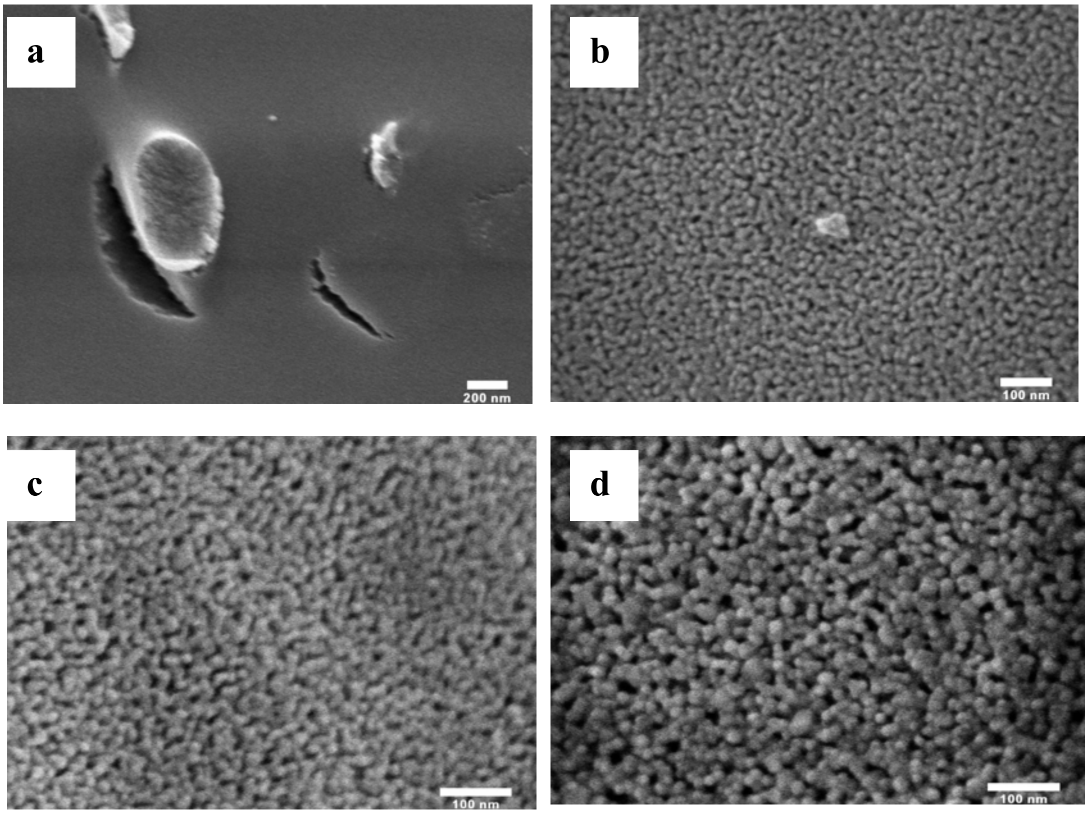

Fig. 2.46. *Growth of ZnO nanoparticles shown by SEM images upon continuous isothermal annealing at 400 ^{o}C for a) 1 h; b) 2 h; c) 3 h; d) 4 h.*

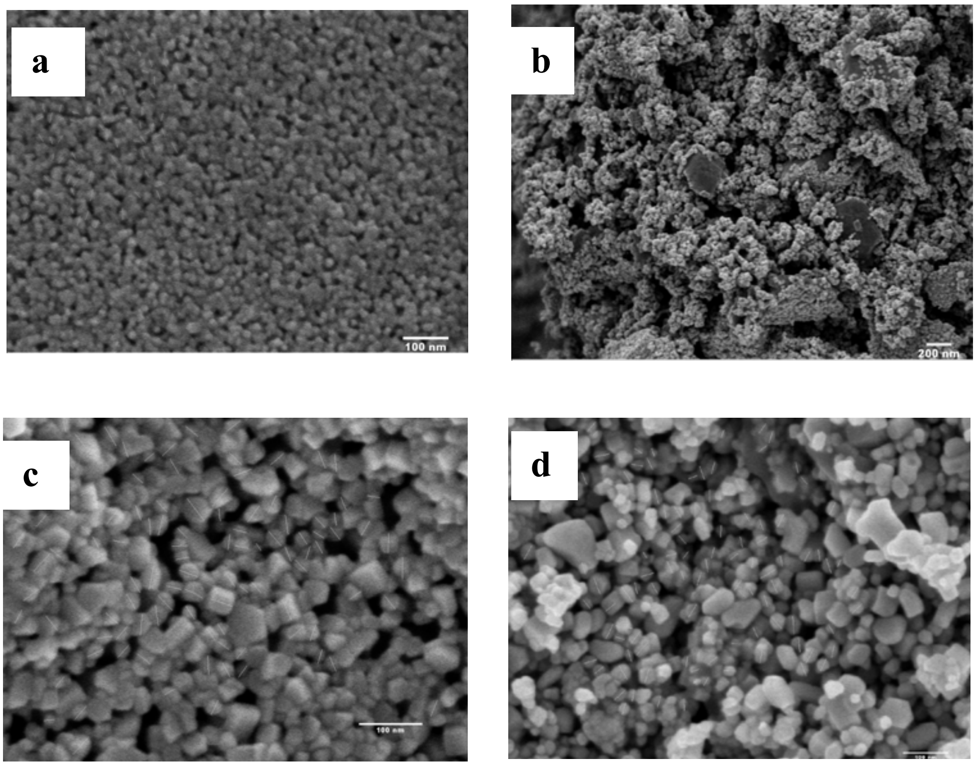

Fig. 2.47. *Morphology change of ZnO nanoparticles upon continuous isothermal annealing at 500 ^{o}C for a) 0 h; b) 1 h; c) 2 h; d) 3 h. The scale bar in a, c, d is 100 nm and in b is 200 nm.*

The thermal annealing of ZnO nanoparticles causes changes of the infrared spectra as seen in Fig. 2.48. The absorption from C-H stretching around 2900 cm^{-1} shrinks with annealing time, indicating the continuous removal of the organic residues in the zinc oxide powder. The pronounced Zn-O stretching band near 500 cm^{-1} is observed to shift to lower wavenumber with annealing time (Fig. 2.48b). Considering the TADC theory,[35] the decrease of this wavenumber corresponds to the decrease of the filling factor, meaning the increase of aggregation degree of the particles, as what is also observed in the microscopic images.

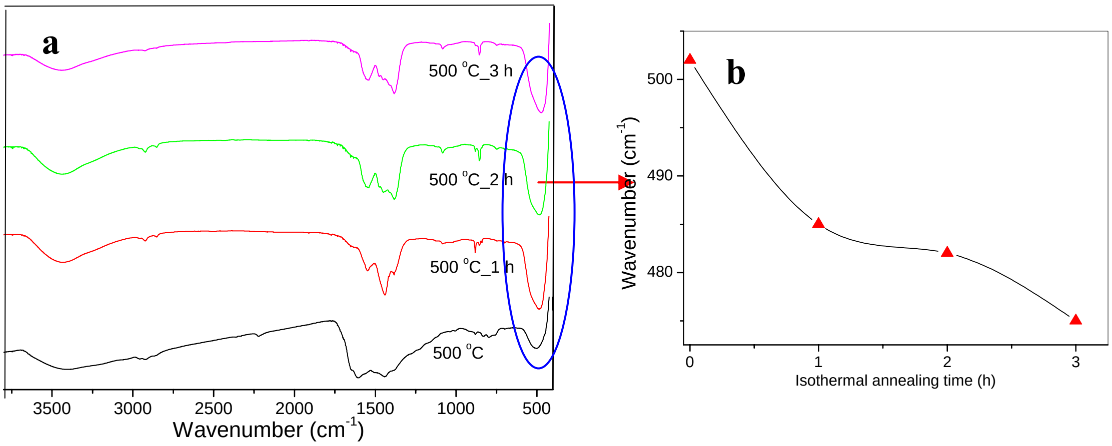

Fig. 2.48. *a) FTIR spectra of ZnO nanoparticles obtained by isothermal annealing for different time; b) the shift of wavenumber of Zn-O stretching versus annealing time.*

The sintering of zinc oxide causes effects on the photoluminescence and EPR spectra of the material, too. Fig. 2.49 gives the PL spectra of ZnO nanocrystals isothermally annealed at 500 °C for 0, 1, 2, 3 hours. The samples are excited with wavelengths of 325 and 370 nm respectively and the excitation spectra are registered at 590 nm.

From the obtained spectra, the following features are observed with the annealing time: (1) The UV or NBE emission is very weak or quenched in all samples; two strong emission centres are found: one is responsible for the blue emission at 438 nm with a shoulder at 421 nm. The other is located in the yellow-to-orange range with a peak at 590 nm. (2) In all cases, the emission obtained with 370 nm excitation is much stronger than that at with 325 nm. Normally, the intensity of the emission is three times as that from shorter wavelength excitation. (3) The position and shape of emission bands remains unchanged with annealing time. (4) However, the intensity of the emission at 590 nm and the exciton peak at 371 nm on the excitation spectra varies with annealing time, which is plotted in Fig. 2.50. It is seen that the intensity increases after short-time annealing at 500 °C, indicating that more defects centers are generated in the ZnO crystal. And from previous results, it is known that the one-hour annealing causes removal of more organic residue and a better crystallinity of the ZnO. However, with longer annealing time, sintering of the crystal takes place, which eliminates some amount of defect centres, leading to a lower PL intensity.

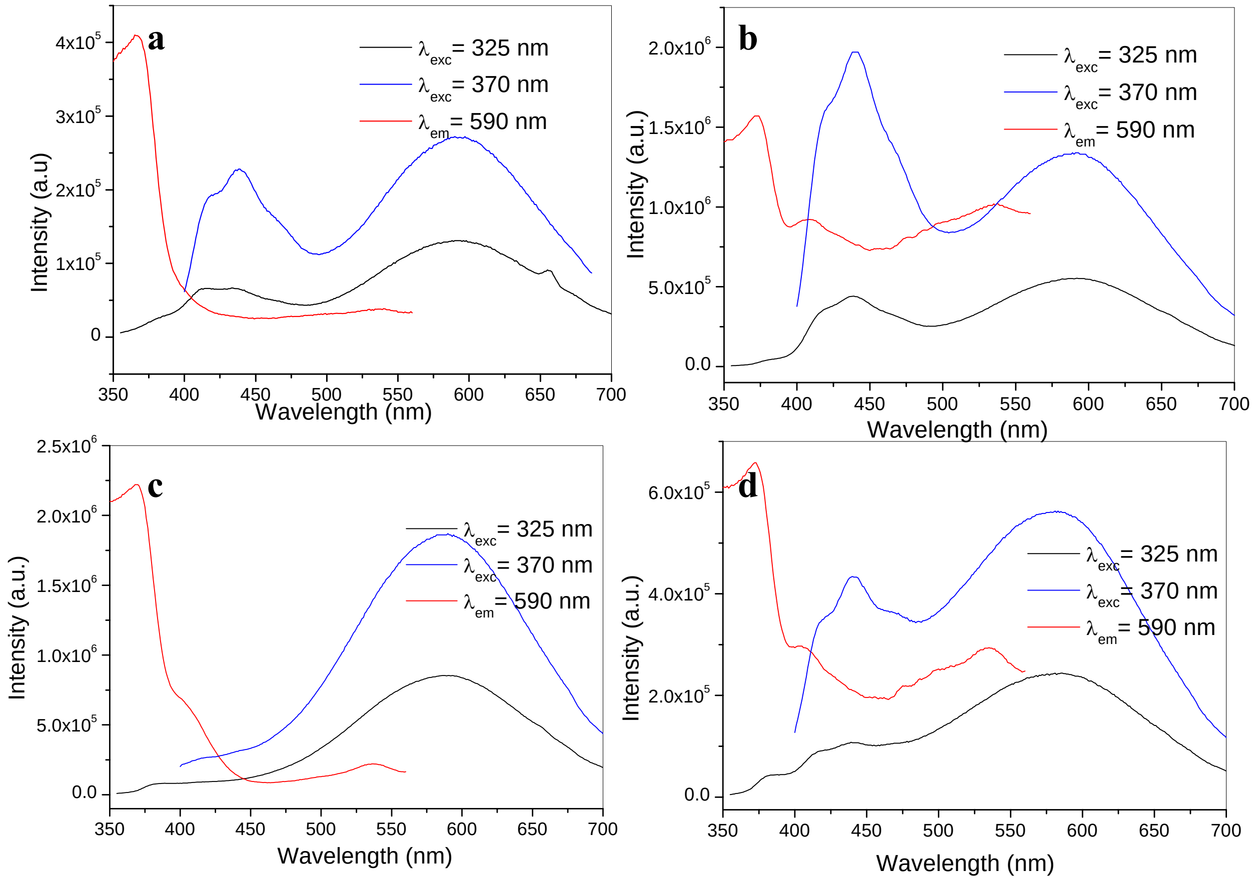

Fig. 2.49. Evolution of PL excitation and emission spectra of ZnO nanoparticles with continuous isothermal annealing at 500 °C for a) 0 h; b) 1 h; c) 2 h; d) 3 h. The excitation wavelength is 325 and 370 nm. The PL excitation is recorded at an emission wavelength of 590 nm.

The EPR spectra of ZnO nanoparticles annealed at different conditions (temperature or time) are shown in Fig. 2.51. The intensity of the signal at *g* = 2.0044, which is ascribable to organic residue formed in the cause of pyrolysis, decreases continuously with annealing time, indicating further removal of organic residue from the crystal.

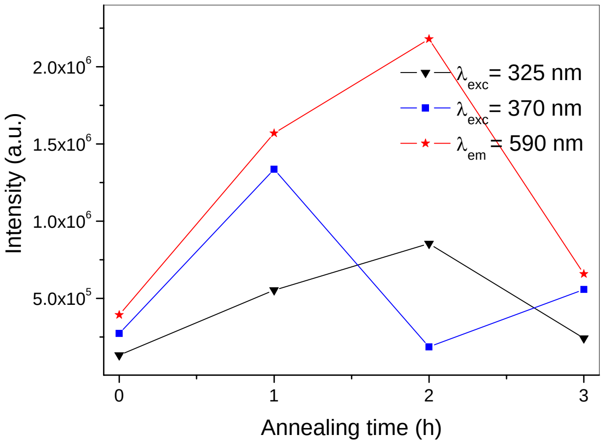

Fig. 2.50. *Intensity variation of emission and excitation peaks versus annealing time of zinc oxide crystals. The triangle and brick stand for the emission at 590 nm excited at 325 and 370 nm respectively; the star represents the peak at 371 nm of the excitation spectra.*

For the sample annealed at 550 °C, the signal at $g = 1.96$ is obviously stronger than that of the other samples, possibly revealing information about the higher density of shallow donor centers in the crystal.

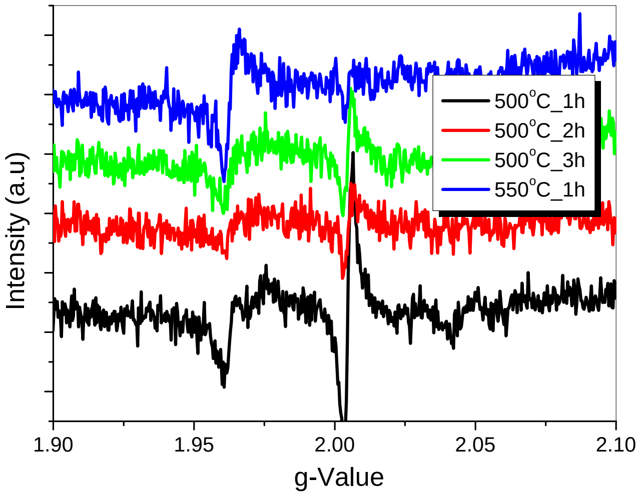

Fig. 2.51. *EPR spectra of ZnO nanoparticles annealed at different conditions.*

In summary, zinc oxide nanoparticles with diameter of 40-100 nm are prepared by application of a versatile polymer-based method. The process starts firstly with formation of a zinc polyacrylate polymer precursor. The ZnPA precursor exhibits typical polyelectrolyte behaviour, i.e. the viscosity of the polymer solution decreases with the increasing of concentration. Calcination of this zinc-loaded precursor in the dry form in a high-temperature oven gives colorless zinc oxide powders. The XRD and TGA results prove that the crystallation of zinc oxide from ZnPA precursor takes place at about 450 ^{o}C. The morphology of ZnO is influenced by some parameters including molecular weight of polyacrylic acid, zinc content in the precursor, calcination temperature etc. Relatively low temperature at 500-550 ^{o}C and short annealing time is key to produce uniform and homogeneous zinc oxide. The optical properties of the as-prepared ZnO are investigated too. The PL spectra show that the NBE emission is significantly quenched and the visible exhibits blue emission at 420 nm and 590 nm in the yellow-to-orange range. Temperature-dependent PL spectra show that the intensity increases with lowering the temperature. Annealing of the ZnO sample causes intensity variation of the emissions but the shape and center of the emission peaks are preserved. The intensity variation reflects the change of amount of defects centers in the ZnO crystal with annealing time. EPR spectra show the signal originated by shallow donor center and signal due to organic residue. However, no correlation between the EPR signal and PL emission could be concluded.

2.6 Experimental section

Preparation of Zinc Polyacrylate Precursor Polymer:

Typically, 1.036 g polyacrylic acid (prepared from 50 % aqueous solution by freeze drying) (Aldrich, $M_n = 5000$) and 0.428 g $Zn(NO_3)_2•6H_2O$ were dissolved in 110 ml water. The solution is stirred for 10 min. Ammonium hydroxide (25% wt) was added dropwisely to adjust the pH to the desired value between 5~10. The reaction mixture was then concentrated to about 20 ml by freeze-drying. The residual viscous liquid was added dropwisely into 120 ml acetone. A colorless precipitate was formed and collected by centrifugation. It was washed with acetone and dried at 40 °C in vacuum.

Preparation of ZnO Nanoparticles:

The obtained precursor material was milled into fine powder and then calcined in a temperature-controlled oven under air flow with a heating rate of 5 °C min_{-1} to 500°C. The sample was isothermally annealed for 1 hour at this temperature and taken out in time.

INSTRUMENTAL

UV spectra were recorded at room temperature with a Perkin-Elmer Lambda 2 UV/Vis/NIR spectrophotometer. The content of Zn in the precursor polymer was determined by Atomic Absorption Spectroscopy (AAS) using a Perkin Elmer 5100 ZL spectrometer. Light-scattering setup consisted of a 200 mW laser operating at 647 nm and an ALV5000 correlator. The sample solutions were filtrated 8 times with Millipore 450 nm filter before measurement. pH values were measured with a Pt/KCl glass electrode attached to a pH meter (Schott CG843 set) with an integrated temperature sensor (Blueline 14pH, Schott). Before the measurements, the pH electrode was calibrated with three buffer solutions at pH 4.006, 6.865 and 9.180 at 20.0 8C (DIN Norm 19266). Viscometric measurements were performed at 20±0.01 ^{o}C using a capillary Ubbelohde-Viscometer from Schott (Germany). TG-MS were measured under oxygen flow on a Mettler Toledo ThermoSTAR TGA/SDTA 851 connected with a Pfeiffer Vacuum GSD 300 T2 pump and a Basler MS/Netsch STA449C mass detector. Differential Scanning Calorimetry (DSC) was measured on a Mettler DSC 30 with heating rate of 5 K/min. Powder XRD was obtained by a Seifert 3000 TT Bragg-Brentano diffractometer using Cu Kα radiation with $\lambda = 0.15406$ nm, $5^{o} \leq 2\theta \leq 120^{o}$. SEM images showing the morphology of ZnO nanoparticles were taken by LEO Gemini 1530 with an inlens detector (electron high tension

(EHT) = 1 kV). TEM images were obtained by Tecnai F20 microscope operating at 200 kV. Energy dispersive X-ray spectroscope (EDX) coupled to the TEM was used for composition determination. The elementary mapping and correspondent TEM images was measured on ZEISS 912 Omega microscope operating at 120 KV with an energy filter. Particle size histograms and distributions were obtained statistically by measuring the dimensions of at least 100 crystals with help of the software ImageJ (National Institute of Health, USA). FTIR spectra were recorded with a Nicolet 730 spectrometer (liquid N2-cooled MCT detector) with pressed pellets, which were made using KBr powder as the diluent. Raman spectrum is recorded at room temperature by a Dilor XY 800 spectrometer with confocal microscope. CW-EPR spectra were measured with an Elexsys 580 spectrometer at frequencies of approximately 9.8 GHz, using an 4103TM cavity at room temperature and an MD4EN Bruker Flexline ENDOR resonator for temperature variation. Room temperature and temperature-dependent photoluminescence (PL) measurements were performed on a Spex Fluorolog spectrometer.

2.7 References

[1] D. Seyferth, W. S. Rees, J. S. Haggerty, A. Lightfoot, *Chem. Mater.* **1989**, *1*, 45.
[2] L. L. Beecroft, C. K. Ober, *Adv. Mater.* **1995**, 7, 1009.
[3] A.Sin, P. Odier, *Adv. Mater.* **2000**, *12,* 649.
[4] M. P. Pechini, U.S. Patent 3 330 697, **1967**.
[5] L.-W. Tai, P. A. Lessing, *J. Mater.Res.* **1992**, *7*, 502.
[6] A. Lessing, *Ceram. Bull.* **1989**, *68*, 1002.
[7] M. Kakihana, T. Okubo, M. Arima, O. Uchiyama, M. Yashima, M. Yoshimura, Y. Nakamura, *Chem. Mater.* **1997**, *9*, 451.
[8] a) H. D. Yu, Z. P. Zhang, M. Y. Han, X. T. Hao, F. R. Zhu, *J. Am.Chem. Soc.* **2005**, *127*, 2378; b) Jr H. He, C. S. Lao, L. J. Chen, D. Davidovic, Z. L. Wang; c) D. W. Bahnemann, C. Kormann, M. R. Hoffmann, *J. Phys. Chem.* **1987**, *91*, 3789.
[9] S. J. Pearton, D. P. Norton, K. Ip,Y. W. Heo, T. Steiner, *Prog. Mater. Sci.* **2005**, *50*, 293.
[10] a) E. G. Kolawole, J. Y. Olayemi, *Macromolecules* **1981,** *14,* 1050; b) H. K. Pan, G. S. Knapp, S. L. Cooper, *Colloid Polym. Sci.* **1984**, *262*, 734; c) B. L. Rivas, E. D. Pereira, I. Moreno-Villoslad, *Prog. Polym. Sci.* **2003,** *28,*173.
[11] S. Yamabi, H. Imai, *J. Mater. Chem.* **2002**, *12*, 3773.
[12] N. Saito, H. Haneda, W. S. Seo, K. Koumoto, *Langmuir* **2001,** *17,* 1461.
[13] a) I. Moreno-Villoslada, B. L. Rivas, *J. Phys. Chem. B* **2002,** *106,* 9708; b) J. G. Zhang, S. Q. Xu, E. Kumacheva, *J. Am. Chem. Soc.* **2004**, *126*, 7908.
[14] D. Casson, A. Rembaum, *Macromolecules* **1972**, *5*, 75.
[15] M. Sedlak, *Langmuir* **1999,** *15,* 4045.
[16] M. Morcellet, M. Wozniak, *Macromolecules* **1991,** *24,* 745.
[17] E. G. Kolawole, J. Y. Olayemi, *Macromolecules* **1981**, *14*, 1950.
[18] C. Goerigk, R. Schweins, K. Huber, M. Ballauff, *Europhys. Lett.* **2004**, *66*, 331.
[19] a) G. S. Manning, *J. Chem. Phys.* **1969**, *51*, 924; b) G. S. Manning, *J. Chem. Phys.* **1969**, *51*, 934; c) G. S. Manning, *J. Chem. Phys.* **1969**, *51*, 3249.
[20] M. H. Hao, S. C. Harvey, *Macromolecules* **1992,** *25,* 2200.
[21] Deacon, G. B. et al. *J. Coord. Chem. Rev.* **1980**, *33*, 227.
[22] M. Nara, H. Torii, M. Tasumi, *J. Phys. Chem.* **1996**, *100*, 19812.
[23] S. Sakohara, M. Ishida, M. A. Anderson, *J. Phys. Chem.* **1998**, *102*, 10169.
[24] B. P. Grady, J. A. Floyd, W. B. Genetti, P. Vanhoorne, R. A. Register, *Polymer* **1999**, *40*, 283.
[25] T. Ishioka, *Polym. J.* **1993**, *11*, 1147.
[26] P. Vanhoorne, R. A. Register, *Macromolecules* **1996**, *29*, 598.
[27] D. J. Yarusso, Y. S. Ding, H. K. Pan, S. L. Cooper, *J. Polym. Sci: Polym. Phys. Ed.* **1984,** *22,* 2073.
[28] T. Ishioka, Y. Shibata, M. Takahashi, I. Kanesaka, *Spectrochimica Acta Part A* **1998**, *54*, 1811.
[29] Y. J. Kwon, K. H. Kima, C. S. Limb, K. B. Shim, *J. Ceram. Process. Res.* **2002**, *3,*146.
[30] A. J. Kozak, K. Wieczorek-Ciurowa, A. Kozak, *J. Therm. Anal. Cal.* **2003**, *74*, 497.
[31] A. V. Ghule, K. Ghule, C. Y. Chen, W. Y. Chen, S. H. Tzing, H. Chang, Y. C. Ling, *J. Mass Spectrom.* **2004**, *39*, 1202.
[32] M. Singbal, V. Cbbabra, P. Kang, D. O. Shah, *Mater. Res. Bull.* **1997**, *32*, 239.
[33] a) P. D. Cozzoli, A. Kornowski, H. Weller, *J. Phys. Chem. B* **2005,** *109,* 2638; b) P. J. Thistlethwaite, M. S. Hook, *Langmuir* **2000**, *16*, 4993.
[34] M. A. Verges, A. Mifsud, C. J. Serna, *J. Chem. Soc. Faraday Trans.***1990**, *86*, 959.
[35] M. G. Kakazey, V. A. Melnikova, T. Sreckovic, T. V. Tomila, M. M. Ristic, *J. Mater. Sci.* **1999,** *34*, 1691.

[36] a) C. J. Youn, T. S. Jeong, M. S. Han, J. H. Kim, *J. Cryst. Growth* **2004**, *261*, 526; b) N. Ashkenov, B. N. Mbenkum, C. Bundesmann, V. Riede, M. Lorenz, D. Spemann, E. M. Kaidashev, A. Kasic, M. Schubert, M. Grundmann, G. Wagner, H. Neumann, V. Darakchieva, H. Arwin, B. Monemar, *Appl. Phys. Lett.* **2003**, *93*, 126.

[37] T. C. Damen, S. P. S. Porto, B. Tell, *Phys. Rev.* **1966**, *142*, 570.

[38] R. H. Callender, S. S. Sussman, M. Selders, R. K. Chang, *Phys. Rev. B* **1973**, *7*, 3788.

[39] B. H. Bairamov, A. Heinrich, G. Irmer, V. V. Toporov, E. Ziegler, *Phys. Status Solidi B* **1983**, *119*, 227.

[40] a) I. Broser, R. K. Germer, H. J. Schulz, and K. Wisznewski, *Solid State Electron.* **1978**, *21*, 1597; b) R. Kuhnert, R. Helbig, *J. Lum.* **1981**, *26*, 203; c) D. J. Robbins, D. C. Herbert, P. J. Dean, *J. Phys. C* **1981**, *14*, 2859.

[41] a) K. Vanheusden, C. H. Seager, W. L. Warren, D. R. Tallant, J. A. Voigt, *Appl. Phys. Lett.* **1996**, *68*, 403; b) K. Vanheusden, W. L. Warren, C. H. Seager, D. R. Tallant, J. A. Voigt, B. E. Gnade, *J. Appl. Phys.* **1996**, *79*, 7983.

[42] Y. Dai, Y. Zhang, Q. K. Li, C. W. Nan, *Chem. Phys. Lett.* **2002**, *358*, 83.

[43] J. Q. Hu, Y. Bando, *Appl. Phys. Lett.* **2003**, *82*, 1401.

[44] M. Liu, A. H. Kitai, P. Mascher, *J. Limin.***1992**, *54*, 35.

[45] H.-J. Egelhaaf, D. Oelkrug, *J. Cryst. Growth* **1996**, *161*, 190.

[46] B. X. Lin, Z. X. Fu, Y. B. Jia, *Appl. Phys. Lett.* **2001**, *79*, 943.

[47] A. B. Djurisic, W. C. H. Choy, V. A. L. Roy, Y. H. Leung, C. Y. Kwong, K. W. Cheah, T. K. G. Rao, W. K. Chan, H. T. Lui, C. Surya, *Adv. Func. Mater.* **2004**, *14*, 856.

[48] L. Guo, S. H. Yang, C. L. Yang, P. Yu, J. N. Wang, W. K. Ge, G. K. L. Wong, Chem. Mater. **2000**, *12*, 2268.

[49] M. Haase, H. Weller, A. Henglein, *J. Phys. Chem.* **1988**, *92*, 482.

[50] D. W. Bahnemann, C. Kormann, M. R. Hoffmann, *J. Phys. Chem.* **1987**, *91*, 3781.

[51] J. Q. Hu, X. L. Ma, Z. Y. Xie, N. B. Wong, C. S. Lee, S. T. Lee, *Chem. Phys. Lett.* **2001**, *344*, 97.

[52] B. J. Jin, S. Im, S. Y. Lee, *Thin Solid Fims* **2000**, *366*, 107.

[53] L. Dai, X. L. Chen, W. J. Wang, T. Zhou, B. Q. Hu, *J. Phys.: Condens. Matter* **2003**, *15*, 2221.

[54] S. Mahamuni, K. Borgohain, B. S. Bendre, V. J. Leppert, S. H. Risbud, *J. Appl. Phys.* **1999**, *85*, 2861.

[55] X. L. Wu, G. G. Siu, C. L. Fu, H. C. Ong, *Appl. Phys. Lett.* **2001**, *78*, 2285.

[56] S. A. Studenikin, N. Golego, M. Cocivera, *J. Appl. Phys.* **1998**, *84*, 2287.

[57] J. Q. Hu, Y. Bando, *Appl. Phys. Lett.* **2003**, *82*, 1401.

[58] S. B. Zhang, S.-H. Wei, A. Zunger, *Phys. Rev. B* **2001**, *63*, 075205.

[59] N. Y. Garces, N. C. Giles, L. E. Halliburton, G. Cantwell, D. B. Eason, D. C. Reynolds, D. C. Look, *Appl. Phys. Lett.* **2002**, *80*, 1334.

[60] D. Li, Y. H. Leung, A. B. Djurisic, Z. T. Liu, M. H. Xie, S. L. Shi, S. J. Xu, W. K. Chan, *Appl. Phys. Lett.* **2004**, *85*, 1601.

[61] a) L. E. Greene, M. Law, J. Goldberger, F. Kim, J. C. Johnson, Y. F. Zhang, R. J. Saykally, P. D. Yang, *Angew. Chem. Int. Ed.* **2003**, *42*, 3031; b) R. Munoz-Espi, *PhD thesis*, University of Mainz, **2006**.

[62] H. Priller, R. Hauschild, J. Zeller, C. Klingshirn, H. Kalt, R. Kling, F. Reuss, Ch. Kirchner, A. Waag, *J. Lum.* **2005**, *112*, 173.

[63] a) A.van Dijken, E. A. Meulenkamp, D. Vanmaekelbergh, A. Meijerink, *J. Phys. Chem.* **2000**, 104, 1715; b) S. A. Studenikin, M. Cocivera, *J. Appl. Phys.* **2002**, *91*, 5060.

3 Formation of ZnO Nanocrystalline Films

3.1 Introduction

3.1.1 Methods of observation

3.1.1.1 Basics of electron microscopy

Electron microscopes (EM) including scanning electron microscope (SEM) and transmission electron microscope (TEM) are powerful tools for the characterization of objects on a very fine scale. The examination may provide important information, such as:

a) Topography: the surface features of an object, its texture;
b) Morphology: the shape and size of the particles making up the object;
c) Composition: the elements and compounds that the object is composed of and the relative amounts of them;
d) Crystallographic Information: arrangement of atoms in the object.

The obtained information is important for understanding the relation between the structure and properties of the materials.

a) Electron gun

Generally speaking, EMs work similarly as their optical counterparts based on the same principle, except that EMs use a focused beam of electrons as probe rather than light to "image" the specimen and gain information . The basic steps for imaging a sample with all types of EMs include formation of an electron beam, interaction between sample and beam, gathering information of the sample and formation of an image.

According to the Reyleigh criteria, the resolution limit of a microscope is restricted by the expression

$$\delta_D = 0.61 \frac{\lambda}{n \sin \alpha}$$

Here, λ is wavelength of the radiation and $n \bullet \sin\alpha$ is the numerical aperture (N.A.) of the lens with the value less than 1.4, which gives a resolution limit of 300 nm for the visible light and 0.03 Å for electrons. Up to now, a realistic resolution in TEM is about 0.1 nm due to the small N. A. of the electron-optics. Electrons are generated from a filament which for instance is heated by a large electric current to overcome the work function of the metal. The filament is usually made of various types of tungsten or lanthanum hexaboride (LaB_6). Field emission guns are also commonly used, where electrons are expelled by applying an electric field very close to the filament tip. The size and proximity of the electric field to the electron reservoir in the filament causes the electrons to tunnel out of the reservoir. The emitted electrons have a

Boltzman energy distribution and they will be confined and focused using metal apertures and magnetic lenses into a thin, focused, nearly monochromatic beam. This beam is focused onto the sample using a magnetic lens.

b) Electron-specimen interaction

The incident electron beam comes to the surface of the sample and strikes onto it. Various photon and electron signals are generated after the interaction with the sample as shown in the Scheme 3.1 below.

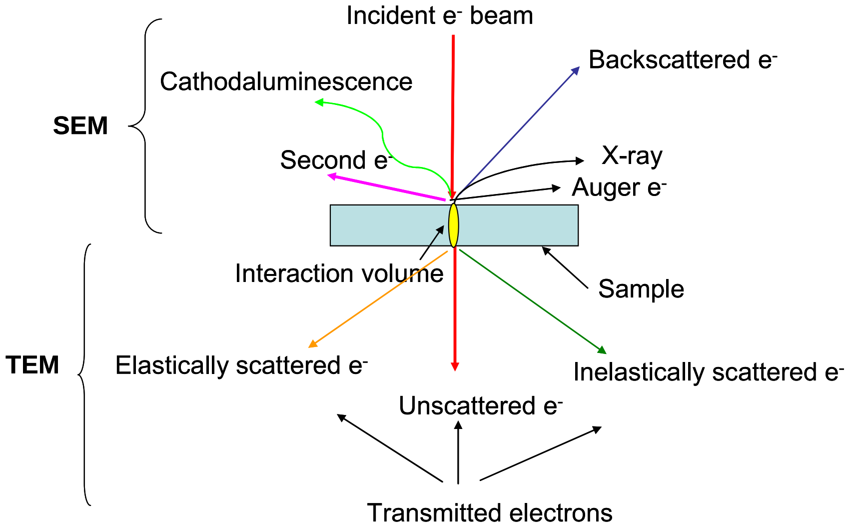

Scheme 3.1

Electron-sample interaction and signals emitted from the sample.

Primary backscattered electron (BSE) and secondary electron (SE) are of main interest for SEM. SE is due to the inelastic scattering of electrons. In this case, the total energies and the momentum of the colliding particles are conserved, but an electron excitation of the atom or solid is stimulated which causes an energy loss ΔE of the primary beam. Normally, SE has only energy less than 50 eV. Because of the very low energy, these electrons originate within a few nanometers from the surface. Therefore, detection of SE may produce a highly-resolved signal of the sample surface.

The elastic scattering is the most important interaction and is the basis of contrast formation in electron microscope. The BSE is due to elastic scattering of electrons which preserve the energy of the primary beam and normally have only a small-angle change of the beam direction. Detection of BSE may provide important information about composition and surface of the sample.

The mechanism of imaging and information gathering of the two different types of EMs has some differences which are described in more details in later sections.

3.1.1.2 Scanning electron microscope

a) General principle

Scanning electron microscopes (SEM) deliver high resolution surface information and are widely used in many fields like materials research, life science as well as semiconductor technology. The general working principle of an SEM is shown in Scheme 3.2.

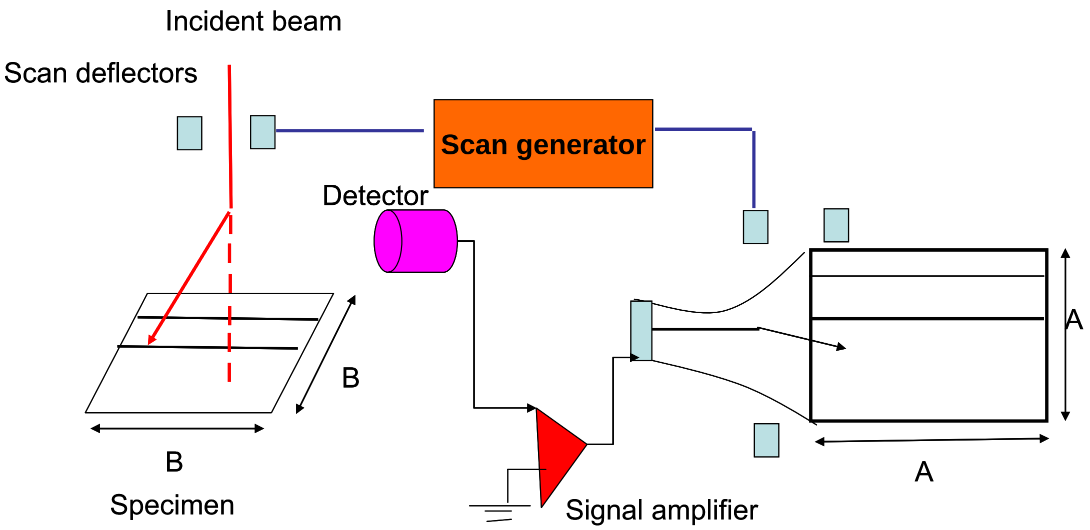

Scheme 3.2

Scheme of the basic working principle of SEM

In general, the electron gun generates a beam of electrons at the top of the microscope by heating of a metallic filament. The electron beam is confined and follows a vertical path through the column of the microscope. It makes its way through electromagnetic lenses which focus and direct the beam down towards the sample. Electrons like BSE and SE are emitted from the sample after interaction with the incident beam. Detectors collect the BSE and SE electrons, and convert them to a signal via a synchronized scan on a cathode ray tube (CRT) display similar to the one in an ordinary television, producing an image. The magnification is determined by the ratio of the scan length on the CRT and that on sample, i.e.

$$M = \frac{L}{l}$$

where M, L, l represent magnification, scan length on display and on sample, respectively.

b) Contrast mechanism

Contrast is defined as the difference in brightness of the pixels that make up the image, which represents a difference in signal from corresponding picture elements on the specimen. This signal brightness is dependent on the signal generated within the specimen and the type of detector used, i.e. affected by both the signals from beam-specimen interaction and the conversion of the signal intensity to image brightness.

Contrast of a SEM image normally consists of three components: number, trajectory, and energy components respectively. The number component is expressed by higher numbers of electrons from the specimen resulting in higher brightness on the image. Trajectory is equally important, since detectors can collect only a portion of the signal emitted. Improper positioning of the detector will result in a low intensity of the detected signal. The energy component is also critical, since the ability to collect and detect the signal is a function of the signal energy.

The most widely used images produced by SEM imaging are the SE image, the BSE compositional image, and the BSE topographic image. It is important to note that many images have a combination of contrast components that contribute to the final image and that the description here summarizes only the most common images.

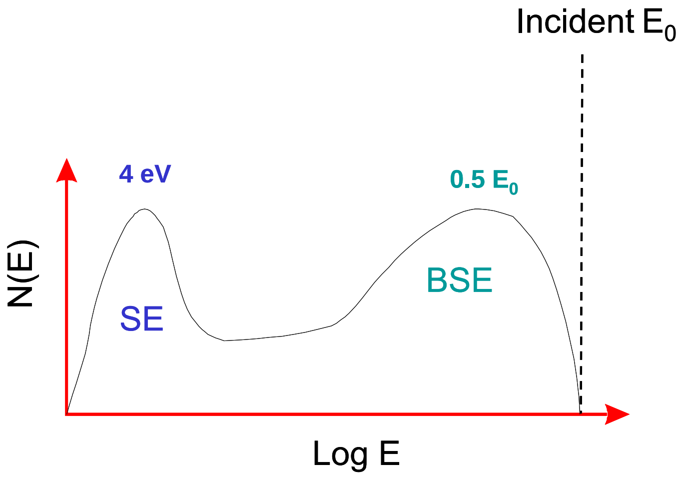

Scheme 3.3

Schematic plot of the energy distribution of electrons emitted from a specimen[1]

As described above, BSE is due to elastic scattering of electrons. Practically, BSEs also undergo several inelastic collisions during their time inside the sample as well and lose some fraction of energy. As indicated in Scheme 3.3, the BSE has an energy distribution with the peak at half of the incident beam energy (0.5 E_0).

The total BSE yield (total fraction of beam electrons that backscatter) from a randomly oriented polycrystal tends to increase monotonically with the atomic number Z, which could be expressed as:[1]

$$\text{BSE}_{\text{yield}} = -0.0254 + 0.016Z - 1.86*10\text{-}4\ Z^2 + 8.3*10\text{-}7Z^3$$

Thus, a general trend is derived that the BSE yield increases with increasing *Z*, flattening out at higher Z. This provides the theoretical base for atomic number contrast. This works best for higher beam energies (> about 5kV).

In addition to the BSE dependence on *Z*, surface orientation as well as the preferred direction of the BSEs complicates the BSE contrast mechanism. Tilt of the sample surface will result in change of the distribution of BSEs, a number component of contrast. For the crystalline samples, the BSE yield may change abruptly, which is called electron channelling effect. This effect is due to the wave nature of the incident beam, which may interact with the periodic structure of the crystal and cause change of the scattering probability of the incident electrons. Thus, BSEs contribute to topographic contrast as well.

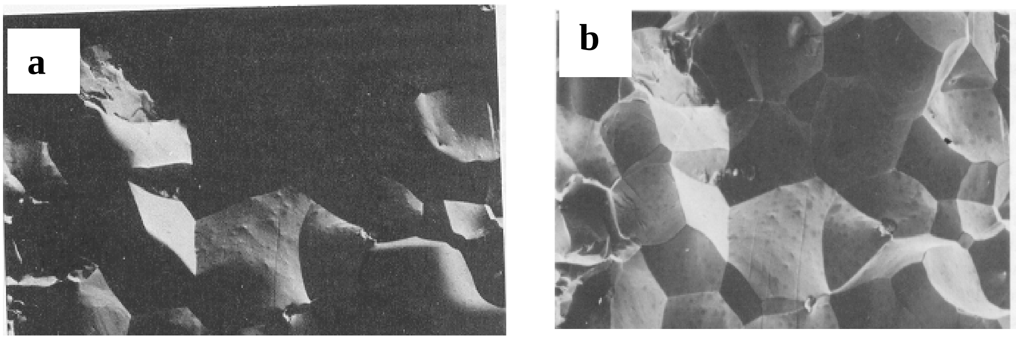

Fig. 3.1. *Topographic contrast of iron fracture due to (a) BSE, (b) SE and BSE component.*

Topographic contrast mostly originates from SEs which provides the most high-resolution image of the sample surface. The tilt of sample introduces a distribution change of the electrons, which contributes a number component to the contrast. Fig. 3.1a shows only the BSE component of contrast and Fig. 3.1b shows both the BSE and SE components. The topographic contrast showing the iron fracture surface is achieved by the Everhart-Thornley detector which can selectively collect different electrons.

3.1.1.3 Transmission electron microscope

a) General introduction

SEM gives no internal information of a sample, while TEM produces an image that is a projection of the entire object revealing both the surface and the internal structures. The incident electron beam interacts with the sample as it passes through the entire thickness of the sample. Different internal structures in the sample can be differentiated because they produce different projections. The samples need to be thin enough, otherwise the electron beam will be blocked. Scheme 1.6 is the schematic drawing of a TEM.

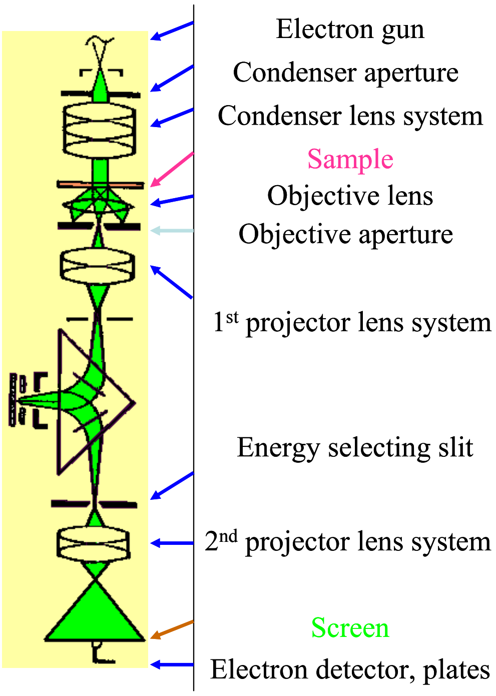

Scheme 3.4

Schematic drawing shows the basic principles of TEM

Like the case of SEM, the incident electron beam strikes the specimen and the transmitted electrons (Scheme 3.4) are focused by the objective lens into an image. The optional objective and selected area metal apertures can restrict the beam. The objective aperture can enhance contrast by blocking out high-angle diffracted electrons and the selected area aperture enables the user to examine the periodic diffraction pattern of the crystalline sample. The image is passed down the column through the intermediate and projector lenses, being enlarged all the way. It strikes the phosphor screen and light is generated, allowing the user to see the image. The darker areas of the image represent those areas of the sample that fewer electrons were transmitted through (they are thicker or denser), vice versa.

b) Contrast machnism

Mass-thickness contrast

The interaction of electrons with heavy atoms in the sample is stronger than with light atoms, which gives the mass contrast. In a sample with homogeneous thickness, areas in which heavy atoms are concentrated appear with darker contrast than such with light atoms. Moreover, thickness may also generate contrast, i.e. more electrons are scattered in thick than in thin areas which causes thin areas to appear bright. And thicker sample results in a larger angular distribution of transmitted electrons as shown in Fig. 3.2.

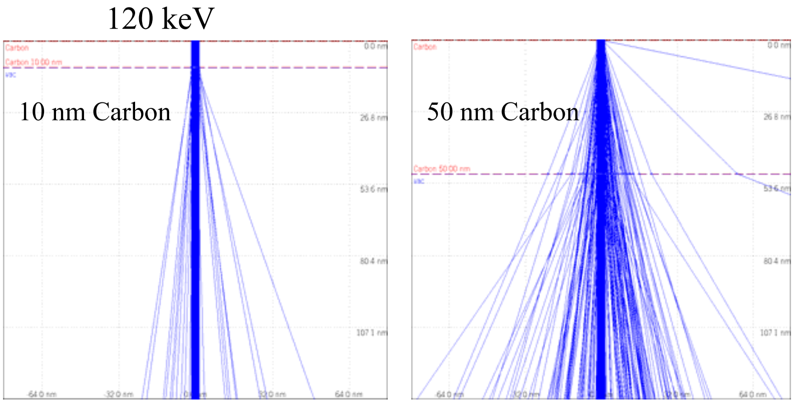

Fig. 3.2. Larger angular distribution of transmitted electrons through a) 10 nm b) 50 nm carbon film.

Certainly, a thick area with light elements might have the same contrast as a thinner area with heavier atoms. For a crystalline area in the sample, due to the strong Bragg diffraction, electrons are scattered and this area appears with dark contrast in the bright field image as well (diffraction contrast).

Phase contrast

Scheme 3.5 shows a schematic presentation of the principle of phase contrast formation. In phase contrast imaging, a parallel beam irradiates the specimen, and the image is formed by interference between many beams. In the figure, we can see both the incident beam and diffracted beam. As is well known, the image contrast may reveal an electrostatic potential under the Scherzer defocus condition which realizes the successful $-\pi/2$ phase shift (ideally) of diffracted beams at the objective lens for a wide frequency range to result in totally $-\pi$ phase shift at the imaging plane. Hence the projected atomic positions are imaged as dark region in case that the sample foil is thin enough (typically less than 5 nm for metallic foils), where weak phase object (WPO) assumption is valid.

Another type of TEM is the scanning transmission electron microscope (STEM), where the beam can be rastered across the sample to form the image. The rastering of the beam across the sample makes these microscopes suitable for analysis techniques such as mapping by energy dispersive X-ray (EDX) spectroscopy, electron energy loss spectroscopy (EELS) and annular dark-field imaging (ADF).

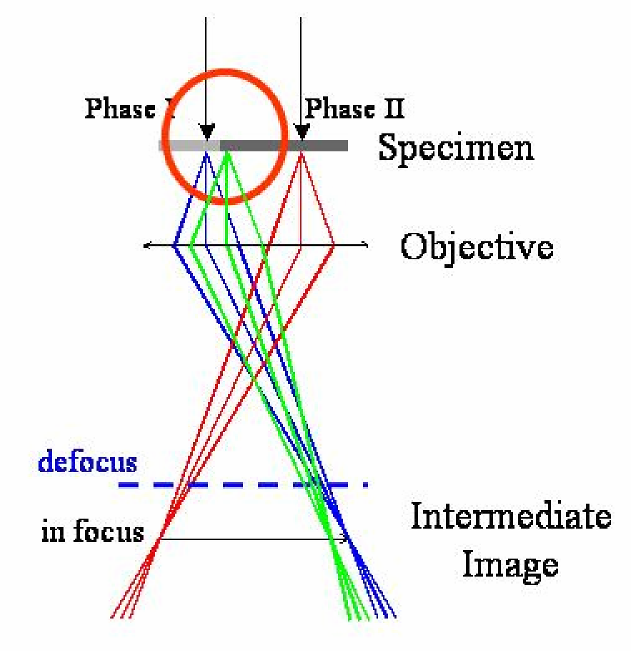

Scheme 3.5

Schematic drawing shows the principle of phase contrast formation

3.1.2 Introduction on the formation of ZnO films

In comparison to the bulk ZnO samples, ZnO films have some characteristic properties and specific applications. ZnO films are promising candidates in some optoelectronic applications like energy windows, liquid crystal displays, solar cells, gas sensors, ultrasonic oscillators, transducers, etc.[3]

Thin films of ZnO with the *c*-axis orientation perpendicular to the substrate show piezoelectric properties and are useful in surface acoustic wave devices, bulk acoustic wave devices, acoustic-optic devices and microelectro mechanical systems.[4]

ZnO is one of the several optical transparent oxides with wide band gap, which exhibits both high transparency and conductivity like indium-tin-oxide (ITO), SnO films. Undoped ZnO films have resistivity of 10^{-3}-10^{-2} Ω cm after deposition,[3, 5] while commercial ITO-coated polyethylene terephthalate (PET) has a resistivity of 7×10^{-4} Ω cm.[6] Therefore, ZnO films might be selected as alternative for ITO, taking advantage of its low cost, high chemical and thermal stability. ZnO thin films doped with metal ions like Al, Ga,[7] etc. with resistivities less than 1 × 10^{-3} Ω cm have been reported and are being applied as transparent conducting electrodes in some important devices in place of usual thin films.

A large variety of techniques have been employed for growth of high-quality ZnO films, including pulsed-laser deposition (PLD),[8] spray pyrolysis,[9] atomic-layer deposition (ALD),[10] molecular beam epitaxy (MBE),[11] chemical-bath deposition (CBD),[12] sol-gel,[13] electrodeposition,[14] and metal organic chemical vapor deposition (MOCVD) method[15] etc. Various Zn-containing precursors have been selected for fabrication of ZnO films, such as liquid dimethyl-Zn and diethyl-Zn complexes[16] or the solid acetate,[17] alkoxide[18] and acetyl-acetonate zinc complexes.[19] Because of their pyrolysis properties, the Zn-containing complex has some advantages over the Tin and Indium counterparts. Generally, Zn complex precursors are more reactive. For example, dimethyl-zinc and diethyl-zinc have very high vapour pressures (> 10 Torr).

In the following, we wish to prove that the polymer-based process employed here provides an efficient and versatile way to produce nanocrystalline metal oxide films like ZnO film.

3.2.Formation of ZnO films

3.2.1 Evolution of the ZnO film

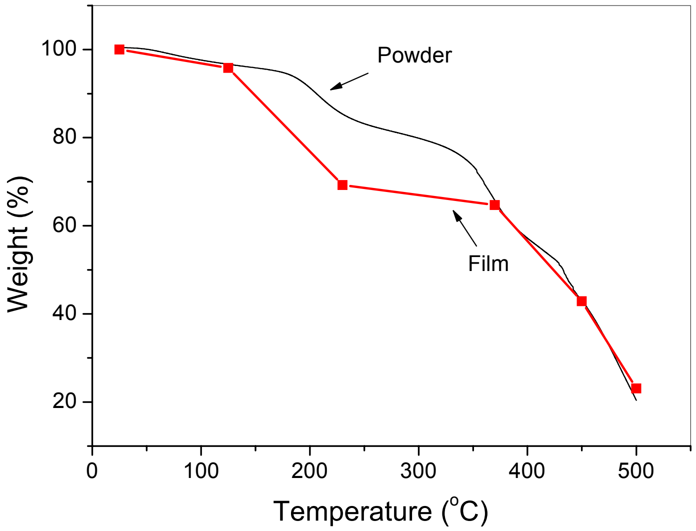

Fig. 3.3. *Weight loss versus temperature of ZnO film in comparison with TGA result of ZnO powder.*

The zinc polyacrylate precursor was deposited onto clean silicon or quartz substrates by the simple drop casting method. A colorless continuous film was obtained after drying at 50 °C in vacuum. Then a series of identical precursor films were put into an oven and heated with a rate of 5 °C/min from room temperature to 500 °C, using air as carrier gas. The films were taken from the hot oven at 230, 370, 450, 500 °C in sequence and the last piece of film was annealed for 1 h at 500 °C. The films become darker with temperature increasing but the last ZnO film appears white. By handling the films with special care, the percentage decrease in mass relative to the initial mass for the films is plotted in Fig.3.3 versus the grown temperature. The obtained curve shows very similar profile with the TGA result of a powder sample, indicating the same decomposition process in both the film and solid state bulk sample.

X-ray diffraction is used to examine the growth of the films as seen in Fig. 3.4. Strong peak at $2\theta = 69^{\circ}$ is due to diffraction of the silicon wafer. The weak peak at $2\theta = 32.9^{\circ}$ is assigned to Si (200) reflection. From room temperature to 450 °C, all the films are amorphous and actually intermediate products between zinc polyacrylate and ZnO crystals. For the film annealed at 500 °C, very weak peaks of ZnO (100), (002) and (101) are observed, indicating the formation of ZnO. The intensity of the peaks increases for the film with isothermal treatment for 1 hour due to the increase in crystallinity of zinc oxide.

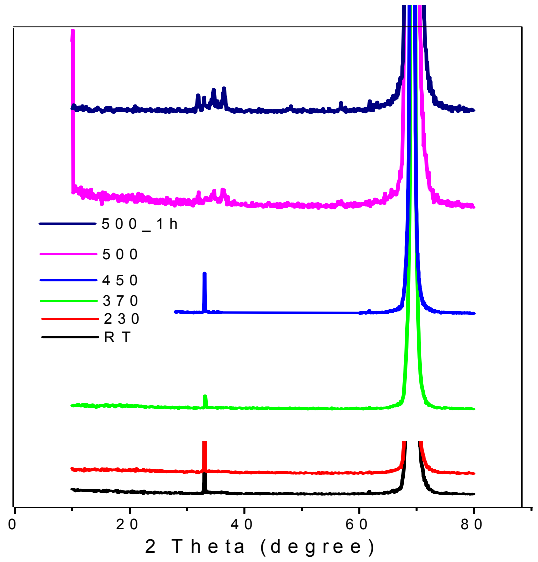

Fig. 3.4. *XRD patterns of ZnO films annealing at different temperature.*

Another series of films was prepared on quartz glass with the same fabrication conditions as those on silicon and examined with UV/Vis spectra, as shown in Fig.3.5. At room temperature and 230 °C, the films show no absorption at all. But this is not the case of the film grown at 370 °C, which shows an intensive absorption with absorption edge and a tail. The absorption edge could be extrapolated to about 400 nm. With even higher annealing temperature at 450 °C, the absorption decreases and shows a similar profile as that obtained at 370 °C. For the film fabricated at 500 °C and the one annealed for an extra hour, both show a typical optical edge at 375 nm of crystalline type material, which is consistent with the pure ZnO bandgap. This proves that the crystallization process is completed after annealing at 450 °C.

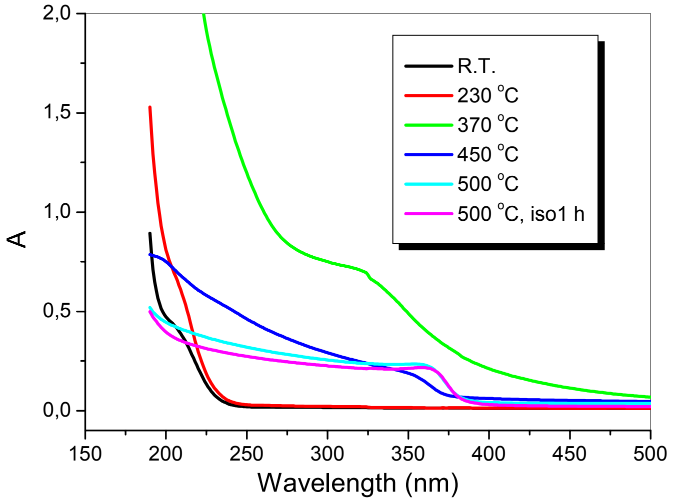

Fig. 3.5. *UV/Vis spectra of the ZnO films annealed at different temperature.*

We note previous reports of several amorphous semiconductors like α-$PbTiO_3$,[20] amorphous silicon[21] and GaP[22], which show similar absorption spectra with distinct exponential absorption edge and tail. Wood et al.[23] summarize the characteristics of some absorption spectra of chalcogenide and some compound glass, as whose absorption spectra could be divided into three regimes, as shown in Scheme 3.6. The first part could be expressed by the relation of

$$\hbar\nu\alpha \propto (\hbar\nu - E_g^{opt})^r$$

α is the absorption constant and E_g^{opt} optical bandgap. The second part is the exponential part, which is called Urbach edge. The expression about the energy and α is given as,

$$\alpha \propto e^{h\nu / E_1}$$

where E_1 is in the range 0.05 - 0.08 eV at room temperature and increases with temperature. The third part is the absorption tail, which is not an artifact of light scattering and can be shifted and sharpened by thermal annealing. The edges are sensitive to the preparation conditions, thermal history and purity.

In Fig. 3.5 the three characteristic regions are evident in the absorption spectrum of the film grown at 370 °C, which changes with the temperature increase. Therefore, the transformation of UV spectra edges of the ZnO films reflects the crystallization process from amorphous precursor to ZnO crystal.

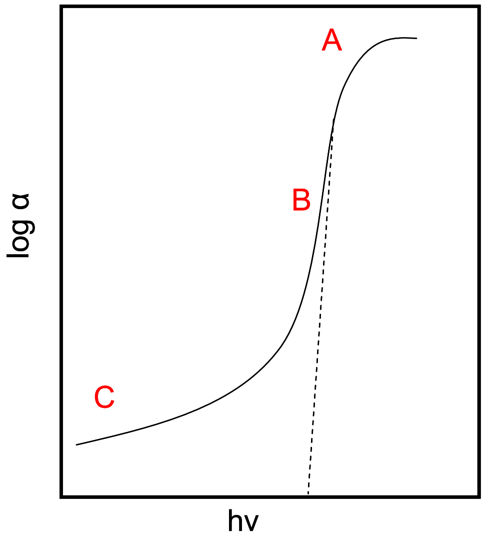

Scheme 3.6

UV absorption of an amorphous semiconductor.[23]

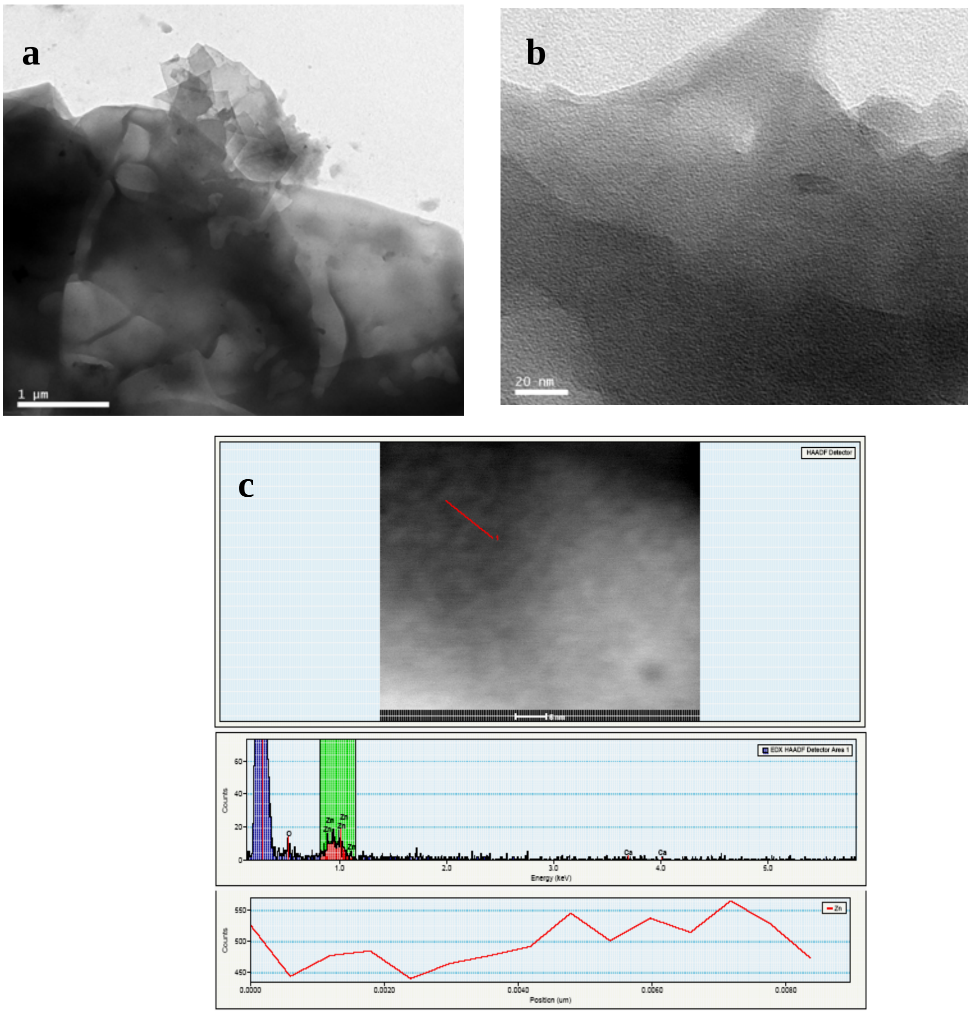

Fig. 3.6. *a, b) TEM images of ZnO film fabricated at 370 °C shown at different scale. c) EDX results of Zn via a line scan as denoted by the red line.*

The growth of ZnO films on silicon wafer are investigated by electron microscopic methods including SEM and TEM. The SEM images are recorded by directly scanning the obtained films, while the TEM samples are prepared by scraping some powder from the films and then depositing on a copper grid covered with carbon film. The morphology of film calcined at 370 ^{o}C is shown in Fig. 3.6.

The layered structure is observed and the darkness arises from the thickness of the sample (Fig. 3.6a). Even with high magnification, no crystalline structure is found (Fig. 3.6b). Energy-dispersive X-ray spectroscopy is coupled to the TEM device for analysis of the composition and compositional distribution of the sample (Fig. 3.6c). The existence of zinc is evident. More importantly, a line scan of zinc as the red line denoted in the image shows that Zn distribution is relatively homogeneous with a fluctuation of ± 10%.

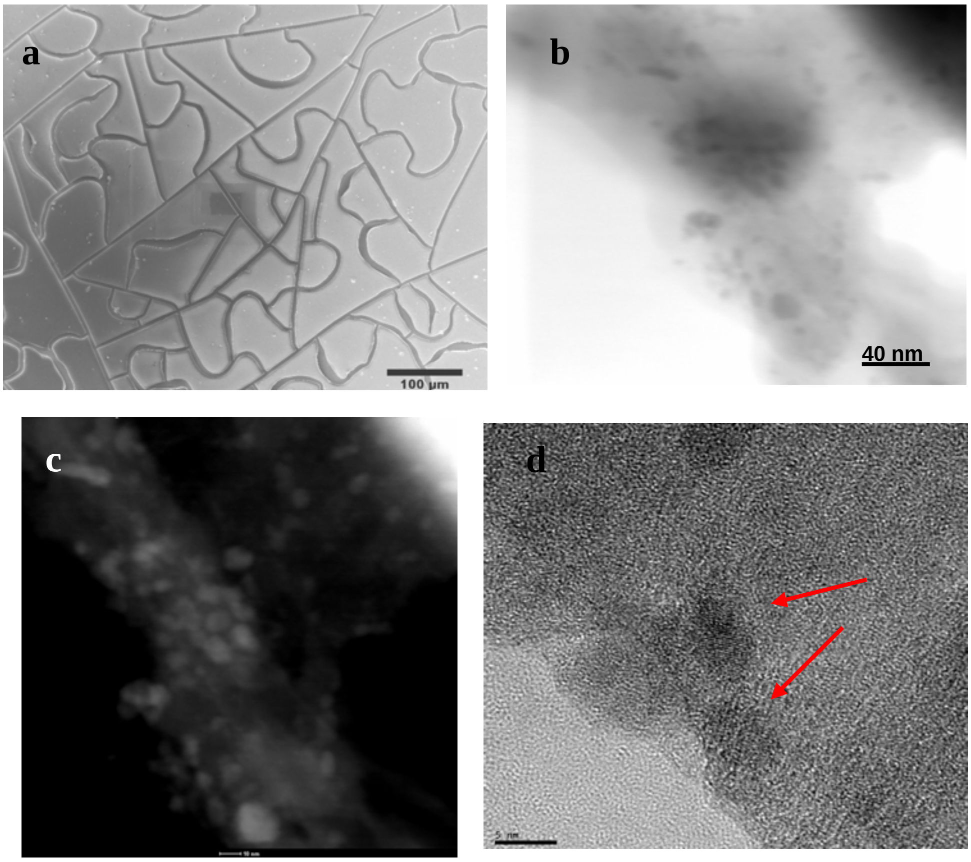

Fig. 3.7. *a) SEM image of ZnO film fabricated at 450 ^{o}C. b) TEM bright-field images and c) TEM dark-field image of the same sample. d) HRTEM of the same sample. Scale bar in c and d are 10 nm and 5 nm respectively.*

SEM image shows that the film fabricated at 450 ^{o}C is semicontinuous with block area in the size of 100 µm (Fig.3.7a). The particulate structures sized less than 10 nm in diameter appear in the film matrix (Fig.3.7b). These particles show clear grain boundaries and appear brighter than the matrix in the dark-field image, indicating possibly the crystalline structure of the particles (Fig.3.7c).[24] HRTEM shows clearly the lattice fringes of crystal material of the particles with a diameter of 5 nm (Fig.3.7d). This indicates the birth of zinc oxide nanoparticles although no XRD scattering in the powder diffractogram is seen due to the very small amount.

For the film fabricated at 500 ^{o}C, SEM shows a continuous film of ZnO nanoparticles with diameter about 20 nm. The thickness of this ZnO film is about 700 nm measured by SEM cross-section image. The surface of the film is covered with soft rods, which shrink within several seconds of electron beam focusing (Fig. 3.8 a,b). These 200 nm-long rods are however undistinguishable under TEM, which demonstrates that they are organic and part of the ZnPA precursor. A lager number of particles with greater size are observed in comparison with the film fabricated at 450 ^{o}C in TEM image (Fig. 3.8c). In HRTEM image, hexagonal shape particles in size of 10-20 nm are shown, which is consistent with the wurtzite structure of zinc oxide (Fig. 3.8d).

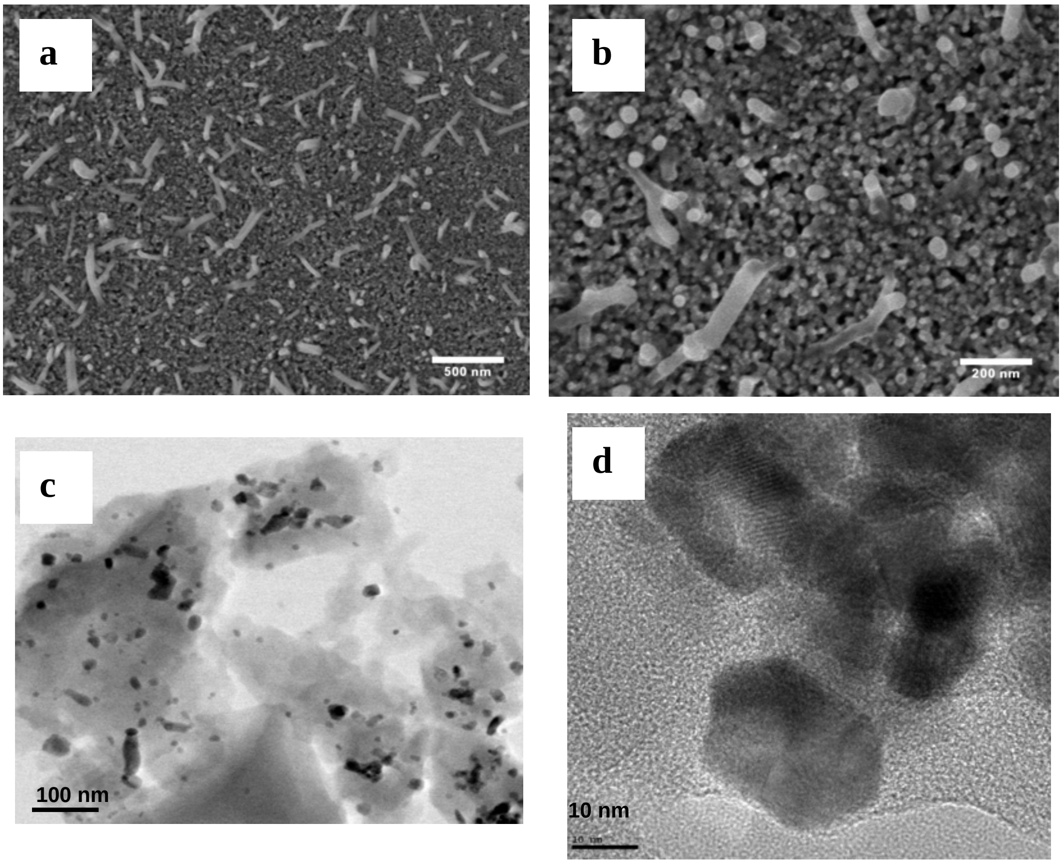

Fig. 3.8. *a,b) SEM images of ZnO films fabricated at 450 ^{o}C. c,d) TEM and HRTEM of the same sample.*

3.2.2 Fabrication of films under different gas atmosphere

3.2.2.1 Introduction

The annealing conditions including temperature and gas atmosphere in the preparation of ZnO films have significant influence on the photoluminescence (PL) properties of the material. In the course of thermal annealing, the intrinsic defects concentration varies, which can be expressed in quasichemical reaction equations as follows:

$$\frac{1}{2}O_2 + V_O^x = O_O^x, \quad [V_O^x] \propto p_{O_2}^{-0.5}, \qquad (1)$$

$$\frac{1}{2}O_2 = V_{Zn}^x = O_O^x, \quad [V_{Zn}^x] \propto p_{O_2}^{0.5}, \qquad (2)$$

$$Zn_i + \frac{1}{2}O_{2(g)} = Zn_{Zn} + O_O, \ [Zn_i] \propto p_{O_2}^{-0.5} \qquad (3)$$

$$\frac{1}{2}O_2 = O_i\ , \ [O_i] \propto p_{O_2}^{0.5} \qquad (4)$$

$$V_{Zn} + \frac{1}{2}O_{2(g)} = O_{Zn}, \quad [O_{Zn}] \propto p_{O_2}^{0.5}[V_{Zn}] \qquad (5)$$

Here, $[V_O^x]$, $[V_{Zn}^x]$, $[Zn_i]$, $[O_i]$, $[O_{Zn}]$ are the concentration of nonionized oxygen, nonionized zinc, interstitial zinc, interstitial oxygen and antisite oxygen. It is seen that an oxygen-rich atmosphere is unfavorable for $[V_O^x]$ and $[Zn_i]$ formation but favorable for creating $[V_{Zn}^x]$, $[O_i]$ and $[O_{Zn}]$.

3.2.2.2 Results and discussion

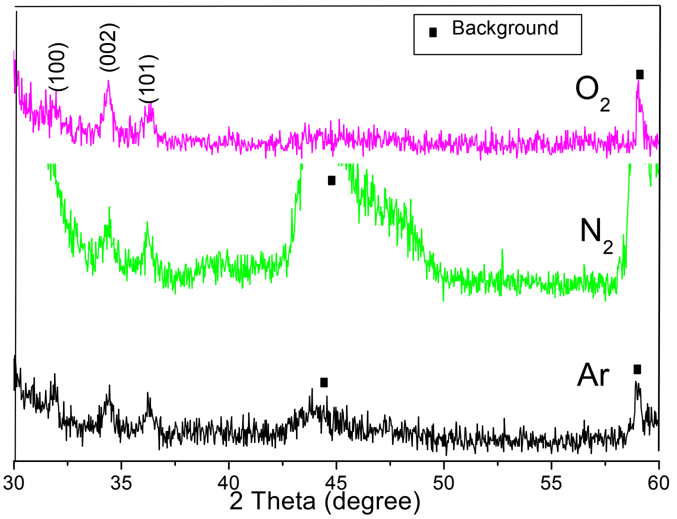

Fig. 3.9. *X-ray diffraction pattern of ZnO films fabricated in different atmosphere.*

In our experiments, four ZnO films were fabricated by annealing of identical ZnPA precursor films on silicon wafer in different gas atmosphere: air, pure oxygen, pure nitrogen and pure argon respectively. The films were prepared at 500 ^oC and annealed at that temperature for 1 hour. The X-ray diffraction patterns of the films fabricated in N_2, O_2 and Ar are shown in Fig. 3.9. All the patterns indicate the formation of the wurtzite-type ZnO phase and no preferential orientation was observed in these films. Like the film fabricated in air, the one obtained in argon is semi-continuous with block sized in the range of 100 μm (Fig.3.10c). However, those films fabricated in nitrogen and oxygen are continuous although defects like crevices are observed (Fig.3.10a,b). The FESEM high-magnification images show surface morphology of the four films as seen in Fig.3.11. In general, in all cases, the particle size of the obtained ZnO is in the range of 20 nm. Mainly single particles are seen and twinned are also observable. The morphology recorded by AFM confirms the SEM results.

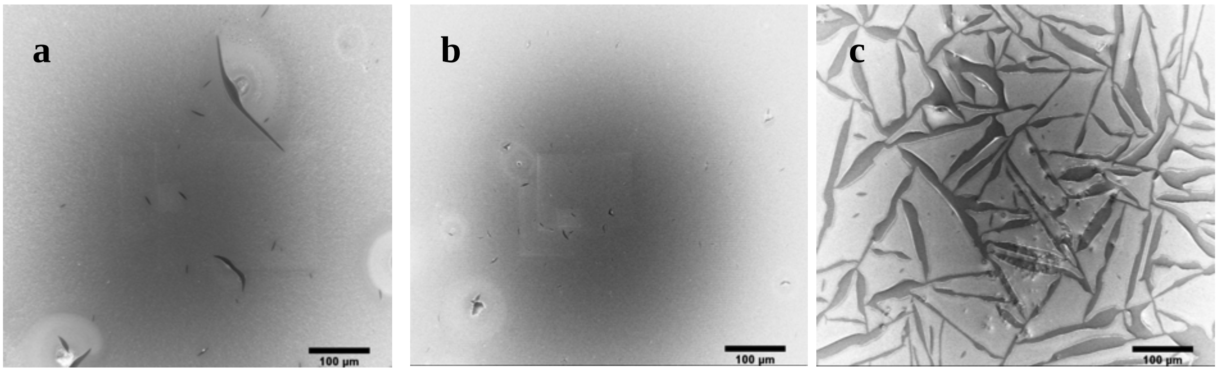

Fig. 3.10. *Low magnification SEM images of ZnO films fabricated in different gas. (a) O_2; (b) N_2; (c) Ar.*

The PL spectra of the films annealed in different gas atmosphere are shown in Fig.3.12. Unlike the spectra of the powder ZnO samples (see Ch. 2.3), in which the UV emission is very weak or quenched due to the high density of intrinsic defect centers in the nanoparticles, all the ZnO films in this experiment show an intense UV emission centered at 382 nm. Especially for the case of the film obtained in O_2, the UV emission is much stronger than seen from the other films, indicating a better crystallinity of the ZnO film. And the difference of the visible emission between the ZnO films and powders is also remarkable. The as-prepared ZnO film has a strong and very broad visible emission centered at about 550 nm but the ZnO powder show this at 590 nm. Unlike the powder sample, no blue emission was observed except for the film obtained from O_2. Obviously, the gas flow has an evident effect on the visible emission of the ZnO film. In pure O_2, the visible emission at 550 nm is weaker than that in the other three films and exhibits a blue emission around 420 nm as seen in the powder sample.

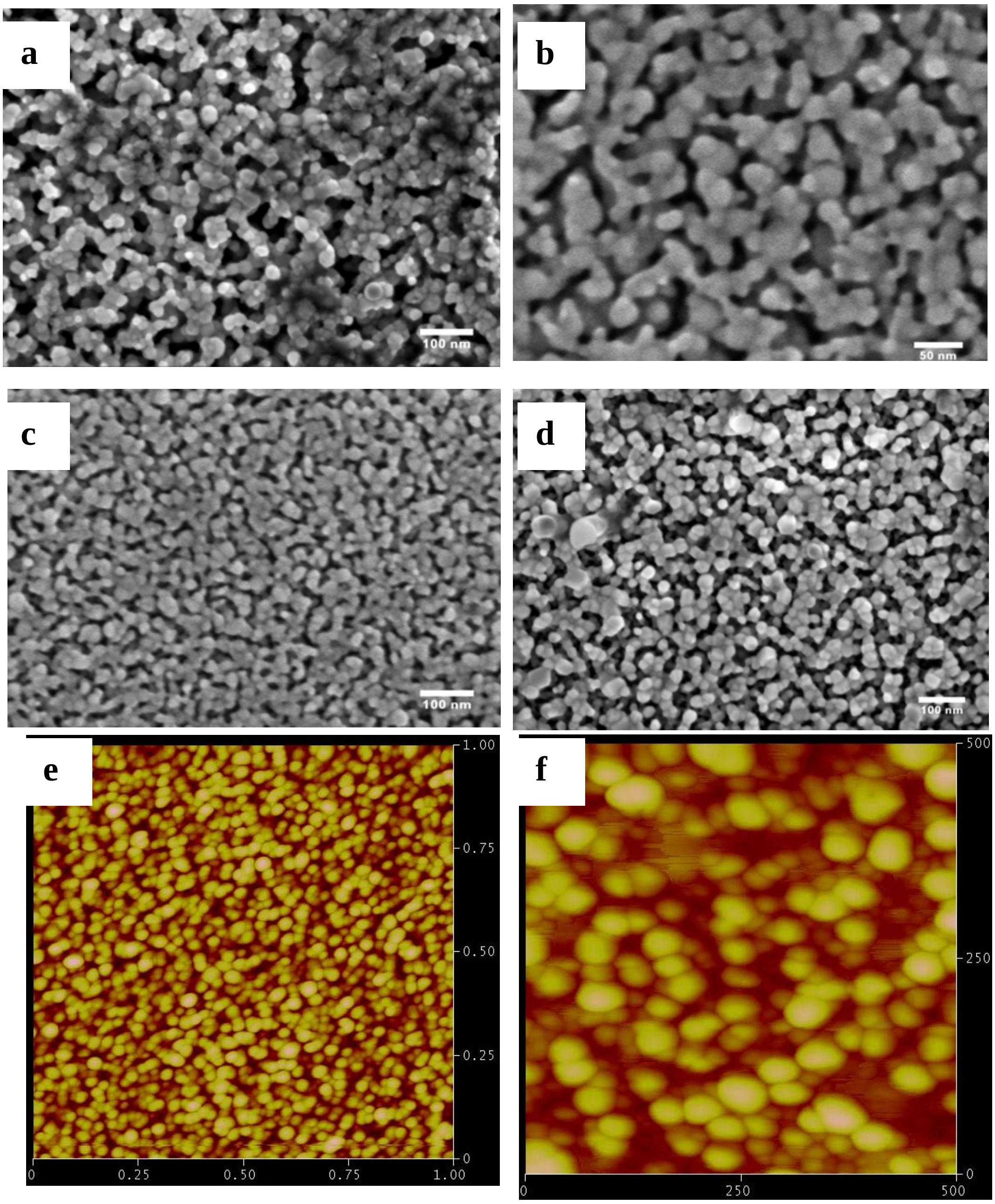

Fig. 3.11. *SEM images of ZnO films fabricated in a) air, b) Ar, c) N_2 and d) O_2; e and f are the AFM images of the ZnO films fabricated in N_2 and O_2, respectively.*

As is well known, the visible emission is due to the intrinsic defects in the crystals. Therefore, the blue emission might be assigned to the oxygen-favorable defects like interstitial oxygen (O_i) or zinc vacancy (V_{Zn}), while the green emission due to the oxygen-unfavorable defects like vacancy (V_O) or interstitial zinc (Zn_i). The emission at 420 nm was reported previously[2] and attributed to the interstitial oxygen, which is reasonable in our case. And the common explanation of the green-emission by assignment to the oxygen vacancy is also consistent with our findings, i.e. in the gas with high oxygen content, the formation of V_O is greatly suppressed, leading to low green-emission band. Fig. 3.12b shows the excitation spectra of the ZnO films. All the spectra show an absorption edge which could be extrapolated to about 375 nm, the bang gap of undoped ZnO.

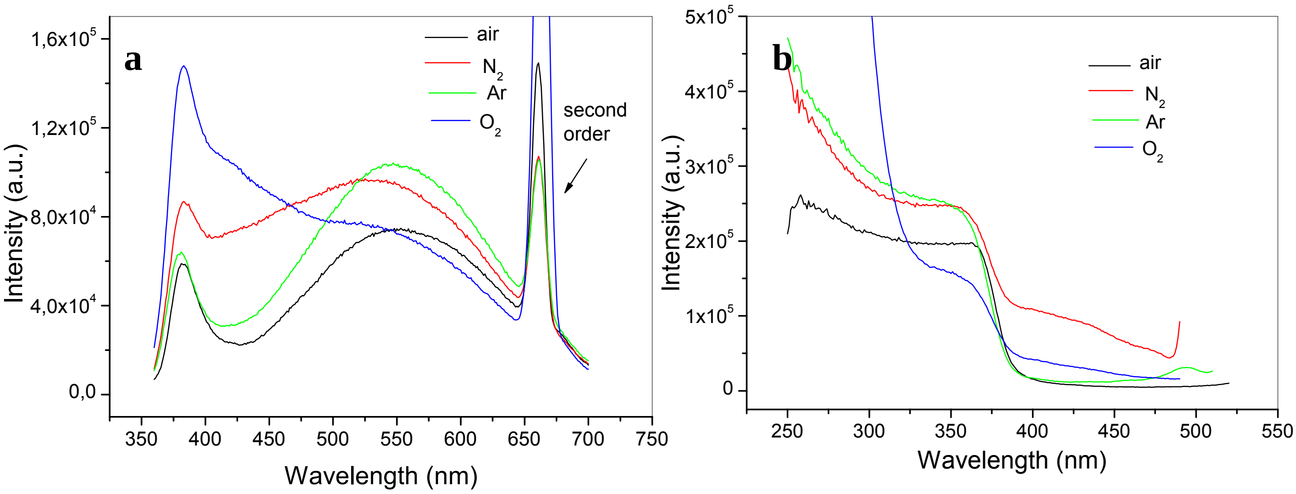

Fig. 3. 12. PL spectra of ZnO films fabricated in different gas atmosphere. a) emission spectra and b) excitation spectra.

In summary, ZnO nanocrystalline films are fabricated by pyrolysis of a drop-cast ZnPA film. The results of XRD, UV spectra as well as the TEM images prove that both the ZnO nanopowder and film undergo same decomposition steps. PL spectra show that in the oxygen atmosphere, blue emission is promoted but the green one is suppressed. This confirms our assumption that the blue emission is generated by crystal defects, namely zinc vacancies, while green emission originates from oxygen vacancies.

3.3 Experimental section

Preparation of Zinc Polyacrylate Precursor Polymer:

Same procedure as described in chapter 2.

Preparation of ZnO Films:

Firstly, an aqueous solution of the obtained zinc polyacrylate polymer precursor is prepared with a concentration of 0.5%~1%. Then several drops of the solution are cast on a clean wafer of silicon or quartz glass. The wafer is put into a vacuum oven and dried at temperature no more than 50 °C in vacuum. A colorless film of the zinc polyacrylate precursor is formed after several hours.

Thereafter, the film is calcined in a temperature-controlled oven under certain gas flow with a heating rate of 5 °C min^{-1} to 500°C. The sample was isothermally annealed for 1 hour at this temperature and taken out in time.

INSTRUMENTAL

UV spectra were recorded at room temperature with a Perkin-Elmer Lambda 2 UV/Vis/NIR spectrophotometer. TG-MS were measured under oxygen flow on a Mettler Toledo ThermoSTAR TGA/SDTA 851 connected with a Pfeiffer Vacuum GSD 300 T2 pump and a Basler MS/Netsch STA449C mass detector. The evolution of films was investigated by XRD recorded on a D500 Diffraktometer operating at 30 kV and 30 mA with a 0.08^{o} step size and 10 s as integration time. The films obtained at different gas atmosphere are record by a Philips pulverdiffractometer. SEM images showing the morphology of ZnO films were taken by LEO Gemini 1530 with an inlens detector. TEM images were obtained by Tecnai F20 microscope operating at 200 kV. Energy dispersive X-ray spectroscope (EDX) coupled to the TEM was used for composition determination. AFM images are recorded by a Veeco Multimode Scanning Probe Microscope (SPM) with tapping mode. Room temperature photoluminescence (PL) measurements were performed on a Spex Fluorolog spectrometer.

3.4 References

[1] J. I. Goldstein, *Scanning electron microscopy and X-ray microanalysis : a text for biologists, materials scientists, and geologists* New York; London : Plenum Press, **1992.**

[2] B. J. Jin, S. Im, S. Y. Lee, *Thin Solid Fims* **2000**, *366*, 107.

[3] B. J. Lokhande, M. D. Uplane, *Appl. Surf. Sci.* **2000**, *267*, 243.

[4] a) S.C. Minnc el al., *Appl. Phys. Lett.* **1995**, *67*, 3918; b) J.-B. Lee, H.-J. Lee, S.-H. Seo, J.-S. Park, *Thin Solid Films* **2001**, *398*, 641.

[5] B.J. Lokhande, P.S. Patil, M. D. Uplane, *Mater. Lett.* **2002**, *57*, 573.

[6] H. Kim, J. S. Horwitz, G. P. Kushto, Z. H. Kafafi, D. B. Chrisey, *Appl. Phys. Lett.* **2001**, *79*, 284.

[7] a) A. V. Singh, R. M. Mehra, A. Yoshida, A. Wakahara, *J. Appl. Phys.* **2004**, *95*, 3640; b) V. Fathollahi, M. M. Amini, *Mater. Lett.* **2001**, *50*, 235.

[8] H. Kim, C. M. Gilmore, *Appl. Phys. Lett.* **2000**, *76*, 259.

[9] F. Paraguay D., W. Estrada L., D.R. Acosta N., E. Andrade, M. Miki-Yoshida, *Thin Solid Films* **1999**, *350*, 192.

[10] P. F. Carcia, R. S. McLean, M. H. Reilly, *Appl. Phys. Lett.* **2006**, *88*, 123509.

[11] Y. S. Jung, O. V. Kononenko, W. K. Choi, *Solid State Commu.* **2006**, *137*, 474.

[12] a) E. Hosono, S. Fujihara, T. Kimura, H. Imai, *J. Colloid Inter. Sci.* **2004**, *272*, 391; b) K. Govender, D. S. Boyle, P. B. Kenway, P. O'Brien, J. Mater. Chem. **2004**, *14*, 2575.

[13] X.-Y. Kang, T.-D. Wang, Y. Han, Tao minde, *Mater. Res. Bull.* **1997**, *32*,1165.

[14] Y. L. Yang, H. W. Yan, B. F. Yang, L. S, Xia, Y. D. Xu, J. Zuo, F. Q. Lu, *J. Phys.Chem.* **2006**, *110*, 846.

[15] S. Oda, H. Toknunaga, N. Kitajima, J. Hana, I. Shimizu, H. Kokado, *Jpn. J. Appl. Phys., Part 1*, **1985**, *24*, 1607.

[16] a) J. Hu, R. G. Gordon, *Mater. Res. Soc. Symp. Proc*. **1991**, *202*, 457; b) J. Hu, R. G. Gordon, *J. Appl. Phys*. **1992**, *71*, 880-890.

[17] S. Jain, T. T. Kodas, M. Hampden-Smith, *Chem. Vap. Deposition* **1998**, *4*, 51-59.

[18] J. Auld, D. J. Houlton, A. C. Jones, S. A. Rushworth, M. A. Malik, P. O'Brien, G. W. Critchlow, *J. Mater. Chem.* **1994**, *4*, 1249.

[19] H. Sato, T. Minami, T. Miyata, S. Takata, M. Ishii, *Thin Solid Films* **1994**, *246*, 65.

[20] E. R. Leite, F. M. Pontes, E. C. Paris, C. A. Paskocimas, E. J. H. Lee, E. Longo, P. S. Pizani, J. A. Varala, V. Mastelaro, *Adv. Mater. Opt. Electron* **1999**, *10*, 235.

[21] G. D. Cody, T. Tiedje, B. Abeles, B. Brooks, Y. Goldstein, *Phys. Rev. Lett.* **1981**, *41*, 1480.

[22] J. E. Davey, T. Pankey, *J. Appl. Phys.* **1969**, *40*, 212.

[23] D .L. Wood, J. Tauc, *Phys. Rev. B* **1972**, *5*, 3144.

[24] B. Fultz, J. M. Howe, *Transmission Electron Microscopy and Diffractometry of Materials*, Vol. 2 Springer-Verlag, Berlin Heigelberg, **2001**, **2002**.

4 Preparation of ZnO-Based Mixed Metal Oxide Nanoparticles

4.1 Introduction

Mixed metal oxides (MMO) have triggered much research activity due to their wide applications in the production of semiconductor devices,[1] ceramics[2] and microelectronic including photoluminescent (PL) devices.[3-4] Stoichiometry and homogeneity of composition are key to the potential applications of such materials.[5] The size and shape of the MMO particles or microstructure of MMO thin films are important parameters that need to be controlled. For example, some research work shows that in the synthesis of metal oxide nanoparticles, the formation of a metastable solid solution[5] or introduction of a second phase[6] could inhibit the particle growth and enhance the thermal stability with regard to undesired phase transitions.

In principle, mixed oxide systems can be classified into three categories:[7] (i) distinct chemical compounds, which for example $ZnSnO_3$ and Zn_2SnO_4 formed in the ZnO-SnO_2 systems, are thermodynamically stable.; (ii) solid solutions, which for example are formed in the TiO_2-SnO_2 system; and (iii) systems that form neither defined stoichiometric compounds nor solid solutions, like TiO_2-WO_3.

Many synthetic methods have been developed, in order to produce MMO of high and reproducible quality. Mechanical mixing of precursors followed by a firing process to achieve the desired MMO is the traditional method. It starts by ball-milling a mixture of different kinds of pure metal oxides or thermally labile metal salts (e.g. carbonates, acetates, nitrates), and the resulting blend is then subjected to a temperature controlled heating protocol.[8] Since it is difficult to control grain growth and segregation phenomena occurring during calcination or sintering, processes and contaminations may be introduced in the course of blending, it is notoriously troublesome to create high quality materials. Spray pyrolysis is another method frequently used to synthesize MMO of homogeneous composition at the atomic length scale.[9] A further method rests on sol-gel chemistry starting from hydrolysis of metal ion containing precursors to produce an intermediate oxy-hydroxyl-gel which is then subjected to controlled heating (calcination) to give ceramic powders of desired composition. Sin and Odier[10] have reported on the synthesis of a series of MMO of the type $La_{0.85}So_{0.15}MnO_3$, $La_2Cu\ NiO_6$ and $BaZrO_3$ in which the EDTA complexes of the metal ions were stabilized in a polyacrylamide gel prepared in situ. The pyrolysis of the dry gel containing the EDTA metal complex at temperatures above 700°C gave the desired MMO. This is a variation of the Pechini method,[11] which has been widely used in the past. For instance in the work of M. Kakihana et al.[12] on the synthesis of the perovskite $PbTiO_3$ citric acid is used as both the complexant and reagent to form a water compatible polyester with ethylene glycol in situ. The gel containing the metal-citric acid complex was then used as precursor in the calcination. An earlier publication by Marcilly, Courty and Delmon has described this type of procedure in general terms.[13] In all of these cases the polymer acts as a thermolabile builder to hold the heterogeneous mixture of precursors together. Hydrothermal synthesis is an approach in which nucleation and growth of the desired MMO particles takes place in water or another liquid medium at relatively low temperature and under mild conditions. $PbZr_{0.7}Ti_{0.3}O_3$ [14] and $BaTiO_3$ [15-17] have been obtained using such a method.

In this experiment, we like to use a polymer-based process which differs in important details from previous methods to prepare MMO powders of controlled composition. The method is actually based on sequential adding two or more kinds of different metal ions with defined ratio for the preparation of a defined polymer-metal salt complex. The polymer precursor is water soluble and can be purified by repeated precipitation/redissolution cycles. The sequential adding of ions prevents the preferential absorption of specific ions by the polymer. The metal ion density which refers to the ratio between the ionogenic sites fixed to the polymer backbone and the number of metal ions per chain can be changed by dilution with non-metallic counterions. The purified complex in dry form is calcined at relatively low temperature to give nanosized crystals of the MMO provided that sintering can be avoided. The composition of the precursor polymer defines the stoichiometry of the MMO in cases in which phase segregation into MMOs of different structure and composition does not occur during calcination.

We illustrate our strategy using the case of zinc-magnesium oxide ($Zn_{1-x}Mg_xO$) as an example as shown in Scheme 4.1. Zinc polyacrylate is first prepared by mixing polyacrylic acid (containing w carboxylic groups) and zinc nitrate (containing m_0 zinc ions) in neutral or basic aqueous solution followed by precipitation into acetone, as already specified in Ch. 2. Suppose in the ZnPA precursor, $2m$ carboxylate groups are occupied by Zn^{2+} and the rest $(w-2m)$ carboxylic acid groups are completely or partially neutralized by NH_4^+. Then the ZnPA powder is redissolved in water; the desired amount of magnesium nitrate (containing n_0 magnesium ions) is added. The n Mg^{2+} ions attack the carboxylate group to replace $2n$ ammonium groups because it is much more difficult to replace Zn^{2+} ions considering the electrostatic interaction of cation with carboxylate group . Here, $2(m+n)/w$ is defined as metal ion density. And we can assume m/n is almost equal to m_0/n_0, which means the ratio between the two metal ions in the final zinc-magnesium polyacrylate (ZnMgPA) complex could be pre-defined by the amount in the feed. This point has been proved in our experiments.

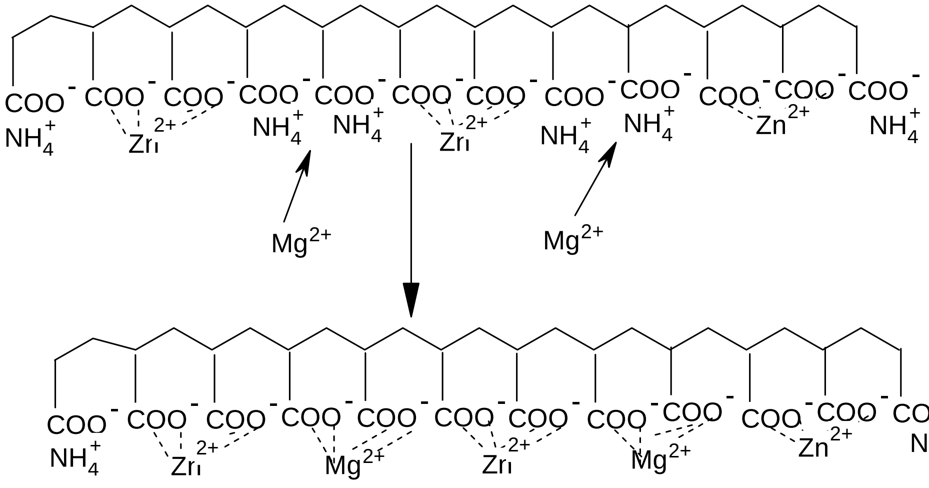

Scheme 4.1

Formation of zinc-magnesium polyacrylate polymer precursor. (The stereochemistry is completely neglected in the scheme. Coordination number of Zn^{2+} *and* Mg^{2+} *is 4. Here the cations are considered as bidentate with carboxylate for simplicity.)*

The method described here is believed to be applicable to a wide range of MMO preparation with very precise stoichiometry. In this chapter, we synthesized two ZnO-based nanometer-sized MMO particles ($Zn_{1-x}Mg_xO$ and $Zn_{1-x}Co_xO$) in a particular range of composition employing this polymer-based method. The precursor is formed by sequential loading zinc and magnesium or cobalt cations and is purified via established methods of polymer chemistry. The calcination of polymer precursor at relatively low temperature gives metastable alloys of the oxide systems. The MMO particles of typically 20-50 nm in diameter are single crystals. The optical and magnetic properties of the materials are discussed too.

4.2 Synthesis of $Zn_{1-x}Mg_xO$ nanoparticles

4.2.1 Preparation of zinc-magnesium polyacrylate precursor

The zinc-magnesium polyacrylate complex is obtained by precipitation of the reaction mixture from acetone. The precipitation serves to purify the precursor by removing the ionic impurities and other undesired species in the reaction mixture. The precursor polymer is completely water soluble. As seen in Fig. 4.1a, the reaction mixture of zinc polyacrylate and magnesium nitrate shows absorption at 300 nm due to nitrate group, which disappears in the redissolved ZnMgPA aqueous solution. This means the ZnMgPA is purified in the precipitation process. The redissolved precursor polymer aqueous solution shows typical polyelectrolyte behaviour similar to zinc polyacrylate.[18-19] The reduced viscosity at very low concentration is very large, but decreases considerably with the concentration increase as shown in Fig. 4.1b.

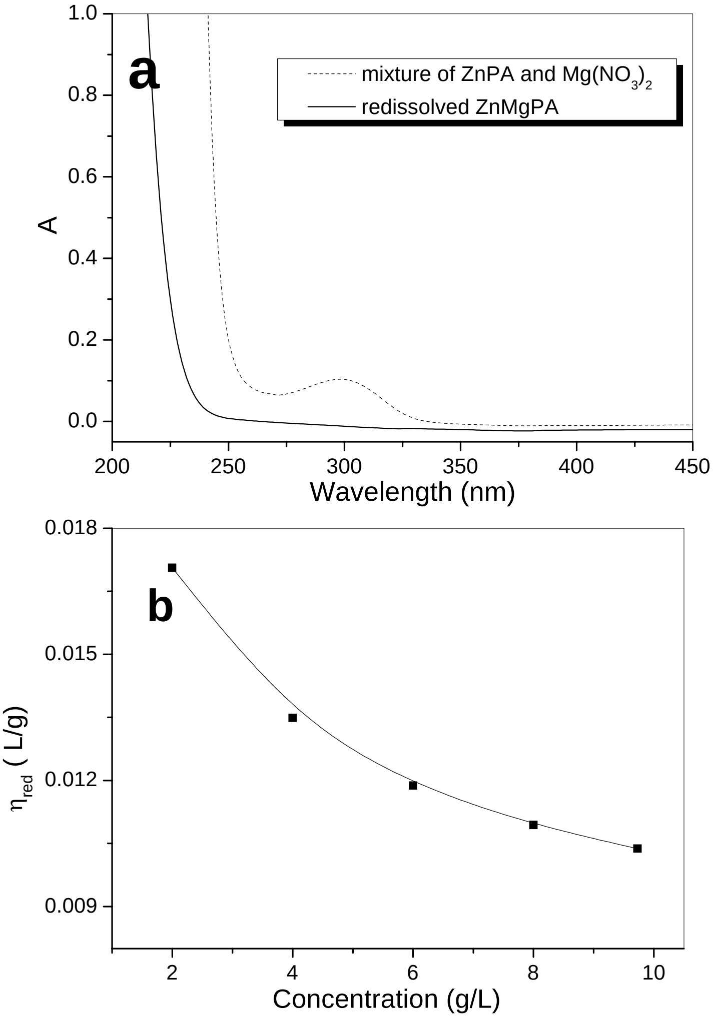

Fig. 4.1. *a) UV spectra of reaction mixture of ZnPA and* $Mg(NO_3)_2$ *and redissolved ZnMgPA aqueous solution. b) Reduced viscosity* (η_{red}) *as a function of redissolved ZnMgPA precursor polymer concentration. The molecular weight of the polymer is 5,000.*

After drying in vacuo, the precursor powder is converted into $Zn_{1-x}Mg_xO$ by calcination in a high-temperature oven under air flow. A typical heating program is preset with a heating rate of 5 °C /min from room temperature to 550 °C and then keeping it at that temperature for 1 hour. The resulting colorless powder is composed of nanosized crystals and it has a composition (i.e. x = [Mg]/ ([Mg]+[Zn])) predefined by the magnesium content to the overall metal content ratio in the polymer precursor as shown in Fig. 4.2. The magnesium content in the polymer precursor reflects this ratio in the feed as well. Here a slight depletion of magnesium in the range of $x = 0.2–0.6$ takes place in the mixed metal oxides samples.

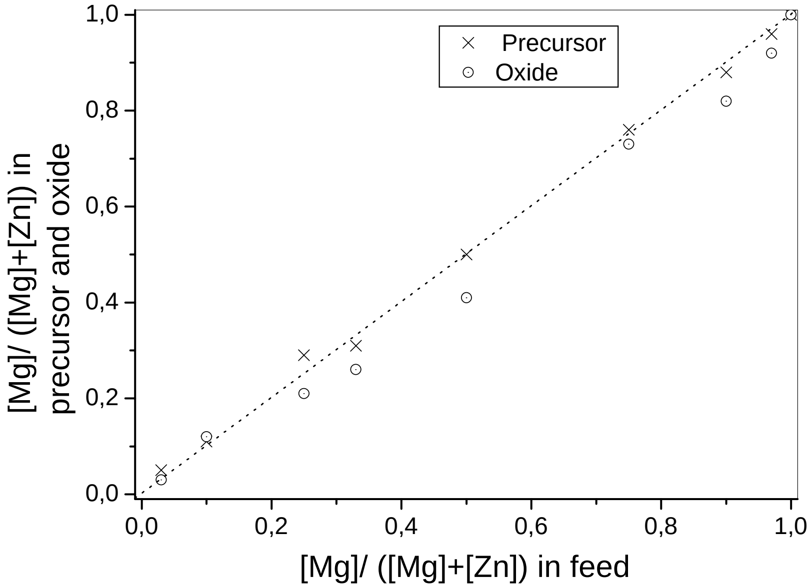

Fig. 4.2. The ratio of Mg content to whole metal content in feed versus that determined in the polymer precursor (cross) and mixed-metal oxide (circle) by means of AAS.

TEM images of a typical zinc magnesium polyacrylate precursor sample are presented in Fig. 4.3. The TEM sample is prepared by dispersing a drop of the dilute precursor solution on a carbon-film covered copper grid. The darker area in the image is formed by the ZnMgPA polymer. The contrast is ascribed to the thickness. From the HAADF image (Fig. 4.3b), very small particles in the size of 2-3 nm in diameter are observed, which is also seen in ZnPA samples possibly due to the aggregation of polymer chain. An energy dispersive X-ray spectroscopy (EDX) line scan was performed to detect the distribution of magnesium and zinc across the sample. The results show similar profiles for the two elements, indicating homogeneous distribution of the both metal ions in the polymer matrix. In other word, no composition aggregation takes place at the atomic scale, which is one prerequisite for production of a solid solution of the oxide system. Like the analogous zinc polyacrylate powder, the zinc-magnesium polyacrylate complex is amorphous as examined by X-ray powder diffraction (Fig. 4.3c).

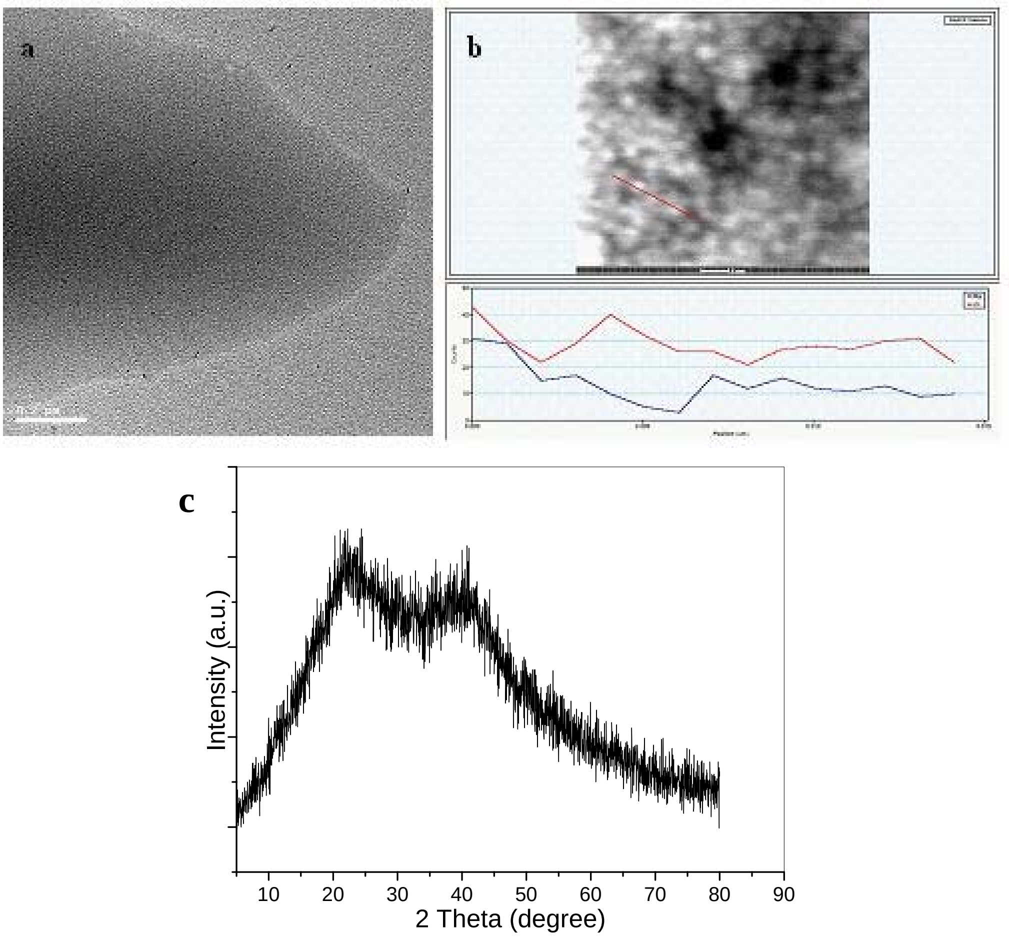

Fig. 4.3. *a) TEM showing the morphology of ZnMgPA with Mn 5000; b) EDX results of Zn and Mg in the sample; c) XRD pattern of a zinc-magnesium polyacrylate powder.*

4.2.2 Characterization of $Zn_{1-x}Mg_xO$ nanoparticles

4.2.2.1 Introduction of lattice parameters of wurtzite zinc oxide

The thermodynamically stable crystallographic phase of zinc oxide is zincite which occurs in nature as mineral. ZnO crystallites in the wurtzite structure can be described as a hexagonal close packed (HCP) lattice of oxygen atoms and zinc atoms. The space group is $P6_3mc$ with zinc atoms residing in tetrahedral interstices. The hexagonal unit cell contains two formula units. The lattice parameters *c* and *a* of wurtzite ZnO as shown in scheme 4.2 are derived from X-ray diffraction patterns. The distance *d* between equivalent lattice planes is related to the angle at which a X-ray reflection is observed as described by the Bragg equation as:

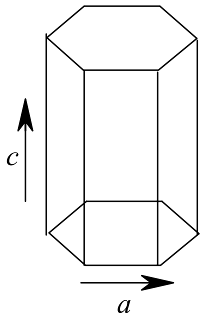

Scheme 4.2

$$n\lambda = 2d \sin\theta \qquad (4.1)$$

Here, λ is the wavelength of the X-rays with the value of 1.5406 Å for Cu Kα radiation and θ is the diffraction angle. In the hexagonal system, the interplanar distance of lattice planes d_{hkl} may be calculated by:

$$d_{hkl} = [(\tfrac{4}{3a^2})(h^2 + hk + k^2) + (l^2 / c^2)]^{-\frac{1}{2}} \tag{4.2}$$

Introducing 1, 0, 0 and 0, 0, 2 to substitute h, k, l in the formula gives the expression of lattice parameter a and c:

$$a = \tfrac{2d_{100}}{\sqrt{3}} \tag{4.3}$$

$$c = 2d_{002} \tag{4.4}$$

The cell parameters obtained here normally are only an approximation due to the existence of systematic deviation. These systematic errors have a definite dependence upon θ, which can be demonstrated by differentiating the Bragg equation with respect to θ:

$$n\lambda = 2d\sin\theta$$

$$0 = 2\frac{\Delta d}{\Delta\theta}\sin\theta + 2d\cos\theta\,,$$

$$\frac{\Delta d}{d} = -\frac{\cos\theta}{\sin\theta}\Delta\theta = -\cot\theta\Delta\theta \tag{4.5}$$

Thus, increasing the angle θ results in an increase in precision of determination of the interplanar spacing d, so that it affects the accuracy by which lattice parameters can be measured.

Table 4.1. *Previous results of wurtzite ZnO lattice parameters.*[20]

a (Å)	c (Å)	c/a	Ref.
3.2496	5.2042	1.6018	21
3.2501	5.2071	1.6021	22
3.286	5.241	1.595	23
3.2498	5.2066	1.6021	24
3.2475	5.2075	1.6035	25
3.2497	5.206	1.602	26
3.2524	5.2108	1.6021	this work*

** data obtained by refinement of the XRD pattern with CELREF*[27]

Some previously reported lattice parameters of wurtzite ZnO determined at room temperature by various experimental measurements and theoretical calculations are listed in Table 4.1.[20] All these values are in good agreement. The lattice constants mostly range from 3.2475 to 3.2501 Å for the a parameter and from 5.2042 to 5.2075 Å for the c parameter. The c/a ratio vary in a slightly wider range, from 1.593 to 1.6035.

The lattice parameters of ZnO may be affected by the following factors including: (1) free-charge concentration, which is main factor of lattice expansion and is proportional to the deformation potential of the conduction-band minimum; (2) crystal defects and ionic radii difference of foreign atoms with respect to the substituted matrix ion; (3) external strains and (4) temperature. With higher temperature, the lattice expands.

The point defects such as zinc antisites, oxygen vacancies, and extended defects, such as threading dislocations, increase the lattice constant. These might be the reasons of a slight expansion of our lattice, which is also seen in our photoluminescence and electron microscopy results.

4.2.2.2 TGA investigation of ZnMgO formation

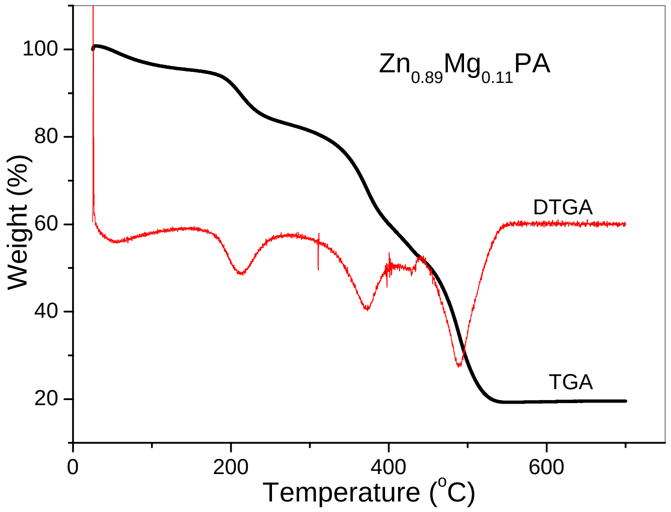

Fig. 4.4. *TGA and DTGA results of* $Zn_{0.89}Mg_{0.11}PA$ *precursor sample.*

TGA of the pyrolysis of a typical zinc-magnesium polyacrylate precursor with magnesium fraction of 0.11 is shown in Fig. 4.4. The profile is very similar to that of zinc polyacrylate and DTGA result shows that the pyrolysis consists of three steps as was also detected for a ZnPA sample. The sample converts to zinc-magnesium oxide with a zinc fraction of 0.88, showing good agreement with the composition of the precursor.

In our experiments, for zinc-rich samples, magnesium is loaded to zinc polyacrylate by replacement of the ammonium ions, which means in all precursor polymers with different composition, the content of zinc in the polymer precursor is constant. Therefore, the increase of magnesium content in the polymer results in higher yield of the final products, which is demonstrated by the TGA in Fig.4.5. The results show also the shift of TGA curves to higher temperature, corresponding to the peaks in DTGA with the increase of magnesium content.

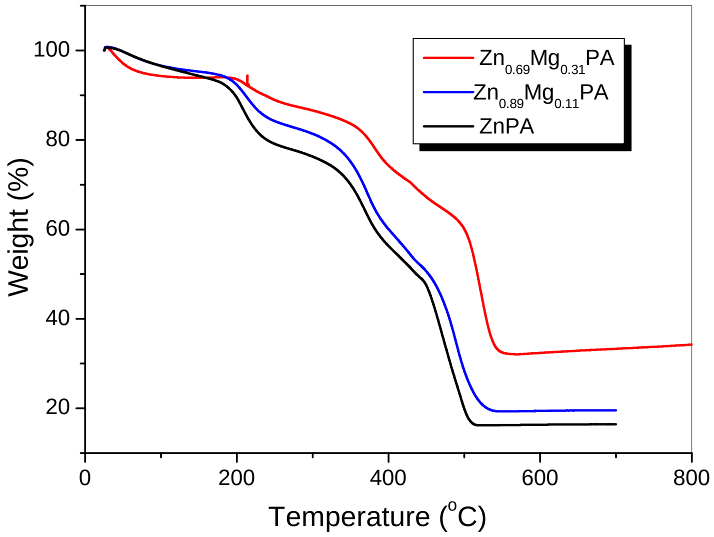

Fig. 4.5. *TGA data of zinc-magnesium polyacrylate samples with different composition.*

4.2.2.3 Characterization of zinc-magnesium oxides

Fig. 4.6 shows the X-ray diffraction patterns of the microcrystalline products over the whole composition range. The patterns of the pure ZnO are indexed according to the known hexagonal phase (zincite) and that of MgO is indexed according to its cubic phase (periclase). Clear indications for segregation into a hexagonal and a cubic phase are found for samples having magnesium content between $0.26 \leq x \leq 0.73$. Samples of $x = 0.21$ and 0.26 showed a very weak (200) reflection of the MgO phase indicating that the majority of the material was in the form of zincite and at a composition of $Zn_{0.88}Mg_{0.12}O$ the hexagonal phase is the only one seen. The appearance of reflections in the powder patterns belonging to two different phases indicate that particles which differ in phase structure and elemental composition have been formed in a particular range of overall composition at the temperature and time interval of the calcination. More importantly, in the diffraction pattern of hexagonal phase, the peaks (002) and (100) position shift is observed, indicating the variation of lattice constant. The (002) shows an obvious shift to larger angle with increase of Mg content, reflecting the *c*-axis shrinkage due to the magnesium incorporation into the hexagonal lattice. The lattice parameters are calculated from the position of the reflections. The results are refined with least-square method using software CELREF[27] to decrease the systematic error.

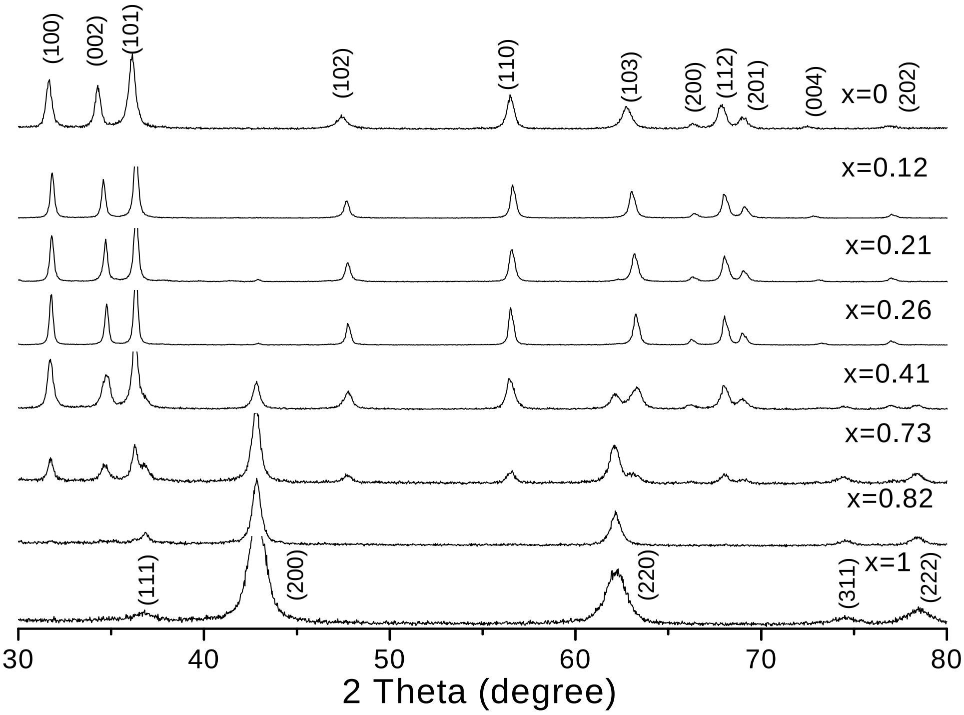

Fig. 4.6. *X-ray diffraction patterns of* $Zn_{1-x}Mg_xO$ *(*$0\leq x \leq 1$*), note that at* $x = 0.21$ *the (200) peak of cubic phase begins to appear.*

Fig. 4.7 shows the dependence of the lattice parameters of the hexagonal phase depending on the overall magnesium content. While the unit cell clearly shrinks along *c* from the value of the pure hexagonal ZnO phase with increasing magnesium content, this is not true for the *a*-axis parameter. These results are roughly in agreement with the data obtained from epitaxially films grown on sapphire by a laser deposition method[28] although in detail there are significant differences. In particular, the onset of MgO segregation from the zincite phase occurs already at smaller values in our samples and the dependence of the *c*-parameter is much stronger. These differences may be a consequence of the different preparation methods and the adhesion to the substrate in the laser deposited films. We also like to mention the work of F.K. Shan et al.[29] who report a linear decrease of the lattice constants with increasing magnesium content between $0\leq x \leq 0.05$ with the same trend seen by us. These authors used laser deposition as well but on glass as the substrate. Their value quoted at $x = 0.05$ is within the error margin of our findings. However, we do not see a similar change in the *a*-axis parameter. To this point our result is in agreement with that of Ohtomo et al. The shrinkage of *c*-axis is due to the smaller radius of the magnesium ion (0.57 Å) in comparison to that of zinc ion (0.60 Å).

Another point needs to be noted here is that the hexagonal phase can accommodate up to 12 mol% MgO while the cubic phase can maintain 18 mol% ZnO in the lattice. In the cubic MgO phase, no peak shift with Zn concentration is found within the limits of experimental error.

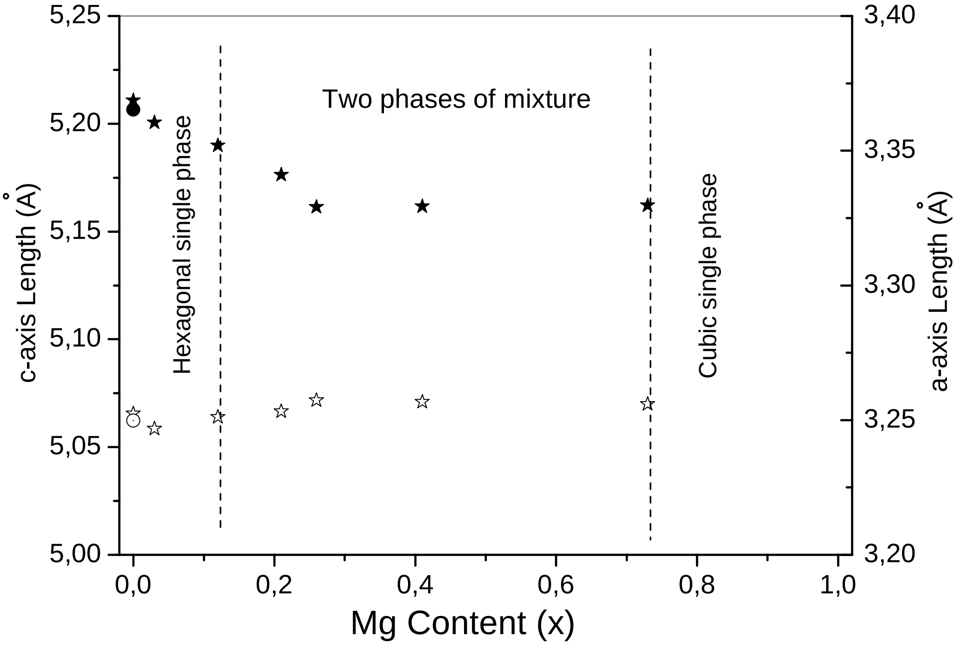

Fig. 4.7. *Cell parameter c (filled star) and a (open star) as a function of the Mg content x. The data were refined by CELREF.*[27] *Filled and open circles indicate the standard values of ZnO cell parameters.*[30] *The two dashed lines mark the phase boundary.*

The data reported in Fig. 4.8 give evidence that our samples consist indeed of nanometer-sized crystals of homogeneous composition. Fig. 4.8a shows a TEM image of a large number of crystals having the overall composition $Zn_{0.88}Mg_{0.12}O$. The particles which appear darker than the others are due to the diffraction contrast. The inset shows the electron diffraction pattern of one particle out of the collection, which is consistent with the pattern of ZnO. Fig. 4.8b presents an HRTEM image of a single particle of this sample showing (100) and (012) lattice fringes and crystalline order on the length scale of the size of the crystals. The interplanar distances are 0.28 and 0.19 nm, respectively by direct measuring on the image.

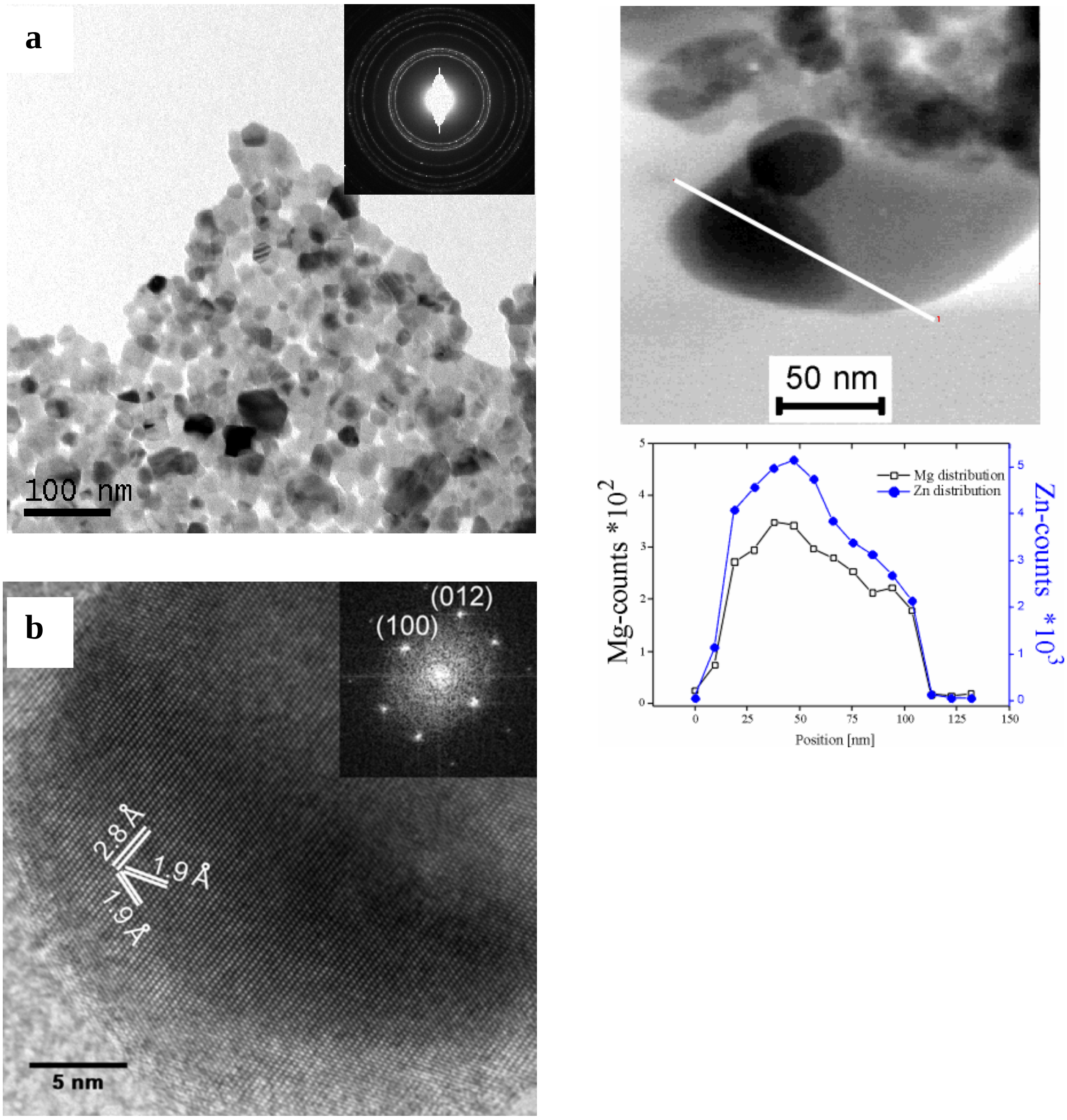

Fig. 4.8. *a) TEM image showing the morphology of* $Zn_{0.88}Mg_{0.12}O$ *nanoparticle. The inset is the electron diffraction pattern. The ring patterns indicated that the nanocrystllites are three-dimensionally randomly oriented. b) HRTEM image of the same sample. The inset is the corresponding fast Fourier transform (FFT) of the image c) EDX results of Zn and Mg with a line scan as denoted by the line.*

Actually, crystal defects like dislocations and stacking faults are also found in some other TEM images. Fig. 4.9 gives an image showing stacking fault in the crystal. An energy dispersive X-ray spectroscopy (EDX) line scan was employed for analyzing the elementary composition of an individual particle (Fig.4.8c). The similarity of the profile of Mg and Zn composition proves that the both elements are homogeneously distributed over the whole particle. In other words, magnesium ions are able to occupy places of zinc ions in the zincite lattice forming a solid solution.

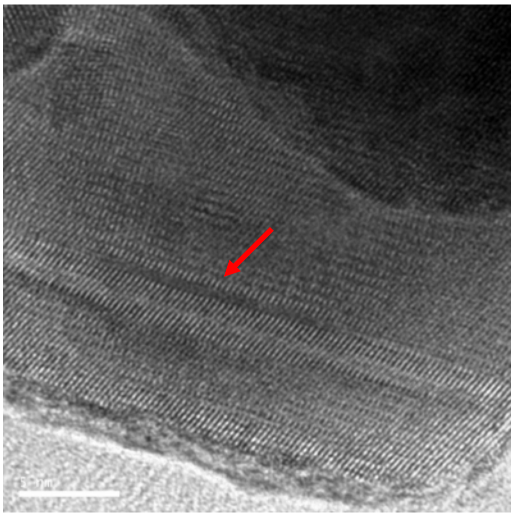

Fig. 4.9. *Stacking fault in a* $Zn_{0.88}Mg_{0.12}O$ *nanoparticle as indicated by the arrow shown in the HRTEM images. The scale bar in the image is 5 nm.*

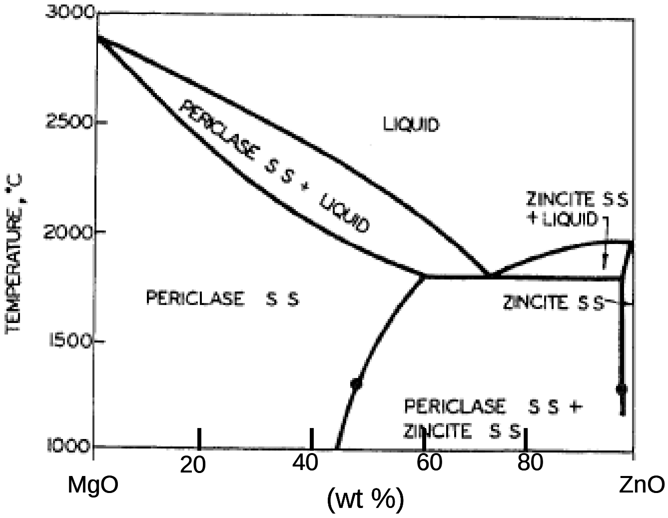

Fig. 4.10. Phase diagram of MgO-ZnO system.[31]

It is remarkable that the phase diagram of the system ZnO/MgO predicts the formation of a solid solution of both components near the ZnO boundary. Segnit et al.[31] determined the phase diagram of the system of ZnO and MgO by measuring the refractive index (Fig. 4.10). Their results show that the amount of ZnO in solid solution in the periclase structure is as much as 56 wt%, while hexagonal ZnO lattice can only accommodate 2 wt% (corresponding to a molar fraction of 0.04) of Mg^{2+} at equilibrium conditions (1600 °C). In our case, the phase formation occurs far from equilibrium and from an amorphous precursor at 550°C. Hence, the as-synthesized nanometer-sized crystals are metastable. In fact, annealing of the solid solution type crystals in the zincite phase at a temperature of 800 °C for two hours shows the beginning of the periclase phase segregation from the zincite phase (Fig. 4.11). The intensity of XRD peak for MgO (200) is about 0.6% of that of ZnO (002).

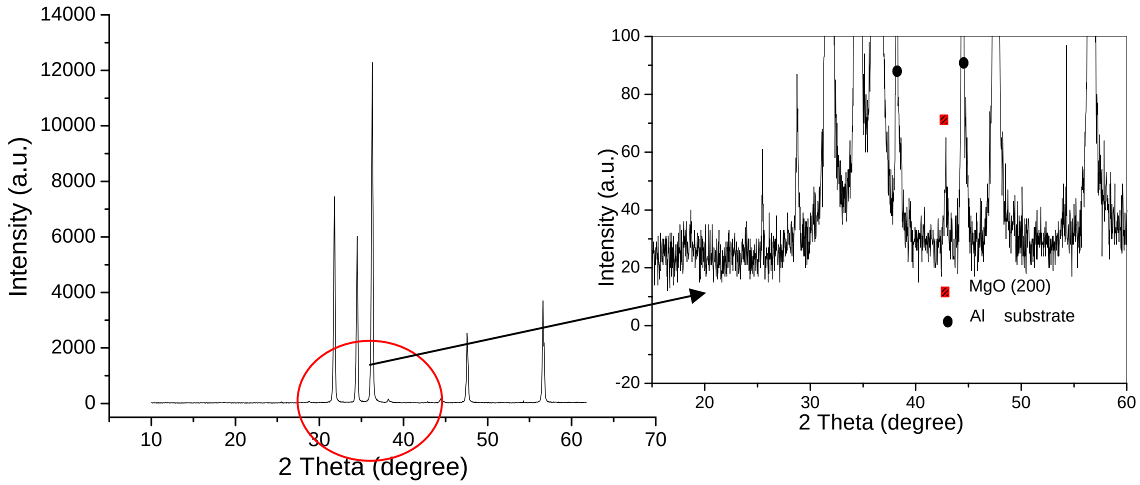

Fig. 4.11. *XRD patterns of* $Zn_{0.88}Mg_{0.12}O$ *nanoparticles annealed for 2 h at 800* ^{o}*C.*

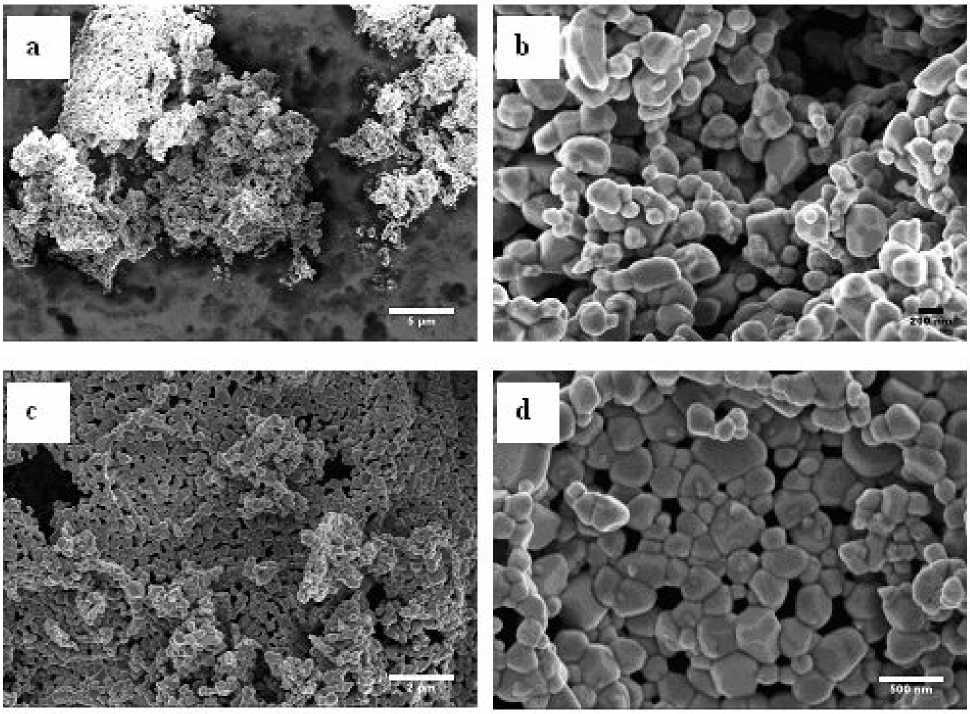

Fig. 4.12. *SEM images of* $Zn_{0.88}Mg_{0.12}O$ *nanoparticles annealed for 2 h at 800* ^{o}*C.*

The $Zn_{0.88}Mg_{0.12}O$ nanoparticles after thermal annealing for 2 hours at 800 ^{o}C exhibit much stronger X-ray scattering as seen in the XRD patterns. The morphology is shown in Fig. 4.12. The particles with diameter around 200 nm and a large size distribution are seen. And part of the nanoparticles is sintered due to high temperature annealing. (Fig. 4.12 c,d).

Scanning electron microscopy (SEM) images show the morphology of some representative samples of the $Zn_{1-x}Mg_xO$ with x 0.82, 0.41, 0.12 and 0.04 respectively (Fig. 4.13). For sample $Zn_{0.18}Mg_{0.82}O$ (Fig. 4.13a), the case of a pure cubic crystal as revealed from XRD pattern, particulate structure is hardly observable. With decreasing of Mg content (Fig. 4.13b, c), particles with size of 10-20 nm are seen with clear particle formation, possibly owing to pinning of the grain boundary.[5] In the pure hexagonal phase (Fig. 4.13d), the crystals are mainly spherical particles with a diameter less than 40 nm.

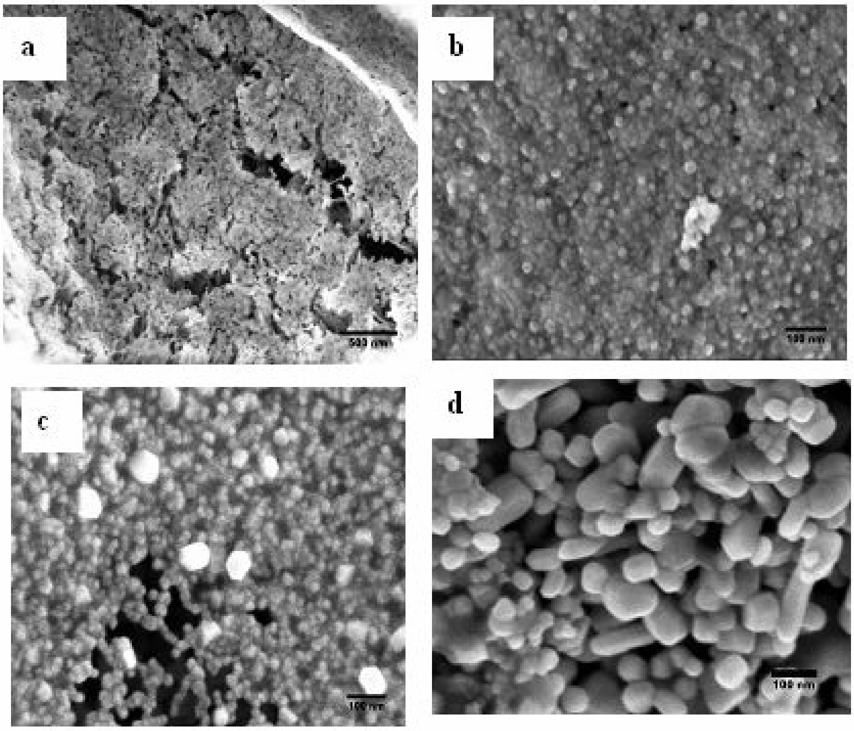

Fig. 4.13. *Scanning electron microscopy images show the morphology of* $Zn_{1-x}Mg_xO$ *samples: a)* $x = 0.82$*; b) 0.41; c) 0.26; d) 0.04. All the samples are prepared at* 550^oC*.*

The existence of magnesium in the metal oxide alloys has significant consequence on the electron paramagnetic property of the materials as seen in Fig. 4.14. In pure ZnO (Ch. 2.3), two EPR signals at $g = 1.9618$ and $g = 2.0044$ are observed and labelled as I and II. Signal I is attributed to shallow donor centres (SDC) irrespective to its identity and signal II is due to the free electrons in the organic residue generated in the cause of pyrolysis. In all the four samples presented here, signal II is strong and the intensity is much larger than the signal I. For the case of signal I, it is evident in the sample of $Zn_{0.98}Mg_{0.02}O$ and decreases in intensity in sample of $x = 0.12$. Thus, the increase of Mg content in the hexagonal phase may suppress the EPR signal of SDC. For samples of $x = 0.21$ and 0.26, where cubic phase begins to segregate from the zincite crystals, the signal I is completely quenched.

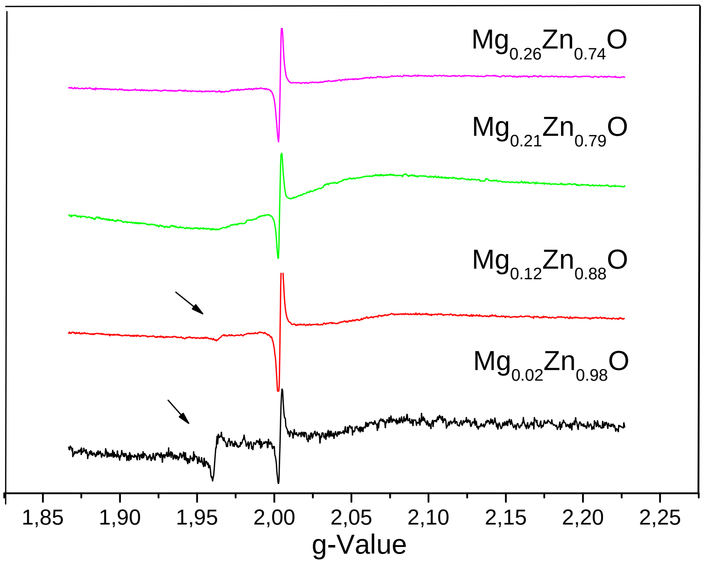

Fig. 4.14. *EPR spectra of zinc magnesium oxides with different composition.*

4.2.2.4. Photoluminescence properties of $Zn_xMg_{1-x}O$ nanoparticles

ZnO is a wide band gap semiconductor (Eg = 3.34 eV) while MgO has a band gap as large as 7.5 eV.[32] Incorporating Mg atoms in ZnO lattice sites will increase the band gap of ZnO. This is called band gap engineering and it will change the electrical and optical properties of the material.[33] For a ternary semiconductor system of $A_xZn_{1-x}O$ where A is the doping ions for instance Mg or Cd, its band gap has a relation with the composition x as:

$$E_g(x) = (1-x)E_{ZnO} + xE_{AO} - bx(a-x) \qquad (4.6)$$

where b is the bowing parameter and E_{AO} and E_{ZnO} are the bandgap energies of compounds AO and ZnO, respectively. The bowing parameter b depends on the difference in electronegativities of the end binaries ZnO and AO.[20, 34]

Many publications deal with the optical properties of ZnMgO, however, mostly for samples obtained in form of thin film on solid substrate such as quartz, sapphire etc.[35] The spectral data and particularly data on photoluminescence reported in the literatures differ considerably and demonstrate that the preparation method of the films or powders has a strong impact on the optics of the material.

ZnO exhibits relatively intense photoluminescence. Generally two peaks are seen in the emission spectrum of pure ZnO. One of these is relatively weak and centred around 3.24 eV, which is associated with the near band edge (NBE) emission. The other one occurs in the visible region of the spectrum. It is frequently recorded with maximum centred around 2.12 eV, intensity and precise position depending on preparation conditions, purity and thermal history of the sample. In our case, doping of magnesium into the ZnO phase has a strong quenching effect on the high energy NBE emission while emission in the visible is enhanced.

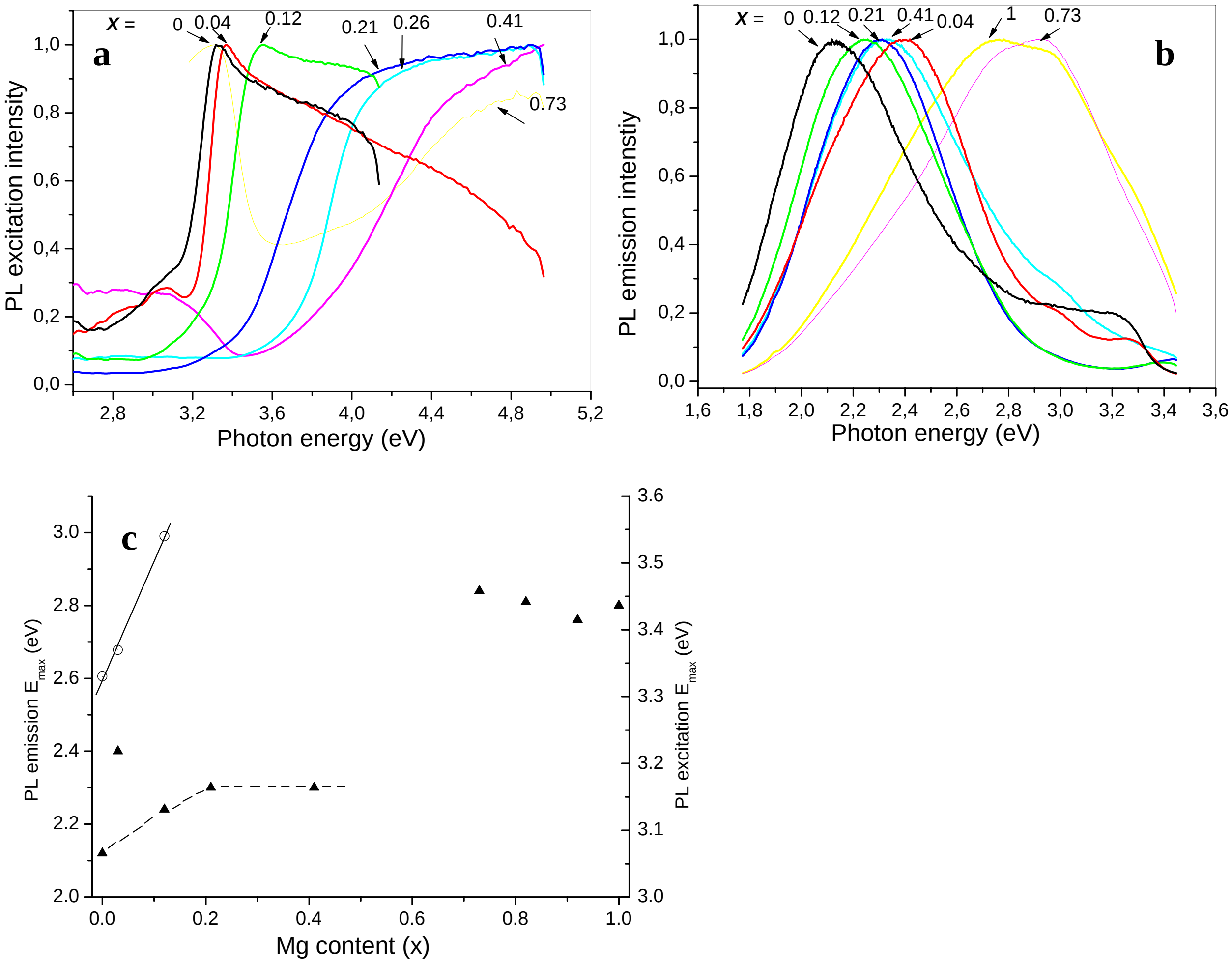

Fig. 4.15. *(a) PL excitation spectra of samples of* $Zn_{1-x}Mg_xO$ *with different x. (b) PL emission spectra of* $Zn_{1-x}Mg_xO$ *samples excited at 325 nm. (c) The maxima of PL emission (triangle) and excitation (circle)* E_{max} *depending on x; the broken line through the data points of PL emission is a guide to the eye.*

Fig.4.15a shows the PL excitation spectra of the emission in the visible for our powder samples of $Zn_{1-x}Mg_xO$ for various values of x. Fig.4.15b shows the corresponding PL emission spectra. The PL excitation spectra were recorded measuring the intensity of the PL emission at the respective maximum for each composition. The excitation spectrum monitors the density of states near the band edge and allows to retrieve the band gap energy from the adsorption edge. The strong dependence of the absorption edge on Mg concentration is evident. This effect had been seen previously and has been discussed in detail for epitaxially grown thin films.[21,22] Our materials behave similar although they are nanosized powders and not monodomain epitaxially grown films.

Another point worth noting is the significant decrease of slope with increasing Mg concentration in the PL excitation spectra near the band edge. This effect is known as alloy broadening, but the excitonic character of the absorption peak remains. The emission in the visible shifts from pure ZnO with maximum at 2.12 eV to 2.32 eV at $x = 0.21$ (when the segregation into MgO and ZnO phase occurs); it then jumps to about 2.8 eV in the MgO phase alloy. The band gap and associated excitation spectral characteristics change nearly linearly with increasing content of Mg in the zinc-rich part of the phase composition as indicated in Fig.4.15c. Contrary to this, the energy of the PL emission and its shape seem to saturate near a composition of $x = 0.2$. We like to interpret this phenomenon by the assumption that the PL emission comes from localized defect centers which are relatively weakly affected by the change in the band structure of the material, which in turn responds strongly to the substitutional replacement of zinc by magnesium. A so far inexplicable phenomenon just for one sample of composition $Zn_{0.96}Mg_{0.04}O$ is observed. This sample showed the maximum of PL emission at 2.4 eV, which is much blue-shifted from what could be expected from the data of the other compositions. At present we must leave it to further experimentation to clarify the origin of this behavior. We also like to note the observation that the NBE emission is quenched on alloying while the emission in the visible is enhanced, which indicates that the number of the defect sites associated with the emission is strongly enhanced.

Fig. 4.16 compares the PL emission and excitation for the sample of $Zn_{0.88}Mg_{0.12}O$ after the production for 1 month and 5 month. We can see the stability of photoluminescence of our sample. After 5 month storage of the sample, the PL properties with the shape and peak position of spectra remain unchanged. The increase of 30% in intensity of the spectra is considered as the measurement deviation here. The stability of the PL properties of our Mg doped-ZnO sample brings considerable advantages in the possible application as nanocrystal emitters.

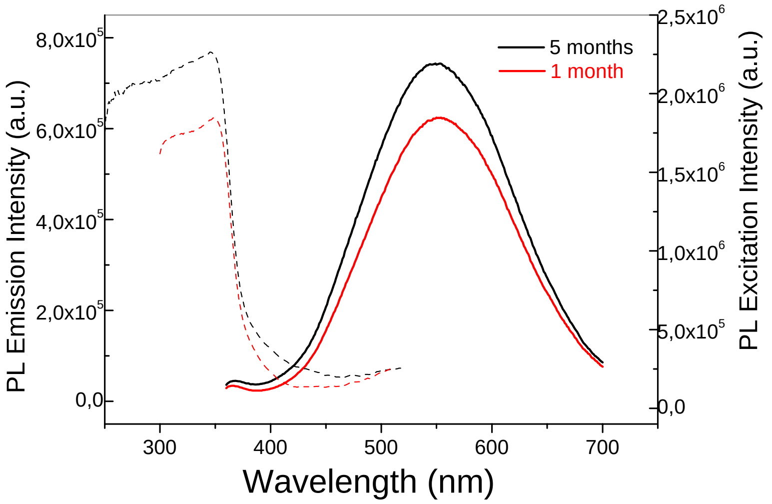

Fig. 4.16. *Comparison of photoluminescence of* $Zn_{0.88}Mg_{0.12}O$ *after production for 1 month and 5 months. The sample is stored in depletion of oxygen. The broken lines are the PL excitation spectra and solid lines are PL emission spectra.*

In summary, we found that the calcination of a polymer-metal salt complex, which can be purified and processed following established methods of polymer chemistry, is useful to prepare nanosized crystals of a typical MMO. The preparation of $Zn_{1-x}Mg_xO$ by controlled pyrolysis of a zinc-magnesium polyacrylate complex is used as an example. The particles of typically 20-50 nm diameter are single crystals and are metastable alloys of the ZnO / MgO systems in a particular range of composition. The incorporation of Mg into ZnO lattice causes shrinkage of lattice parameter of ***c***, but it has less effect on ***a***. Effects of band gap engineering on the optical band gap are seen and are in general agreement with expectation. The photoluminescence in the visible is enhanced while the high energy emission in the UV region is suppressed by incorporation magnesium on zinc lattice sites. This points toward the usefulness of our approach to create photo emissive materials with enhanced sensitivity. However, significant differences in the emission profiles are seen in our materials compared to the reported data from literature, indicating the impact of processing conditions on the electronic properties.

4.3 Synthesize of $Zn_{1-x}Co_xO$ nanoparticles

4.3.1 Introduction

4.3.1.1 Fundamentals of magnetism

Definitions: Magnetism is a result of moving charges. At the atomic scale, the electron motions consist of orbital motion and spin motion, which are the origins of the macroscopic magnetic phenomena in materials. H is normally used to represent the magnetic field strength and specifically, it is denoted for fields that result solely from free currents, for instance, a magnetic field generated from an electric current flowing in a wire. M stands for the magnetic moment per unit volume of a magnetic material, which is the consequence of the two motions of electrons. M is considered as equivalent or effective current. The magnetic induction B describes the general case of magnetic field due to both the free and equivalent currents. This relation could be expressed as:

$$B = H + 4\pi M \tag{4.7}$$

Currently, there are three systems of units: cgs, SI (Sommerfeld) and SI (Kennelly) in widespread use. Each has their own merits and disadvantages. The dimensions of H, M, B are oersted (Oe), emu·cm^{-3} and gauss (G), respectively.

Susceptibility κ is defined to measure how effective an applied field may induce a magnetic field in a material, expressed as:

$$\kappa = M / H \tag{4.8}$$

Another important quantity is permeability defined by

$$\mu = B / H \tag{4.9}$$

From expressions above, it is easy to derive that

$$\mu = 1 + 4\pi\kappa \tag{4.10}$$

And it can be seen κ has a unit of emu·cm^{-3}·Oe^{-1}.

Magnetic materials are classified into three major categories by the nature of the interaction with a magnetic field of the material.

I. *Ferromagnetism*: a strong attraction toward a magnetic pole. For example, iron, cobalt, nickel, etc.

II. *Paramagnetism*: a weakly attraction toward a magnetic pole. For example, oxygen, iron sulphate, titanium, etc. Typical value of κ is in the range of 10^{-3} to 10^{-5}.

III. *Diamagnetic*: a weakly repulsion from a magnetic pole. The vast majority of substances belong to this category, for example, water, sodium chloride, calcium carbonate, etc. $\kappa < 0$, with typical value from 10^{-5} to 10^{-6}.

Origin of Paramagnetism: Paramagnetism occurs when the atomic, ionic, or molecular constituents have a nonzero magnetic moment. The source of atomic scale magnetic moments is unbalanced angular momentum of electrons including orbital or spin momentum. Both angular momenta yield a magnetic moment given by

$$\mu = g\mu_B J \tag{4.11}$$

where μ_B is the Bohr magneton (equal to 9.27×10^{-21} emu) and g is the called g factor with typical value of 2.00 for a free electron. And due to only pure spin moment in a free electron and $J = S = 0.5$, the formula (3.11) gives $\mu = \mu_B$. In transition metal atoms or ions with partially filled d-shells, the odd number of electrons gives intrinsic spin moments.
Langevin model presents the relation of temperature and magnetic properties. In an applied field the moment tends to align with the field and energy of interaction for N atoms each with a magnetic moment of μ is

$$U = -\overrightarrow{\mu}\cdot\overrightarrow{H} = -\mu H\cos\theta \tag{4.12}$$

where θ is the angle between $\overrightarrow{\mu}$ and $\overrightarrow{H}$. We need the average of cosθ to calculate the total moment of macroscopic body, i.e.

$$M = N\mu\langle\cos\theta\rangle \tag{4.13}$$

Mathematic treatment gives

$$M = N\mu L(x) \quad \text{(a)}; \qquad L(x) = \coth x - x^{-1} \quad \text{(b)}; \qquad x = \mu H / kT \quad \text{(c)} \tag{4.14}$$

The formula (3.14b) is called Langevin function and x is the dimensionless parameter describing the ratio of magnetic alignment energy to the thermal randomizing energy.
For small x, $L(x) \approx x/3$ (4.15)

Hence gives the magnetization

$$M = \frac{C}{T}H \tag{4.16}$$

here, $C = N\mu^2/3k$, k is the Boltzmann constant, $k = 1.38\times10^{-16}$ erg K^{-1}. This expression is called Curie law. It can be written in another form as $\kappa = C/T$.

Origin of Ferromagnetism: The Curie law describes many materials with paramagnetism property. However, many other materials display a modified behaviour as

$$\kappa = C/(T-\theta) \tag{4.17}$$

which is called Curie-Weiss law. θ is a critical temperature with value either positive or negative. It is seen that a net magnetization ($M \neq 0$) may be achieved even if the applied magnetic field H is zero. This is called a spontaneous magnetization, which is used to describe ferromagnetism. The true physical origin of ferromagnetism is elucidated by Heisenberg, who gave an expression of exchange energy of two neighbouring spin interaction

$$E_{ex} = -2J_{ex}\overrightarrow{S_i} \cdot \overrightarrow{S_j} \qquad (4.18)$$

J_{ex} is called exchange integral. If it is positive, the parallel spins lead to ferromagnetism. If J_{ex} is negative, the antiparallel configuration leads to antiferromagnetism.

4.3.1.2 ZnO-based dilute magnetic semiconductor material

The success in preparation of zinc-magnesium oxide nanoparticles using a polymer precursor motivates us to further apply this method to synthesize other mixed metal oxides. We note the recent vast interests in the field of dilute magnetic semiconductors (DMS), which is promising for the new generation information technology devices based on electron spin transition, named 'spintronics'. The key technique to achieve a spintronic material is the development of materials with high Currie temperature (*Tc*) near room temperature.[20, 37]

ZnO-based materials doped with 3*d*-transition metal ions (*t*M) such as Co^{2+},[38] Fe^{2+}[39] and Mn^{2+}[37c] have been proposed as favourable candidates for room-temperature ferromagnetism upon theoretical calculation. Some researchers have already reported that they have observed high-*Tc* doped-ZnO materials in their experiments. However, reports also suggest the ferromagnetism is sensitive to preparation conditions, which is most possibly due to the uncontrolled formation of lattice defects. The existence of intrinsic high-*Tc* ferromagnetism is questioned because of the fact that in some instances the ferromagnetism originates actually from the phase-segregated metal or binary oxide clusters.[40] Thus, deeper insight to this kind of DMS materials is still necessary.

Previous research mostly works on the *t*M substituted zinc oxide films grown on solid substrates like silicon or quartz glass. Only a few research has been carried out on ZnO bulk samples prepared by direct chemical route.[41] On the other hand, bulk samples rather than films may minimize the surface impurity to remove the exterior effects. In this work, we attempt to prepare cobalt-doped ZnO via pyrolysis of a polymer precursor containing the desired amount of cobalt and zinc ions. The magnetic properties of the resulting metal oxide are investigated towards understanding the relationship between eventually observed ferromagnetism and preparation method.

4.3.2 Preparation of zinc-cobalt polyacrylate precursor and its thermal property

In the light of these considerations, zinc-cobalt oxide was prepared via a polymer precursor in a gram scale production. The synthesis is based on the stepwise loading of metal ions to polyacrylic acid. For a zinc-rich sample, zinc polyacrylate is prepared first. Then desired amount of cobalt(II) nitrate was mixed together with certain amount of ZnPA in water. The reaction mixture had a pH normally over 5, thus adjustment of pH is not necessary in this step. The reaction mixture appears as pink, due to the octahedral coordination of Co(II) ions. The reaction mixtures are poured into acetone to remove undesired salt and other species.

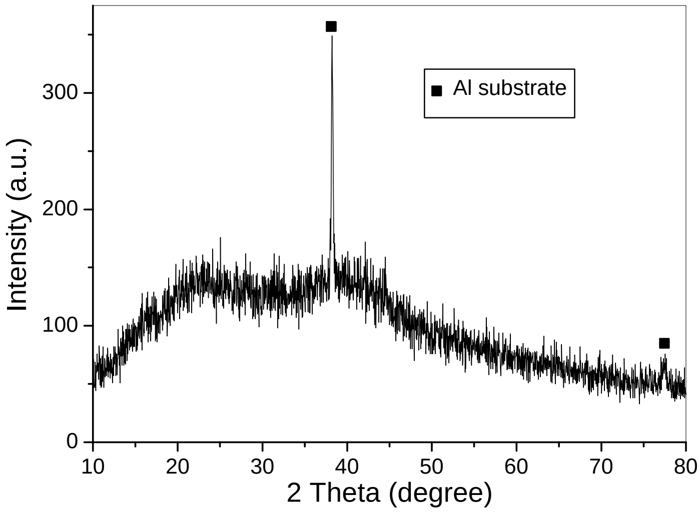

Fig. 4.17. *XRD pattern of zinc-cobalt polyacrylate precursor powder.*

The precipitate was collected and dried in vacuo at 50 °C over night. Deep purple powders were obtained and then subject to heating treatment with preset program. The obtained zinc-cobalt polyacrylate complex polymer powder was calcined in a high temperature oven with a heating ramp of 5 K/min from room temperature to 550 °C and then annealed at this temperature for 1 h. The final product appeared as green powder and with higher amount of cobalt ions, the sample colour of the oxides becomes darker and finally changes to black. For the Co-rich samples ($x > 0.5$), the analogous cobalt polyacrylate (CoPA) complex was first prepared, and then zinc was incorporated as described above. Here, x is again defined as $\frac{[Co]}{[Zn]+[Co]}$ similar as in the case of zinc-magnesium oxide. The X-ray diffraction pattern indicates the amorphous status of the obtained zinc-cobalt polyacrylate (ZnCoPA) precursor (Fig.4.17).

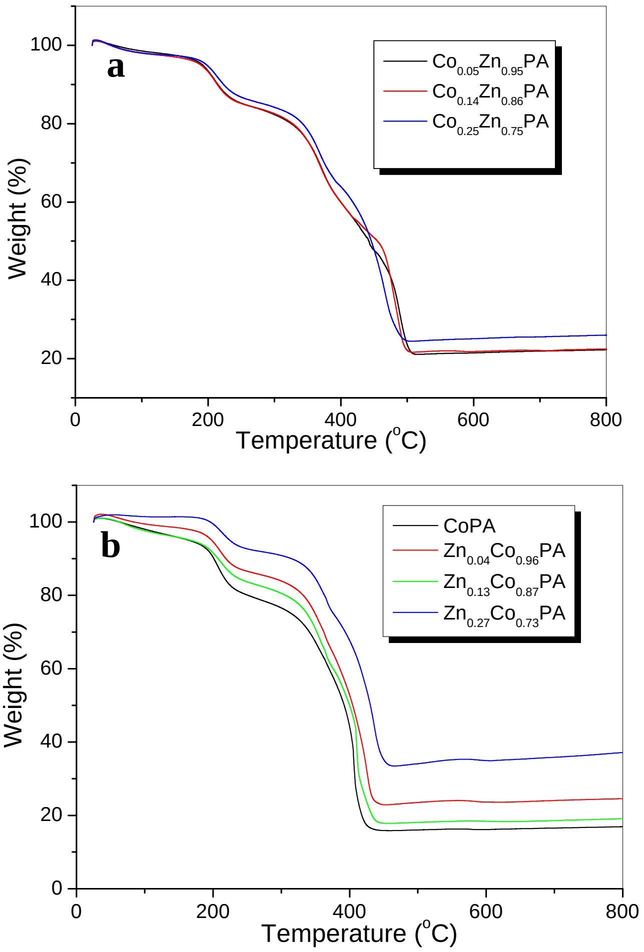

Fig. 4.18. *TGA results of zinc-cobalt polyacrylate of a) zinc-rich and b) cobalt-rich samples. The heating rate is 5 K/min for all the samples.*

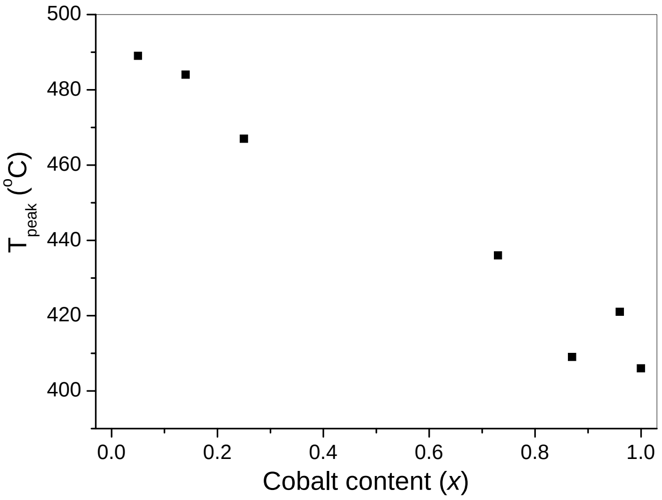

Fig. 4.19. *The peak temperature of the third reaction step in ZnCoPA samples versus cobalt content x.*

The thermal properties of the polymer precursor are investigated by means of thermogravimetric analysis (TGA) as shown in Fig. 4.18. Compared the decomposition process of the Zn-rich and Co-rich samples, it is found that the T_f, referred to the temperature at which the cumulative mass-change first reaches its maximal value corresponding to the completion of reaction, for the former samples are obviously higher. By first-order differential treatment of the TGA results, the obtained DTGA curves show three peaks in all cases, indicating the whole decomposition reaction consists of three steps. The first two peak temperatures (T_{peak}) are centred at 210 ± 3 and 367 ± 5 °C, independent upon the content of cobalt x. However, the value of the third T_{peak} differs, exhibiting a strong dependence on x. The result is plotted in Fig. 4.19.

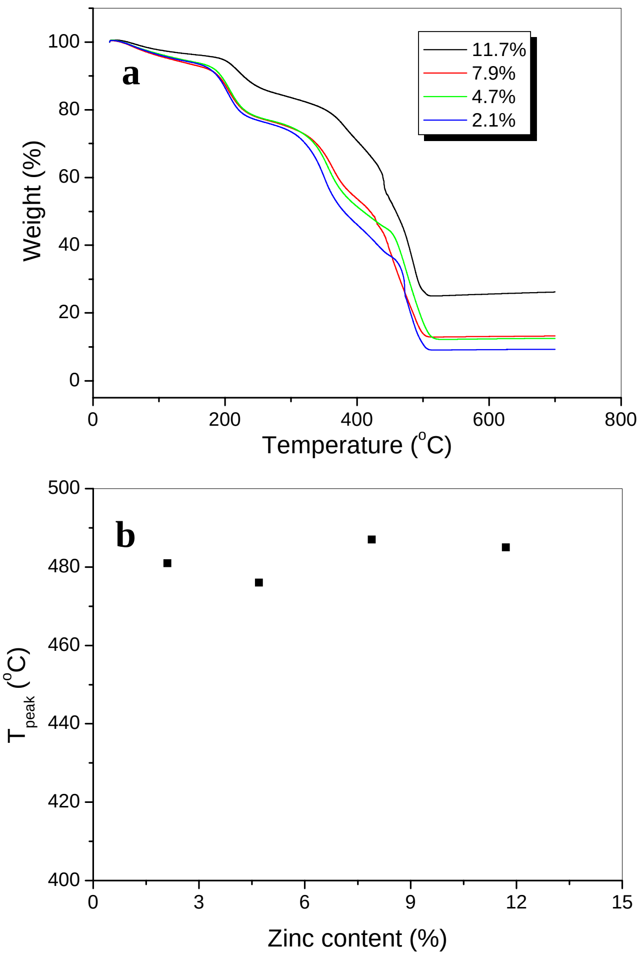

Fig. 4.20. (a) *TGA results of zinc polyacrylate samples with different zinc content. (b) The third T_{peak} of ZnPA samples versus zinc content in the precursor polymer.*

From previous analysis of zinc polyacrylate, we already know that in the first two steps the decomposition of the organic parts takes place and the crystallization process actually happens only in the third step. Therefore, the T_{peak} of the third step could be influenced by two parameters: the type and content of the metal ions in the polymer precursor. A controlled TGA experiment was carried out, in which a series of zinc polyacrylate powders with different zinc content varied from 2.1% to 11.7% was investigated for its decomposition properties by TGA using the same heating program as zinc-cobalt polyacrylate. Unlike the results of ZnCoPA, all ZnPA samples show almost same T_f value, independent on the zinc content as shown in Fig. 4.20. The value of third T_{peak} in DTGA is within the range of 480-490 ^oC (Fig. 4.20b). Thus, we can infer that the considerable change of the third T_{peak} in ZnCoPA decomposition is due to the loading of cobalt ions in the polymer precursor. With increasing content of cobalt, the T_{peak} or T_f decreases rapidly.

4.3.3 Characterization of $Zn_{1-x}Co_xO$ nanoparticles

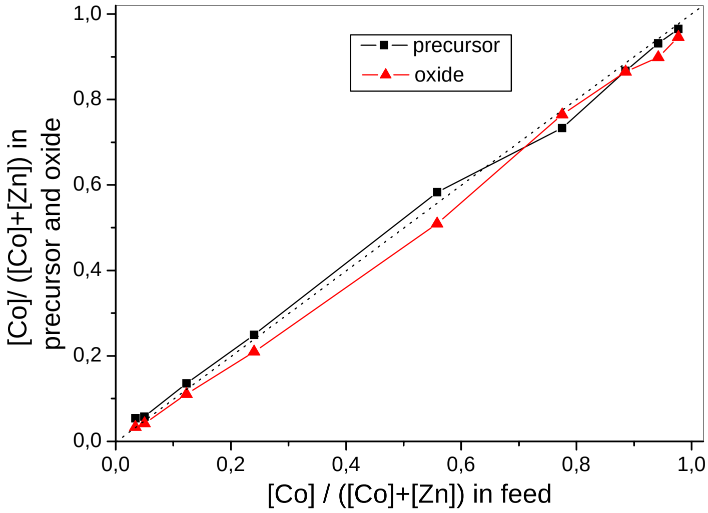

Fig. 4.21. *Co content in the feed versus that determined in the precursor and in oxide.*

The predetermination of composition in the polymer precursor as well as the final MMO by sequential adding different metal ions in the feed is shown again in the case of zinc-cobalt oxide, although very small deviation happens in some composition range (Fig. 4.21). All the precursors sample are water soluble independent on the composition, while the solubility of ZnCoO powder in water differs with one another. It decreases with the cobalt content increasing in the oxide and becomes almost insoluble even at the presence of high concentration hydrochloric acid, when x is over 0.15. Therefore, the composition of precursor samples is determined by means of atomic absorption spectroscopy (AAS), while the oxide samples are examined by a solid-state method: energy dispersive X-ray spectroscopy.

Fig. 4.22 shows the powder X-ray diffraction patterns of $Zn_{1-x}Co_xO$ in the whole composition range. Those diffractograms in the range of $0 \leq x \leq 0.11$ exhibit the expected peak positions for the hexagonal ZnO phase (wurtzite) and for the range of $0.79 \leq x \leq 1$ the diffractograms belong to the cubic Co_3O_4 phase (spinel). The appearance of a single phase in the both ranges indicates the homogeneous distribution or doping of low content foreign metal ions (cobalt and zinc in the two cases respectively) in the host crystal lattice.

For the compositions in between, both crystalline phases, wurtzite and spinel are shown, indicating the phase segregation in this range. Due to the poor contrast between Co and Zn in x-ray diffraction, the data could not be used to refine the relative amounts of these ions in the hexagonal structure.

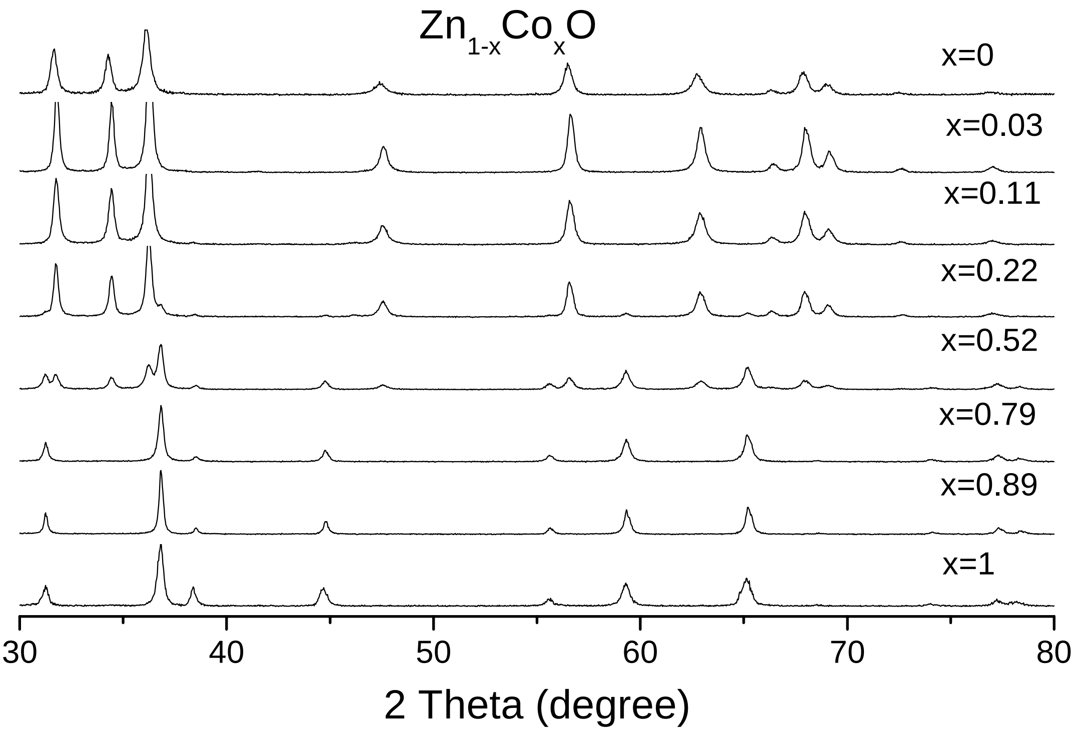

Fig. 4.22. *X-ray diffraction patterns of* $Zn_{1-x}Co_xO$ *(*$0 \leq x \leq 1$*).*

A detailed analysis of the position and the intensity variation of the (100) and (002) reflection for MMO samples containing the wurtzite phase ($0 \leq x \leq 0.52$) was carried out as seen in Fig. 4.23. With increasing cobalt content in the mixed oxides, the intensity of the both peaks decreases continuously, which may reflect the crystallinity deterioration. Unlike the case of zinc-magnesium oxide, an evident shift of peak position of (100) and (002), corresponding to the variation of a and c cell parameter, is not seen for the samples of zinc-cobalt oxide. These two peaks were fitted to Lorentzian curves, which is common for XRD data analysis. The fitting results as listed in Table 4.2 show that the full width at half maximum (FWHM) has a small deviation with the x, indicating the particle size variation of the crystals according to Scherer formula

$$L_{hkl} = \frac{0.9\lambda}{\beta \cos\theta} \tag{3.19}$$

where λ is the radiation wavelength with 0.15406 nm for copper K_α, β is FWHM of the peaks.

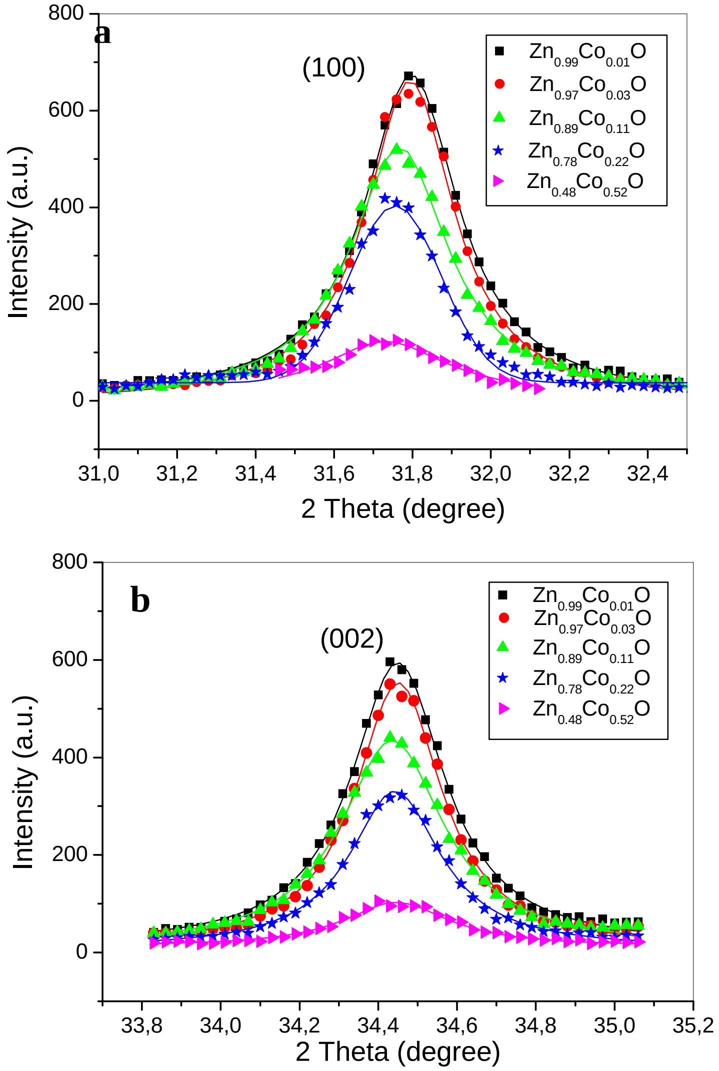

Fig. 4.23. *a) (100) and b) (002) reflection of the of wurtzite phase of* $Zn_{1-x}Co_xO$ samples. *Experimental data are fitted to Lorentzian curves (represented as solid lines).*

The slight deviation in the peak position of (002) and (100) is however within the limit of experimental error. Thus, the cell parameters do not change with composition variation in the wurtzite $Zn_{1-x}Co_xO$ samples. It is well known that in octahedral coordination the Co^{2+} has a much lager size, which will cause the significant increase of lattice parameters. And for Co^{3+}, it is not easy to replace the zinc lattice size due to the difference in the valence. Therefore, it is assumed that cobalt ions are incorporated in the hexagonal phase in our samples in the divalent state in tetrahedral ligand field. The incorporation of cobalt (II) ions into the ZnO lattice doesn't cause the lattice distortion due to the size matching between the divalent high-spin Co in tetrahedral coordination (0.58 Å) and divalent Zn in tetrahedral coordination (0.60 Å).

Table 4.2. *Data analysis of the (100) and (002) reflection in the wurtzite phase. Particle size is calculated by equation (3.19).*

Cobalt content	(100)			(002)		
(x)	2θ (°)	β (°)	L_{100} (nm)	2θ (°)	β (°)	L_{002} (nm)
0.01	31.80	0.295	28.0	34.45	0.291	28.6
0.03	31.80	0.275	30.1	34.45	0.268	31.0
0.11	31.77	0.306	27.0	34.44	0.319	26.1
0.22	31.76	0.234	35.3	34.44	0.283	29.4
0.52	31.73	0.388	21.3	34.45	0.328	25.4

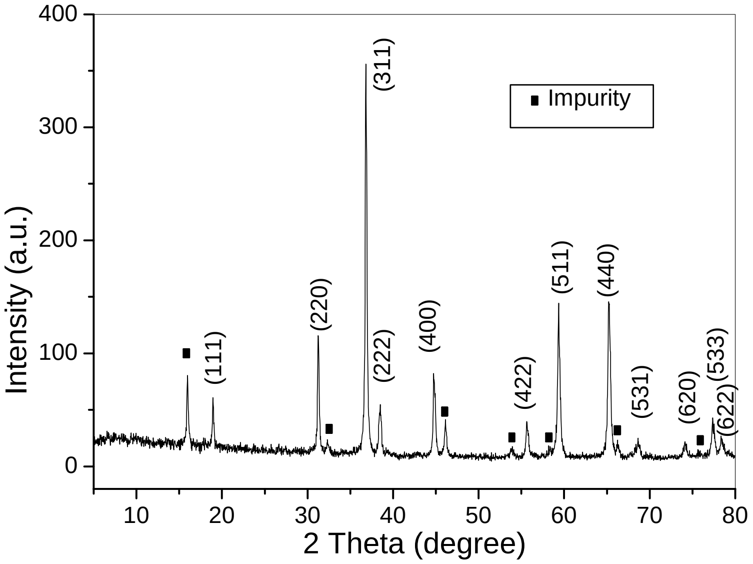

Fig. 4.24. *Typical XRD pattern of the as-synthesized Co_3O_4.*

For the spinel phase of zinc-cobalt oxide, the crystals of Co_3O_4 begins to segregate from the wurtzite phase when $x = 0.22$, but the majority of material at this composition is still in the form of hexagonal zinc oxide. And at $x = 0.79$, the spinel phase is the only crystal structure in the mixed metal oxide. It is already known that the Co_3O_4 crystallizes in the cubic system in form of a spinel. The space group of this metal oxide is $Fd\bar{3}m$ with lattice parameter 8.084 Å.[42] Fig.4.24 gives the typical XRD pattern of the as-synthesized Co_3O_4, which is confirmed with the JCPDS file No. 43-1003. The marked peaks are impurity diffractions which are not indexed. But the formation of metal cluster like cobalt or zinc and binary oxide like CoO and Co_2O_3 is excluded. Two peaks appear at the vicinity of cobalt(II) hydroxide (100) and (110), which indicates that possibly $Co(OH)_2$ could be partial of the impurities present in the material.

Fig. 4.25 shows the normalized PL emission spectra of $Zn_{0.97}Co_{0.03}O$ excited at 325 and 370 nm respectively and the excitation spectrum registered at 440 nm. The excitation spectrum shows an exciton peak at 378 nm which corresponds to the band gap of zinc oxide. The near band gap emission, which reflects the recombination of the free exciton, is quenched due to the doping effects similar to the case of Mg-doped ZnO system. In the visible range, a blue emission with two centres at 418 and 439 nm is seen, which is assigned to crystal defect center of zinc vacancy, while the emission in the yellow-to-orange range is missing. The quenching of both NBE and visible emissions has been reported in the cobalt doped ZnO nanowires and films on single-crystal sapphire when the doping concentration was over 2%.[43] A possible explanation is the enhancement of non-radiative recombination due to the Co substitution. Controversial results also emerged very recently. Chang and coworkers[44] reported the large-scale synthesis of windmill shaped cobalt-doped zinc oxide by the vapour phase deposition method. The PL spectra of $Zn_{0.95}Co_{0.05}O$ in this morphology showed both intensive NBE and green emissions with the emission center at 375 nm and 380 nm respectively. The difference in PL spectra of reported zinc-cobalt oxide may reflect the influence of preparation conditions on the optical properties of this kind of materials.

Magnification of the emission spectra in the range of 600-700 nm shows a weak emission centred at about 680 nm, whose intensity is even lower when excited at 370 nm. This new emission peak is prevailing in all of our wurtzite samples and corresponds well with the $^4T_1(P) \rightarrow {}^4A_2(F)$ ligand field transition, indicating Co^{2+} ion in a tetrahedral crystal field.[43a] This is another important proof of the divalent state of cobalt ions in the wurtzite lattice in addition to the XRD results. The emission might reflect rather more a single process, but indicate a mixed $^4T_1(P)$, $^2T_1(G)$, $^2E(G) \rightarrow {}^4A_2(F)$ transition between cobalt *d*-levels incorporated in the ZnO host. It was detected that it splits into three satellite peaks at very low temperature (below 8 K)[43].

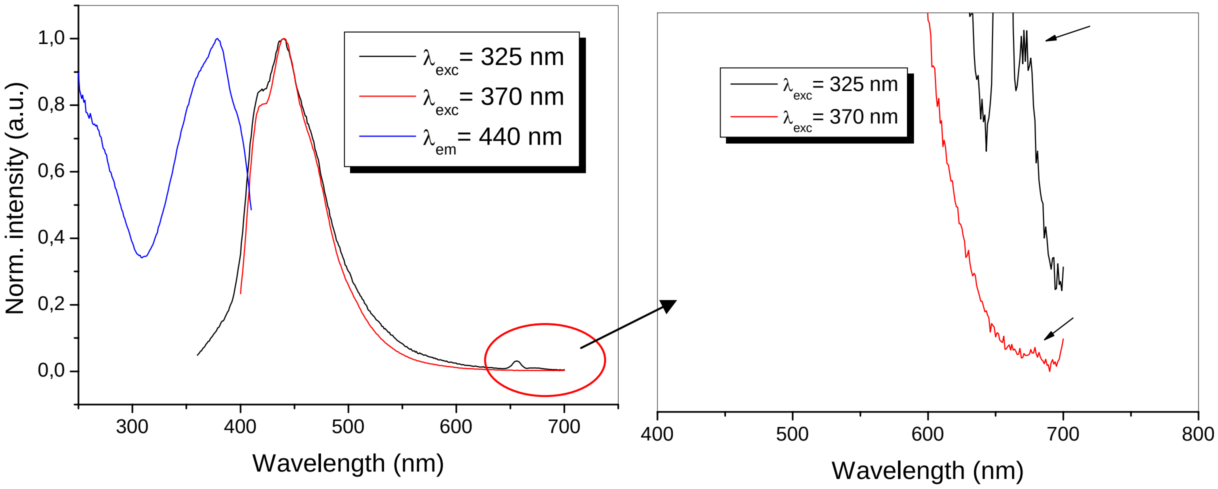

Fig. 4.25. *PL emission spectra of* $Zn_{0.97}Co_{0.03}O$ *excited at 325 and 370 nm as well as the excitation spectra registered at 440 nm.*

The absorption spectra can also give information on electronic status of Co ions in a crystal field. The as-synthesized $Zn_{0.96}Co_{0.04}O$ was firstly dispersed as a suspension in ethanol applying a short-time sonic treatment. Then a film of the nanoparticles was made by deposition of a few drops of the suspension on a clean quartz glass for UV/Vis measurement. The absorption spectra (Fig. 4.26) show two absorption centres at 566 and 680 nm despite the intensive scattering of the particles, which is due to ${}^4A_2(F) \rightarrow {}^2A_1(G)$ and ${}^2E(G) \rightarrow {}^4A_2(F)$ respectively.[41c, 45] This proves again that the Co^{2+} is in a tetrahedral field with high-spin d^7 configuration $e^4t_2^3$. In other word, the cobalt ions occupy zinc ion lattice sites in a hexagonal crystal.

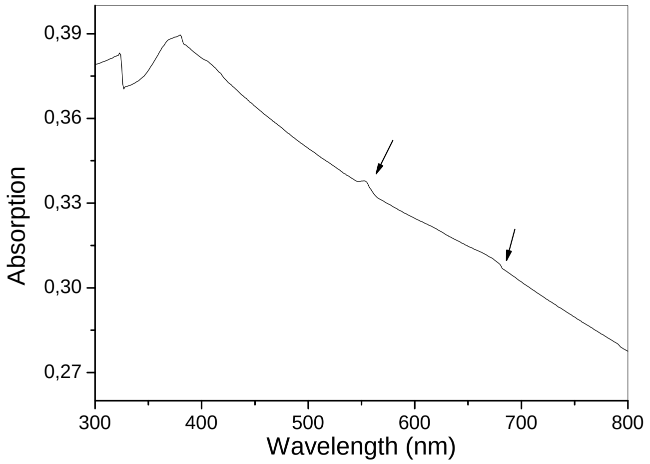

Fig. 4.26. *UV absorption spectra of* $Zn_{0.96}Co_{0.04}O$ *nanoparticles.*

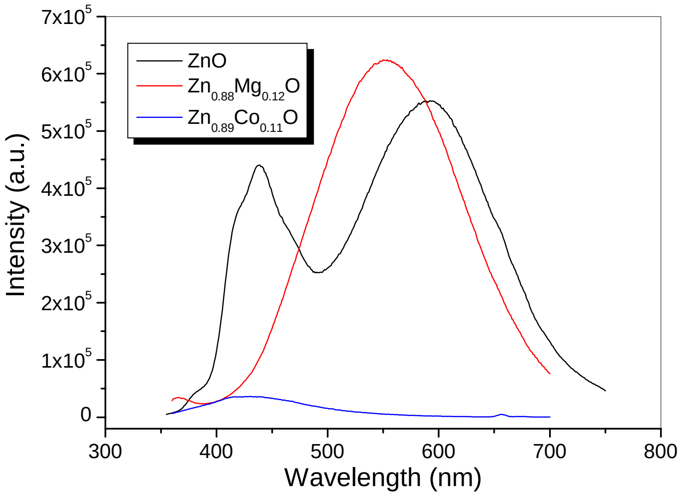

Fig. 4.27. *PL spectra of pure ZnO, $Zn_{0.88}Mg_{0.12}O$ and $Zn_{0.89}Co_{0.11}O$.*

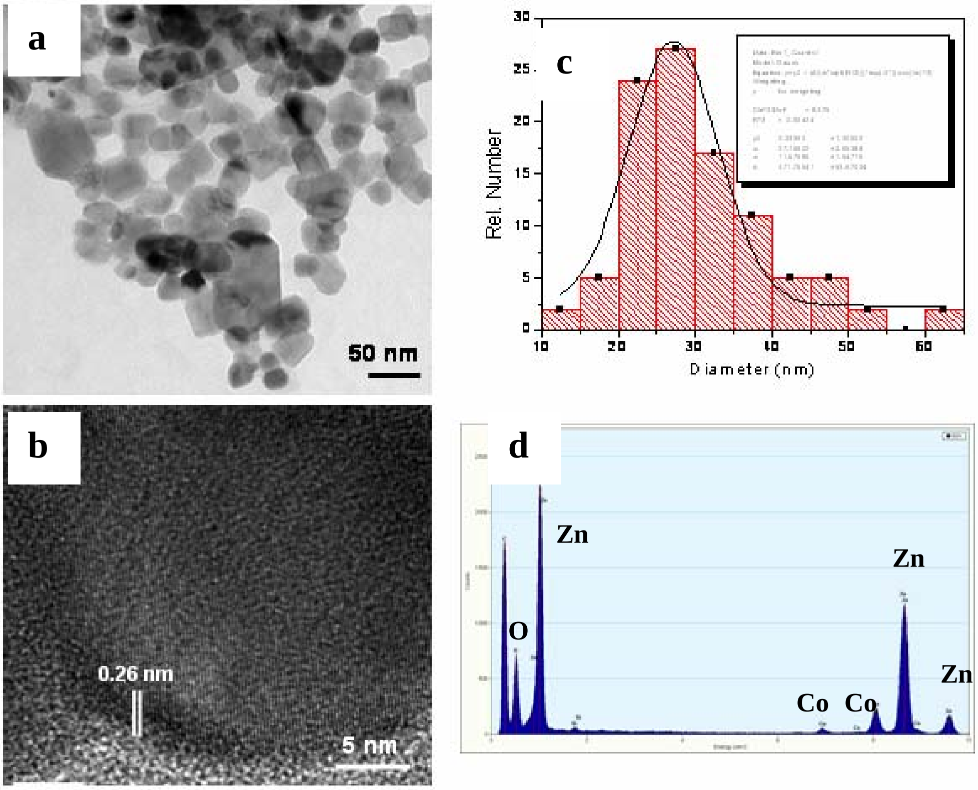

Fig. 4.28. *(a) Low magnification TEM image of the $Zn_{0.97}Co_{0.03}O$ nanoparticles. (b) Histogram computed for 100 particles shown in this image resulting in an average diameter of 27.2 nm. (c) HRTEM image of a single particle of the same sample. (d) EDX result of the sample.*

Another point that needs to be mentioned is the intensity variation of the photoluminescent spectra amongst the different ZnO-based materials synthesized via our method (Fig.4.27). In comparison to pure ZnO nanopowders, the intensity of visible emission for Mg doped ZnO material is enhanced, due to the introduction of high concentration of defects in the host crystal. The position of the emission centre shifts to lower wavelength (higher energy) side in that the doping causes the enlargement of ZnO band gap. For the case of cobalt doping, the emissions are significantly suppressed. This tuneable photoluminescence property implies the promising applications in the optoelectronic device for Mg-doped ZnO.

The morphology of the $Zn_{1-x}Co_xO$ samples with different compositions was examined by means of TEM. The low magnification image shows that the sample consists of nanosized particles with diameter less than 40 nm with a quite large size distribution (Fig. 4.28a). EDX measurement shows clear indication of presence of zinc and cobalt with the overall composition of this sample $Zn_{0.97}Co_{0.03}O$ (Fig. 4.28d). The sintering of the crystals has not yet taken place. The size and size distribution of the crystals of this sample was evaluated choosing 100 particles with clear boundary at random. Gaussian fit of the histogram gives the average diameter of 27.2 nm for the nanoparticles (Fig. 4.28 b). Fig. 4.28c presents an HRTEM image of a single particle of this sample showing (002) lattice fringes and crystalline order on the length scale of the size of the crystals. The interplanar distances are 0.26 nm by direct evaluation on the image. The well-resolved lattice fringes indicate that the particle exists of a pure single phase and is highly crystalline in nature.

For sample with overall composition of $Zn_{0.78}Co_{0.22}O$, where the spinel phase start to segregate from the wurtzite phase, the particles size are around 50 nm and heavy aggregation of particles is observed (Fig. 4.29a, b). Considerable degree of sintering has taken place in this sample. As revealed by X-ray diffraction pattern, spinel phase oxide forms already at this composition. A cubic particle with clear lattice fringes is found as shown in the high-resolution TEM image (Fig. 4.29c). The interplanar distance is 0.47 and 0.28 nm, matching the (111) and (022) plane of Co_3O_4 respectively. In Fig. 4.29d, a particle of wurtzite structure is observed. A stacking fault is shown as denoted by the arrow. In most metal oxides, crystal defects of different nature and concentration as well as location have significant consequences on the optical and electronic properties of the material. The correlation of crystal defects with PL features of ZnO has attracted tremendous research interests and been intensively investigated in recent years.[50] In general, the emission in the near-band-edge, so called NBE emission has been unambiguously assigned to free exciton recombination. However, the emission in the visible ranging from blue to the red emission has been observed in various ZnO nanostructures and films. These visible emissions are believed to be related to crystal defects like oxygen vacancies, zinc vacancies, interstitial oxygen, etc. However, no consensus on the origin of the visible emission of zinc oxide has been hitherto reached. Probably, preparation methods and conditions have important influence on the visible emission reflecting from the numerous research works.

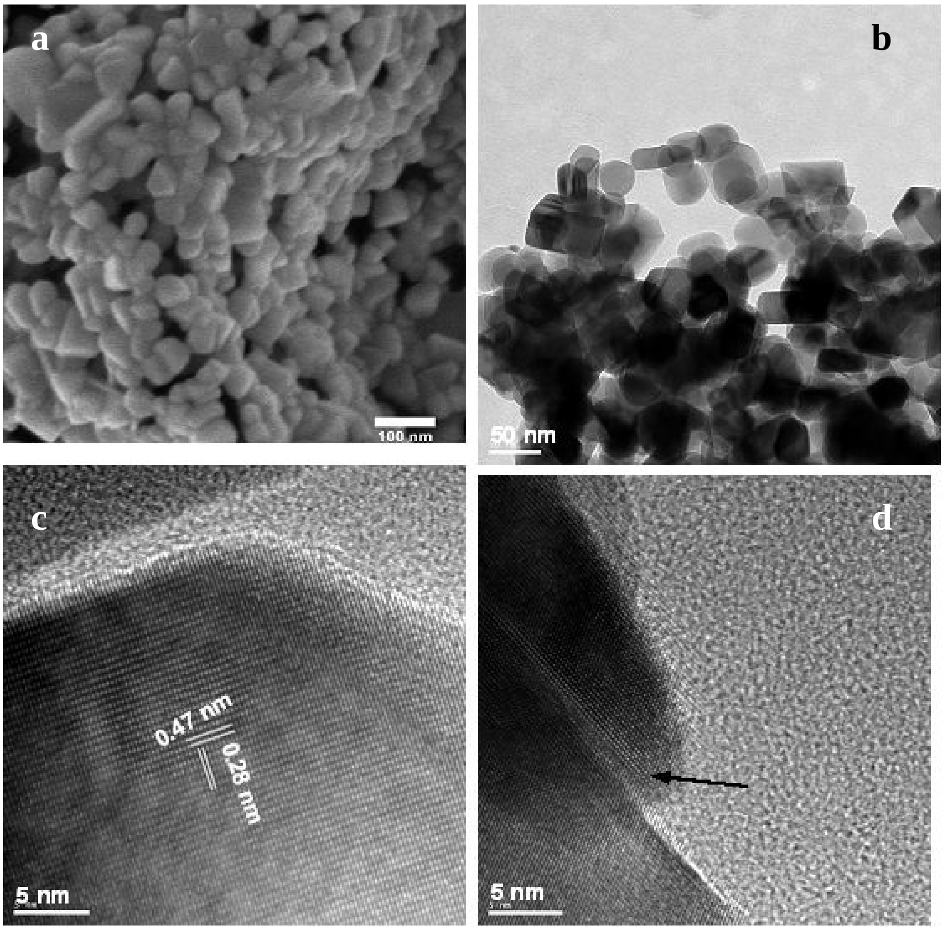

Fig. 4.29. *(a) SEM image showing the overall morphology of* $Zn_{0.78}Co_{0.22}O$ *nanoparticles. (b) Low magnification image showing the sintering of the particles (c) HRTEM image of a single particle of spinel and (d) stacking fault in a wurtzite particle.*

Combining the XRD and TEM results, we prove that the cobalt ion can replace the zinc ion position in the hexagonal lattice. The solubility of cobalt (II) ions in a hexagonal phase is less than 0.22 for the zinc-cobalt oxide by the method using a polymer precursor. We note the report of Kim et al.,[46] who prepared a $Zn_{0.75}Co_{0.25}O$ film on sapphire (0001) substrates by a laser deposition method. His film shows a single phase wurtzite structure when the substrate temperature was kept below 600 °C, but the conditions like substrate temperature and O_2

pressure may introduce impurity phase of Co, CoO and/or ZnO into the film. Risbud and coworkers[41b] have prepared bulk cobalt doped ZnO powders and found the solubility limit for cobalt ions is over 20%. They also reported a linear relation between the lattice parameter and cobalt content, which is not seen in our case.

For the case of pure spinel phase, $Zn_{0.11}Co_{0.89}O$ was checked by electron microscopy as well (Fig. 4.30). The size of the particles as revealed by SEM (Fig. 4.30 b) and low magnification TEM is less than 100 nm. However, the size of the particles has a large distribution (Fig. 4.30a). Only cubic phase particles are found which is consistent with the XRD results. The well-resolved lattice fringes indicate that the particle is highly crystalline.

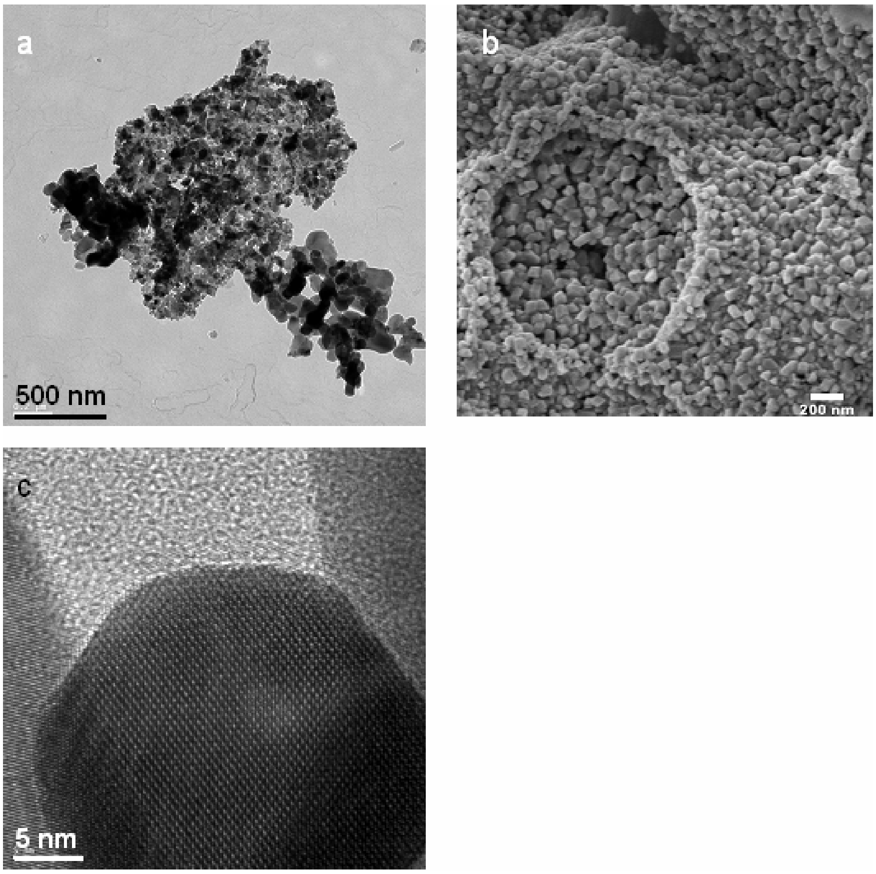

Fig. 4.30. (a) Low magnification image showing the morphology of $Zn_{0.11}Co_{0.89}O$ *nanoparticles. (b) SEM image of the same sample (c) HRTEM image of a single particle of spinel phase.*

4.3.4 Magnetic Properties of the $Zn_{1-x}Co_xO$ Samples

Several cases of ferromagnetic $Zn_{1-x}Co_xO$ films have been reported in the last few years. Ueda et al.[38a] prepared Co-doped ZnO film on an Al_3O_2 by PLD technique. The film with

15% Co doping showed a T_C is over 280 K. However, the authors also claimed that the reproducibility was poor (about 10%). Pan and coworkers[38b] deposited $Zn_{0.96}Co_{0.04}$ film on a $LiNbO_3$ (104) substrate by a direct current reactive magnetron cosputtering method. A giant magnetic moment of 6.1 μ_B / Co and a high Curie temperature T_C of 790 K were observed. These authors suggest a supercoupling mechanism in terms of bound magnetic polarons to explain the ferromagnetism. The related theory was worked out in detail by Coey *et al*,[37a] who proposed that the ferromagnetic exchange is mediated by shallow donor electrons that form bound magnetic polarons, which overlap to form a spin-split impurity band. On theoretical grounds, high Curie temperatures should be achieved via hybridization and charge transfer from a donor-derived impurity band to unoccupied 3*d* states at the Fermi level.

However, Yoon et al.[47] proved that their transition metal-doped ZnO including Co, Mn, and Fe are rather antiferromagnetic than ferromagnetic according to a Curie–Weiss behavior of susceptibility. Lawes[41a] also found no any evidence of ferromagnetic ordering in their Co or Mn doped ZnO powders. And several more groups claimed the finding of ferromagnetic features is due to the presence of cobalt metal clusters as a second phase in the mixed metal oxides.

Gamelin et al.[48] presented an interesting result of a reversible ferromagnetic ordering at 300 K. A double-exchange mechanism was proposed for magnetic ordering that involves electron delocalization within a sub-conduction-band cobalt impurity level.

Another recent work by Lin *et al.*[37b] showed that additional Cu doping into bulk $Zn_{0.98}Co_{0.02}O$ could be achieved and gave rise to room-temperature ferromagnetism. They demonstrated that the copper and cobalt codoped-ZnO film grown by a standard solid-state reaction method have a homogeneous distribution of metal ions without a secondary phase from the results of x-ray diffraction and EDX.

All this controversial results possibly indicate the effects of preparation methods on the magnetic properties of the materials. The nature of the ferromagnetic phenomena in dilute magnetic semiconductors is obviously not yet clear.

This work presents a chemical synthesis method to prepare mixed metal oxides via a polymer precursor. Doping of cobalt in zinc lattice site has been achieved as demonstrated by XRD, TEM and PL. A sample here with a composition of $Zn_{0.97}Co_{0.03}O$ was obtained at 480 ^oC and annealed for 1 h at this temperature under nitrogen atmosphere. Its ferromagnetic property was examined using a superconductive quantum interference device (SQUID) magnetometer. Fig. 4.31a shows the magnetization versus temperature curve measured during cooling in an applied field of 1 kOe. The results indicate no ferromagnetism but rather paramagnetic behaviour of this sample. Due to the discontinuous change of the magnetization values in different temperatures, we have problems to fit our data using a Curie-Weiss law. However, no hysteresis loop was observed in the $M-H$ data at 300 K (Fig. 4.31b). Both results confirm that our sample does not show ferromagnetic ordering.

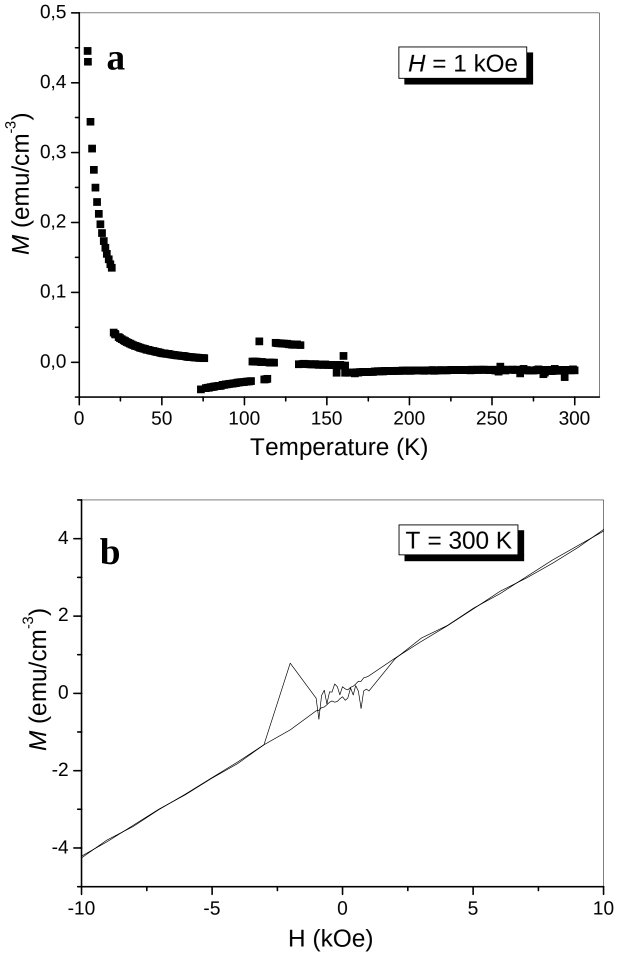

Fig. 4.31. *Magnetization measurement for* $Zn_{0.97}Co_{0.03}O$ *nanopowders. a) temperature dependence of the magnetization measured in a constant field of 1000 Oe and b) Magnetization versus field measured at 300 K.*

In conclusion, we successfully prepared another ZnO-based mixed metal oxide ($Zn_{1-x}Co_xO$) via our polymer-based method. The composition of the obtained oxides corresponds to the predetermined metal ion content in the feed and the resulting zinc-cobalt polyacrylate precursor polymer. In the wurtzite phase, the cobalt ions are divalent with high-spin $3d^7$ state and they occupy zinc lattice sites in the hexagonal structure as proved by XRD, absorption and photoluminescence spectra. The incorporation of cobalt ions considerably suppresses the emission of the material. The $Zn_{1-x}Co_xO$ consists of nanometer sized particles with diameter

20-50 nm. Magnetic property of the material is checked too and ferromagnetic ordering is not found in our sample.

4.4 Experimental section

Preparation of Zinc Polyacrylate Precursor Polymer:

Typically, 1.036 g polyacrylic acid (prepared from 50 % aqueous solution by freeze drying) (Aldrich, $M_w = 5000$) and 0.428 g $Zn(NO_3)_2•6H_2O$ were dissolved in 110 ml water. The solution is stirred for 10 min. Ammonium hydroxide (25% wt) was added dropwisely to adjust the pH to the desired value between 5~10. The reaction mixture was now concentrated to about 20 ml by freeze-drying. The residual viscous liquid was dropped into 120 ml acetone. A colorless precipitate was formed and collected by centrifugation. It was washed with acetone and dried at 40 °C in vacuum.

Preparation of $Zn_{1-x}Mg_xO$:

For a zinc-rich sample (x < 0.5): 0.5g zinc polyacrylate was redissolved in 50 ml water and stirred for 10 min. A solution of 0.144 g $Mg(NO_3)_2•6H_2O$ in 15 ml water was added. The pH was adjusted to 7 with ammonia. The mixed solution was concentrated to 20 ml by freeze-drying and then poured dropwisely into 100 ml of acetone. The precursor was collected by centrifugation, washed with acetone and dried in vacuo.

The precursor material was milled into fine powder and then calcined in a temperature-controlled oven under air flow with a heating rate of 5 °C min^{-1} to 550°C. The sample was isothermally annealed for 1 hour at this temperature and taken out from the hot oven in time.

For the Mg-rich samples (x>0.5), magnesium polyacrylate complex was first prepared analogously and then zinc was incorporated as described above.

Preparation of $Zn_{1-x}Co_xO$:

The synthesis route is very similar as that of $Zn_{1-x}Mg_xO$:

For a zinc-rich sample (x < 0.5):

500 mg zinc polyacrylate was redissolved in 50 ml water and stirred for 10 min. A solution of 5.66 mg $Co(NO_3)_2•6H_2O$ in 15 ml water was added. The pH was adjusted to 7 with ammonia. The mixed solution was concentrated to 20 ml by freeze-drying or rotary-evaporator at 50 ^oC under reduced pressure and then poured dropwisely into 100 ml of acetone. The precursor was collected by centrifugation, washed with acetone and dried in vacuo.

The precursor material was milled into fine powder and then calcined in a temperature-controlled oven under air flow with a heating rate of 5 °C min^{-1} to 550°C. The sample was isothermally annealed for 1 hour at this temperature and taken out from the hot oven in time.

For the Co-rich samples (x>0.5), cobalt polyacrylate complex was first prepared analogously and then zinc was incorporated as described above.

INSTRUMENTAL

The composition with regard to Zn and Mg or Co in the precursors polymer was determined by Atomic Absorption Spectroscopy (AAS) using a Perkin Elmer 5100 ZL spectrometer. The Zinc-magnesium polyacrylate complexes were directly dissolved in water, while the $Zn_{1-x}Mg_xO$ samples were measured after dissolving them with concentrated HCI. The zinc-cobalt polyacrylate composition was dissolved in water for composition determination using AAS. Energy dispersive X-ray spectroscope (EDX) coupled to the TEM was used for zinc-cobalt oxide composition determination. pH values were measured with a Pt/KCI glass electrode attached to a pH meter (Schott CG 843 set). Viscometric measurements were performed at $20\pm0.01\ ^{o}C$ using a capillary Ubbelohde-Viscometer from Schott (Germany). The optimal temperature for calcination was worked out by thermogravimetric analysis (TGA), using a Mettler Toledo TGA/SDTA 851 e instrument. Powder XRD patterns were recorded on a Seifert 3000 TT Bragg-Brentano diffractometer using Cu $K\alpha$ radiation with $\lambda = 0.15406$ nm, operating at 40 kV and 30 mA with a 0.03^{o} step size in the range of $5° \leq 2\theta \leq 80°$. SEM images showing the morphology of nanoparticles were taken by LEO Gemini 1530 with an inlens detector (electron high tension (EHT) = 1 kV). TEM images were obtained by Tecnai F20 microscope operating at 200 kV. UV spectra were recorded at room temperature with a Perkin-Elmer Lambda 2 UV/Vis/NIR spectrophotometer. Particle size histograms and distributions were obtained statistically by measuring the dimensions of at least 100 crystals with help of the software ImageJ (National Institute of Health, USA). CW-EPR spectra were measured with a Elexsys 580 spectrometer at frequencies of approximately 9.8 GHz, using an 4103TM cavity at room temperature. Photoluminescence (PL) measurements were performed at room temperature on a Spex Fluorolog spectrometer. Magnetic measurements were performed using a commercial superconducting quantum interference device (SQUID, Quantum Design MPMS-XL-5). Both the magnetization as a function of field at 300 K and the temperature dependence of the magnetization at 1000 Oe are measured.

4.5 References

[1] T. T. Emons, J. Li, L. F. Nazar, *J. Am. Chem. Soc.* **2002**, *124*, 8516.
[2] P. Limthongkul, H. Wang, Y.-M. Chiang, *Chem. Mater.* **2001,** *13,* 2397.
[3] L. L. Beecroft, C. K. Ober, *Adv. Mater.* **1995**, 7, 1009.
[4] A. Taden, M. Antonietti, A. Heilig, K. Landfester, *Chem. Mater.* **2004**, *16,* 5081.
[5] E. R. Leite, A. P. Maciel, I. T. Weber, P. N. Lisboa-Filho, E. Longo, C. O. Paiva-Santos, A.V. C. Andrade, C. A. Pakoscimas, Y. Maniette, W. H. Shreiner, *Adv. Mater.* **2002,** *14,* 905.
[6] N.-L. Wu, S.-Y. Wang, I. A. Rusakova, *Science* **1999**, *285*, 1375.
[7] a) K. Zakrewska, *Thin Solid Films* **2001**, *391*, 229; b) M. M. Oliveira, D. C. Schnitzler, A. J. G. Zarbin, *Chem. Mater.* **2003,** *15,* 1903.
[8] T. Ishii, R. Furuichi, T. Nagasawa, K. Yokoyama, *J. Themal Anal.* **1980**, *19,* 467.
[9] J. Marchal, T. John, R. Baranwal, T. Hinklin, R. M. Laine, *Chem. Mater.* **2004,** *16,* 822.
[10] A. Sin, P. Odier, *Adv. Mater.* **2000**, *12,* 649.
[11] M. P. Pechini, U.S. Patent 3 330 697, 1967.
[12] M. Kakihana, T. Okubo, M. Arima, O. Uchiyama, M. Yashima, M. Yoshimura, *Chem. Mater.* **1997,** *9,* 451.
[13] C. Marcilly, P. Courty, B. Delmon, *J. Am. Ceram. Soc.* **1970**, *53*, 56.
[14] M. Oledzka, M. M. Lencka, P. Pinceloup, K. Mikulka-Bolen, L. E. McCandlish, R. E. Riman, *Chem. Mater.* **2003**, *15*, 1090.
[15] M. Oledzka, N. E. Brese, R. E. Riman, *Chem. Mater.* **1999,** *11,* 1931.
[16] B. Grohe, G. Miehe, G. Wegner, *J. Mater. Res.* **2001**, *16*, 1901.
[17] M. Niederberger, G. Garnweitner, N. Pinna, M. Antonietti, *J. Am. Chem. Soc.* **2004**, *126*, 9120.
[18] W.-M. Kulicke, C. Clasen, *Viscometry of Polymers and Polyelectrolytes*, Springer-Verlag, Berlin Heidelberg, **2004**, p. 61.
[19] S. Förster, M. Schmidt, *Adv. Polym. Sci.* **1995**, *120*, 51.
[20] Ü. Özgür, Ya. I. Alivov, C. Liu, A. Teke, M. A. Reshchikov, S. Doğan, V. Avrutin, S.-J. Cho, H. Morkoç, *J. Appl. Phys.* **2005**, *98*, 041301.
[21] H. Karzel et al., *Phys. Rev. B* **1996**, *53*, 11425.
[22] E. Kisi, M. M. Elcombe, *Acta Crystallogr., Sect. C: Cryst. Struct.Commun.* **1989**, *C45*, 1867.
[23] M. Catti, Y. Noel, R. Dovesi, *J. Phys. Chem. Solids* **2003**, *64*, 2183.
[24] S. Desgreniers, *Phys. Rev. B* **1998**, *58*, 14102.
[25] L. Gerward, J. S. Olsen, *J. Synchrotron Radiat.* **1995**, *2*, 233.
[26] R. R. Reeber, *J. Appl. Phys.* **1970**, *41*, 5063.
[27] The software can be downloaded free of charge via www.ccp14.ac.uk/ccp/webmirrors/lmgp-laugier-bochu/.
[28] A. Ohtomo, M. Kawasaki, T. Koida, K. Masubuchi, H. Koinuma, Y. Sakurai, Y. Yoshida, T. Yasuda, Y. Segawa, *Appl. Phys. Lett.* **1998**, *72*, 2466.
[29] F. K. Shan, B. I. Kim, G. X. Liu, Z. F. Liu, J. Y. Sohn, W. J. Lee, B. C. Shin, Y. S. Yu, *J. Appl. Phys.* **2004**, *95*, 4772.
[30] The data was obtained from the Joint Committee on Powder Diffraction Standards (JCPDS) card 36-1451, International Center for Diffraction Data.
[31] E. R. Segnit, A. E. Holland, *J. Am. Ceram. Soc.* **1965**, *48*, 409.
[32] J. Chen, W. Z. Shen, *Appl. Phys. Lett.* **2003**, *83*, 2154.
[33] a) A. Ourmazd, R. Hall, R. T. Tung in Materials Science and Technology, Vol. 4 (Eds: R. W. Cahn, P. Haasen, E. J. Kramer), WILEY-VCH, Weinheim, 1996, p. 3818; b) R. E. Bailey, S. M. Nie, *J. Am. Chem. Soc.* **2003**, *125*, 7100. (c) S. Kim, B. Fisher, H.-J. Eisler, M. Bawendi, *J. Am. Chem. Soc.* **2003**, *125*, 11466.

[34] T. Makino, Y. Segawa, M. Kawasaki, A. Ohtomo, R. Shiroki, K. Tamura, T. Yasuda, H. Koinuma, *Appl. Phys. Lett.* **2001**, *78*, 1237.

[35] a) A. Ohtomo, R. Shiroki, I. Ohkubo, H. Koinoma, M. Kawasaki, *Appl. Phys. Lett.* **1999**, *75*, 4088; b) Y. Jin, B. Zhang, S. Yang, Y. Wang, J. Chen, H. Zhang, C. Huang, C. Cao, H. Cao, R. P. H. Chang, *Solid State Commun.* **2001**, *119*, 409; c) D. X. Zhao, Y. C. Liu, D. Z. Shen, Y. M. Lu, J. Y. Zhang, X. W. Fan, *J. Appl. Phys.* **2001**, *90*, 5561; d) A. Dev, S. Chakrabarti, S. Kar, S. Chaudhuri, *J. Nanoparticle Res.* **2005**, *7*, 195.

[36] K. Vanheusden, C. H. Seager, W. L. Warren, D. R. Tallant, J. A. Voigt, *Appl. Phys. Lett.* **1996,** *68*, 403.

[37] a) J. M. D. Coey, M. Venkatesan, C. B. Fitzgerald, *Nature Mater.* **2005**, *4*, 173 ; b) H.-T. Lin, T.-S. Chin, J.-C. Shih, S.-H. Lin, T.-M. Hong, R.-T. Huang, F.-R. Chen, J.-J. Kai, *Appl. Phys. Lett.* **2004,** *85*, 621; c) J. M. Baik, J.-L. Lee, *Adv. Mater.* **2005**, *17*, 2745; d) D. P. Norton, M. E. Overberg, S. J. Pearton, K. Pruessner, J. D. Budai, L. A. Boatner, M. F. Chisholm, J. S. Lee, Z. G. Khim, Y. D. Park, R. G. Wilson, *Appl. Phys. Lett.* **2003**, *81*, 5488.

[38] a) K. Ueda, H. Tabata, T. Kawai, *Appl. Phys. Lett.* **2001**, *79*, 988; b)C. Song, K. W. Geng, F. Zeng, X. B. Wang, Y. X. Shen, F. Pan, Y. N. Xie, T. Liu, H. T. Zhou, Z. Fan, *Phys. Rev. B* **2006**, *73*, 024405.

[39] Z. Jin *et al.*, *Appl. Phys. Lett.* **2001**, *78*, 3824.

[40] J. H. Park, M. G. Kim, H. M. Jang, S. Ryu, Y. M. Kim, *Appl. Phys. Lett.* **2004**, *84*, 1338.

[41] a) G. Lawes, A. S. Risbud, A. P. Ramirez, R. Seshadri, *Phys. Rev. B* **2005**, *71*, 045201; b) A. S. Risbud, N. A. Spaldin, Z. Q. Chen, S. Stemmer, R. Seshadri, *Phys. Rev. B* **2003**, *68*, 205202; c) D. A. Schwartz, N. S. Norberg, Q. P. Nguyen, J. M. Parker, D. R. Gamelin, *J. Am.Chem. Soc.* **2003**, *125*, 13205.

[42] a) B. Liu, H. C. Zeng, *Small* **2005**, *1*, 566; b) H. Yoshikawa, K. Hayashida, Y. Kozuka, A. Horiguchi, K. Awaga, S. Bandow, S. Iijima, *Appl. Phys. Lett.* **2004**, *85*, 5287.

[43] a) B. D. Yuhas, D. O. Zitoun, P. J. Pauzauskie, R. R. He, P. D. Yang, *Angew. Chem. Int. Ed.* **2006**, *45*, 420; b) P. Koidl, *Phys. Rev. B* **1977**, *15*, 2493.

[44] a) P. Lommens, P. F. Smet, C. de Mello Donega, A. Meijerink, L. Piraux, S. Michotte, S. Matefi-Tempfli, D. Poelman, Z. Hens, *J. Lumin.* **2006**, *118*, 245; b) P. Koidl, *Phys. Rev. B* **1977**, *15*, 2493.

[45] Y. Q. Chang, Y. N. Wu, M. W. Wang, H. Z. Zhang, D. P. Yu, Z. Wang, Y. Long, R. C. Ye, *J. Cryst. Growth* **2006**, *289*, 183.

[46] a) K. J. Kim, Y. R. Park, *Appl. Phys. Lett.* **2002**, *81*, 1420; b) Y.-Z. Yoo, T. Fukumura, Z. Jin, K. Hasegawa, M. Kawasaki, P. Ahmet, T. Chikyow, H. Koinuma, *J. Appl. Phys.* **2001**, *90*, 4246; c) S. Deka, P.A. Joy, *Solid State Commun.* **2005**, *134,* 665.

[47] J. H. Kim, H. Kim, D. Kim, Y. E. Ihm, W. K. Choo, *J. Appl. Phys.* **2002**, *92*, 6066.

[48] S. W. Yoon, S.-B. Cho, S. C. We, S. Yoon, B. J. Suh, H. K. Song, Y. J. Shin, *J. Appl. Phys.* **2003**, *93*, 7879.

[49] D. A. Schwartz, D. R. Gamelin, *Adv. Mater.* **2004**, *16*, 2115.

[50] a) S. Mahamuni, K. Borgohain, B. S. Bendre, V. J. Leppert, S. H. Risbud, *J. Appl. Phys.* **1999**, *85*, 2861 ; b) X. L. Wu, G. G. Siu, C. L. Fu, H. C. Ong, *Appl. Phys. Lett.* **2001**, *78*, 2285; S. A. Studenikin, N. Golego, M. Cocivera, *J. Appl. Phys.* **1998**, *84*, 2287; d) J. Q. Hu, Y. Bando, *Appl. Phys. Lett.* **2003**, *82*, 1401.

5 Formation of ZnO Nanoparticles via Inverse Miniemulsion Polymerization

5.1 Introduction

5.1.1 Fundamentals

Emulsions are defined as dispersed systems consisting of liquid droplets (dispersed phase) in a liquid (continuous phase).[1] The wide applications of emulsions have since long attracted great interests in academia and industry. Conventionally, a system with organic substance as disperse phase and water as the continuous phase is called ‘oil-in-water’ emulsion. On the contrary, the so-called ‘water-in-oil’ emulsions or ‘inverse’ emulsion refer to the systems where water is the disperse phase in an organic continuous phase. Systems containing restricted aqueous/hydrophilic environment has been used as small reactor or ‘nanoreactor’ in that the droplets or micelles (see scheme 5.1) normally has a size from several tens of nanometers to microns. Here, Emulsion polymerization is possible when a monomer is employed as the disperse phase at appropriate reaction conditions. The resulting polymer particles of colloidal dimensions in water are called latex.

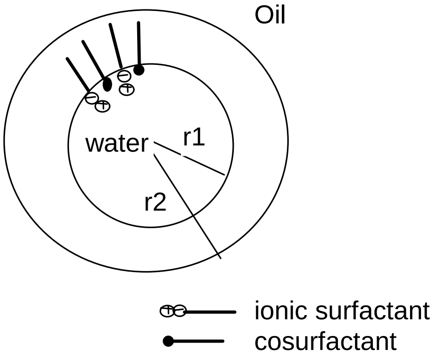

Scheme 5.1 *Schulman’s model of a reverse micelle*[2]

The term emulsion encompasses three types of related categories: Conventional emulsions (or sometimes called macroemulsion), microemulsion and miniemulsion. They differ from one another in many aspects, especially in the droplet size and stability.

*** *Macroemulsion*** is kinetically stabilized system, which forms below a threshold concentration of surfactant dependent on the oil phase as well as the chemistry of the emulsifier. The droplet in this system is large, normally in the range of 1-10 μm in diameter. Empty and oil-swollen surfactant micelles coexist in the initial state. In the course of polymerization, monomer diffuses through the water phase to the micelles in order to sustain polymer particle growth. Particles are formed with a diameter of usually more than 100 nm. The polymerization in this kind of system is named macroemulsion polymerization. The latex particle size does not depend on that of the primary emulsion droplet, which is kinetically controlled by parameters like temperature or the amount of initiator.

*** *Microemulsion*** is formed beyond the threshold emulsifier concentration and thus becomes thermodynamically stable with an interfacial tension at the oil/water interface close to zero. The system consists of droplets with 5 to 50 nm in diameter, leading to optical transparency. By incorporating a monomer in either the dispersed or continuous phase, polymerization reaction may take place. Because initiation reaction cannot start in all microdroplets simultaneously, polymer chains are formed only in some droplets. This thermodynamic non-equilibrium state usually leads to an increase in particle size. The polymer particles coexist with empty micelles. A major problem often arises from phase separation occurring in the process of polymerization. A cosurfactant (alcohol) is often required which may lead to chain transfer reactions causing limit of the molecular weight of the polymer.

*** *Miniemulsion*** is critically stabilized with respect to colloidal stability, which requires high shear to reach a steady state. The stability of the emulsion and the size of the resulting particles in this system are in between that of macro emulsions and micro emulsions. The size of droplets in this system is usually in the range of 50-500 nm. A miniemulsion typical for an oil-in-water case consists of oil (e.g., a water-insoluble monomer), water, a surfactant, and a highly water-insoluble compound (hydrophobe). The composition is subjected to high rate shearing to achieve homogenization using normal untrasonicators or microfluidizers. Key factors that govern the miniemulsion formulation are the type of homogenization and the hydrophobe that needs to be added.

a) Influence of type of homogenization

Homogenization of an emulsion can be achieved by several techniques. In early years, simple stirring was applied and Omni-mixer and Ultraturrax was also reported to obtain small and homogeneously distributed droplets. Nowadays, ultrasonication is widely used to meet the high shear requirement. The mechanical emulsification starts with a premixing of the fluid phases containing surface-active agents and further additives. The process undergoes two steps. At the first step, the deformation and disruption of droplets take place resulting in an increase of the specific surface area of the emulsion. Then, these newly formed interfaces are stabilized by surfactants.

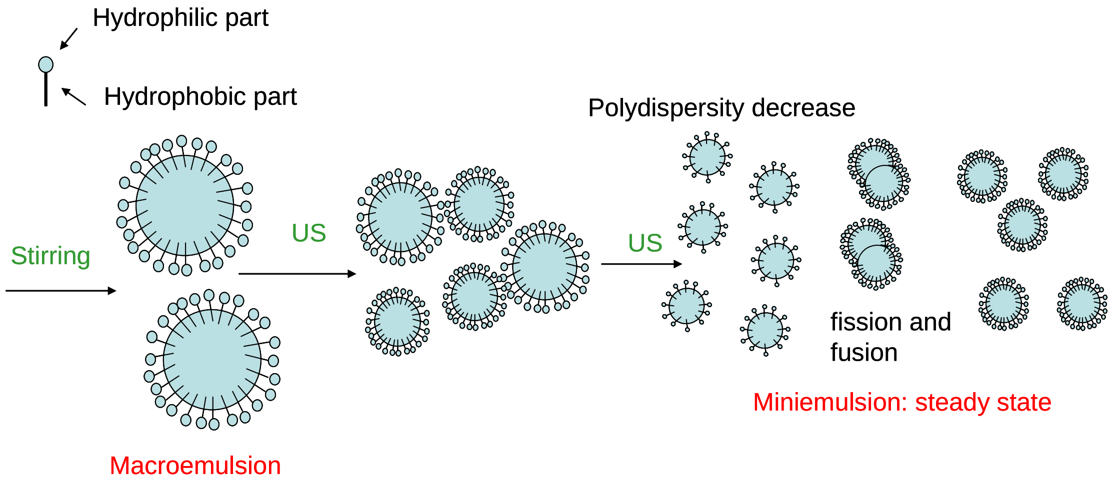

Scheme 5.2

Scheme for the formation of miniemulsion via ultrasonication (US).[3]

In a monomeric miniemulsion, the droplet size is, in turn, determined by monomer amount, aqueous amount, monomer solubility, level of surfactant, and level of hydrophobe. The droplet size initially is a function of the intensity of shear. Monomer droplets also change quite rapidly in size after sonication in order to approach a pseudo-steady state in size. Once this state is reached, the size of the monomer droplet is no longer a function of the intensity of shear, assuming a required minimum is used. During ultrasonication, the droplet size decreases constantly until a constant size is reached (scheme 5.2).

b) Influence of the hydrophobe

Two mechanism including Ostwald ripening and coalescence, which are the hindrance to a stable miniemulsion, may cause the growth of the droplets after homogenization. Surfactant may suppress the coalescence. Adding a hydrophobic compound to the disperse phase may control Ostwald ripening providing an osmotic pressure inside the droplets to balance the Laplace pressure. The Laplace pressure Δp is the vapour pressure difference between the inner and the outer part of a droplet of radius r, expressed as

$$\Delta p = \gamma(2/r) \qquad (5.1)$$

where γ is the surface tension for the oil/water interface. The surface tension tends to compress the droplet, increasing the internal pressure. The Laplace pressure is offset by an osmotic pressure (Π), caused by a different chemical potential due to the well-known van't Hoff equation

$$\Pi = nRT/V \qquad (5.2)$$

However, this pressure equilibrium cannot be established immediately after homogenization. The addition of a very hydrophobic material rapidly suppresses the Oswald ripening of the droplets, whereas slow droplet growth by coalescence does not stop until the pressures are equilibrated. Thus, the steady-state miniemulsification leads to a system of critical stability. The droplet size is the compromise between fission by ultrasound and fusion by collisions and the minidroplets are as small as possible for the time scales involved.

Analogous to direct miniemulsions, the osmotic pressure in inverse miniemulsions can be suppressed by an agent insoluble in the continuous phase, a so-called lipophobe. In this case, due to the low solubility of most salts in organic solvents, they are proper candidates as lipophobes in water-in-oil miniemulsions.

In miniemulsion polymerization, the latexes are essentially a polymerized copy of the original droplets, the size of which is essentially given by the dispersion process and droplet stability, but not by polymerization parameters. In other word, before and after polymerization, the droplet size is the same.

5.1.2 Synthesis of inorganic crystals in emulsion

The concept of ‘nanoreactor’ has emerged in recent years and is widely applied in the synthesis of nanoparticles of inorganic materials. Due to the stability and proper size ranging from several tens of nanometers to several microns in various emulsion systems, emulsions or inverse emulsions are ideal nanoreactors for preparation of nanoparticles of metal oxides.

Brese et al.[4] synthesized cross-linked functionalized acrylic emulsion polymer and suspension polymers, which complex with metallic ions and can be converted to metal oxides upon calcination at low temperature. They have demonstrated the method is successful in the formation of ZrO_2, CeO_2, $LiMn_2O_4$, $Ba_2YCu_3O_7$, as well as catalysts in the Au/Pt and Pt/CeO2 systems.

Reverse micelles and microemulsions are widely used system, in which both nanoparticles and nanostructures are synthesized in the aqueous pool as disperse phase of ordered mesophases in a nonpolar medium. Normally, two identical microemulsions are prepared, each containing the water-soluble precursor salt and then mixed together. With mixing the two microemulsions, the precursor precipitate resulting from the reaction of the two salts takes place in the aqueous core after period of inter-droplet exchange and nuclei aggregation. This method has succeeded in metallic,[5] calcium carbonate,[6], barium sulphate[7] and zeolite[8] nanoparticles preparation. For instance, Hingorani et al.[9] successfully synthesized a nanosized zinc-containing precursor in water-to-oil microemulsion system which was converted to ZnO nanoparticles after calcinations. In their report, the aqueous disperse phase consists of 10-25 nm micelles which contain the soluble metal salt in the continuous phase of a hydrocarbon. The ZnO-precursor nanoparticle is also produced in ethanol-in-oil microemulsion. Mann and coworkers[10] employed supersaturated reverse micelles and microemulsions as organized reaction microenvironments for barium sulfate precipitation. The as-prepared amorphous barium sulfate is 2-4 nm in size formed in reverse micelles. In contrast, in microemulsions, highly elongated filaments of crystalline barium sulfate, with lengths up to 100 micron and 20-50 nm in width were formed.

An extraordinary virtue of this method is to generate very small nanoparticles. However, a stable inverse microemulsion consumes tremendous amount of surfactant, while the yield of inorganic crystals is relatively low. This limits its applications in industry.

In comparison with microemulsion, the miniemulsion shows special advantages as nanoreactor, used as the size template of the final products. During the reaction each droplet converts in a one-to-one process with preservation of particle number and the amount of material in each droplet. The amount of surfactant used in this system is rather low. Landfester et al.[11] showed that the miniemulsification of low melting salts and metals enables the direct synthesis of nanoparticles of high homogeneity with diameters between 150 and 400 nm. They have prepared a pigment (Fe_2O_3), magnetic nanoparticles (Fe_3O_4), an abrasive ($CaCO_3$), a ceramic precursor (ZrO_2), and low-melting metals used in electric fuses as model systems. The inverse miniemulsion method is also applicable in film preparation of inorganic phosphors.[12]

In this work, we prepare zinc oxide nanoparticles via pyrolysis of a polymer precursor, which is obtained by inverse miniemulsion polymerization.

5.1.3 Introduction to dynamic light scattering

Dynamic light scattering or as it is sometimes called photon correlation spectroscopy (PCS) or quasi-elastic light scattering (QELS), is an important technique for particles size measurement. It is based on the fluctuations of the scattered intensity of light due to Brownian motion of the particles. The scattering fluctuation in the medium is correlated by means of an intensity-time autocorrelator, which monitors the scattering intensities in small time intervals τ over a total observation time $t=n\cdot\tau$ with n the number of time intervals. The autocorrelation function is defined as:

$$g^{(2)}(t) \cong \langle I(t=0) \bullet I(t=n\cdot\tau) \rangle \qquad (5.3)$$

where the bracket denotes an average over typically 10^6-10^8 single correlations.
From this expression we can derive the correlation function of the electric field $g^{(1)}(t)$ as

$$g^{(1)}(t) = \left(\frac{g^{(2)}(t) - A}{A} \right)^{1/2} \tag{5.4}$$

with A being the experimentally determined baseline. For monodisperse particles the autocorrelation function can be written as monoexponential decay function

$$g^{(1)}(t) = B \cdot \exp(-tDq^2) \tag{5.5}$$

where D is the translational diffusion coefficient, q is the scattering vector given by

$$q = \frac{4\pi n}{\lambda_0} \sin(\frac{\theta}{2}) \tag{5.6}$$

with n the refractive index in the medium, λ_0 the light wavelength in vacuum, θ the scattering angle. B appears as the signal-to-noise ratio in the equation.
For polydisperse system, an analogous relation is given by

$$g^{(1)}(t) = B \frac{\Sigma m_i M_i \exp(-tDq^2)}{\Sigma m_i M_i} \tag{5.7}$$

Therefore, the z-averaged diffusion coefficient D_Z is determined by

$$-\left[\frac{\ln(g^{(1)}(\tau)}{dt} \right]_{t \to 0} = q^2 \frac{\sum m_i M_i D_i}{\sum m_i M_i} = q^2 D_z \tag{5.8}$$

The diffusion coefficient is dependent on the scattering angle, which is due to the intermolecular interaction, local mode and polydispersity. The original diffusion coefficient D_0 of the scattering particle can be obtained by plotting apparent diffusion coefficient (D_{app}) versus q^2 with extrapolating q to zero. D_0 can be transformed to the hydrodynamic radius R_h by application of Stokes-Einstein relation as

$$D_0 = \frac{k_B T}{6\pi\eta R_h} \tag{5.9}$$

with k_B, T, η are the Boltzmann constant, the temperature and the solvent viscosity respectively.

5.2 Results and Discussion

5.2.1 Synthesis of the polymer precursor via inverse miniemulsion polymerization

Above have presented a method to prepare metal oxides or mixed metal oxides via a polymer precursor loaded with different metal ions. Here, we present an alternative way for preparation of binary metal oxides by controlled calcination of a polymer precursor, which is formed via inverse miniemulsion polymerization of metal salts of acrylic acid. The metal containing polymer precursor acts as size template and is converted to a very fine powder of crystalline metal oxide. Zinc oxide nanoparticles are prepared as a model, the synthesis procedure of which is described in scheme 5.3.

In the first step, two separate solutions are prepared. One is the aqueous solution containing zinc salt (zinc nitrate here) and acrylic acid; the other is an organic solution containing the surfactant, hexadecane and a large amount solvent cyclohexane. The two solutions are mixed together with rapid stirring for half an hour and are then subject to ultrasonication to form a stable water-in-oil miniemulsion. The zinc nitrate works as both the reaction reagent and lipophobe which establishes the osmotic pressure to balance the Laplace pressure. The formed micelle is in the size of 50-100 nm dependent on the formation conditions. With adding initiator BPO (Benzoylperoxide), miniemulsion polymerization reaction can be started at 70 ^{o}C. The obtained milky miniemulsion is the latex of zinc-loaded polymer precursor. After precipitation from a nonsolvent acetone, the zinc polyacrylate is collected via centrifugation and dried over night in vacuo. Zinc oxide is formed upon calcinations of the precursor powder from room temperature to 500 ^{o}C under air flow.

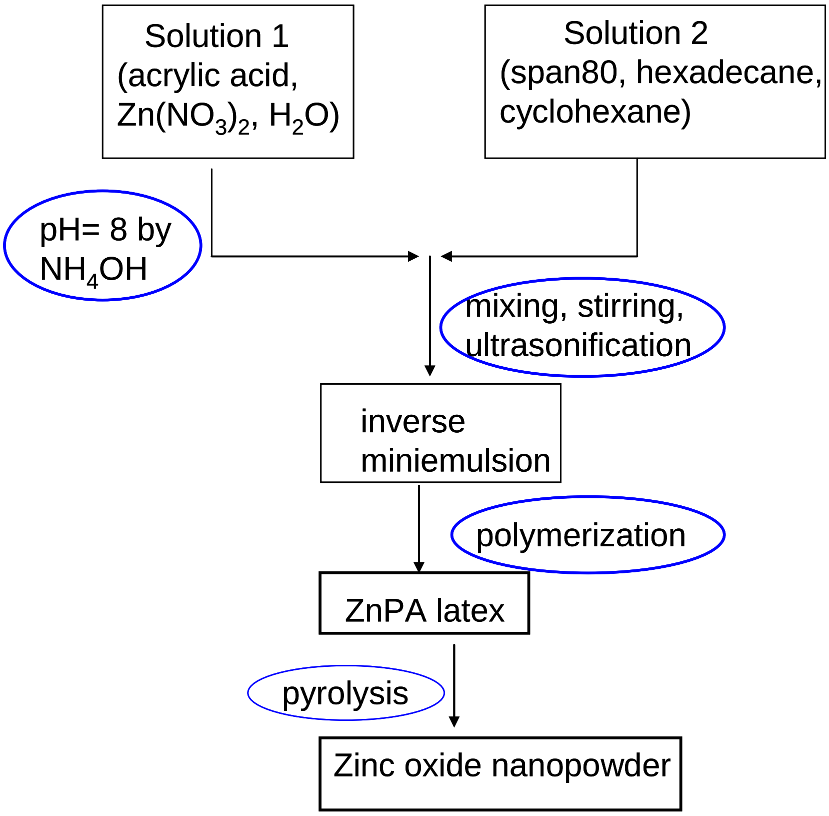

Scheme 5.3

Scheme of the synthesis of zinc oxide via inverse miniemulsion

In order to obtain a stable water-in-oil miniemulsion, a series of surfactants were examined including an anionic surfactant sodium dodecyl sulphate (SDS), non-ionic surfactant polyethylene oxide derivate (i.e. Lutonsol AT50, C_{16}/C_{18}-EO_{50}) and sorbitane monostearate (Span 60) and sobitan monooleate (Span 80). However, except Span 60 and Span 80, the other surfactants show poor behaviour in maintenance an emulsion stable against phase separation. In our experiment, a typical recipe for the inverse miniemulsion is listed in Table 5.1.

Table 5.1. *Standard recipe for formation of an inverse miniemulsion.*

Disperse (aqueous) Phase	**Amount**
Acrylic acid	1 g
$Zn(NO_3)_2 \cdot 6H_2O$	0.43 g
Water	4.5 g
Continuous (oil) Phase	**Amount**
Span 80	0.5 g
Hexadecane	2 g
Cyclohexane	40 g

Dynamic light scattering is employed to determine the size of the inverse micelles. Fig. 5.1a gives the correlation function of a typical inverse miniemulsion measured at a scattering angle of 85° at room temperature. Fig. 5.1b is the inverse Laplace transformation of the correlation function, which clearly shows a strong peak, indicating only one mode in the solution with the hydrodynamic radius of the micelle 69 nm in diameter. Moreover, the size of the micelle is unchanged at different scattering angle, reflecting the spherical structure of the micelles of the inverse miniemulsion (Fig. 5.2).

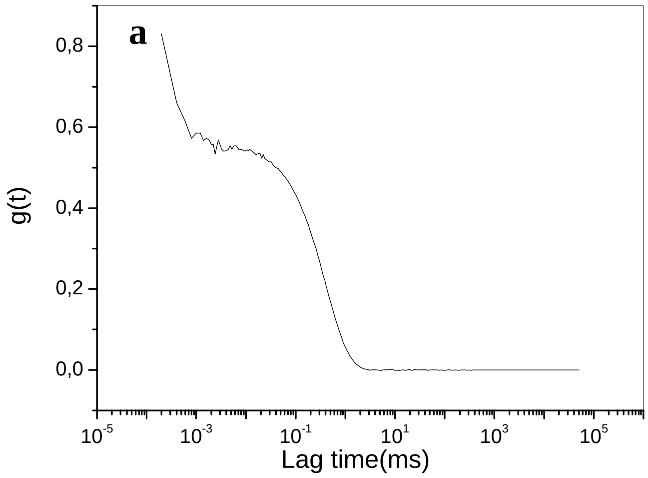

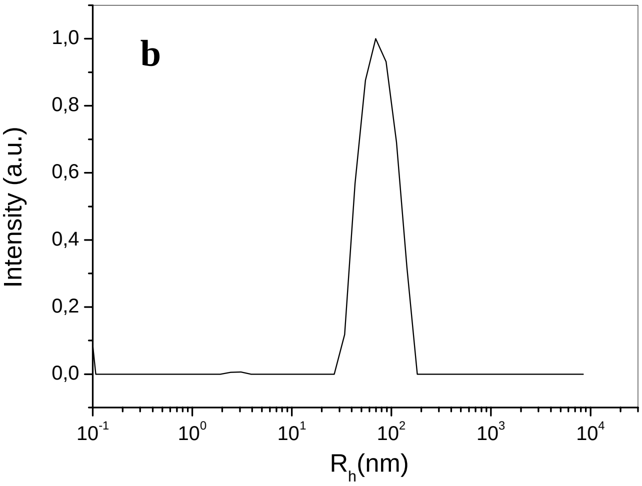

Fig. 5.1. *a) DLS correlation function; and b) size distribution of a typical inverse miniemulsion. The miniemulsion is formed according to Table 5.1 but using span60 as surfactant. The scattering angle is 85^o here.*

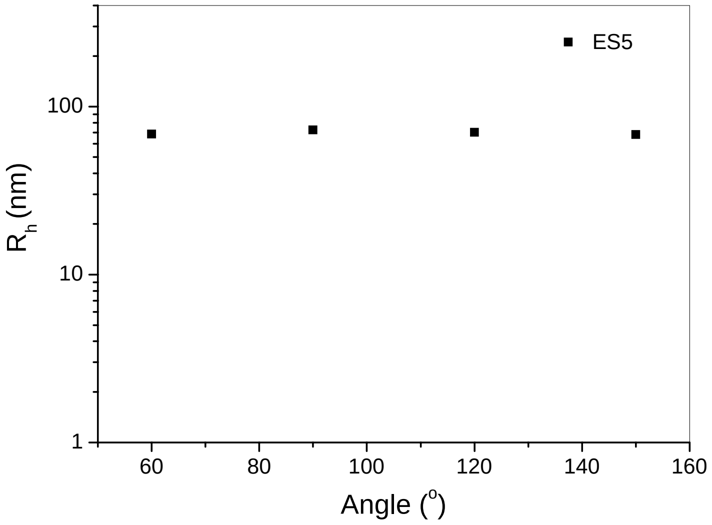

Fig. 5.2. *Hydrodynamic radius of micelle of the inverse miniemulsion at different scattering angle.*

Table 5.2. *Size of micelles formed at different conditions.*

Continuous Phase	Surfactant	Amount (g)	Size (nm)
n-Octane	Span 60	1	81
Cyclohexane	Span 60	0.5	69
Cyclohexane	Span 80	1	82
Cyclohexane	Span 80	0.3	98

The micelle size of the inverse miniemulsion prepared at different conditions is shown in Table 5.2. It is seen that the particle size of all the micelles is in the range of 50-100 nm in diameter. The type of surfactant and its amount affect the size of the formed micelles. Scheme 5.3 shows the chemical formula of the surfactants. It is also shown that with more surfactant, a slightly smaller micelle is formed.

Span 60

Span 80

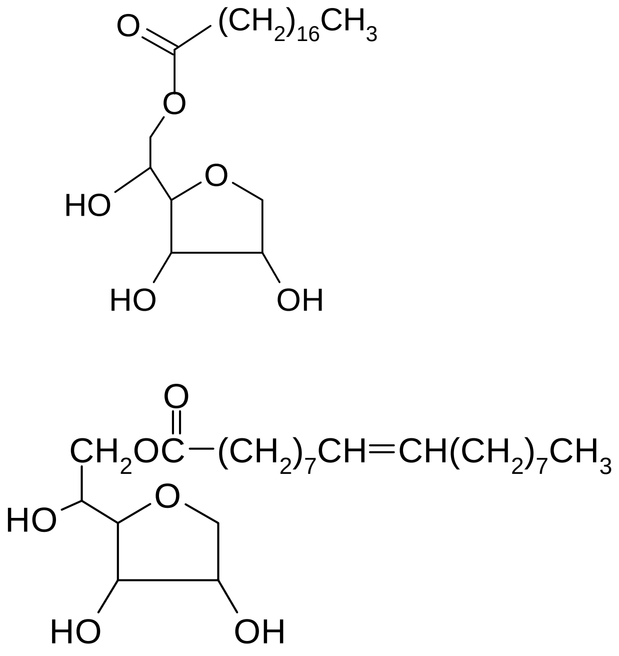

Scheme 5.3

Chemical formula of surfactants of Span 60 and Span 80

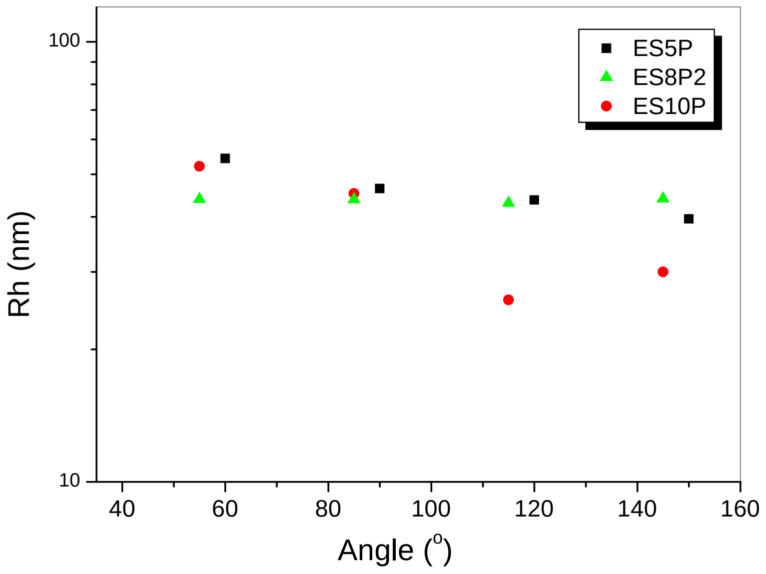

Fig. 5.3. *Particle size of polymer latex synthesized at different conditions versus scattering angle. (ES5P: 0.5 g Span 60, polymerized at 70 °C; ES8P2: 0.5 g Span 80, polymerized at 70 °C; ES10P: 0.3 g Span 80, polymerized at 70 °C).*

The polymerization process forms the latex of zinc polyacrylate at relatively low temperature (not more than 70 °C). It is well known that in the basic medium part of carboxylic group of the acrylic acid may complex with zinc ion, leading to formation zinc acrylate. Thus, the essence of this reaction is the copolymerization of zinc acrylate and acrylic acid in the pool of nanosized micelles. The micelle size before and after polymerization should have no significant change. Fig.5.3 gives several latex sizes determined by means of DLS as well.

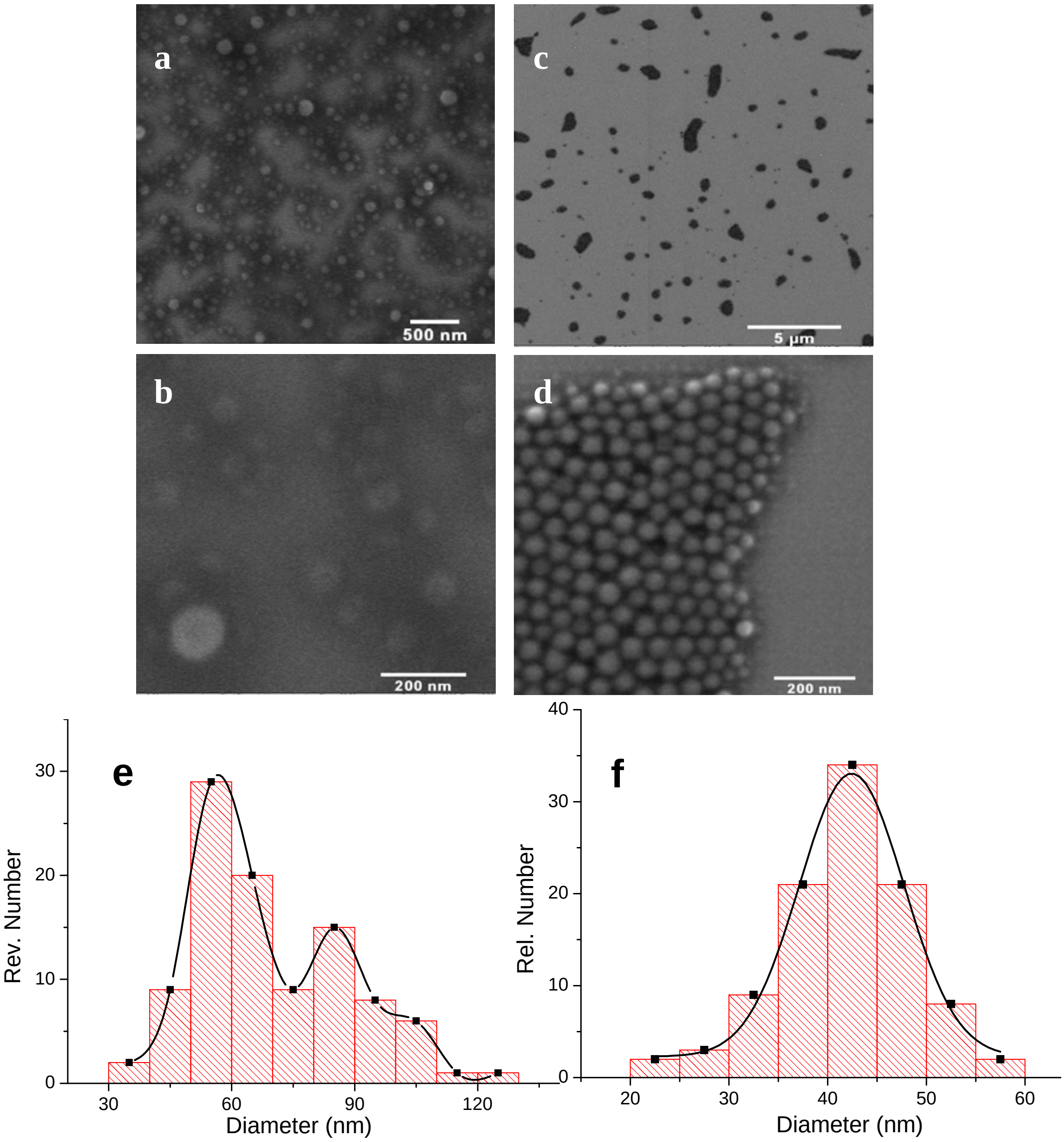

Fig. 5.4. *SEM image of polymer latexes. (a, b) ES5P; (c, d) ES8P2. The polymerization time for the both samples is 2 hours. (e) and (f) is size of the ES5P and ES8P2 respectively determined by the statistic work. The solid line in (f) is Gaussian fit of the histogram.*

All the polymer latices are polymerized for 2 hours with BPO as initiator. The latex size remains invariable at different scattering angles in the range from 50° to 150°, which indicates the shape of the latex is spherical. The inverse latex is 50-70 nm in diameter dependent on the preparation conditions, which is consistent with the micelles size. This complies with the character of the miniemulsion, in which the size of the latex is predefined by the micelle forming as 'one-to-one copy'.[2,13]

The polymer latex is examined with Scanning Electron Microscopy (Fig. 5.4). The size of the latex is ranging from 50 to 100 nm, correctly consistent with the DLS results. It can be also seen that the proper choice of surfactant affects the morphology of the resulting latex. Using Span 80 (sample ES8P2) instead of Span 60 (sample ES5P), a more homogeneous morphology with narrow size distribution of the latex is obtained. This is due to that the inverse miniemulsion with Span 80 is more stable than that with Span 60, which suffers from coalescence and Oswald ripening leading to larger particles. Imperfect polymer particles are seen in the latex using Span 60 (Fig. 5.5). A statistic work is carried out for determination of the size and size distribution. The size distribution profile shows that ES5P (Fig. 5.4e) actually is multimodal with the main peaks at 57 and 85 nm. For sample ES8P2 (Fig. 5.4f), the size of the latex is monodisperse, with the value of 44.2 nm obtained by Gaussian fit of the histogram.

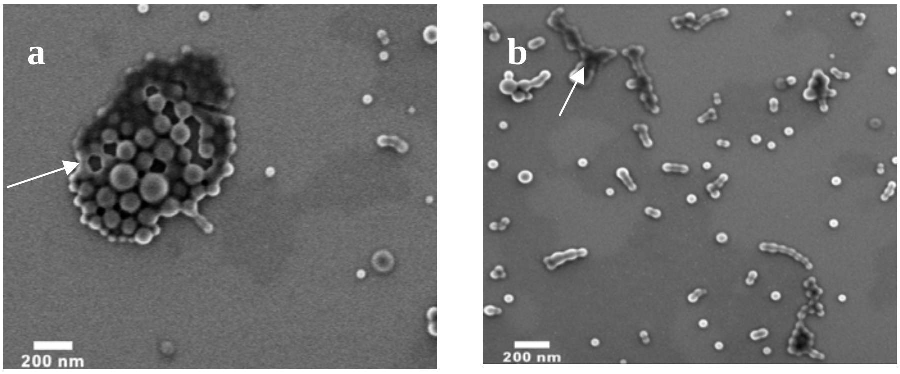

Fig. 5.5. *SEM images showing imperfect latexes formed by using surfactant Span 60 (sample ES5P). In (a) and (b), coalescence of the particles and aggregation are observed as denoted by the arrows.*

The prepared polymer latex is collected by precipitation into acetone. The obtained powder after drying in vacuo for hours appears slightly yellow. X-ray diffraction result indicates it to be non-crystalline (Fig. 5.6). The powder sample is measured on an aluminium substrate, the scattering of which is indicated in the diffractogram. The ZnPA polymer powders show only two big halos very similar to the diffractogram of precursor samples prepared by the polymer-salt complex method.

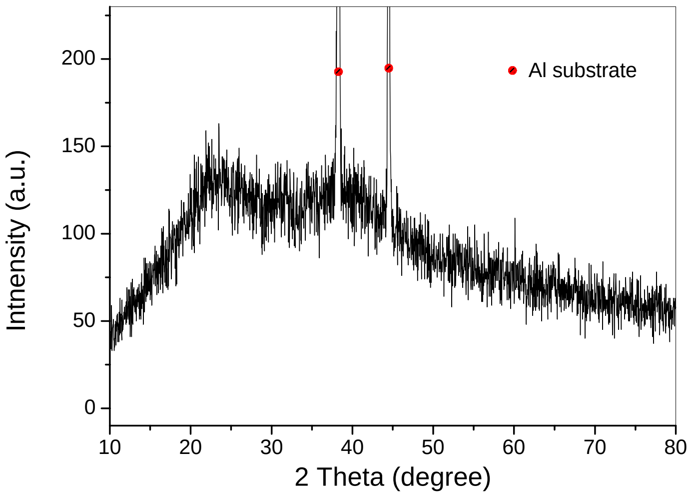

.

Fig. 5.6. *X-ray diffraction pattern of the ZnPA powder obtained by inverse miniemulsion polymerization.*

5.2.2 Formation of zinc oxide nanoparticles

The ZnPA polymer precursor converts to zinc oxide upon controlled calcination using air as carrying gas with a preset heating program. To work out the proper heating program, thermogravimetric analysis is carried out (Fig. 5.7).

Table 5.3. Composition of the ZnPA polymer samples.

Sample	C(%)	H(%)	N(%)	*Zn (%)
ES5P	47.81	5.4	/	2.7
ES8P	35.57	6.91	9.52	6.0
ES8P2	37.78	6.76	10.71	5.6

** determined by atomic absorption spectroscopy (AAS).*

In general, the decomposition consists of three weight loss steps, i.e. 150-260 °C , 260-350 °C and 350-500 °C, corresponding to three major peaks in the first-order differential analysis (DTGA) curves centred at around 200, 370, 480 °C respectively. The yield of the final product is in the range of 10%-20% dependent on the loading of zinc in the samples. The composition of the precursor samples is analyzed by elemental analysis for Hydrogen, Carbon and Nitrogen as well. Zinc content is determined by atomic absorption spectroscopy (AAS) shown in Table 5.3. The obvious lower content of zinc in sample ES5P may reflect the poor efficiency of Span 60 as emulsifier, with which the inverse miniemulsion is unstable, causing less zinc nitrate in the water pool.

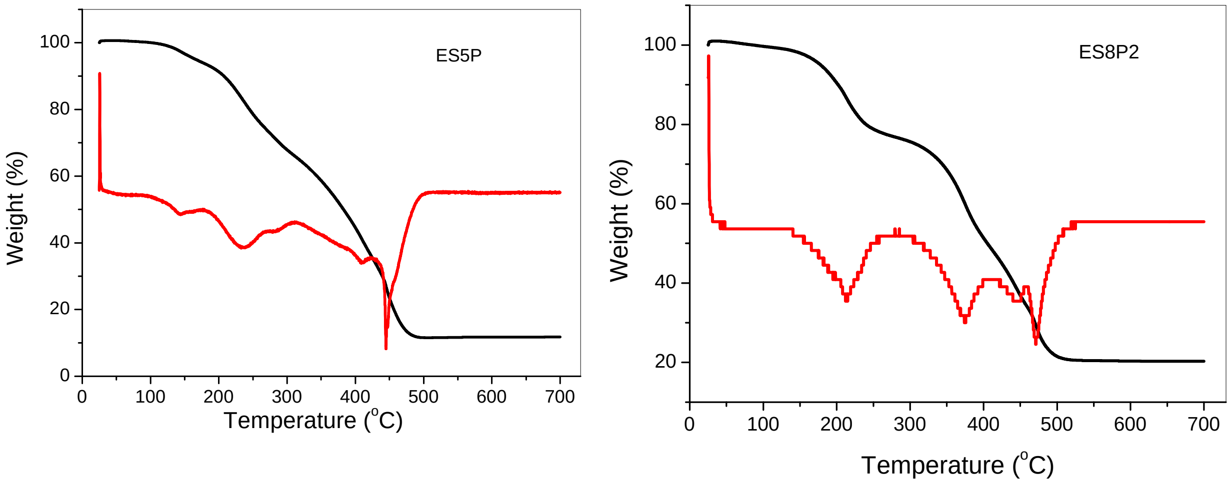

Fig. 5.7. *TGA and DTGA plots of ZnPA samples of ES5P and ES8P2.*

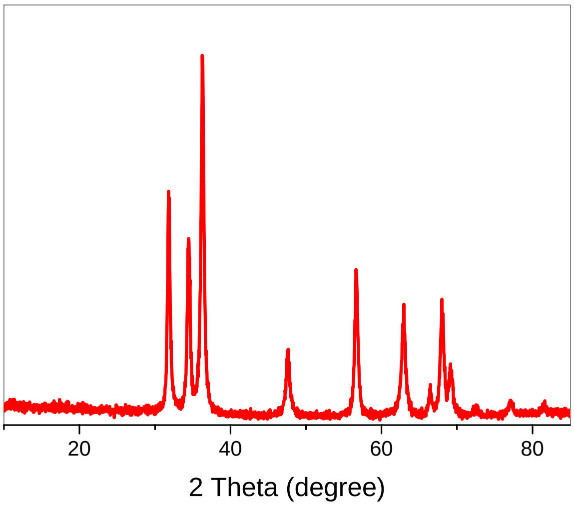

Fig. 5.8. *X-ray diffraction pattern of the as-prepared powder product upon calcination of ZnPA precursor.*

A typical program is to heat from room temperature to 500 °C with a heating rate of 5 °C/min and then anneal the sample at 500 °C for 1 hour. The obtained powder sample is colourless, and is proved to be wurtzite type zinc oxide crystals by means of XRD (Fig. 5.8). The diffraction pattern is identical with that of JCPDS file No. 36-1451. The particle size of the crystal according to the Scherer formula is 20.4 nm.

The morphology of the obtained ZnO is investigated by SEM as well. Generally, the powders consist of mainly single particles as well as slight agglomerates. The size of the nanoparticles is about 20-30 nm (Fig. 5.9 b, d) with uniform size distribution, which is consistent with the XRD result. In the scale of micron, the powders are layer-like aggregates (Fig.5.9a, c).

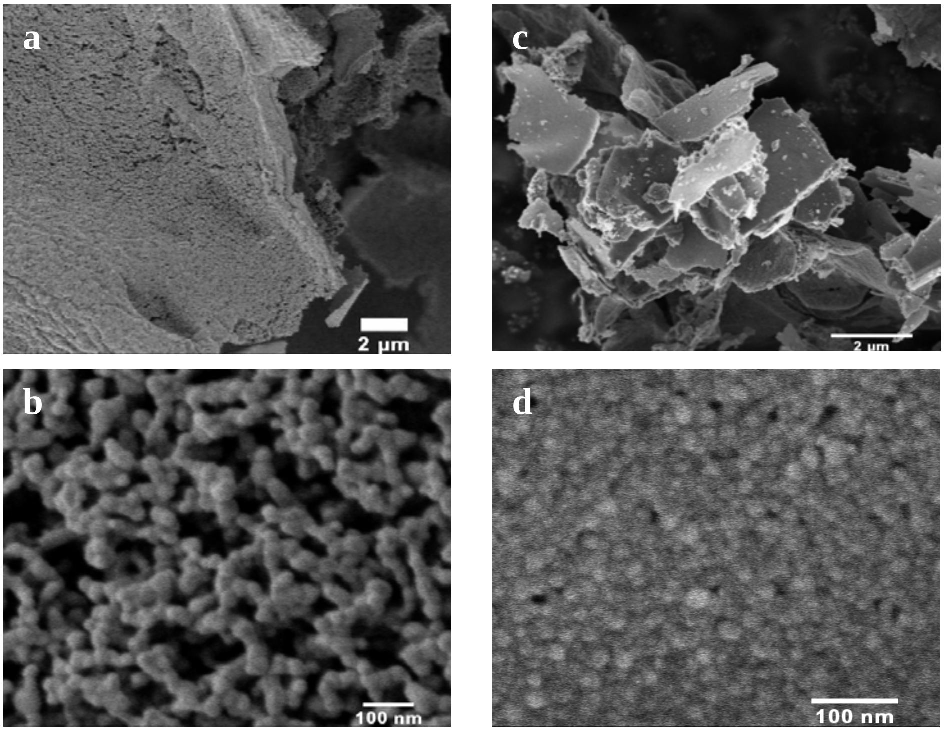

Fig. 5.9. *SEM images of ZnO nanoparticles upon calcination of polymer precursor at 500 °C. (a, b) ZnO123; (c, d) ZnO127 derived from precursor ES5P and ES8P2 respectively.*

The optical properties are one of the most important features of zinc oxide, which ensures its promising applications in photovoltaic and optoelectronic devices.[14] The photoluminescent spectra of a typical as-synthesized zinc oxide is shown in Fig. 5.10. The sample is excited at 325 and 370 nm respectively at room temperature. When excited at 325 nm, a weak NBE emission at 375 nm due to the direct recombination of free excitons is observable. The low intensity of emission possibly indicates high density of crystal defects in the sample. The blue emission is seen also in this sample; whereas the yellow-to-orange emission centred at 598 nm shows most intensive band. The yellow-to-orange emission has been reported for ZnO film and single-crystal tubular ZnO whiskers. In both cases it is attributed to crystal defect of interstitial oxygen, while for blue emission no consensus in its origin has been achieved. Considering that our zinc oxide is prepared in oxygen-rich atmosphere, we attentively assign the blue emission to zinc vacancy and emission at 598 nm to interstitial oxygen. Compared to emission centre at 583 nm for the zinc oxide prepared by polymer-salt complex method, the emission exhibits a red shift of 15 nm. This may be due to the different preparation method.

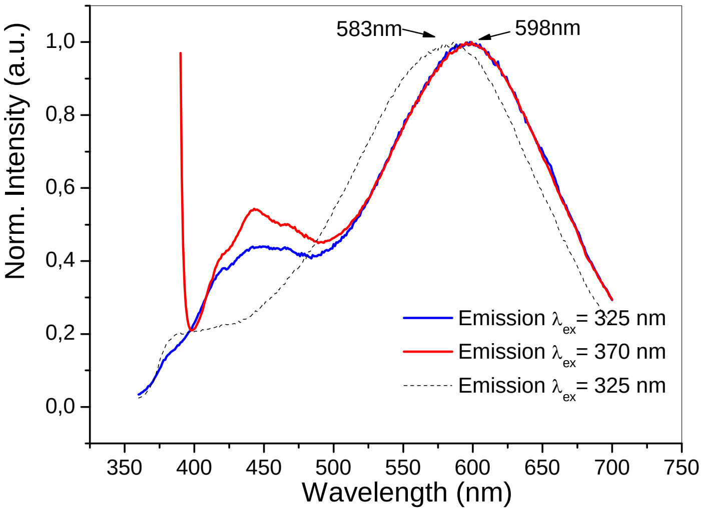

Fig. 5.10. *PL spectra of as-synthesized zinc oxide nanopowders excited at 325 and 370 nm respectively. The doted line stands for the PL spectrum of zinc oxide prepared via the polymer-salt complex method described in Ch.2.*

Infrared spectrum of the ZnO nanopowders is investigated using the conventional pellet method with KBr as diluent. A typical spectrum of the ZnO nanoparticles is presented in the range of 400-4000 cm^{-1} (Fig. 5.11). Above 2000 cm^{-1}, the absorption at 3432 cm^{-1} is due to OH- stretching at the particle surface. The weak bands at 2920 and 2850 cm^{-1} could be assigned to the antisymmetric and symmetric C-H stretching respectively,[15] which reveals the trace amount of the organic residue from the polymer precursor. For the frequency below 2000 cm^{-1}, the intense bands at 1630 and 1424 cm^{-1} may be ascribed to antisymmetric and symmetric carboxylate stretching, which is complexed with surface Zn of the ZnO crystal. Their frequency difference ($\Delta\nu = 206$ cm^{-1}) reveals that the mode of binding of the carboxylate group onto the ZnO surface might be unidentate.[16] The spectrum bears an obvious difference to that of the ZnO sample prepared by the polymer-salt complex method, giving another proof that the material property is strongly influenced by the preparation methods and conditions. The strong band centred at 449 cm^{-1} is the characteristic Zn-O bonds stretching in zinc oxide. Using the mechanism of TADC,[17] in the case of ZnO nanoparticle, the filling factor f for the as-prepared ZnO is 0.6, which indicates a state of slightly aggregation, consistent with the morphology as the SEM images show.

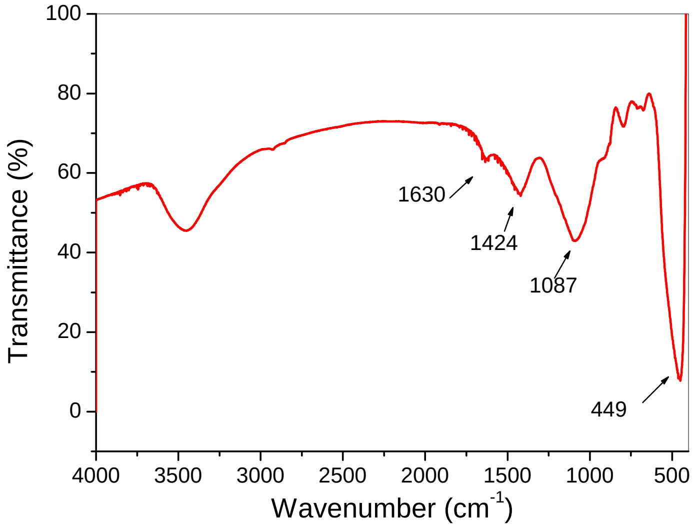

Fig. 5.11. *FT-IR spectrum in the range of 400-4000 cm^{-1} of the as-prepared zinc oxide nanopowder.*

In summary, we have successfully prepared zinc oxide nanoparticles with 20-40 nm in diameter upon calcination of zinc-loaded polymer powders. The polymer precursor is synthesized via inverse miniemulsion polymerization of the acrylic acid and zinc nitrate mixture in the water pool. The obtained polymer latex has a size of 50-100 nm predefined by the size of the corresponding inverse micelles. The photoluminescence property of the as-prepared zinc oxide is checked, which exhibits strong orange-to-yellow emission with 15 nm red shift in comparison with the ZnO obtained by the polymer-salt complex method. And the IR spectra of the samples differ with each other as well. The FT-IR spectrum shows that the as-prepared ZnO surface involves unidentate complex between zinc ions and carboxylate and also reveals a slight aggregated state of the sample morphology. The difference in the optical property between the ZnO samples prepared from different preparation methods actually reflects the difference of composition and architecture of the precursor polymers. We assume that in the polymer-salt complex method, the precursor in a great extent preserves the structure of the neutralized polyacrylic acid or polyacrylate as a linear polymer. Zinc ions are homogeneously distributed in the polymer chain. However, in the case of the method employed here, the polymerization of the zinc acrylate and acrylic acid may generate entangled and crosslinked polymer chains. The zinc ions accumulate mostly at crosslinking points of the polymer because the zinc acrylate works as crosslinker. This has significant effect on the morphology of the final zinc oxide products such as particle size, aggregation degree. The complex mode between the carboxylate and zinc as well as the defects density and location in the zinc oxide nanocrystals are affected too.

5.3 Experimental section

Preparation of inverse miniemulsion: Two solutions are prepared firstly. One is aqueous solution containing 1 g acrylic acid and 0.43 g $Zn(NO_3)_2{\cdot}6H_2O$ in 4.5 g water. The solution is adjusted to pH 8 by 25% ammonia. The other solution contains 0.5 g Span 80 and 2 g hexadecane in 40 g cyclohexane. The two solutions are mixed together and subjected to continuous stirring for half an hour. Then, a transparent inverse miniemulsion is formed after 90 seconds of untrasonication at 90% intensity.

Preparation of zinc containing polymer precursor: The obtained miniemulsion is transferred to a preheated oil bath and polymerized at 70 ^{o}C for 2 hours with adding 30 mg BPO as initiator. After completion of polymerization, the miniemulsion is milk-like. Slight yellow polymer precursor precipitates out upon pouring the miniemulsion into 3-5 times volume of acetone. The precursor was collected by centrifugation, washed with acetone and dried in vacuo.

Formation of zinc oxide nanoparticles: The precursor material was milled into fine powder and then calcined in a temperature-controlled oven under air flow with a heating rate of 5 °C min^{-1} to 550°C. The sample was isothermally annealed for 1 hour at this temperature and taken out from the hot oven in time.

INSTRUMENTAL

Dynamic light-scattering setup consisted of a 100 mW laser operating at 647.1 nm and an ALV5000e correlator. The sample solutions were filtrated with Millipore 450 nm filter before measurement and measured in 20mm cylindrical quartz cuvettes from Hellma.
pH values were measured with a Pt/KCl glass electrode attached to a pH meter (Schott CG843 set) with an integrated temperature sensor (Blueline 14pH, Schott). Before the measurements, the pH electrode was calibrated with three buffer solutions at pH 4.006, 6.865 and 9.180 at 20.0 8C (DIN Norm 19266). The zinc content in the precursors material is determined by atomic absorption spectroscopy (AAS) using a Perkin Elmer 5100 ZL spectrometer. Elementary analysis for Carbon, Hydrogen and Nitrogen was performed in the

lab of Institut für Organische Chemie in Johannes Gutenberg Universität Mainz. The optimal temperature for calcination was worked out by thermogravimetric analysis (TGA), using a Mettler Toledo TGA/SDTA 851 e instrument. Powder XRD was obtained by a Philips pulverdiffractometer using Cu Kα radiation with λ = 0.15406 nm, operating at 40 kV and 30 mA with a 0.03^{o} step size and 4 seconds as integration time. SEM images showing the morphology of ZnO nanoparticles were taken by LEO Gemini 1530 with an inlens detector (electron high tension (EHT) = 1 kV). FTIR spectra were recorded with a Nicolet 730 spectrometer (liquid N2-cooled MCT detector) with pressed pellets, which were made using KBr powder as the diluent. Room temperature photoluminescence (PL) measurements were performed on a Spex Fluorolog spectrometer.

5.4 References

[1] T. P. Hoar, J. H. Schulman, *Nature* **1943**, *152*, 102.
[2] X. E. E. Reynhout, M. Beckers, J. Meuldijk, B. A. H. Drinkenburg, *J. Polym. Sci. Part A: Polym. Chem.* **2005**, *43*, 725.
[3] a) M. Antonietti, K. Landfester, *Prog. Polym Sci.* **2002**, *27*, 689; b) K. Landfester, *Macromol. Rapid Commun.* **2001**, *22*, 896.
[4] L. Manziek, E. Langenmayr, A. Lamola, M. Gallagher, N. Brese, N. Annan, *Chem. Mater.* **1998**, *10*, 3101.
[5] M. Kishida, T. Fujita, K. Umakoshi, J. Ishiyama, H. Nagata, K. Wakabayashi, *J. Chem. Soc. Chem. Commun.* **1995**, *7*, 763.
[6] K. Kandori, K. Kon-No, A. Kitahara, *J. Colloid Interface Sci.* **1987**, *122*, 78.
[7] L. Qi, J. Ma, H. Cheng, Z. Zhao, *Colloids Surf. A* **1996** *108*, 117.
[8] P. K.Dutta, M. Jakupca, K. S. N. Reddy, L. Salvati, *Nature* **1995**, *374*, 44.
[9] S. Hingorani, V. Pillai, P. Kumar, M. S. Multani, D. O. Shah, *Mat. Res. Bull.* **1993**, *28*, 1303.
[10] J. D. Hopwood, S. Mann, *Chem. Mater.* **1997,** *9,* 1819.
[11] M. Willert, R. Rothe, K. Landfester, M. Antonietti, *Chem. Mater.* **2001**, *13*, 4681.
[12] A. Taden, M. Antonietti, A. Heilig, K. Landfester, *Chem. Mater.* **2004**, *16*, 5081.
[13] L. Herschke, PhD Dissertation, Johannes Gutenberg-Universität Mainz, Germany, **2004**.
[14] a) Ü. Özgür, Y. I. Alivov, C. Liu, A. Teke, M. A. Reshchikov, S. Doğan, V. Avrutin, S.-J. Cho, H. Morkoç, *J. Appl. Phys.* **2005**, *98*, 041301; b) D. Li, Y. H. Leung, A. B. Djurisic, Z. T. Liu, M. H. Xie, S. L. Shi, S. J. Xu, W. K. Chan, *Appl. Phys. Lett.* **2004**, *85*, 1601; c) G.-C. Yi, C. R. Wang, W. I. Park, *Semicond. Sci. Technol.* **2005**, *20*, S22; d) L. Spanhel, M. A. Anderson, *J. Am. Chem. Soc.* **1991**, *113,* 2826.
[15] a) P. D. Cozzoli, A. Kornowski, H. Weller, *J. Phys. Chem. B* **2005,** *109,* 2638; b) P. J. Thistlethwaite, M. S. Hook, *Langmuir* **2000**, *16*, 4993.
[16] S. Sakohara, M. Ispida, M. A. Anderson, *J. Phys. Chem. B* **1998**, *102,* 10169.
[17] a) M. A. Verges, A. Mifsud, C. J. Serna, *J. Chem. Soc. Faraday Trans.***1990**, *86*, 959; b) M. G. Kakazey, V. A. Melnikova, T. Sreckovic, T. V. Tomila, M. M. Ristic, *J. Mater. Sci.* **1999,** *34*, 1691.

6 Surface Modification of ZnO Nanoparticles

6.1 Introduction

6.1.1 Definition of Zeta potential

Solid, liquid and gas are the fundamental states of matter. If one of these states is finely dispersed in another, it is called a ‘colloidal system’. These materials are of specially practical importance in scientific fundamental research and industrial application. Particles in a colloidal suspension or emulsion usually carry an electrical charge. Zeta potential is an important parameter of particles, which may help understand and control colloidal suspensions. In certain circumstances, the particles always tend to adhere to one another and form aggregates of successively increasing size, which may settle out eventually. Therefore, the stability of colloidal particles is of special concern in research works for decades.

DLVO Theory: Derjaguin, Verwey, Landau and Overbeek developed a theory (DVLO theory) in the 1940s that suggests the stability of a particle in solution is dependent upon its total potential energy function E_N.

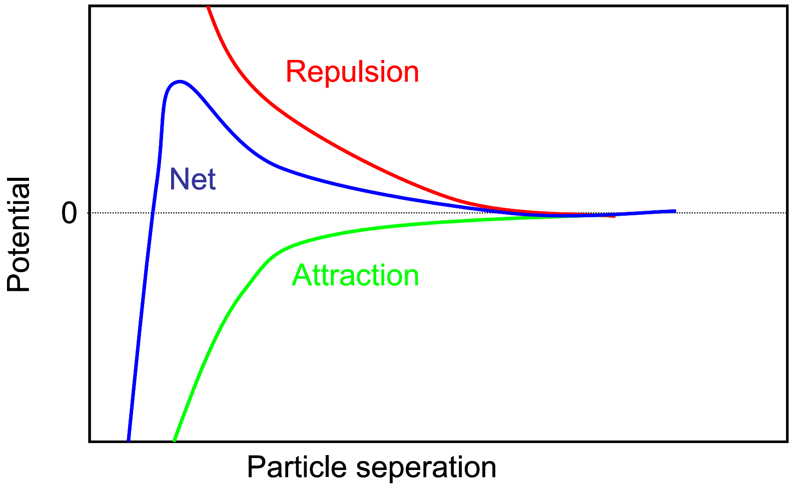

Scheme 6.1

Variation of free energy with particle separation according to DVLO theory

The total or net energy is influenced by several competing contributions and might be expressed as:

$$E_N = E_A + E_R + E_S \qquad (6.1)$$

where E_A and E_R are the attractive and repulsive energy of particles respectively. E_S stands for the energy contribution of solvent. Because solvent only has a marginal contribution over the last few nanometers of separation, E_N is primarily dependent on the balance of E_A and E_R (Scheme 6.1). This theory proposes that an energy barrier resulting from the repulsive force prevents two particles approaching one another and adhering together. In case that the particles collide with sufficient energy to overcome the barrier, they will come into contact, where they adhere strongly and irreversibly together due to the attractive force. Thus the colloidal system is stable, if the particles have a sufficiently high repulsion. On the contrary, if a repulsion mechanism does not exist then coagulation will take place.

Electrical Double Layer: The double layer model is used to visualize the ionic environment in the vicinity of a charged particle and explains how electrical repulsive forces occur.
The development of a net charge at particle surface affects the distribution of ions in the surrounding interfacial region, resulting in an increased concentration of counter ions (ions of opposite charge to that of the particle) close to the surface, forming an electrical double layer (Scheme 6.2).

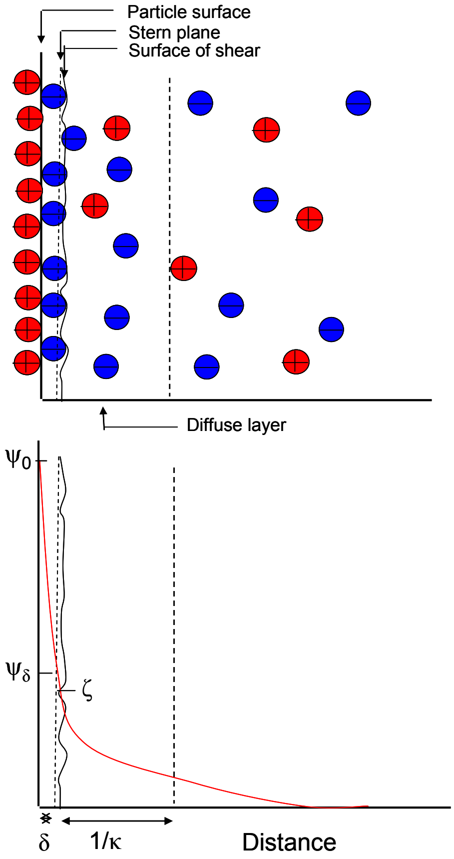

Scheme 6.2.

The double layer structures with indication of the different parts and respective potential.

The liquid layer surrounding the particle consists of two parts: an inner region, namely the Stern layer, where the ions are strongly bound to the particle and an outer, called diffuse layer region where the ions are less firmly attached. Within the diffuse layer there is a notional boundary inside which the ions and particles form a stable entity. When a particle moves (e.g. due to gravity), ions within the boundary move with it, but any ions beyond the boundary do not travel with the particle. This boundary is called the surface of hydrodynamic shear or slipping plane.

The potential that exists at this boundary is known as the *Zeta potential*, ζ. Due to the experimental problems in determination of the electrostatic potential at the beginning of the diffuse layer, this potential normally is simply approximated by measuring the ζ-potential. In aqueous solution, pH is the most important parameter that affects zeta potential. A zeta potential value on its own without defining the solution conditions is a virtually meaningless number.

The existence of electrical charges on the surface of particles enables them to interact with an applied electric field, which is collectively defined as *electrokinetic effects*. There are four distinct effects depending on the way in which the motion is induced, including electrophoresis, electro-osmosis, streaming potential and sedimentation potential.

Electrophoresis: It is defined as a phenomenon that charged particles suspended in the electrolyte are attracted towards the electrode of opposite charge, when an electric field is applied across an electrolyte. The movement of charged particles in electrophoresis is opposed by viscous forces. When equilibrium is established between these two opposing forces, the particles move with constant velocity v. The velocity of a particle in a unit electric field is referred to as its electrophoretic mobility, expressed by Henry's equation as

$$\mu_E = \frac{2\varepsilon\xi}{3\eta} f(\kappa r) \qquad (6.2)$$

where η is the viscosity of medium; ε is the dielectric constant of the medium and $f(\kappa r)$ is a function of the *Debye length* (κ, reciprocal value of the thickness of the double layer) and the radius of the particle (r). Two values are generally used as approximations for the $f(\kappa r)$ determination - either 1.5 or 1.0.

Electrophoretic determination of zeta potential is most commonly made in aqueous media and moderate electrolyte concentration. $f(\kappa r)$ in this case is 1.5, and this is referred to as the Smoluchowski approximation for systems with particles larger than about 0.2 microns dispersed in electrolytes containing more that 10^{-3} molar salt. For small particles in low dielectric constant media (e.g. non-aqueous media), $f(\kappa r)$ becomes 1.0 and allows an equally simple calculation. This is referred to as the Huckel approximation.

6.1.2 Review on surface modification and applications

Nanoparticles or nanocrystals of semiconductor materials are of great interests for science and technology, which have been extensively studied in the last decade due to its wide application in light emitting diodes,[1] catalyst,[2] gas sensor[3] and biolabels.[4] Their different characteristics with bulk materials are due to the small grain size and high interfacial surface areas. The surface of the nanoparticles is therefore unstable because of the high free energy. In order to minimize the surface energy, the particles either tend to aggregate with one another or absorb small molecules on their surface.

Early research in the field of colloid synthesis often met problems of flocculation or precipitation of final products. For preventing the colloid particles from agglomerating or further growing, thus maintaining particles in solution, stabilizers are added to the reaction system. The stabilizer is chemically or physically absorbed on the surface of the growing colloidal particles, quenching further adding crystal units to the bulk. Thus, nanometer-sized semiconductors or even quantum dots might be obtained. In other word, the stabilizer in this category of reactions may work as ‘size controller’. In the 1980s, Henglein[5] reported the successful preparations of CdS particles in aqueous solution adding polyphosphate as stabilizer. This might be one of the pioneering works in this field. Nowadays, various kinds of stabilizers such as trioctyl phosphine,[6] thiols,[7] amines,[8] amino acid[9] and polymers[10] have been widely used in nanostructured colloid synthesis.

The technique using stabilizer in colloidal chemistry is inherently connected with a more common method for functionalizing the surface of nanoparticles, named ‘surface modification’. The basic principle is to anchor external small molecules or polymers to the particles surface via reaction of the surface groups with the ligands.[11] Surface modification improves physical and chemical properties to nanomaterials. At the same time, surface ligands with chemical specificity can introduce a higher level of nanoparticles structural organization and new chemical/physical properties related to their collective behavior.

For example, long-term stability of nanoparticles in both solution and bulk polymers is still a technically challenge.[12] The nanoparticles tend to aggregate irreversibly together under ambient condition. Surface-modified method can significantly enhance the stability of nanoparticles and improve their compatibility with polymer matrix to form nanocomposites. Whang et al.[12b] successfully prepared highly transparent and stable luminescent

ZnO/poly(hydroxyethyl methacrylate) nanocomposites via copolymerization of monomer with organic molecule (TPM)-modified ZnO nanoparticles. The stability of ZnO nanoparticles are highly improved after the TPM modification.

The surface modification of nanoparticles with organic molecules is useful in medical application. For instance, magnetic nanoparticles such as iron oxide offer great opportunities toward developing drug delivery vehicles as anticancer agent.[13] The surface of the iron oxide nanoparticles are modified with hydrophilic polymers such as pluronic polymers (imparting aqueous dispersity to the nanoparticles), which may bind chemically with the therapeutic agents on the polymer layers. These particles preserve the magnetic properties and show good magnetic targeting ability of the carrier system in vivo. All in all, surface modification is an important technique in modern material science.

In this work, we attempt to modify (doped-) zinc oxide nanoparticles, which are obtained from pyrolysis of polymer precursor, with a small molecule (tetrabutylammonium phosphate). Our aim is to enhance the stability of the nanoparticles and their dispersibility in bulk polymer to form stable ZnO/polymer nanocomposite.

6.2 Results and discussion

6.2.1 The preparation route for surface modification of ZnO nanoparticles

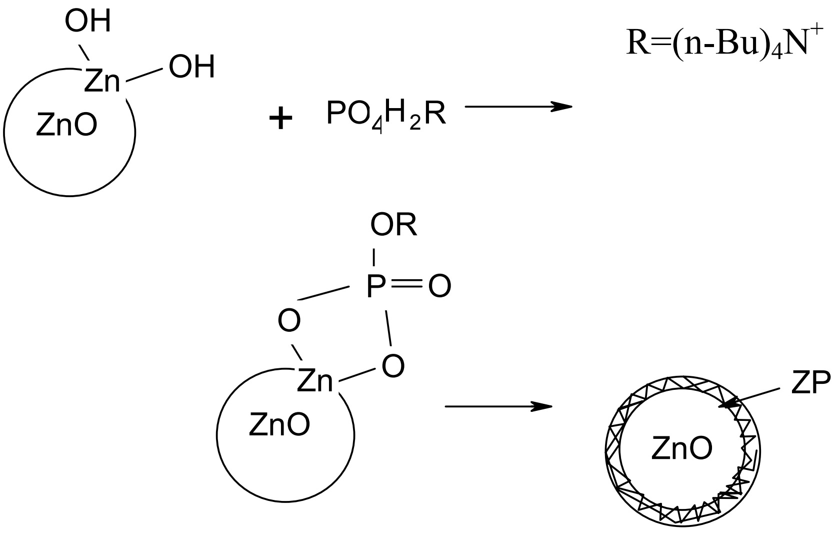

Fig. 6.1. *Scheme representing the surface modification of ZnO nanoparticles in this work.*

Fig. 6.1 shows the schematic representation of general route of our surface modification reaction. The method is similar as the work of Feddern,[14] but we make some important changes. Firstly, we use ultrasonication to enhance the reaction between the nanoparticles and modifier, while they didn't use it; secondly, the surface modification was applied on ZnO quantum dots in their case, but our ZnO nanoparticles normally have size in the range of 20-50 nm; Mostly importantly, they didn't give any characterization on the success of anchoring of the modifier on the ZnO surface. In other word, we for the first time give clear experimental evidences of surface anchoring of modifier molecules.

The procedure starts from preparation of the surface modifier-tetrabutylammonium phosphate via the neutralization reaction between the tetrabutylammonium hydroxide and phosphoric acid in alcoholic medium. The chemical reaction could be described as

$$[(n\text{-}Bu)_4]NOH + H_3PO_4 \longrightarrow [(n\text{-}Bu)_4NO]PO(OH)_2 + [(n\text{-}Bu)_4NO]_2PO(OH)$$

The two products are monosalt and bisalt, which differ with each other in the number of hydroxide or tetrabutylammonium group. The ratio between them is dependent on pH and stoichiometry of the reactants.

Thereafter, the obtained modifier solution was added into the alcoholic suspension of zinc oxide nanoparticles (typical concentration of 1-5 g/L) with the zinc to phosphate ratio of 1:10. An opalescent dispersion is obtained after the reaction between the phosphate groups with the hydroxide groups on the particle surface. Vigorous stirring and ultrasonication is applied to the reaction mixture to enhance the interaction. The modified nanoparticle is assumed to have a core-shell structure with zinc oxide in the core and the organic molecules at the shell as indicated in Fig. 6.1. The modified particles could be purified and collected with ultracentrifugation after several washing procedures.

6.2.2 Characterization of the modified-ZnO nanoparticles

The object of this work is to achieve grafting of functionalized group on the metal oxide surface without destructing the morphology of the metal oxide, i.e. the spherical shape and the particle size. Thus, acidity and a proper ratio between zinc and phosphate are very important. We tried to directly use phosphoric acid to modify zinc oxide nanoparticles with different ratio of Zn/P from 1:1 to 1:100. UV spectra are recorded for the reaction mixture in each case as seen in Fig. 6.2a. For pure ZnO and the reaction mixture with ZnO and H_3PO_4 of 1:1 and 1:10, an evident absorption peak at 373 nm is observed, which is consistent with the ZnO bandgap (3.3 eV). This peak however disappears for the solution with ratio of ZnO and H_3PO_4

as 1:100, indicating the complete dissolution of ZnO nanoparticles in very strong acidic environment. Thus, we partially neutralize the phosphoric acid and choose zinc to phosphate ratio as 1:10, so that the ZnO has enough possibility to react with the modifier but without dissolution. Fig. 6.2b shows the UV spectra of the modified ZnO nanoparticles in ethanol solution after redispersion. The absorption peak at bandgap clearly indicates the preservation of ZnO particles.

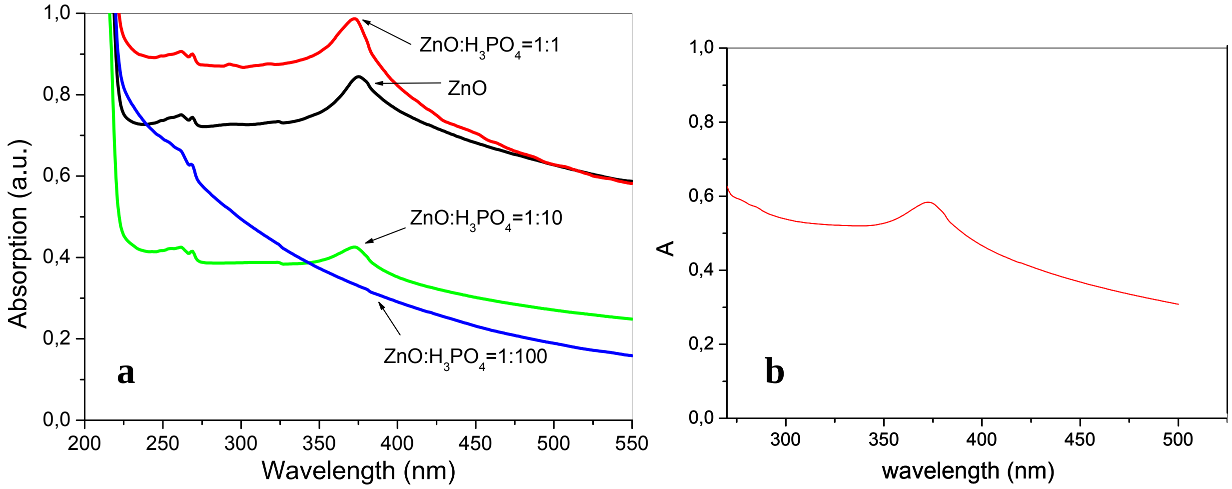

Fig. 6.2. *a) UV spectra of reaction mixture of ZnO nanoparticles with different amount of* H_3PO_4*; b) UV spectra of the modified ZnO nanoparticles dispersion in ethanol.*

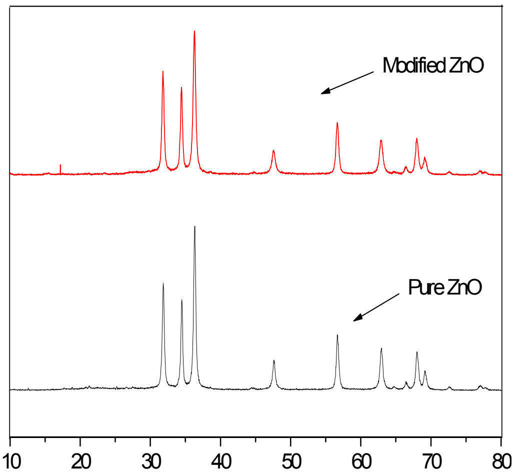

Fig. 6.3. *X-ray diffraction patterns of pure ZnO and modified ZnO nanoparticles.*

The phosphate-modified ZnO powders are investigated by X-ray diffraction (Fig. 6.3), the diffractogram of which corresponds to wurtzite-type zinc oxide. In comparison with the unmodified ZnO, no significant changes in the diffractogram are seen, which is possibly due to the very thin layer of the coating for only several nanometers as expected. Similar results are found in OA-Pluronic-stabilized iron oxide nanoparticles[13a] and phosphate-modified zirconia particles.[15] Thin modifier layer does not change the XRD pattern of the nanoparticles in all these cases. In the XRD result of Feddern, they found the formation of zinc phosphate, due to the reaction of ZnO quantum dots and modifiers.

Evidence of successful coating of tetrabutylammonia phosphate is given by elementary analysis. The results show that the modified ZnO nanoparticles contain 1.3% carbon and 0.31% hydrogen. The ratio of C/H is 1:2.86, which is very close to the ratio of the two elements in the tetrabutyl group (1:2.25), indicating unambiguously the existence of the modifier in the sample. For unmodified ZnO nanoparticles, the content of carbon or hydrogen is below the determination limit of the device. Table 6.1 lists elementary analysis results of some samples. It shows different concentration of organics on the particles surface obtained at different reaction conditions.

Table 6.1. *Composition of the modified ZnO samples.**

Sample	C(%)	H(%)	C/H
ZnOSIIIC	1.3	0.31	1:2.86
ZnOSIVA	1.22	1.04	1:10.2
ZnOSIIB	2.77	0.73	1:3.16

** the results are obtained by average of two independent measurements.*

To confirm that the phosphate group is chemically adsorbed to the surface of zinc oxide nanoparticles, FT-IR spectra were recorded at room temperature for unmodified and modified ZnO powders. In Fig 6.4a, the zinc oxide sample, named ZnO127, prepared by pyrolysis of zinc-loaded polymer particles made in inverse miniemulsion (Ch. 5). Beyond 3000 cm^{-1}, the band of hydroxide groups is clearly shown. In the range of 2000-3000 cm^{-1}, intense absorptions at 2926 and 2845 cm^{-1} are observed in the modified ZnO nanoparticles, which are however not clear in the unmodified ZnO. These two peaks are assigned to the antisymmetric and symmetric C-H stretching vibrations of the -CH_2- groups in the hydrocarbon moiety (in this case, the butyl groups).[16] Other than the broad peak at 1094 cm^{-1} due to C-O in the unmodified ZnO nanoparticles, P-O stretching at 1038 cm^{-1} is observed for modified ZnO,[19] indicating the success anchoring of modifier molecule on the particle surface. The strong peak at 451 cm^{-1} is the characteristic peak of Zn-O stretching shown in both samples.

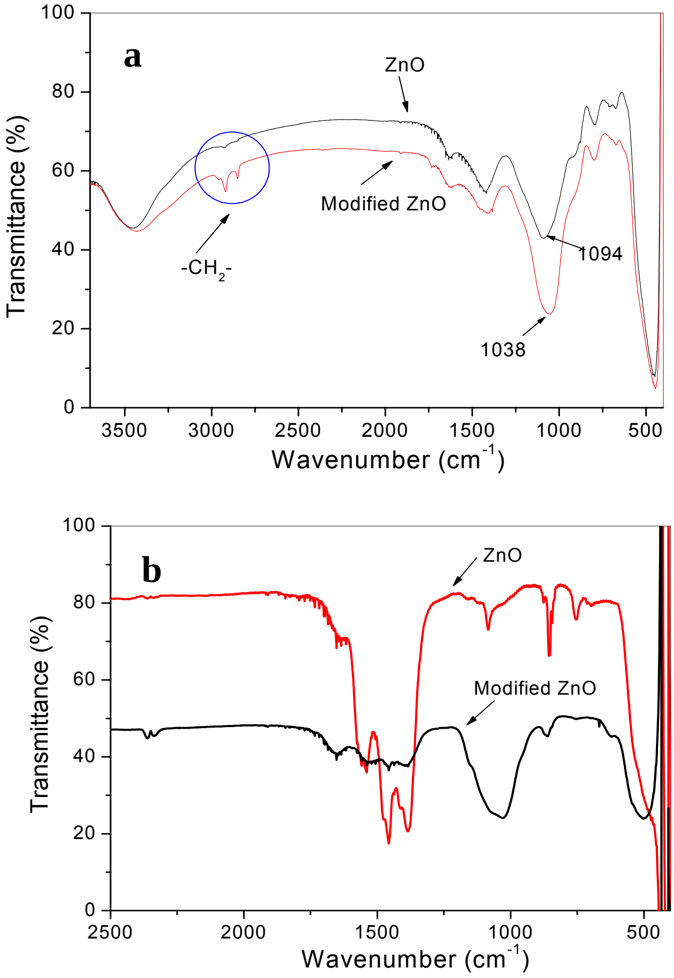

Fig. 6.4. *FT-IR spectra of pure ZnO and modified ZnO nanoparticles. (a) sample ZnO123; (b) sample ZnO180.*

The differences in the spectra in the range of 800-1500 cm^{-1} are more evident in Fig. 6.4b, which shows the spectra of another zinc oxide sample (ZnO180). This sample is obtained by the polymer- salt complex method as described in Ch2. The intense bands of antisymmetric and symmetric stretching of carboxylate group shrink considerably due to the replacement by phosphate groups. More importantly, the strong P-O stretching at 1030 cm^{-1} with a shoulder at 942 cm^{-1} due to P-O-H bond[20] appears in the modified ZnO sample, which is however not shown in the unmodified sample.

It is expected that the modifier molecules could be bound to zinc ions through one or two P-O-Zn bond, namely unidentate and bidentate coordination. This is reflected by ^{31}P solid state NMR spectrum as seen in Fig. 6.5, which shows two peaks at 7.7 and 9.5 ppm. Similar results have been reported in phosphonate-modified titania particles and zirconia particles, where the phosphate has three possible coordination types with Ti^{4+} or Zr^{4+}. Accordingly, three chemical shifts could be detected by ^{31}PNMR. And it is found that the bidentate coordination has a large chemical shift than the tridentate coordination case in the modified titania sample. Therefore, we tentatively assign the signal at 9.5 ppm to unidentate coordination between phosphate and zinc ion in our case.

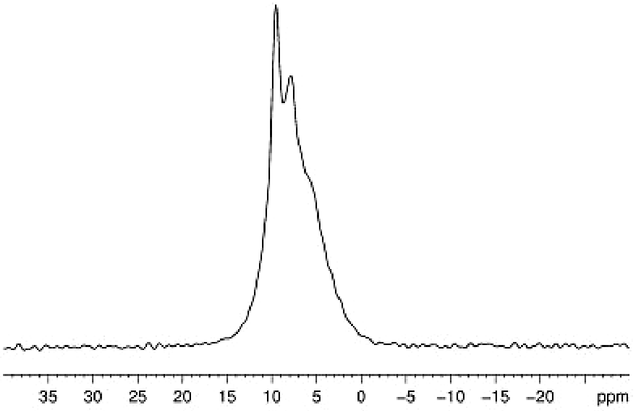

Fig. 6.5. *MAS-^{31}PNMR spectra of the modified zinc oxide nanoparticles sample.*

The size of the ZnO samples is measured by dynamic light scattering method with the Malvern Zetasizer at a fixed angle of 90°. Fig. 6.6 presents the size and size distribution of ZnO nanoparticles and modified ZnO nanoparticles. We note the difference in the results of intensity and number size distribution. As well known, the intensity of light scattering is proportional to the 6th power of particle size. Therefore, the possible introduction of dust into the sample may greatly distort the results. Fig. 6.6a shows the size distribution calculated on number and intensity for the sample of modified ZnO nanoparticles respectively. The significant difference between them indicates the existence of aggregates in the sample as well as possible dust particles. Previously, we used scanning electron microscopy to study the morphology of the ZnO nanoparticles and calculate the size distribution based on a statistic work (see Ch 2, 3 and 4). The size distribution obtained by SEM is actually a number distribution, which is comparable with the DLS number results. Therefore, in this work we only use the results of number size distribution.

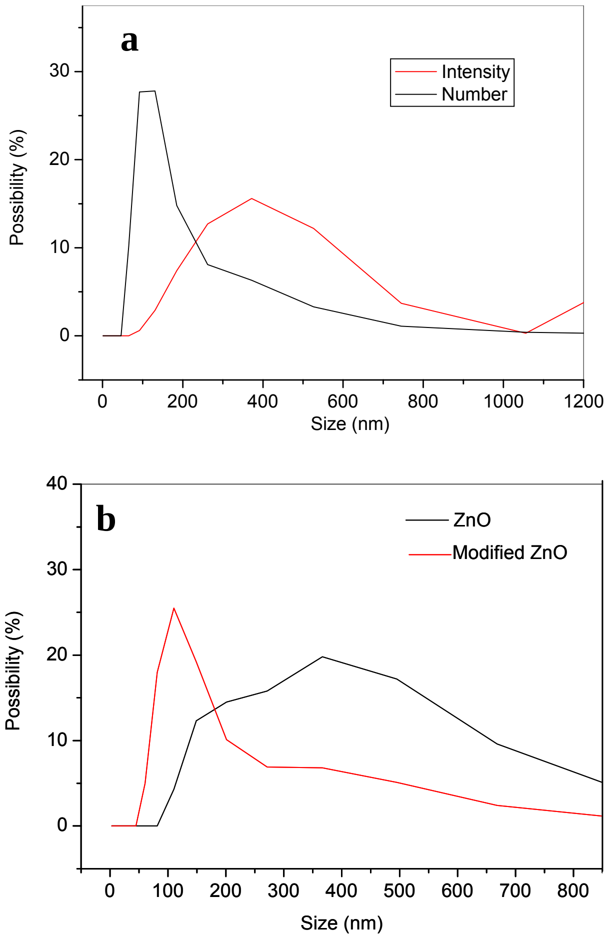

Fig. 6.6. *(a) Dynamic light scattering results showing difference in intensity and number distribution of modified ZnO in water dispersion. (b) DLS results showing size and size distribution of ZnO nanoparticles before and after surface modification.*

Fig. 6.6b compares the size and number size distribution of ZnO nanoparticles before and after the surface modification. It is seen that for the unmodified ZnO, the size of the particles has a wide number distribution with centre at 250 and 400 nm, indicating a large amount of particle aggregates. After the surface modification, the size of the particles decreases to about 120 nm and the size is monodisperse. The component of particle aggregates in the sample decreases from about 15% to less than 4%, which suggests that the weak aggregates could be separated into single particles or small clusters by means of this surface modification.

The change in morphology of ZnO nanopowders by surface modification is checked by means of SEM as shown in Fig. 6.7. This zinc oxide sample used here is named ZnO127. The unmodified particles show aggregate structure with particle size around 20-50 nm (Fig. 6.7 a, b). For the modified nanopowders, the particle shape and size is unchanged compared with the unmodified zinc oxide, indicating that the surface reaction does not destroy the spherical structure of the particles. Especially, the surface coating with organics on the particles is clearly shown in Fig. 6.7c,d. Actually, most particles are single particle for modified zinc oxide. In the solid-state powders, these particles are stacked together but are readily redispersed in either ethanol or water.

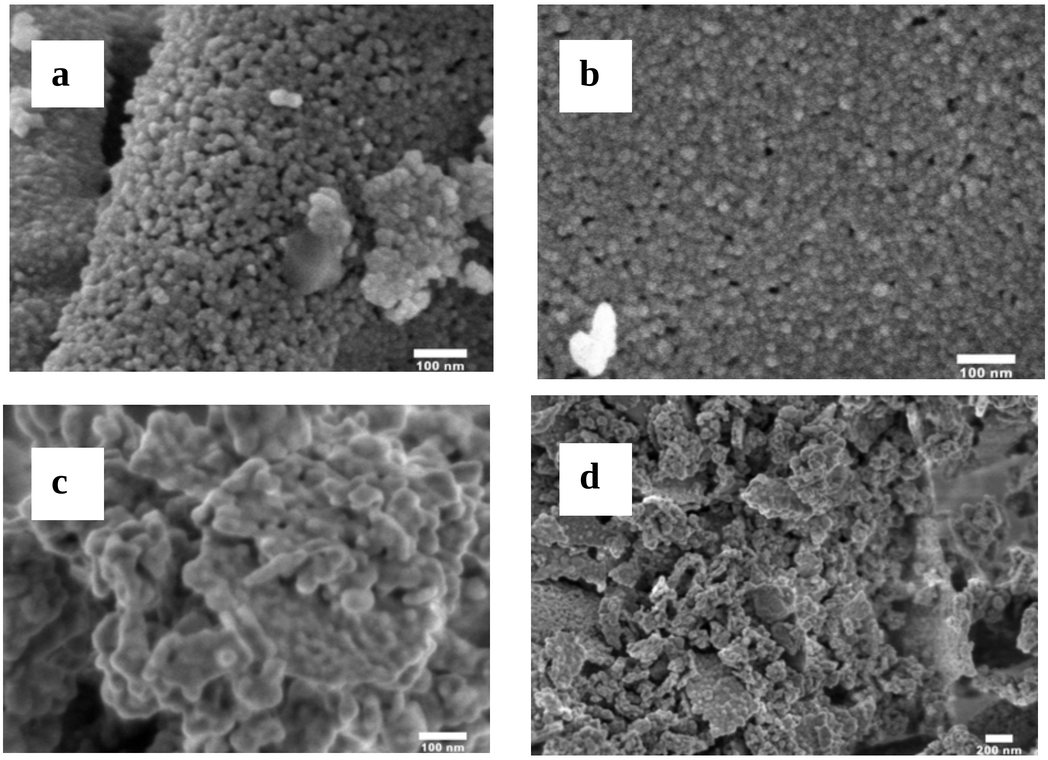

Fig. 6.7. *SEM images showing the morphology of (a, b) unmodified ZnO nanopowders and (c, d) modified ZnO nanopowders.*

SEM samples could be prepared by dropping the ZnO dispersion onto a silicon wafer for direct observation. Fig. 6.8 a,b shows the morphology of the nanopowders of magnesium-doped zinc oxide, which consists of mainly particle aggregates in the solid state. The particle has a wide size distribution as seen from the image. After the surface modification, we see small portion of the aggregate sized at 1 micron and mostly the well-separated particles (Fig. 6.8 c,d). The size of the individual particles varies from 20 nm to 100 nm, showing that the doped-ZnO has a wider size distribution than pure ZnO nanoparticles obtained by a similar synthetic procedure.

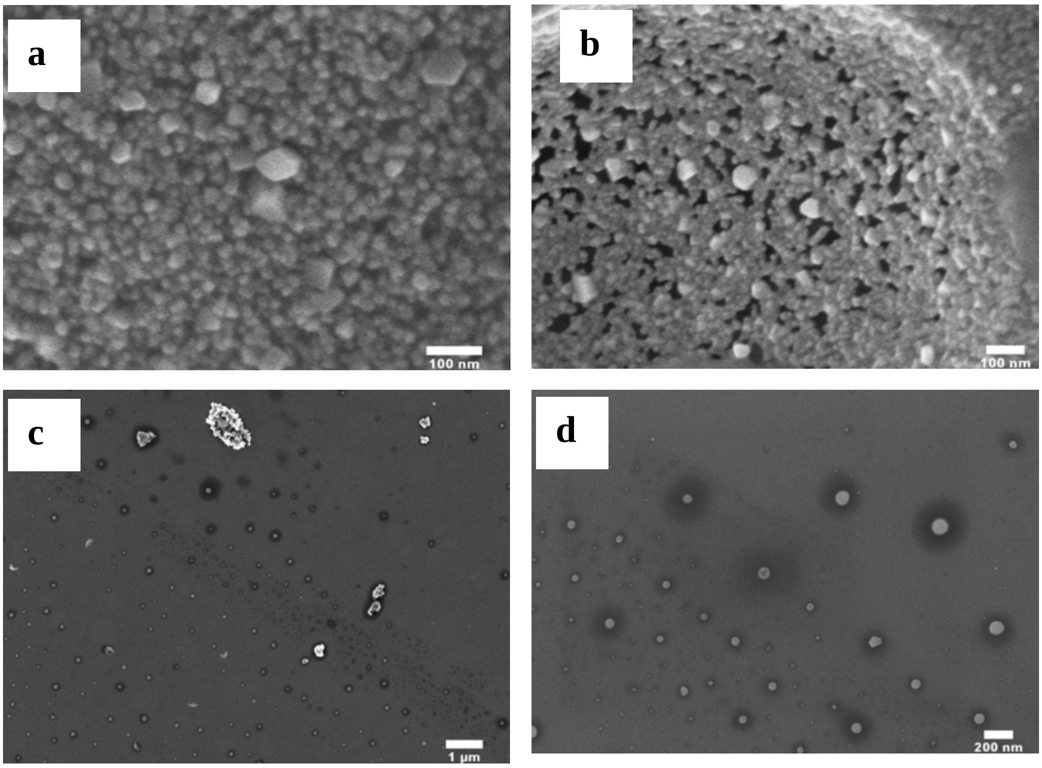

Fig. 6.8. *(a, b) SEM showing the morphology of Mg-doped ZnO nanopowders. (c, d) SEM images of the modified nanoparticles. Sample is prepared by dropping particle dispersion on a clean silicon wafer.*

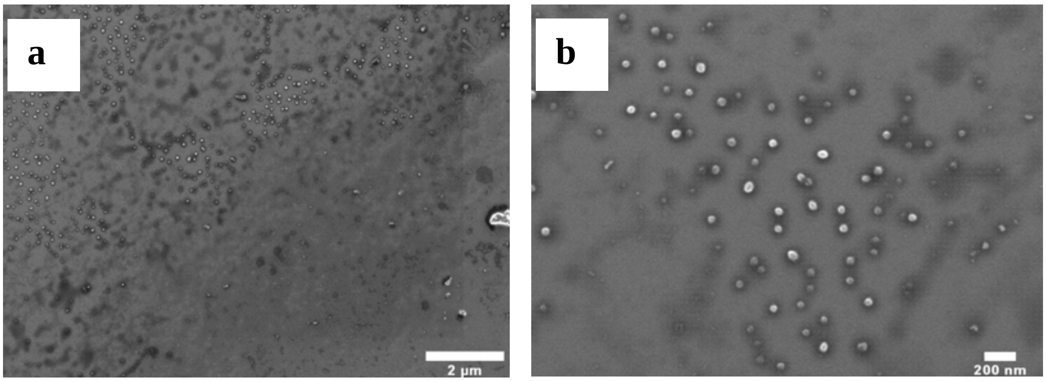

Fig.6.9. *SEM images of ZnO nanoparticles modified with H_3PO_4.*

As controlled experiment for comparison, the undoped-ZnO nanoparticles treated directly with phosphoric acid with Zn/P 1:10 are also studied. The modified particles are redispersed in ethanol. The SEM samples are prepared using similar procedure with the sample of Fig. 6.8 on a silicon wafer for investigation. In the images, most particles are well dispersed and aggregates are rarely observed (Fig. 6.9). The results prove that the essence of this surface reaction is the neutralization of acidic groups of the modifier with ZnO surface hydroxide groups or possible opening of Zn-O-Zn bonds. The reason we use tetrabutylammonium phosphate here is based on two considerations: firstly, $[(n\text{-Bu})_4]NOH$ is employed to decrease the acidity of H_3PO_4 to avoid etching or devouring the ZnO nanoparticles, which would impair the utility of the material; Secondly, the organic groups $[(n\text{-Bu})_4]N^+$ may improve the compatibility of the particles with polymeric matrix to form a stable nanocomposite.

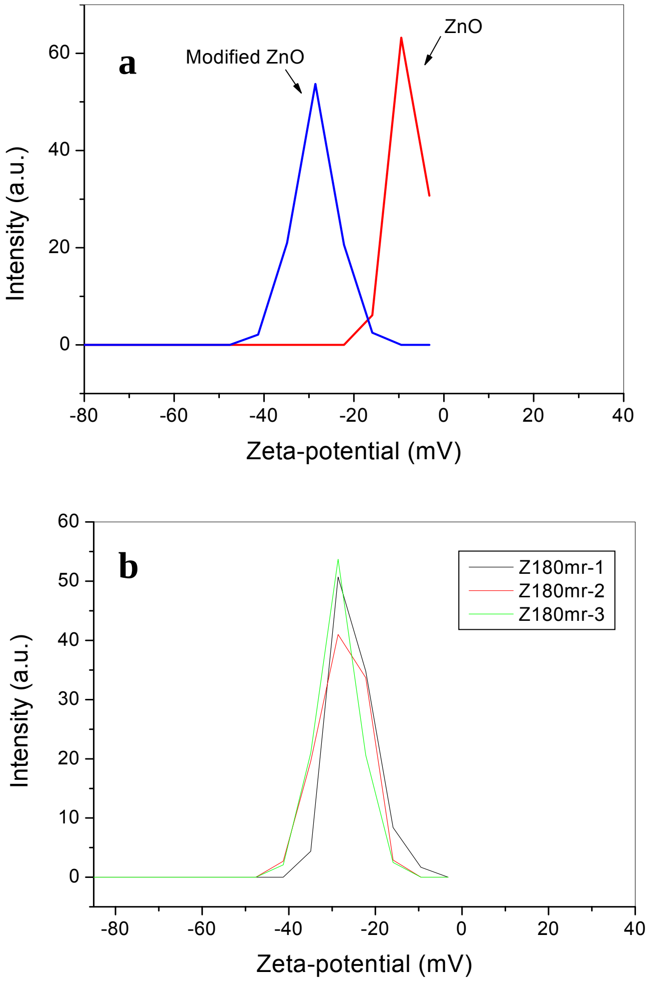

Fig. 6.10. *(a) Zeta-potential results of the unmodified and modified ZnO nanoparticles. (b) Zeta-potential results of three individual measurement of the modified ZnO dispersion showing excellent reproducibility.*

The stability of colloid particles could be achieved by two mechanisms, steric repulsion and electrostatic stabilization. As an important method to achieve colloid stability, the surface modification of particles will alter the charge density of the particle surface, leading to drastically changes of some surface properties, including surface charge in solution, polarizability in the dried state, and hydrophobic character. The Zeta-potential experiment of the unmodified and modified ZnO nanoparticles was carried out in 10^{-3} KNO_3 water dispersion with ZnO concentration of 0.05%-0.1%. The use of salt solution is to balance the ion strength of the ZnO dispersion, according to Music's method.[17] For unmodified ZnO particles, the pH of the dispersion is around 8.5 and the Zeta-potential is -9.3 mV, while the modified ZnO has a similar pH value with Zeta-potential of -28.8 mV (Fig. 6.10a). The change of Zeta-potential unambiguously indicates the success of the surface modification using this method. The increase of negative charge at the surface is due to the anchoring of phosphate groups. As is well known, a dispersion is considered stable when the absolute value of the zeta-potential exceeds 30 mV. Therefore, our modified ZnO nanoparticles dispersion is nearly stable. The experiment shows excellent reproducibility with deviation of less than 0.2% for three separate measurements (Fig. 6.10b).

In summary, we succeed in surface modification of ZnO nanoparticles, which were prepared by pyrolysis of a polymeric precursor, with a salt of tetrabutylammonium phosphate. The surface reaction achieves anchoring the phosphate groups on the particle with preservation the spherical shape and size of the particles. This was evaluated by means of elementary analysis, FT-IR, ^{31}PNMR, and electron microscopy. Light scattering results indicate the decrease in size of ZnO particle aggregates after the surface reaction. The stability of the ZnO nanoparticles in aqueous dispersion is enhanced as shown in the significant change of the value of zeta-potential from -9.3 mV (unmodified ZnO) to -28.8 mV (modified ZnO). The modified ZnO nanoparticle is promising for preparation of ZnO/polymer nanocomposite.

6.3 Experimental Section

Preparation of tetrabutylammonium phosphate: 6.7 ml 85% H_3PO_4 (0.1 mol) is dissolved in 20 ml ethanol followed with dropwise adding 40% tetrabutylammonium hydroxide aqueous solution with pH values less than 8.0. The solution is stirred for half an hour after the mixing. Then, the solution is diluted to 250 ml in volume with adding large amount of ethanol, the phosphate concentration of which is calculated to be 0.4 mol/l.

Surface modification of ZnO Nanoparticles: Typically, 40 mg zinc oxide nanopowders were added to 20 ml ethanol to form a suspension after vigorous stirring for 30 min. Then, 12.5 ml prepared tetrabutylammonium phosphate solution (0.4 N) is dropwise added to the ZnO suspension and the ratio of ZnO and phosphate is kept at 1:10.A slight opalescent dispersion is obtained after stirring the mixture for 30 min followed with untrasonication for 90 sec with 90% amplitude. Thereafter, the solid of modified ZnO nanoparticle are collected by ultracentrifugation. The solids are purified with the redispersion-washing-ultracentrifugation circles successively with ethanol-water mixture (80 vol.%-20 vol.%), pure ethanol and acetone to remove the unreacted phosphate and other species similar with Koch's method.[18] Finally, a white powder is obtained after drying it in vacuo over night.

INSTRUMENTAL

UV spectra were recorded at room temperature with a Perkin-Elmer Lambda 2 UV/Vis/NIR spectrophotometer. The concentration of a ZnO or modified ZnO dispersion is 0.5g/L. Electrophoretic mobilities were measured by the so-called light scattering electrophoresis (also known as laser Doppler microelectrophoresis) with the same automatic device used for the particle size determination (Malvern Zetasizer 3000HS). The zeta-potential was calculated from the electrophoretic mobilities according the Hückel model. The measurements were performed by dispersing about 10 mg of a sample into 20 ml 10^{-3}M KNO_3 solution using an ultrasound bath. The pH value of the suspension was regulated by the addition of 0.1 M KOH or HNO_3 solution.

pH values were measured with a Pt/KCl glass electrode attached to a pH meter (Schott CG843 set) with an integrated temperature sensor (Blueline 14pH, Schott). Before the measurements, the pH electrode was calibrated with three buffer solutions at pH 4.006, 6.865 and 9.180 at 20.0 8C (DIN Norm 19266).

FTIR spectra were recorded with a Nicolet 730 spectrometer (liquid N2-cooled MCT detector) with pressed pellets, which were made using KBr powder as the diluent.

Elementary analysis for carbon, nitrogen and hydrogen was done in the lab of inorganic chemistry in the University of Mainz.

^{31}P liquid and solid-state MAS-NMR spectra were recorded on a Bruker DSX 300 MHz spectrometer at room temperature. Chemical shifts are calibrated with 85% H_3PO_4.

Room temperature powder XRD was obtained by a Philips pulverdiffractometer using Cu Kα radiation with $\lambda = 0.15406$ nm, operating at 40 kV and 30 mA with a 0.03^{o} step size and 4 seconds as integration time.

SEM images showing the morphology of ZnO nanoparticles were taken by LEO Gemini 1530 with an inlens detector (electron high tension (EHT) = 1 kV).

6.4 References

[1] a) L. S. Li, N. Pradhan, Y. Wang, X. Peng, *Nano. Lett.* **2004**, *4*, 2261; b) N. Pradhan, D. Goorskey, J. Thessing, X. Peng, *J. Am.Chem. Soc.* **2005**, *127*, 17586.
[2] L. N. Lewis, *Chem. Rev.* **1993**, *93*, 2693.
[3] E. R. Leite, I. T. Weber, E. Longo, J. A. Varela, *Adv. Mater.* **2000**, *12*, 965; b) C. J. Martinez, B. Hockey, C. B. Montgomery, S. Semancik, *Langmuir* **2005**, *21*, 7937.
[4] S. Mornet, S. Vasseur, F. Grasset, E. Duguet, *J. Mater. Chem.* **2004**, *14*, 2161.
[5] L. Spanhel, M. Haase, H. Weller, A.Henglein, *J. Am. Chem. Soc.* **1987**, *109*, 5649.
[6] C. B. Murray, D. J. Norris, M. G. Bawendi, *J. Am. Chem. Soc.* **1993**, *115*, 8706.
[7] a) G. Carotenuto, L. Nicolais, *J. Mater. Chem.* **2003**, *13*, 1038; b) C. L. Li, N. Murase, *Langmuir*, **2004**, *20*, 1.
[8] a) N. Pinna, G. Garnweitner, M. Antonietti, M. Niederberger, *J. Am. Chem. Soc.* **2005**, *127*, 5608; b) H. Zhang, Z. Cui, Y. Wang, K. Zhang, X. Ji, C. Lu, B. Yang, M. Gao, *Adv. Mater.* **2003**, *15*, 777.
[9] K. Kanie, T. Sugimoto, *Chem. Commun.* **2004**, *14*, 1584.
[10] K. Niesz, M. Grass, G. A. Somorjai, *Nano. Lett.* **2005**, *5*, 2238; b) a) M. Oner, J. Norwig, W. H. Meyer, G. Wegner, *Chem. Mater.* **1998,** *10,* 460; c) G. Wegner, P. Baum, M. Müller, J. Norwig, K. Landfester, *Macromol. Symp.* **2001**, *175*, 349; d) T. S. Ahmadi, Z. L. Wang, T. C. Green, A. Henglein, M. A. El-Sayed, *Science*, **1996**, *272*, 1924; e) V. Juttukonda, R. L. Paddock, J. E. Raymond, D. Denomme, A. E. Richardson, L. E. Slusher, B. D. Fahlman, *J. Am. Chem. Soc.* **2006**, *128*, 420.
[11] T. Ni, D. K. Nagesha, J. Robles, N. F. Materer, S. Müssig, N. A. Kotov, *J. Am. Chem. Soc.* **2002**, *124*, 3980.
[12] a) F. M. Pavel, R. A. Mackay, *Langmuir* **2000**, *16*, 8568; b) C.-H. Hung, W.-T. Whang, *J. Mater. Chem*, **2005**, *15*, 267.
[13] a) T. K. Jain, M. A. Morales, S. K. Sahoo, D. L. Leslie-Pelecky, V. Labhasetwar, *Mol. Pharm.* **2005**, *2*, 194; b) Tiefenauer, L. X.; Kuhne, G.; Andres, R. Y. *Bioconjugate Chem.* **1993**, *4*, 347.
[14] K. Feddern, *PhD Thesis*, Universität Hamburg, Germany, **2002**.
[15] D. Carriere, M. Moreau, P. Barboux, J.-P. Boilot, O. Spalla, *Langmuir* **2004,** *20,* 3449.
[16] P. D. Cozzoli, A. Kornowski, H. Weller, *J. Phys. Chem. B* **2005,** *109,* 2638.
[17] S. Music, D. Dragcevic, M. Maljkovic, S. Popovic, *Mater. Chem. Phys.* **2002**, *77*, 521.
[18] U. Koch, A. Fojtik, H. Weller, A. Henglein, *Chem. Phys. Lett.* **1985,** *122,* 507.
[19] G. Guerrero, P. H. Mutin, A. Vioux, *Chem. Mater.* **2001,** *13,* 4367.
[20] a) J. Randon, P. Blanc, R. Paterson, *J. Membrane Sci.* **1995**, *98*, 119; b) P. D. Cozzoli, M. L. Curri, A. Agostano, G. Leo, M. Lomascolo, *J. Phys. Chem. B* **2003**, *107,* 4756.

7 Summary and Outlook

We have explored a versatile method for the production of binary metal oxides and mixed metal oxides in the form of both nanopowders and nanocrystalline films. The method is simple, environmentally friendly and is believed to be applicable to the preparation of a wide range of metal oxides preparation. It is also worthwhile to note that the method may be scaled up for production which is valuable for industry.

Zinc oxide nanoparticle preparation is a good example for application of this method. The zinc polyacrylate is formed firstly by mixing of polyacrylate and zinc nitrate followed with precipitation in nonsolvent. The obtained precursor exhibits typical polyelectrolyte behaviour, i.e. the viscosity of the polymer solution decreases with the increasing of concentration. Thermal treatment or calcination of this zinc-loaded precursor forms colorless zinc oxide powders. Combination of XRD and TGA results proves that the crystallization of zinc oxide takes place over 370 ^{o}C. The obtained ZnO is as spherical nanoparticles with diameter of 40-100 nm. The morphology of ZnO is influenced by some parameters including molecular weight of polyacrylic acid, zinc content in the precursor and calcination temperature. Photoluminescence is used to study the as-prepared ZnO. The PL spectra show that the NBE emission is significantly quenched but emissions at 420 nm and 590 nm are seen in the visible. The intensity of emission at 590 nm increases with lowering the measurement temperature as indicated by temperature-dependent photoluminescence results. Annealing of the ZnO sample causes intensity variation of the emissions but the shape and center of the emission peaks are preserved. The intensity increases after short-time of annealing at 500 ^{o}C indicating that more defects centers in the ZnO crystal are generated. However, with longer annealing time, sintering of the crystals causes elimination of the defect centres, leading to a lower PL intensity. EPR spectra show the shallow-donor-center generated signals. However, no correlation between the EPR signal and PL emission could be concluded.

The polymer-metal ion complex is water soluble, which provides an efficient and cheap way to produce metal oxide films like ZnO nanocrystalline film. The evolution of the amorphous ZnPA film to the ZnO film exhibits a similar process as bulk sample. PL spectra show that in oxygen atmosphere, blue emission is promoted but the green one is suppressed. This confirms our assumption that blue emission is generated by crystal defects mainly zinc vacancies, while the green emission comes from oxygen vacancies.

Nanometer-sized mixed metal oxide (MMO) particles ($Zn_{1-x}Mg_xO$) with very precise stoichiometry are prepared employing this polymer-based method. The precursor is formed by loading a polyacrylate with metal ions followed by purification of the polymer metal ion complex via repeated precipitation/redissolution cycles. Calcination of the polymer precursor at 550 °C gives particles of the metastable solid solution of ZnO / MgO system in the composition range ($x < 0.2$ and $x \geq 0.82$). The MMO crystal particles are typically 20-50 nm in diameter. Doping of the ZnO by Mg^{2+} causes a shrinkage of lattice parameter ***c***. Effects of band gap engineering on the optical band gap are reported. The photoluminescence in the visible is also affected and its maximum shifts from 2.12 eV (pure ZnO) to 2.32 eV at x =0.21. The crystalline MMO particles start to undergo segregation into hexagonal and cubic phases upon annealing at 800 °C

Another case of ZnO-based mixed metal oxide ($Zn_{1-x}Co_xO$) is prepared via pyrolysis of the zinc and cobalt ions-loaded polymer precursor. The composition of the obtained MMOs conforms to the predetermined metal ion content in the zinc-cobalt polyacrylate precursor polymer. In the wurtzite phase, the cobalt ions are divalent in the high-spin $3d^7$ state and they occupy the zinc lattice site in the hexagonal structure as proved by XRD, absorption and photoluminescence spectra. The incorporation of cobalt ions does not cause the change of lattice parameter, but it does considerably suppress the PL emission of the material. The $Zn_{1-x}Co_xO$ is nanometer-sized particles in diameter of 20-50 nm. Magnetic property of the material is checked too and ferromagnetic ordering is not found in our sample.

The success in the two ZnO-based MMO nanocrystal preparation makes us believe that this method is promising for preparation of powders of a wide scope of mixed metal oxide alloys of metastable type from a polymer metal ion complex as the precursor, which is converted to the MMO at relatively low temperature where sintering is not yet prevailing.

An alternative chemical route to synthesize a metal oxide via metal ion-loaded polymeric particles made by inverse miniemulsion polymerization is presented. Zinc oxide nanopowders are prepared by this method. Zinc nitrate is used as both the zinc source and lipophobe which establishes the osmotic pressure to balance the Laplace pressure, maintaining the stability of droplets in the organic medium. The zinc-loaded polymer latex is prepared this way with polymeric particle diameters of 50-100 nm. Calcination of the precursor in the dry form gives zinc oxide nanoparticles sized around 20-40 nm diameter. The PL and IR spectra of this ZnO show differences with the ZnO sample obtained by calcination of the polymer-zinc complex. The reason is assumed to be ascribed to the difference of composition and architecture of the precursor polymers. In the polymer-salt complex method, the precursor in a great extent preserves the structure of the neutralized polyacrylic acid or polyacrylate as a linear polymer. However, the polymer latex may contain entangled and crosslinked polymer chains formed in the course of polymerization, leading to inhomogeneous distribution of zinc in the polymer chain. This has significant effect on the morphology of the final zinc oxide products such as particle size, aggregation degree. The complex mode between the carboxylate and zinc as well as the defects density and location in the nanocrystals are affected too.

Our aim in the long run is to synthesize useful nanocomposite material for optoelectronic application, which requires the obtained ZnO or doped-ZnO nanoparticles to be homogeneously incorporated into a polymer matrix. However, the stability of the inorganic particles in a polymer is still a technical challenge. Modification of the ZnO nanoparticles is therefore the crucial step to the formation of stable nanocomposites. The nanoparticles are treated in ethanolic solution of tetrabutylammonium phosphate with applying ultrasonication. The results of elementary analysis, FT-IR, ^{31}PNMR, and electron microscopy confirm the successful anchoring the phosphate groups on the particle surface without destructing the spherical shape and size of the particles. SEM images show that the weakly-aggregated particles in the powder form are separated after surface modification. And stability of the ZnO nanoparticles in aqueous dispersion is enhanced as shown in the significant increase of absolute value of zeta-potential due to the change of their surface charge density.

Acknowledgement

I should acknowledge all the people who have made their contributions to this work. Without their kind help in science as well as my life, a completion of this PhD dissertation is impossible.

First of all, the financial supports from Max Planck Society, including the scholarship from the International Max Planck Research School for Polymer Materials Science (IMPRS-PMS) in my first year study, are acknowledged.

I express my gratitude to Prof. Dr. G. Wegner, who offers me this working opportunity in his research group. I appreciate his patience, intelligence and valuable time for the continuous teaching and many scientific discussions in the last three years.

Dr. I. Lieberwirth, my project leader, is acknowledged for all of his advice since my arrival at the MPIP. Especially, he measured all my TEM samples and provided all the TEM images presented in this dissertation.

My sincere gratitude extends to Dr. B. Mathiasch for his assistance in measurement of AAS. The useful data from him are crucial to know the composition of the polymer precursors and the mixed metal oxides. Prof. Dr. G. Jeschke is thanked for his readiness and involvement in the measurement of EPR spectra.

I would also like to extend my thanks to Prof. Dr. W. Tremel, my second supervisor, for his useful comments and suggestions. I should also thank him to have offered me a teaching assistant position in his chemistry course.

Mr. H. Menges is acknowledged for his willingness and continuous assistance in the measurement of PL and Raman spectra. And Mr. W. Scholdei is thanked for his introduction in IR instrument and useful techniques. Mr. M. Bach is thanked for XRD measurement of the ZnO films. I thank Mr. Y. Yao for the time spent for measurement of NMR spectra and helpful advices for result interpretation.

Dr. H.-D. Werner is thanked for offering the possibility to conduct the X-ray diffraction measurements with the equipment of the Institute of Geosciences at the University of Mainz. His scientific assistant, Mr. R. Meffert is also acknowledged for his friendly technical help.

My appreciation goes to the colleagues in the AK Wegner. Mr. G. Glasser is thanked for his patience in measurement of all my SEM samples. My thanks are also extended to Ms. B. Müller and Ms. C. Rosenauer for DLS measurement. Dr. F. Laquai is thanked for the time-resolved PL measurement. His suave manner and meticulous work impressed me very much. Ms. K. Kirchhoff (TEM), Ms. P. Räder (Thermoanalysis) and Mr. M. Steiert (XRD) are acknowledged for imparting me the experimental techniques. Ms. S. Brand, my lab supervisor, cannot be forgotten. I appreciate her direction and cooperation in the security as well as the everyday running of the lab in the last years.

Finally, my families' unconditional supports are always my source of strength. Whenever I feel lonely and frustrated, their encouragement and comfort drive me to go further. I am indebted for their love and for being always on my side in the ups and downs during the past years. I thank my wife, Miss D. M. Li, who came to accompany me in my last year of study, gave me a lot of help in my life. I dedicate this dissertation to them.